

THE MINISTRY OF SCIENCE AND HIGHER EDUCATION OF THE RUSSIAN FEDERATION



ST. PETERSBURG STATE
POLYTECHNICAL UNIVERSITY
JOURNAL

Physics
and Mathematics

**VOLUME 18, No.2,
2025**

Peter the Great St. Petersburg
Polytechnic University
2025

ST. PETERSBURG STATE POLYTECHNICAL UNIVERSITY JOURNAL. PHYSICS AND MATHEMATICS

JOURNAL EDITORIAL COUNCIL

A.I. Borovkov – vice-rector for perspective projects;

V.A.I. Rudskoy – full member of RAS;

A.E. Zhukov – corresponding member of RAS.

JOURNAL EDITORIAL BOARD

V.K. Ivanov – Dr. Sci. (phys.-math.), prof., SPbPU, St. Petersburg, Russia, – editor-in-chief;

A.E. Fotiadi – Dr. Sci. (phys.-math.), prof., SPbPU, St. Petersburg, Russia, – deputy editor-in-chief;

V.M. Kapralova – Candidate of Phys.-Math. Sci., associate prof., SPbPU, St. Petersburg, Russia, – executive secretary;

V.I. Antonov – Dr. Sci. (phys.-math.), prof., SPbPU, St. Petersburg, Russia;

I.B. Bezprozvanny – Dr. Sci. (biology), prof., The University of Texas Southwestern Medical Center, Dallas, TX, USA;

A.V. Blinov – Dr. Sci. (phys.-math.), prof., SPbPU, St. Petersburg, Russia;

A.S. Cherepanov – Dr. Sci. (phys.-math.), prof., SPbPU, St. Petersburg, Russia;

D.V. Donetski – Dr. Sci. (phys.-math.), prof., State University of New York at Stony Brook, NY, USA;

V.V. Dubov – Dr. Sci. (phys.-math.), prof., SPbPU, St. Petersburg, Russia;

D.A. Firsov – Dr. Sci. (phys.-math.), prof., SPbPU, St. Petersburg, Russia;

P.A. Karaseov – Dr. Sci. (phys.-math.), prof., SPbPU, St. Petersburg, Russia;

A.S. Kheifets – Ph.D., prof., Australian National University, Canberra, Australia;

O.S. Loboda – Candidate of Phys.-Math. Sci., associate prof., SPbPU, St. Petersburg, Russia;

J.B. Malherbe – Dr. Sci. (physics), prof., University of Pretoria, Republic of South Africa;

V.M. Ostryakov – Dr. Sci. (phys.-math.), prof., SPbPU, St. Petersburg, Russia;

V.E. Privalov – Dr. Sci. (phys.-math.), prof., SPbPU, St. Petersburg, Russia;

E.M. Smirnov – Dr. Sci. (phys.-math.), prof., SPbPU, St. Petersburg, Russia;

A.V. Solov'yov – Dr. Sci. (phys.-math.), prof., MBN Research Center, Frankfurt am Main, Germany;

A.K. Tagantsev – Dr. Sci. (phys.-math.), prof., Swiss Federal Institute of Technology, Lausanne, Switzerland;

I.N. Toptygin – Dr. Sci. (phys.-math.), prof., SPbPU, St. Petersburg, Russia.

The journal is included in the List of leading peer-reviewed scientific journals and other editions to publish major findings of theses for the research degrees of Doctor of Sciences and Candidate of Sciences.

The publications are presented in the VINITI RAS Abstract Journal and Ulrich's Periodical Directory International Database.

The journal is published since 2008 as part of the periodical edition 'Nauchno-tekhnicheskie vedomosti SPb-GPU'.

The journal is registered with the Federal Service for Supervision in the Sphere of Telecom, Information Technologies and Mass Communications (ROSKOMNADZOR). Certificate ПИ № ФС77-52144 issued December 11, 2012.

The journal is distributed through the CIS countries catalogue, the «Press of Russia» joint catalogue and the «Press by subscription» Internet catalogue. The subscription index is 71823.

The journal is in the **Web of Science** (Emerging Sources Citation Index), **Scopus**, the **Russian Science Citation Index** (RSCI) and the **Directory of Open Access Journals** (DOAJ) databases.

© Scientific Electronic Library (<http://www.elibrary.ru>).

No part of this publication may be reproduced without clear reference to the source.

The views of the authors may not represent the views of the Editorial Board.

Address: 195251 Politekhnikeskaya St. 29, St. Petersburg, Russia.

Phone: 8 (812) 552-62-16.

<http://ntv.spbstu.ru/physics>

© Peter the Great St. Petersburg
Polytechnic University, 2025



НАУЧНО-ТЕХНИЧЕСКИЕ ВЕДОМОСТИ

САНКТ-ПЕТЕРБУРГСКОГО ГОСУДАРСТВЕННОГО
ПОЛИТЕХНИЧЕСКОГО УНИВЕРСИТЕТА

Физико-математические
науки

ТОМ 18, №2
2025

НАУЧНО-ТЕХНИЧЕСКИЕ ВЕДОМОСТИ САНКТ-ПЕТЕРБУРГСКОГО ГОСУДАРСТВЕННОГО ПОЛИТЕХНИЧЕСКОГО УНИВЕРСИТЕТА. ФИЗИКО-МАТЕМАТИЧЕСКИЕ НАУКИ

РЕДАКЦИОННЫЙ СОВЕТ ЖУРНАЛА

Боровков А.И., проректор по перспективным проектам;

Жуков А.Е., чл.-кор. РАН;

Рудской А.И., академик РАН.

РЕДАКЦИОННАЯ КОЛЛЕГИЯ ЖУРНАЛА

Иванов В.К., д-р физ.-мат. наук, профессор, СПбПУ, СПб., Россия, – главный редактор;

Фотиади А.Э., д-р физ.-мат. наук, профессор, СПбПУ, СПб., Россия, – зам. главного редактора;

Капралова В.М., канд. физ.-мат. наук, доцент, СПбПУ, СПб., Россия – ответственный секретарь;

Антонов В.И., д-р физ.-мат. наук, профессор, СПбПУ, СПб., Россия;

Безпрозванный И.Б., д-р биол. наук, профессор, Юго-Западный медицинский центр
Техасского университета, Даллас, США;

Блинов А.В., д-р физ.-мат. наук, профессор, СПбПУ, СПб., Россия;

Донецкий Д.В., д-р физ.-мат. наук, профессор, университет штата Нью-Йорк в Стоуни-Брук, США;

Дубов В.В., д-р физ.-мат. наук, профессор, СПбПУ, СПб., Россия;

Карасёв П.А., д-р физ.-мат. наук, профессор, СПбПУ, СПб., Россия;

Лобода О.С., канд. физ.-мат. наук, доцент, СПбПУ, СПб., Россия;

Малерб Й.Б., Dr.Sc. (Physics), профессор, университет Претории, ЮАР;

Остряков В.М., д-р физ.-мат. наук, профессор, СПбПУ, СПб., Россия;

Привалов В.Е., д-р физ.-мат. наук, профессор, СПбПУ, СПб., Россия;

Смирнов Е.М., д-р физ.-мат. наук, профессор, СПбПУ, СПб., Россия;

Соловьёв А.В., д-р физ.-мат. наук, профессор, Научно-исследовательский центр мезобионаносистем (MBN),
Франкфурт-на-Майне, Германия;

Таганцев А.К., д-р физ.-мат. наук, профессор, Швейцарский федеральный институт технологий,
Лозанна, Швейцария;

Топтыгин И.Н., д-р физ.-мат. наук, профессор, СПбПУ, СПб., Россия;

Фирсов Д.А., д-р физ.-мат. наук, профессор, СПбПУ, СПб., Россия;

Хейфец А.С., Ph.D. (Physics), профессор, Австралийский национальный университет,
Канберра, Австралия;

Черепанов А.С., д-р физ.-мат. наук, профессор, СПбПУ, СПб., Россия.

Журнал с 2002 г. входит в Перечень ведущих рецензируемых научных журналов и изданий, в которых должны быть опубликованы основные результаты диссертаций на соискание ученых степеней доктора и кандидата наук.

Сведения о публикациях представлены в Реферативном журнале ВИНТИ РАН, в международной справочной системе «Ulrich's Periodical Directory».

С 2008 года выпускается в составе сериального периодического издания «Научно-технические ведомости СПбГПУ».

Журнал зарегистрирован Федеральной службой по надзору в сфере информационных технологий и массовых коммуникаций (Роскомнадзор). Свидетельство о регистрации ПИ № ФС77-52144 от 11 декабря 2012 г.

Распространяется по Каталогу стран СНГ, Объединенному каталогу «Пресса России» и по Интернет-каталогу «Пресса по подписке». Подписной индекс 71823.

Журнал индексируется в базах данных **Web of Science** (Emerging Sources Citation Index), **Scopus**, а также включен в базы данных «**Российский индекс научного цитирования**» (РИНЦ), размещенную на платформе Научной электронной библиотеки на сайте <http://www.elibrary.ru>, и «**Directory of Open Access Journals**» (DOAJ).

При перепечатке материалов ссылка на журнал обязательна.

Точка зрения редакции может не совпадать с мнением авторов статей.

Адрес редакции и издательства:

Россия, 195251, Санкт-Петербург, ул. Политехническая, д. 29.

Тел. редакции 8 (812) 552-62-16.

<http://ntv.spbstu.ru/physics>

Contents

Condensed matter physics

Goltaev A. S., Fedina S. V., Fedorov V. V., Mozharov A. M., Novikova K. N., Maksimova A. A., Baranov A. I., Kaveev A. K., Pavlov A. V., Miniv D. V., Ustimenko R. V., Vinnichenko M. Ya., Mukhin I. S. *Infrared photodetectors based on InAsP epitaxial nanowires on silicon* 9

Obrazcov K. V., Chibisov A. N., Mamonova M. V. *The influence of hole states on the electronic and electrostatic properties of 2D layers based on the silicon-germanium-silicon heterostructure* 22

Simulation of physical processes

Antonova O. V., Ivanov M. V., Mikhailov A. A., Kuzmin V. A. *Application of mathematical modeling for describing the behavior of layered panels with a tetrahedral core* 30

Experimental technique and devices

Ermak S. V., Semenov V. V., Sergeeva M. V. *The effect of the magnetic field on the shielding efficiency in a rubidium atomic clock* 41

Kuptsov V. D. *The X-ray absorption immersion technology for enrichment of diamond ores: physical foundations and practical implementation* 49

Physical electronics

Berdnikov A. S., Egorova A. V., Krasnova N. K., Masyukevich S. V., Solov'ev K. V. *The influence of field misalignment and electric field asymmetry on the stability zones of a combined ion trap* ... 60

Physical materials technology

Ryabko A. A., Ovezov M. K., Maximov A. I., Permiakov N. V., Tuchkovskiy A. K., Vrublevskiy I. A., Muratova E. N., Aleshin A. N., Moshnikov V. A. *Polycrystalline films of $\text{MA}_x\text{MEA}_{1-x}\text{PbI}_3$ hybrid perovskites obtained by the solution method: Crystallization and morphology* 69

Zagidullina I. A., Guzhova A. A., Karulina E. A., Kulemina S. M. *The effect of PLA-based composite material history on its electret properties* 82

Kiselevich V. V. *An electrical lifetime of polymers in terms of the catastrophe theory* 93

Zolotarevsky N. Yu., Belikova Yu. A., Petrov S. N., Zisman A. A. *Formation of bainite below martensite start temperature in quenching low carbon steel* 109

Nuclear physics

Berdnikov Ya. A., Ivanishchev D. A., Kotov D. O., Malaev M. V., Riabov A. Yu. *Feasibility to measure the properties of charged $K^*(892)$ mesons and $\Sigma(1385)$ baryons in collisions of bismuth nuclei at an energy of 9.2 GeV in the NICA collider using the MPD experimental setup* 119

Applied and computational mathematics

Golovitskii A. P. *An inverse problem of differential equation systems in connection with the study of semiconductor materials and biomedical processes* 132

Theoretical physics

Ipatov A. N., Kupriianov G. A. *Collective excitations in the bulk doped semiconductor cadmium sulfide nanocrystal* 144

Содержание

Физика конденсированного состояния

- Голтаев А. С., Федина С. В., Фёдоров В. В., Можаров А. М., Новикова К. Н., Максимова А. А., Баранов А. И., Кавеев А. К., Павлов А. В., Минив Д. В., Устименко Р. В., Винниченко М. Я., Мухин И. С. *Фотодетекторы инфракрасного диапазона на основе эпитаксиальных нитевидных нанокристаллов InAsP на кремнии* 9
- Образцов К. В., Чибисов А. Н., Мамонова М. В. *Влияние дырочных состояний на электронные и электростатические свойства двумерных слоев на основе гетероструктуры кремний-германий-кремний* 22

Математическое моделирование физических процессов

- Антонова О. В., Иванов М. В., Михайлов А. А., Кузьмин В. А. *Применение математического моделирования для описания поведения слоистых панелей с тетраэдральным наполнителем* 30

Приборы и техника физического эксперимента

- Ермак С. В., Семенов В. В., Сергеева М. В. *Влияние магнитного поля на эффективность магнитного экранирования в рубидиевых атомных часах* 41
- Купцов В. Д. *Рентгено-абсорбционная иммерсионная технология обогащения алмазосодержащих руд: физические основы и практическая реализация* 49

Физическая электроника

- Бердников А. С., Егорова А. В., Краснова Н. К., Масюкевич С. В., Соловьев К. В. *Влияние несоосности полей и асимметрии электрического поля на зоны устойчивости комбинированной ионной ловушки* 60

Физическое материаловедение

- Рябко А. А., Овезов М. К., Максимов А. И., Пермьяков Н. В., Тучковский А. К., Врублевский И. А., Муратова Е. Н., Алешин А. Н., Мошников В. А. *Кристаллизация и морфология поликристаллических пленок гибридных перовскитов $\text{MA}_x\text{MEA}_{1-x}\text{PbI}_3$ полученных раствором методом* 69
- Загидуллина И. А., Гужова А. А., Карулина Е. А., Кулемина С. М. *Влияние предыстории композиционных материалов на основе полилактида на их электретные свойства (статья на английском языке)* 82
- Киселевич В. В. *Электрическая долговечность полимеров с точки зрения теории катастроф* 93
- Золоторевский Н. Ю., Беликова Ю. А., Петров С. Н., Зисман А. А. *Образование бейнита в температурном интервале мартенситного превращения при закалке низкоуглеродистой стали (статья на английском языке)* 109

Ядерная физика

Бердников Я. А., Иванищев Д. А., Котов Д. О., Малаев М. В., Рябов А. Ю. *Возможности измерять свойства заряженных $K^*(892)$ -мезонов и $\Sigma(1385)$ -барионов в столкновениях ядер висмута при энергии 9,2 ГэВ в ускорителе NICA на экспериментальной установке MPD* 119

Прикладная и вычислительная математика

Головицкий А. П. *Обратная задача систем дифференциальных уравнений в связи с изучением полупроводниковых материалов и биомедицинских процессов* 132

Теоретическая физика

Ипатов А. Н., Куприянов Г. А. *Коллективные возбуждения в объемно-легированных полупроводниковых нанокристаллах сульфида кадмия* 144

CONDENSED MATTER PHYSICS

Original article

DOI: <https://doi.org/10.18721/JPM.18201>

INFRARED PHOTODETECTORS BASED ON INASP EPITAXIAL NANOWIRES ON SILICON

*A. S. Goltaev¹✉, S. V. Fedina^{1,2}, V. V. Fedorov^{1,2}, A. M. Mozharov^{1,2},
K. N. Novikova^{1,2}, A. A. Maksimova¹, A. I. Baranov¹, A. K. Kaveev^{1,3},
A. V. Pavlov^{1,2}, D. V. Miniv¹, R. V. Ustimenko²,
M. Ya. Vinnichenko², I. S. Mukhin^{1,2}*

¹ Alferov University of RAS, St. Petersburg, Russia;

² Peter the Great St. Petersburg Polytechnic University, St. Petersburg, Russia;

³ Ioffe Institute, St. Petersburg, Russia

✉ goltaev@goltaev.ru

Abstract. In the paper, the upgraded technology of forming the epitaxial arrays of InAsP nanowires (NWs) synthesized on silicon substrates using molecular beam epitaxy has been presented. The optical and electrophysical properties of the NWs were studied. Based on the grown structures, a prototype of a short-wave infrared photodiode for a range from 1.2 μm to 1.9 μm was fabricated. Its band structures were numerically simulated. The temperature dependencies of the current-voltage characteristics and the spectral sensitivity of the photodetector prototype based on the NWs were experimentally studied. The external quantum efficiency of photoconversion of radiation with a wavelength of 1380 nm was found to be about 0.25% at 100 K.

Keywords: InAsP, silicon substrate, molecular beam epitaxy, nanowires, photodetector, quantum efficiency

Funding: A. V. Pavlov thanks the Russian Science Foundation (Agreement No. 23-72-01091) for financial support in calculating the InAsP zone diagram. The work on epitaxial synthesis, prototyping of IR photodiodes and their characterization was carried out with the financial support of the Ministry of Science and Higher Education of the Russian Federation within the framework of the State Assignment for Fundamental Research (subject code FSEG-2023-0007).

Citation: Goltaev A. S., Fedina S. V., Fedorov V. V., Mozharov A. M., Novikova K. N., Maksimova A. A., Baranov A. I., Kaveev A. K., Pavlov A. V., Miniv D. V., Ustimenko R. V., Vinnichenko M. Ya., Mukhin I. S., Infrared photodetectors based on InAsP epitaxial nanowires on silicon, St. Petersburg State Polytechnical University Journal. Physics and Mathematics. 18 (2) (2025) 9–21. DOI: <https://doi.org/10.18721/JPM.18201>

This is an open access article under the CC BY-NC 4.0 license (<https://creativecommons.org/licenses/by-nc/4.0/>)

Научная статья
УДК 621.383.52
DOI: <https://doi.org/10.18721/JPM.18201>

ФОТОДЕТЕКТОРЫ ИНФРАКРАСНОГО ДИАПАЗОНА НА ОСНОВЕ ЭПИТАКСИАЛЬНЫХ НИТЕВИДНЫХ НАНОКРИСТАЛЛОВ InAsP НА КРЕМНИИ

А. С. Голтаев¹✉, С. В. Федина^{1,2}, В. В. Фёдоров^{1,2}, А. М. Можаров^{1,2},
К. Н. Новикова^{1,2}, А. А. Максимова¹, А. И. Баранов¹, А. К. Кавеев^{1,3},
А. В. Павлов^{1,2}, Д. В. Минив¹, Р. В. Устименко²,
М. Я. Винниченко², И. С. Мухин^{1,2}

¹ Академический университет им. Ж. И. Алфёрова РАН, Санкт-Петербург, Россия;

² Санкт-Петербургский политехнический университет Петра Великого, Санкт-Петербург, Россия;

³ Физико-технический институт им. А. Ф. Иоффе РАН, Санкт-Петербург, Россия

✉ goltaev@goltaev.ru

Аннотация. В работе представлена усовершенствованная технология формирования эпитаксиальных массивов нитевидных нанокристаллов (ННК) InAsP, синтезированных на подложках кремния методом молекулярно-пучковой эпитаксии; исследованы оптические и электрофизические свойства этих ННК. На основе выращенных структур создан прототип фотодиода коротковолнового инфракрасного диапазона (1,2 – 1,9 мкм). Промоделированы зонные диаграммы фотодиода. Экспериментально исследованы температурные зависимости вольтамперных характеристик и спектральной чувствительности этого прототипа. Установлено, что внешняя квантовая эффективность фотопреобразования излучения с длиной волны 1380 нм составила примерно 0,25 % при температуре 100 К.

Ключевые слова: InAsP, кремниевая подложка, молекулярно-пучковая эпитаксия, нитевидный нанокристалл, фотодетектор, квантовая эффективность

Финансирование: А. В. Павлов благодарит Российский научный фонд (соглашение № 23-72- 01091) за финансовую поддержку при расчете зонной диаграммы InAsP. Работы по эпитаксиальному синтезу, созданию прототипов ИК-фотодиодов и их характеристике выполнены при финансовой поддержке Министерства науки и высшего образования РФ в рамках Государственного задания на проведение фундаментальных исследований (код темы FSEG0007-2023-).

Ссылка для цитирования: Голтаев А. С., Федина С. В., Фёдоров В. В., Можаров А. М., Новикова К. Н., Максимова А. А., Баранов А. И., Кавеев А. К., Павлов А. В., Минив Д. В., Устименко Р. В., Винниченко М. Я., Мухин И. С. Фотодетекторы инфракрасного диапазона на основе эпитаксиальных нитевидных нанокристаллов InAsP на кремнии // Научно-технические ведомости СПбГПУ. Физико-математические науки. 2025. Т. 18. № 2. С. 9–21. DOI: <https://doi.org/10.18721/JPM.18201>

Статья открытого доступа, распространяемая по лицензии CC BY-NC 4.0 (<https://creativecommons.org/licenses/by-nc/4.0/>)

Introduction

Heterostructures based on narrow-gap semiconductors (with the band gap less than 1 eV) are widely used in infrared (IR) optoelectronics [1, 2]. The practical significance of research in this field lies in the possibility of fabricating multispectral IR radiometers and thermal imagers for reconnaissance and surveillance systems as well as chemical sensor arrays used for detection and



identification of explosives. The most popular material platform for IR detectors is indium arsenide (InAs). The choice of the narrow-gap (band gap E_g is 0.35 eV at a temperature of 300 K) InAs semiconductor material is due to the high mobility of charge carriers (more than $10^4 \text{ cm}^2/(\text{V}\cdot\text{s})$) and the long lifetime of minority carriers. However, further advances in detector manufacturing are limited by two main factors. First, the small band gap inevitably leads to accelerated thermal generation rates and is accompanied by nonradiative recombination of charge carriers, which in turn leads to high dark currents, increased noise levels, and decreased sensitivity of photodetector arrays [3]. Secondly, lattice mismatch between the layers of planar A^3B^5 heterostructure and substrate significantly limits the possibilities for controlling the band profile of heterostructures [4].

The performance characteristics of photodetector arrays can be improved by transition from planar structures to structures with a well-developed surface, namely, to arrays of nanowires (NWs) [5]. In this case, due to developed lateral surface of the NWs, nanostructures of high crystalline perfection can be grown on lattice-mismatched substrates, in particular, on silicon. Moreover, NW arrays are characterized by stronger light absorption compared with planar layers of the same composition and equivalent thickness [6, 7]. The addition of phosphorus to the InAsP solid solution causes an increase in the band gap with a consequent decrease in dark currents and corresponding noise from photodetectors operating in the short-wavelength IR range (1.0–3.5 μm) [8].

In this paper, we propose an improved technological approach to fabrication of photodetectors in the near and short-wavelength IR ranges (1.3–1.9 μm) using InAsP NW arrays epitaxially grown on silicon substrates as the active area. The effects of localization and resonant amplification of the IR electromagnetic field in the NWs can significantly improve the characteristics of such photodetectors:

- reduce the volume of their active area while maintaining their sensitivity;
- reduce their dark current;
- increase the performance of devices based on them [9].

Materials and methods

The InAsP/Si heterojunction is a type II junction with partial band overlap, which determines the choice of diode polarity. As follows from the band diagram (Fig. 1), only the combination of InAsP with n -type conductivity and Si substrate with p -type conductivity (n -InAsP/ p -Si) is possible for the array to function as a photodiode. The inverse combination (p -InAsP/ n -Si) will lead to the formation of barriers for charge carriers. Thus, the built-in field is generated at the n -InAsP/ p -Si

heterojunction (see Fig. 1,*a*). It is known that the surface states of NWs strongly influence the energy band diagram of nanostructures.

In view of the above, defects were added to the lateral surface of the considered model for InAsP NWs, whose presence in the case of InAsP material with the band gap of about 600–650 MeV leads to forced injection of electrons from the defect levels, band bending near the surface (see Fig. 1,*b*) and additional contribution to separation of charge carriers during photodiode operation.

InAsP NW arrays were epitaxially grown on silicon substrates doped to p -type conductivity (boron-doped p -type Si(111)). The substrates had a diameter of 3 inches, were misoriented by 4° toward (111), and had a resistivity of 0.4–0.6 $\Omega\cdot\text{cm}$.

The Veeco GEN III molecular beam epitaxy (MBE) system used was equipped with an In effusion cell as well as P_2 and As_4 cracker cells with needle valves acting as molecular sources. The intensity of molecular beams of group V and III

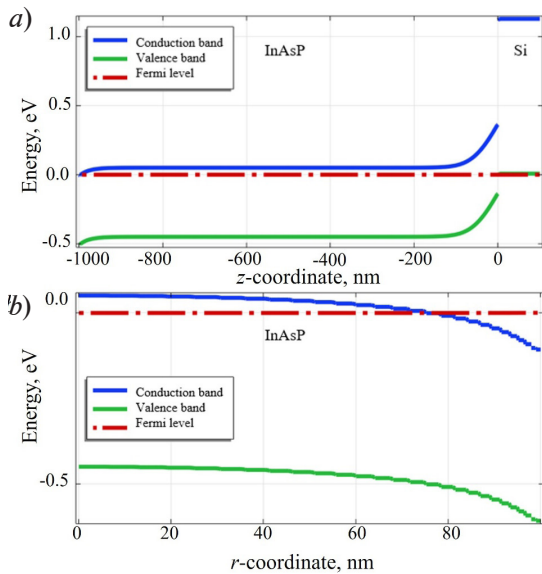


Fig. 1. Band structure of n -InAsP/ p -Si photodiode in longitudinal (*a*) and transverse (*b*) directions

elements was taken proportional to the pressure measured by a Bayard–Alpert ionization gauge. The substrate temperature (growth temperature) was measured by a thermocouple calibrated by the phase transition temperature of Si(111) $7\times 7 \leftrightarrow 1\times 1$ surface reconstruction. Monitoring of the growth process and analysis of the crystal structure of NWs was performed *in situ* by reflection high-energy electron diffraction (RHEED).

The main stages of formation of NW arrays on silicon are shown in Fig. 2. Before the NWs were grown by MBE, the silicon substrates were cleaned by a modified Shiraki method [10]. At the final stage of cleaning, it was carried out by wet chemical oxidation in boiling aqueous solution of ammonia and hydrogen peroxide ($\text{NH}_4\text{OH} : \text{H}_2\text{O}_2 : \text{H}_2\text{O}$) in a ratio of 1 : 1 : 3. As a result of the procedure, a thin (about 1.5 nm) layer of SiO_x oxide was formed on the silicon surface (see Fig. 2,a)

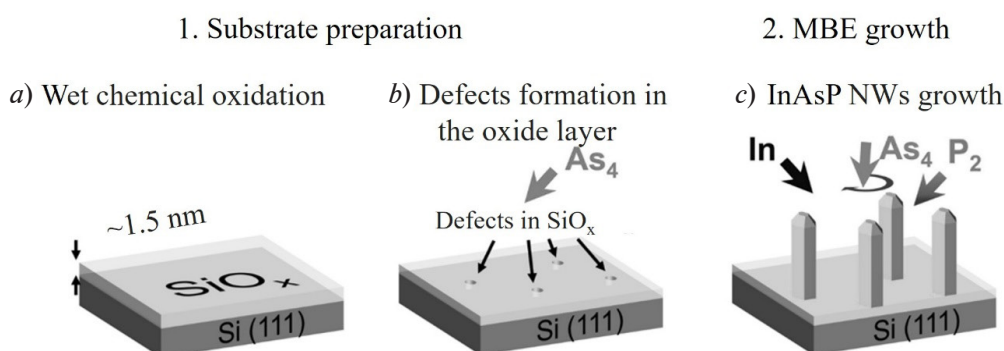


Fig. 2. Main stages of epitaxial growth of InAsP NW arrays on silicon: substrate preparation 1, material growth by molecular beam epitaxy 2; cleaning by wet chemical oxidation (a), formation of defects in SiO_x oxide layer (b); growth of NWs (c)

Immediately before the start of the epitaxial growth stage, silicon substrates were subjected to thermal annealing under ultrahigh vacuum conditions for 30 minutes at a temperature of 780 °C, which led to the formation of defects in the layer of surface silicon oxide serving as NW nucleation centers (Fig. 2,b) [11, 12]. Then, as the substrate cooled to the growth temperature in As_4 flux, the As-substituted silicon surface stabilized in the defect regions of the SiO_x surface layer (Fig. 2,b) [13]. The formation of NWs was initiated by switching group V sources to the necessary fluxes and opening the indium shutter (Fig. 2,c). To ensure uniform distribution of molecular fluxes during the growth process, the substrate was rotated at a speed of 5 rpm. In general, varying the group V growth fluxes makes it possible to regulate the incorporation of phosphorus and arsenic atoms into InAsP NWs, thus controlling the band gap of the NWs to ensure a given spectral sensitivity of photodetectors based on them.

The considered NW arrays were grown at a substrate temperature of 520 °C for 60 minutes and a P/As flux ratio of 1. InAsP NWs were not doped during growth; due to the large number of surface states on the lateral surface of the NWs, the synthesized nanostructures were characterized by *n*-type conductivity. Reference samples of InAs NWs were additionally grown.

Notably, the method applied for self-induced growth of NW arrays allows to achieve an extremely high surface density of NWs ($\geq 10 \mu\text{m}^{-2}$), which significantly reduces light scattering, manifesting as an opaque black surface of the sample. To fabricate photodetector arrays, we used the grown InAsP NWs with a diameter of 110 ± 41 nm, a length of 900 ± 300 nm, and a surface density of $5.5 \mu\text{m}^{-2}$. The morphology of the synthesized arrays was studied by scanning electron microscopy (SEM) using a Zeiss SUPRA 25-30-63 microscope. (see the SEM image in the inset in Fig. 4,a).

Studies of the crystalline structure of NWs by transmission electron microscopy (TEM) show that the axis of NW growth coincides with the [0001] axis. A large number of packing defects are observed in NWs along the (0001) growth plane [14, 15].

The photoluminescent (PL) properties of NW arrays were studied using a Bruker Vertex 80v FT-IR spectrometer equipped with a KBr beam splitter and Ge optical windows. The resolution of the photoluminescence spectra was about 8 MeV. A closed-cycle cryostat (Janis PTCM-4-7,



USA) with zinc selenide windows was used for low-temperature measurements. A continuous-wave diode-pumped solid-state Nd:YAG laser ($\lambda = 1064$ nm) was used to excite the photoluminescent response. The measurements were carried out with *p*-polarization and a 45° incidence angle of pump radiation. An opto-mechanical modulator with a frequency of 340 Hz was used to modulate the laser radiation. The PL signal was recorded by an InSb photodiode cooled with liquid nitrogen and detected by an SR830 DSP lock-in amplifier.

The virtual crystal approximation (VCA) was used to model the electro-optical properties of solid solutions. The plane -wave basis was used to represent wave functions; the PBEsol exchange-correlation functional was used for geometry optimization [16]; the TB09 meta-GGA potential was used for correct description of electronic properties and for construction of band diagrams [17]. The calculations were carried out taking into account the spin-orbit interaction. According to the calculation results (see Fig. 3,*b*), the observed shift in the position of the PL maximum corresponds to $\text{InAs}_{0.81}\text{P}_{0.19}$.

The electrophysical characteristics and spectral dependence of the photoconversion efficiency of the array were measured by a four-probe system mounted on a cold finger of a nitrogen cryostat. A halogen lamp and a monochromator (SOLAR Laser Systems M266-IV) were used as a tunable source of monochromatic radiation. The photocurrent was measured using a Stanford Research System SR570 current preamplifier and a Stanford Research System SR830 lock-in amplifier. A reference photodiode with known characteristics in the spectral range of 600–2000 nm was used for calibration.

Fabrication of photodetector mesa structures

To study the functional characteristics of the arrays, photodetector mesa structures were fabricated by post-growth technologies based on InAsP NW arrays epitaxially grown on Si. Fig. 3 schematically shows the stages of the formation and a simplified diagram of the NW-based photodetector.

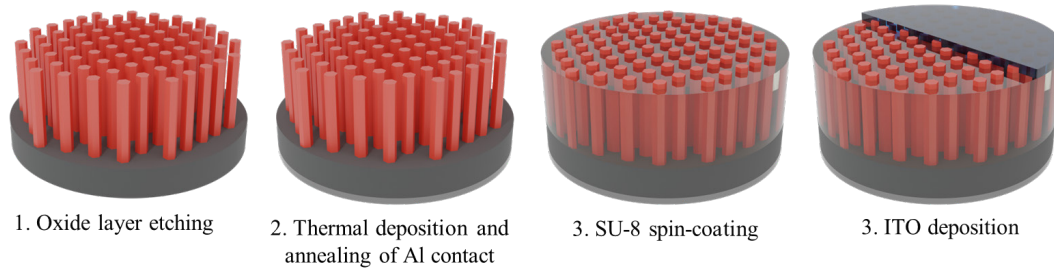


Fig. 3. Fabrication stages and schematic structure of InAsP NW photodetector on Si substrate:

H^+ etching and removal of oxide layer from the back of the substrate (1); thermal deposition and subsequent annealing of Al contact (2); planarization of NW array with SU-8 epoxy resin layer (3); deposition of transparent upper contact made of ITO (4)

At the first stage, H^+ hydrogen plasma was etched at a pressure of 500 mTorr with a discharge power of 20 W for 5 minutes; this treatment is necessary to suppress surface states and recombination centers at the heterojunction between InAs/Si NWs [18]. After the oxide layer is removed, an ohmic back contact (aluminum, 200 nm thick) to the silicon substrate was formed by vacuum thermal evaporation (heating of the target with an electron beam) and rapid thermal annealing (300°C). For partial planarization of the NW array, a layer of epoxy resin (SU-8 photoresist) was applied to the front side of the array by spin-coating, filling the free space between the NWs in the array. The thickness of the applied photoresist layer, controlled by SEM, ensured the formation of front contact to the tips of the NWs (see Fig. 3). To remove the surface oxide from the tips of the NWs, the structures were pretreated in 1 : 3 HCl : H_2O solution. The transparent top contact was a 200 nm thick indium tin oxide (ITO) layer deposited through a shadow mask by high-frequency magnetron sputtering; the Boc Edwards Auto 500 RF 10 Thermal Resistance Evaporator Coater (Great Britain) was used for this purpose.

Results and discussion

The characteristic PL spectra obtained at 5 K from arrays of reference InAs NWs and InAsP solid solution NWs are shown in Fig. 4, *a*. Evidently, the position of the maximum of InAsP NWs is shifted to the region of higher energies by about 120 MeV relative to InAs NWs; this is a consequence of the wider band gap of the InAsP solid solution.

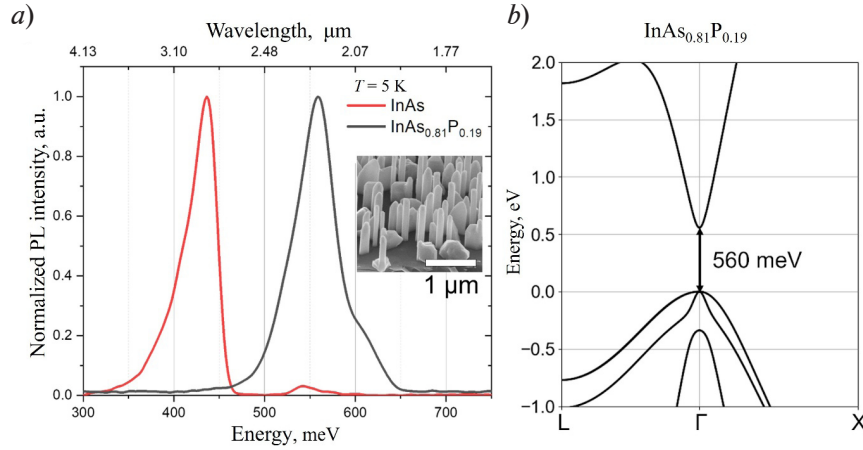


Fig. 4. Low-temperature PL spectra from InAs and InAsP NW arrays epitaxially grown on Si (*a*) and calculated band diagram of $\text{InAs}_{0.81}\text{P}_{0.19}$ with sphalerite crystal structure (*b*)
Inset: SEM image of InAsP NWs

To estimate the phosphorus concentration in the sample under consideration, measurement results of low-temperature PL were compared with the simulation results obtained within the framework of density functional theory (see Fig. 3, *b*). The simulations were carried out in the ABINIT program [19].

Fig. 5, *a* shows the measured and calculated dark I – V characteristics (VAC) at various temperatures. Numerical simulation shows that a constant current value should be observed for a negative bias in the ideal case. This means that the main contribution to the system is made only by thermally generated charge carriers. The direct branch reflects an exponential dependence, which corresponds to the process of injection of holes from silicon substrate into the InAsP array.

The experimentally obtained I – V curve (dependence of the reverse current on the magnitude of reverse-bias voltage) indicates the presence of leakage currents in the array, associated with non-radiative recombination. The latter is caused by the capture of charge carriers into trap states forming near the InAsP/Si interface. A decrease in the operating temperature leads to slowdown

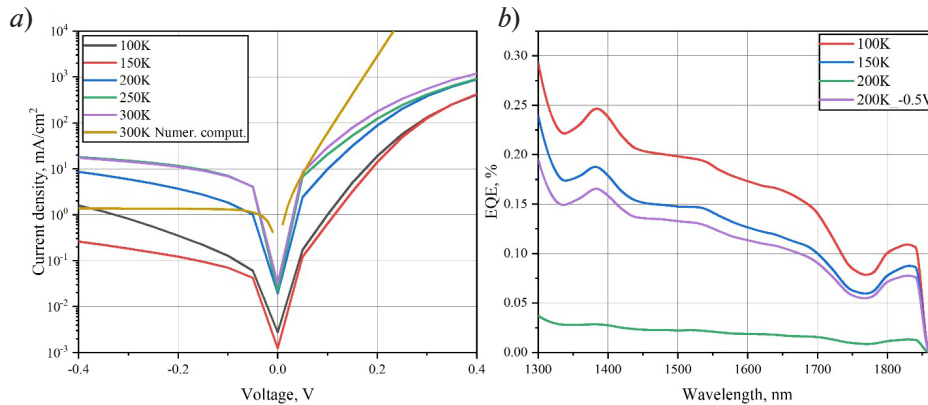


Fig. 5. Electrophysical and spectral temperature-dependent characteristics of photodiode: dependences of current density normalized by the area of the NW array in mesa on voltage (*a*); spectrum of external quantum efficiency (EQE) (*b*)



in both thermal generation of carriers and their recombination through defects, which is manifested as a decrease in reverse current. In addition, there is an increase in the knee voltage of the diode caused by an increase in the band gap of InAsP with a decrease in temperature. The positive branch has a characteristic bend associated with the presence of a series resistance in the measuring circuit, induced, in particular, by the current-collecting top contact.

Spectral dependences of the external quantum efficiency (EQE) of photoconversion were experimentally obtained for the considered photodetector array at zero bias in the wavelength range of 1300–1900 nm. These EQE spectra are shown in Fig. 5, *b*. Notably, the photoresponse for wavelengths less than 1300 nm due to absorption in the silicon substrate was not considered in this study. For example, there is no photoresponse outside the absorption range of silicon at 200 K and above (without the application of an external electric bias), which indicates a high recombination rate of photogenerated charge carriers. As the temperature decreases below 200 K, the photocurrent in the long-wavelength region of the spectrum begins to increase. At 100 K, the EQE value at a wavelength of 1380 nm reaches 0.25%.

We can assume that this behavior of EQE is caused by a change in the carrier transport mechanism in the active area of the NW array with a decrease in temperature. The Debye screening length of the array was estimated to verify this assumption. It was found that at 300 K, the calculated Debye length for InAsP is about 150 nm (particle concentration $n_i = 8 \cdot 10^{14} \text{ cm}^{-3}$), which is significantly shorter than the length of the NWs. Therefore, thermally generated charge carriers effectively screen the built-in electric field, and primarily diffusive carrier transport takes place in the active area of the array. Due to the small lateral size and well-developed surface of the NWs, this type of transport is ineffective, which leads to preferential recombination of photogenerated carriers on the surface states.

As the temperature decreases, the Debye length increases, and the screening area increases. The main transport mechanism in the region of incomplete screening is carrier drift in the built-in electric field between *p*-Si and *n*-InAsP, which occurs due to the difference in the positions of the Fermi levels in the materials.

It can be concluded from the above that the diffusion length of photogenerated carriers in the considered arrays at $T \geq 200 \text{ K}$ is insufficient for effective separation of charge carriers. This is probably due to high density of packaging defects in NWs, reducing the mobility of charge carriers.

Analysis of the observed nonuniform spectral dependence of the array's photoresponse leads us to conclude that the light absorption efficiency strongly depends on the diameter and surface density of the NWs in the array [20]. The calculation data and accounting for the morphology of the NW array (the NW diameter is about 110 nm, the surface density is about $5.5 \text{ } \mu\text{m}^{-2}$) suggest that the absorption coefficient of radiation with a wavelength of 1300 nm in the given array does not exceed 5–7%.

Therefore, to further increase the sensitivity of the InAsP NW-based IR photodetector, it is necessary to optimize the morphological parameters of the NW array by increasing their diameter to 400–500 nm and surface density to $10 \text{ } \mu\text{m}^{-2}$ or more.

Conclusion

We carried out comprehensive studies on the formation of InAsP NW arrays as well as their optical and electrophysical properties. Post-growth technologies were developed to fabricate prototype photodetectors based on InAsP NW arrays on the surface of Si(111) substrate. The temperature dependences of their spectral sensitivity and electrophysical characteristics were studied. We established that the experimentally measured external quantum efficiency of the system under study reaches 0.25% for the IR range.

REFERENCES

1. **Abrand A., Baboli M. A., Fedorenko A., et al.**, Localized self-assembly of InAs nanowire arrays on reusable Si substrates for substrate-free optoelectronics, *ACS Appl. Nano Mater.* 5 (1) (2022) 840–851.
2. **Song C., Wang P., Qian Y., et al.**, Enhanced terahertz radiation from InAs (100) with an embedded InGaAs hole blocking layer, *Opt. Express*. 28 (18) (2020) 25750–25756.
3. **Sze S. M.**, Physics of semiconductor devices, 1st Edition, John Wiley & Sons Inc., Chichester, UK, 1969.
4. **Martyniuk P., Antoszewski J., Martyniuk M., et al.**, New concepts in infrared photodetector designs, *Appl. Phys. Rev.* 1 (4) (2014) 041102.
5. **Mertensson T., Svensson C. P. T., Wacaser B. A. et al.**, Epitaxial III–V nanowires on silicon, *Nano Lett.* 4 (10) (2004) 1987–1990.
6. **LaPierre R. R., Robson M., Azizur-Rahman K. M., et al.**, A review of III–V nanowire infrared photodetectors and sensors, *J. Phys. D: Appl. Phys.* 50 (12) (2017) 123001.
7. **Li Z., He Z., Xi C., et al.**, Review on III–V semiconductor nanowire array infrared photodetectors, *Adv. Mater. Technol.* 8 (13) (2023) 2202126.
8. **Robson M., Azizur-Rahman K. M., Parent D., et al.**, Multispectral absorptance from large-diameter InAsSb nanowire arrays in a single epitaxial growth on silicon, *Nano Futures*. 1 (3) (2017) 035001.
9. **Wang, B., Leu P. W.**, Tunable and selective resonant absorption in vertical nanowires, *Opt. Lett.* 37 (18) (2012) 3756–3758.
10. **Ishizaka A., Shiraki Y.**, Low temperature surface cleaning of silicon and its application to silicon MBE, *J. Electrochem. Soc.* 133 (4) (1986) 666.
11. **Koblmaier G., Hertenberger S., Vizbaras K.**, Self-induced growth of vertical free-standing InAs nanowires on Si (111) by molecular beam epitaxy, *Nanotechnol.* 21 (36) (2010) 365602.
12. **Fedorov V. V., Berdnikov Y., Sibirev N. V., et al.**, Tailoring morphology and vertical yield of self-catalyzed GaP nanowires on template-free Si substrates, *Nanomater.* 11 (8) (2021) 1949.
13. **Tomioka K., Motohisa J., Hara S., Fukui T.**, Control of InAs nanowire growth directions on Si, *Nano Lett.* 8 (10) (2008) 3475–3480.
14. **Fedorov V., Vinnichenko M., Ustimenko R., et al.**, Non-uniformly strained core–shell InAs/InP nanowires for mid-infrared photonic applications, *ACS Appl. Nano Mater.* 6 (7) (2023) 5460–5468.
15. **Kaveev A. K., Fedorov V. V., Dvoretckaya L. N., et al.**, Formation of single and heterostructured nanowires based on InAs_{1-x}P_x solid solutions on Si (111), *Semicond.* 58 (4) (2024) 327–330.
16. **Perdew J. P., Ruzsinszky A., Csonka G. I., et al.**, Generalized gradient approximation for solids and their surfaces, *Phys. Rev. Lett.* 2008. arXiv:0707.2088 [cond-mat.other]. <https://doi.org/10.48550/arXiv.0707.2088>.
17. **Tran F., Blaha P.**, Accurate band gaps of semiconductors and insulators with a semilocal exchange-correlation potential, *Phys. Rev. Lett.* 102 (22) 2009 226401.
18. **Shugurov K. Yu., Mozharov A. M., Bolshakov A. D., et al.**, GaN nanowires/*p*-Si interface passivation by hydrogen plasma treatment, *J. Phys.: Conf. Ser.* 1537(1). (2020) 012012.
19. **Gonze X., Amadon B., Antonius G., et al.**, The Abinit project: Impact, environment and recent developments, *Comput. Phys. Commun.* 248 (March) (2020) 107042.
20. **Dvoretckaia L., Mozharov A., Pavlov A., et al.**, Numerical study of detectivity for near-IR photodetectors based on InAsP NWs, *Scr. Mater.* 226 (15 March) (2023) 115246.



СПИСОК ЛИТЕРАТУРЫ

1. Abrand A., Baboli M. A., Fedorenko A., Polly S. J., Manfreda-Schulz E., Hubbard S. M., Mohseni P. K. Localized self-assembly of InAs nanowire arrays on reusable Si substrates for substrate-free optoelectronics // *ACS Applied Nano Materials*. 2022. Vol. 5. No. 1. Pp. 840–851.
2. Song C., Wang P., Qian Y., Zhou G., Nutzel R. Enhanced terahertz radiation from InAs (100) with an embedded InGaAs hole blocking layer // *Optics Express*. 2020. Vol. 28, No. 18. Pp. 25750–25756.
3. Зи С. М. Физика полупроводниковых приборов. М.: Мир. 1973, 456 с.
4. Martyniuk P., Antoszewski J., Martyniuk M., Faraone L., Rogalski A. New concepts in infrared photodetector designs // *Applied Physics Reviews*. 2014. Vol. 1. No. 4. P. 041102.
5. Mertensson T., Svensson C. P. T., Wacaser B. A., Larsson M. W., Seifert W., Deppert K., Gustafsson A., Wallenberg L. R., Samuelson L. Epitaxial III–V nanowires on silicon // *Nano Letters*. 2004. Vol. 4. No. 10. Pp. 1987–1990.
6. LaPierre R. R., Robson M., Azizur-Rahman K. M., Kuyanov P. A review of III–V nanowire infrared photodetectors and sensors // *Journal of Physics D: Applied Physics*. 2017. Vol. 50. No. 12. P. 123001.
7. Li Z., He Z., Xi C., Zhang F., Huang L., Yu Y., Tan H.H., Jagadish C., Fu L. Review on III–V semiconductor nanowire array infrared photodetectors // *Advanced Materials Technologies*. 2023. Vol. 8. No. 13. P. 2202126.
8. Robson M., Azizur-Rahman K. M., Parent D., Wojdylo P., Thompson D. A., LaPierre R. R. Multispectral absorptance from large-diameter InAsSb nanowire arrays in a single epitaxial growth on silicon // *Nano Futures*. 2017. Vol. 1. No. 3. P. 035001.
9. Wang B., Leu P. W. Tunable and selective resonant absorption in vertical nanowires // *Optics Letters*. 2012. Vol. 37. No. 18. Pp. 3756–3758.
10. Ishizaka A., Shiraki Y. Low temperature surface cleaning of silicon and its application to silicon MBE // *Journal of the Electrochemical Society*. 1986. Vol. 133. No. 4. P. 666.
11. Koblmüller G., Hertenberger S., Vizbaras K., Bichler M., Bao F., Zhang J.-P., Abstreiter G. Self-induced growth of vertical free-standing InAs nanowires on Si(111) by molecular beam epitaxy // *Nanotechnology*. 2010. Vol. 21. No. 36. P. 365602.
12. Fedorov V. V., Berdnikov Y., Sibirev N. V., et al. Tailoring morphology and vertical yield of self-catalyzed GaP nanowires on template-free Si substrates // *Nanomaterials*. 2021. Vol. 11. No. 8. P. 1949.
13. Tomioka K., Motohisa J., Hara S., Fukui T. Control of InAs nanowire growth directions on Si // *Nano Letters*. 2008. Vol. 8. No. 10. Pp. 3475–3480.
14. Fedorov V., Vinnichenko M., Ustimenko R., et al. Non-uniformly strained core–shell InAs/InP nanowires for mid-infrared photonic applications // *ACS Applied Nano Materials Journal*. 2023. Vol. 6. No. 7. Pp. 5460–5468.
15. Kaveev A. K., Fedorov V. V., Dvoretckaya L. N., Fedina S. V., Mukhin I. S. Formation of single and heterostructured nanowires based on $\text{InAs}_{1-x}\text{P}_x$ solid solutions on Si (111) // *Semiconductors*. 2024. Vol. 58. No. 4. Pp. 327–330.
16. Perdew J. P., Ruzsinszky A., Csonka G. I., Vydrov O. A., Scuseria G. E., Constantin L. A., Zhou X., Burke K. Generalized gradient approximation for solids and their surfaces // *Physical Review Letters*. 2008 arXiv:0707.2088 [cond-mat.other]. <https://doi.org/10.48550/arXiv.0707.2088>.
17. Tran F., Blaha P. Accurate band gaps of semiconductors and insulators with a semilocal exchange-correlation potential // *Physical Review Letters*. 2009. Vol. 102. No. 22. P. 226401.
18. Shugurov K. Yu., Mozharov A. M., Bolshakov A. D., Fedorov V. V., Uvarov A. V., Kudryashov D. A., Mikhailovskii V. Yu., Cirilin G. E., Mukhin I. S. GaN nanowires/*p*-Si interface passivation by hydrogen plasma treatment // *Journal of Physics: Conference Series*. 2020. Vol. 1537. No. 1. P. 012012.
19. Gonze X., Amadon B., Antonius G., et al. The Abinit project: Impact, environment and recent developments // *Computer Physics Communications*. 2020. Vol. 248. March. P. 107042.
20. Dvoretckaia L., Mozharov A., Pavlov A., Polozkov R., Mukhin I. Numerical study of detectivity for near-IR photodetectors based on InAsP NWs // *Scripta Materialia*. 2023. Vol. 226. 15 March. P. 115246.

THE AUTHORS

GOLTAEV Aleksandr S.

Alferov University of RAS

8 Khlopin St., St. Petersburg, 194021, Russia

goltaev@goltaev.ru

ORCID: 0000-0001-8179-3169

FEDINA Sergey V.

Alferov University of RAS

Peter the Great St. Petersburg Polytechnic University

8 Khlopin St., St. Petersburg, 194021, Russia

fedina.serg@yandex.ru

ORCID: 0000-0001-7521-3754

FEDOROV Vladimir V.

Alferov University of RAS

Peter the Great St. Petersburg Polytechnic University

8 Khlopin St., St. Petersburg, 194021, Russia

burunduk.uk@gmail.com

ORCID: 0000-0001-5547-9387

MOZHAROV Alexey M.

Alferov University of RAS

Peter the Great St. Petersburg Polytechnic University

8 Khlopin St., St. Petersburg, 194021, Russia

alex000090@gmail.com

ORCID: 0000-0002-8661-4083

NOVIKOVA Kristina N.

Alferov University of RAS

Peter the Great St. Petersburg Polytechnic University

8 Khlopin St., St. Petersburg, 194021, Russia

novikova_k@spbau.ru

ORCID: 0000-0001-8440-494X

MAKSIMOVA Alina A.

Alferov University of RAS

8 Khlopin St., St. Petersburg, 194021, Russia

deer.blackgreen@yandex.ru

ORCID: 0000-0002-3503-7458

BARANOV Artem I.

Alferov University of RAS

8 Khlopin St., St. Petersburg, 194021, Russia

baranov_art@spbau.ru

ORCID: 0000-0002-4894-6503

KAVEEV Andrey K.

Alferov University of RAS

Ioffe Institute of RAS

26 Polytekhnicheskaya St., St. Petersburg, 194021, Russia

kaveev@mail.ioffe.ru

ORCID: 0000-0002-3640-677X

PAVLOV Alexander V.

Alferov University of RAS



Peter the Great St. Petersburg Polytechnic University
8 Khlopin St., St. Petersburg, 194021, Russia
a.pavlov@physics.spbstu.ru
ORCID: 0000-0003-1125-6653

MINIV Dmitry V.
Alferov University of RAS
8 Khlopin St., St. Petersburg, 194021, Russia
dimin46@mail.ru
ORCID: 0009-0006-3064-4175

USTIMENKO Ratmir V.
Peter the Great St. Petersburg Polytechnic University
29 Politechnicheskaya St., St. Petersburg, 195251, Russia
ustimenko_rv@spbstu.ru
ORCID: 0000-0003-4123-4375

VINNICHENKO Maksim Ya.
Peter the Great St. Petersburg Polytechnic University
29 Politechnicheskaya St., St. Petersburg, 195251, Russia
mvin@spbstu.ru
ORCID: 0000-0002-6118-0098

MUKHIN Ivan S.
Alferov University of RAS
Peter the Great St. Petersburg Polytechnic University
8 Khlopin St., St. Petersburg, 194021, Russia
imukhin@yandex.ru
ORCID: 0000-0001-9792-045X

СВЕДЕНИЯ ОБ АВТОРАХ

ГОЛТАЕВ Александр Сергеевич — лаборант лаборатории возобновляемых источников энергии Санкт-Петербургского академического университета имени Ж. И. Алфёрова РАН.

194021, Россия, г. Санкт-Петербург, ул. Хлопина, 8, к. 3

goltaev@goltaev.ru

ORCID: 0000-0001-8179-3169

ФЕДИНА Сергей Викторович — лаборант лаборатории возобновляемых источников энергии Санкт-Петербургского академического университета имени Ж. И. Алфёрова РАН, инженер-исследователь научно-исследовательской лаборатории эпитаксиальных наноструктур соединений A^3B^5 на кремнии Санкт-Петербургского политехнического университета Петра Великого.

194021, Россия, Санкт-Петербург, ул. Хлопина, 8, к. 3

fedina.serg@yandex.ru

ORCID: 0000-0001-7521-3754

ФЁДОРОВ Владимир Викторович — кандидат физико-математических наук, старший научный сотрудник лаборатории возобновляемых источников энергии Санкт-Петербургского академического университета имени Ж. И. Алфёрова РАН, старший научный сотрудник высшей инженерно-физической школы Санкт-Петербургского политехнического университета Петра Великого.

194021, Россия, г. Санкт-Петербург, ул. Хлопина, 8, к. 3

burunduk.uk@gmail.com

ORCID: 0000-0001-5547-9387

МОЖАРОВ Алексей Михайлович — кандидат физико-математических наук, старший научный сотрудник Центра приоритетных направлений науки и технологий Санкт-Петербургского академического университета имени Ж. И. Алфёрова РАН, старший научный сотрудник научно-исследовательской лаборатории эпитаксиальных наноструктур соединений A^3B^5 на кремнии Санкт-Петербургского политехнического университета Петра Великого.

194021, Россия, г. Санкт-Петербург, ул. Хлопина, 8, к. 3

alex000090@gmail.com

ORCID: 0000-0002-8661-4083

НОВИКОВА Кристина Николаевна — лаборант лаборатории возобновляемых источников энергии Санкт-Петербургского академического университета имени Ж. И. Алфёрова РАН, инженер-исследователь научно-исследовательской лаборатории эпитаксиальных наноструктур соединений A^3B^5 на кремнии Санкт-Петербургского политехнического университета Петра Великого.

194021, Россия, г. Санкт-Петербург, ул. Хлопина, 8, к. 3

novikova_k@spbau.ru

ORCID: 0000-0001-8440-494X

МАКСИМОВА Алина Андреевна — инженер лаборатории возобновляемых источников энергии Санкт-Петербургского академического университета имени Ж. И. Алфёрова РАН.

194021, Россия, г. Санкт-Петербург, ул. Хлопина, 8, к. 3

deer.blackgreen@yandex.ru

ORCID: 0000-0002-3503-7458

БАРАНОВ Артем Игоревич — кандидат физико-математических наук, младший научный сотрудник лаборатории возобновляемых источников энергии Санкт-Петербургского академического университета имени Ж. И. Алфёрова РАН.

194021, Россия, г. Санкт-Петербург, ул. Хлопина, 8, к. 3

baranov_art@spbau.ru

ORCID: 0000-0002-4894-6503



КАБЕЕВ Андрей Камильевич — доктор физико-математических наук, старший научный сотрудник лаборатории возобновляемых источников энергии Санкт-Петербургского академического университета имени Ж. И. Алфёрова РАН, ведущий научный сотрудник лаборатории мощных полупроводниковых приборов Физико-технического института имени А. Ф. Иоффе РАН.

194021, Россия, г. Санкт-Петербург, Политехническая ул., 26

kaveev@mail.ioffe.ru

ORCID: 0000-0002-3640-677X

ПАВЛОВ Александр Валерьевич — кандидат физико-математических наук, младший научный сотрудник лаборатории возобновляемых источников энергии Санкт-Петербургского академического университета имени Ж. И. Алфёрова РАН, младший научный сотрудник научно-исследовательской лаборатории эпитаксиальных наноструктур соединений A^3B^5 на кремнии Санкт-Петербургского политехнического университета Петра Великого.

194021, Россия, Санкт-Петербург, ул. Хлопина, 8, к. 3

a.pavlov@physics.spbstu.ru

ORCID: 0000-0003-1125-6653

МИНИВ Дмитрий Владимирович — лаборант лаборатории возобновляемых источников энергии Санкт-Петербургского академического университета имени Ж. И. Алфёрова РАН.

194021, Россия, г. Санкт-Петербург, ул. Хлопина, 8, к. 3

dimin46@mail.ru

ORCID: 0009-0006-3064-4175

УСТИМЕНКО Ратмир Владленович — аспирант Высшей инженерно-физической школы Санкт-Петербургского политехнического университета Петра Великого.

195251, Россия, г. Санкт-Петербург, Политехническая ул., 29

ustimenko_rv@spbstu.ru

ORCID: 0000-0003-4123-4375

ВИННИЧЕНКО Максим Яковлевич — кандидат физико-математических наук, заместитель директора Института электроники и телекоммуникаций, доцент Высшей инженерно-физической школы Санкт-Петербургского политехнического университета Петра Великого.

195251, Россия, г. Санкт-Петербург, Политехническая ул., 29

mvin@spbstu.ru

ORCID: 0000-0002-6118-0098

МУХИН Иван Сергеевич — доктор физико-математических наук, заведующий лабораторией возобновляемых источников энергии Санкт-Петербургского академического университета имени Ж. И. Алфёрова РАН, профессор Высшей инженерно-физической школы Санкт-Петербургского политехнического университета Петра Великого.

194021, Россия, г. Санкт-Петербург, ул. Хлопина, 8, к. 3

imukhin@yandex.ru

ORCID: 0000-0001-9792-045X

Received 19.11.2024. Approved after reviewing 16.12.2024. Accepted 16.12.2024.

Статья поступила в редакцию 19.11.2024. Одобрена после рецензирования 16.12.2024. Принята 16.12.2024.

Brief communication

DOI: <https://doi.org/10.18721/JPM.18202>

THE INFLUENCE OF HOLE STATES ON THE ELECTRONIC AND ELECTROSTATIC PROPERTIES OF 2D LAYERS BASED ON THE SILICON-GERMANIUM-SILICON HETEROSTRUCTURE

K. V. Obrazcov^{1,2✉}, A. N. Chibisov², M. V. Mamonova³

¹ Pacific National University, Khabarovsk, Russia;

² Computing Center of the Far Eastern Branch of the RAS, Khabarovsk, Russia;

³ Omsk State University named after Dostoevsky, Omsk, Russia

✉ 2018102293@pnu.edu.ru

Abstract The performance of a hole qubit in the Si/Ge/Si heterostructure is considered in this work. For this purpose, a quantum mechanical study using density functional theory and the pseudopotential method has been carried out. The zone structure and density of electronic states were constructed for the elementary structure. It was found that the bulk of these states are localized in the energy range from -2 to -4 eV. For the constructed supercell the yield work was calculated and the contribution of electron hole to the electrostatic potential of the system was evaluated. The analysis of the obtained results showed that the change of the yield work in the system is associated with the shift of the energy vacuum level.

Keywords: silicon, germanium, density functional theory, two-dimensional layer, work function, heterostructure

Funding: The reported studies of atomic and electronic structure were carried out within the framework of the State Assignment of Ministry of Science and Higher Education of the Russian Federation (Project FEME-2024-0005). The calculations of the work function and electrostatic potential were carried out within the framework of the Russian Science Foundation Project No. 24-13-20024.

Citation: Obrazcov K. V., Chibisov A. N., Mamonova M. V., The influence of hole states on the electronic and electrostatic properties of 2D layers based on the silicon-germanium-silicon heterostructure, St. Petersburg State Polytechnical University Journal. Physics and Mathematics. 18 (2) (2025) 22–29. DOI: <https://doi.org/10.18721/JPM.18202>

This is an open access article under the CC BY-NC 4.0 license (<https://creativecommons.org/licenses/by-nc/4.0/>)



Краткое сообщение

УДК 537.9:004.94

DOI: <https://doi.org/10.18721/JPM.18202>

ВЛИЯНИЕ ДЫРОЧНЫХ СОСТОЯНИЙ НА ЭЛЕКТРОННЫЕ И ЭЛЕКТРОСТАТИЧЕСКИЕ СВОЙСТВА ДВУХМЕРНЫХ СЛОЕВ НА ОСНОВЕ ГЕТЕРОСТРУКТУРЫ КРЕМНИЙ-ГЕРМАНИЙ-КРЕМНИЙ

*К. В. Образцов^{1,2✉}, А. Н. Чибисов², М. В. Мамонова³*¹ Тихоокеанский государственный университет, г. Хабаровск, Россия;² Вычислительный центр Дальневосточного отделения РАН, г. Хабаровск, Россия;³ Омский государственный университет имени Ф. М. Достоевского, г. Омск, Россия

✉ 2018102293@pnu.edu.ru

Аннотация. В работе рассматривается поведение дырочного кубита в гетероструктуре Si/Ge/Si. С этой целью проведено квантовомеханическое исследование с применением теории функционала плотности и метода псевдопотенциала. Для элементарной структуры была построена зонная структура и плотность электронных состояний. Установлено, что основная часть этих состояний локализована в диапазоне энергий от -2 до -4 эВ. Для построенной суперъячейки была рассчитана работа выхода и выполнена оценка вклада электронной дырки в электростатический потенциал системы. Анализ полученных результатов показал, что изменение работы выхода в системе связано со смещением уровня энергетического вакуума.

Ключевые слова: кремний, германий, теория функционала плотности, двухмерный слой, работа выхода, гетероструктура

Финансирование: Исследования атомной и электронной структуры выполнены в соответствии с Государственным заданием Министерства науки и высшего образования Российской Федерации (проект FEME-2024-0005). Расчеты работы выхода и электростатического потенциала были выполнены в рамках проекта Российского научного фонда № 24-13-20024.

Ссылка для цитирования: Образцов К. В., Чибисов А. Н., Мамонова М. В. Влияние дырочных состояний на электронные и электростатические свойства двухмерных слоев на основе гетероструктуры кремний-германий-кремний // Научно-технические ведомости СПбГПУ. Физико-математические науки. 2025. Т. 18. № 2. С. 22–29. DOI: <https://doi.org/10.18721/JPM.18202>

Статья открытого доступа, распространяемая по лицензии CC BY-NC 4.0 (<https://creativecommons.org/licenses/by-nc/4.0/>)

Introduction

Creating a quantum computer is a crucial challenge for modern microelectronics. Quantum computers are devices based on the principles of quantum mechanics using quantum bits (or qubits) to process information. Unlike classical bits in classical computers, capable of representing only one of two states (0 or 1), qubits can be in a superposition of several states simultaneously [1, 2], which allows quantum computers to perform calculations faster and more efficiently by orders of magnitude. They can be used to solve complex mathematical problems, in cryptography, optimization, simulation of molecular and chemical processes, artificial intelligence research and in many other fields. The creation of quantum computers promises to transform the way information is processed, opening up new opportunities for innovation and scientific discovery [3–5]. Today, there are many implementations of quantum processors. Photon-based qubits and superconducting qubits are the most popular.

In this paper, we consider a hole as a qubit. The main advantage of the hole qubit is its strong spin-orbit interaction and the ability to form superconducting pair correlations. It is these properties of holes that are extremely important for fast control of hole qubits [6, 7]. Possible materials for such a computer are 2D allotropic modifications of silicon (silicene) or germanium (germanene) using a hole qubit [8, 9].

For this purpose, in this paper we decided to consider the Si/Ge/Si interface. This structure has unique electromagnetic properties due to lattice mismatch between silicon and germanium [10]. In this case, due to the low effective mass of the holes [11, 12], it is possible to obtain a qubit with a long coherence time and a convenient way to control its state using an external magnetic field. The structure itself has excellent compatibility with the existing microelectronic components [13] and it is easy to integrate it into existing electronics manufacturing.

The goal of this paper was a quantum mechanical study of the behavior of a hole qubit in a two-dimensional silicon-germanium-silicon (Si/Ge/Si) layer using density functional theory (DFT) within the framework of noncollinear magnetization.

Experimental technique

The characteristics of the structures were calculated using the VASP software package [14–16] based on DFT and the pseudopotential method. Noncollinear calculations were performed taking into account the spin-orbit coupling and additional corrections in the Generalized Gradient Approximation (GGA+U) [17]. To calculate the magnetic and electronic properties, the initial magnetic moment was first found for each atom, then complete relaxation of the system was carried out taking into account the generalized theory of local spin density and the resulting magnetization on the atoms was determined based on the results obtained. A plane-wave basis set with a cut-off energy of 450 eV was used. An $18 \times 18 \times 1$ k -point grid was used for the unit cells. For the enlarged cell, a $6 \times 6 \times 1$ k -point grid was used, constructed according to the Monkhorst–Pack scheme [18].

Results and discussion

The first stage in the study of the atomic and electronic structure of 2D Si/Ge/Si interface considered the separate structures of silicene and germanene. At the first stage, we performed complete relaxation of the atomic structures of silicene and germanene to find the minimum forces and total electronic energy for the given systems. Relaxation of the structure was carried out preserving the symmetry of the cell; the procedure was performed for the cell parameters and atomic coordinates.

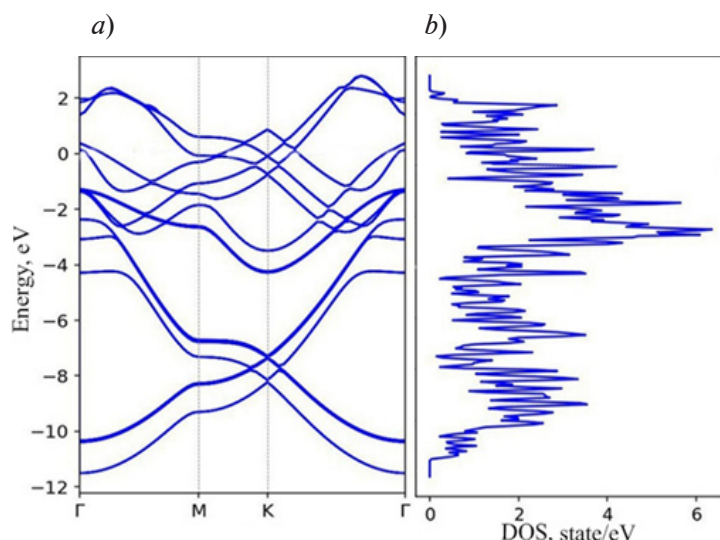


Fig. 1. Band structure (a) and density of states (b) constructed for Si/Ge/Si interface

At the second stage, we built the atomic structure of 2D Si/Ge/Si interface, a sandwich where the germanene layer was located between two silicene layers. At the third and subsequent stages, complete atomic relaxation of the structure was performed by the same principle as achieved separately for silicene and germanene.

The VASPKIT software package was used for postprocessing of the obtained data, the density of states and the band structure were calculated for the given interface. Calculations were performed with the number of k -points equal to 20. For clarity, the density of states was compared with the band structure of the studied material (Fig. 1).

Analysis of the data in Fig. 1 allows to conclude that the highest-energy states are localized in the range from -2 to -4 eV. The resulting band structure looks very similar to the individual band structures of silicene and



germanene. This indicates the appearance of new energy levels as a result of superposition of two structures, and this in turn causes the formation of interface states at the interfaces between silicon and germanium structures.

For further analysis of the electronic and magnetic properties of the selected system, it was necessary to enlarge the initial system. For this purpose, translation of the initial interface cell was performed with a threefold increase in parameters a and b . As a result, a supercell with the following structural parameters was formed: $a = 11.421 \text{ \AA}$, $b = 11.421 \text{ \AA}$, $c = 25.166 \text{ \AA}$. The parameter c was chosen equal to 25.166 \AA to exclude the influence of interaction between the translated slabs. The Si–Si interatomic distance in the silicene layer was equal to 2.260 \AA and the Ge–Ge distance in the germanene layer was 2.486 \AA . The distance between the layers was equal to 3.647 \AA . The resulting supercell consisted of a total of 54 atoms (Fig. 2).

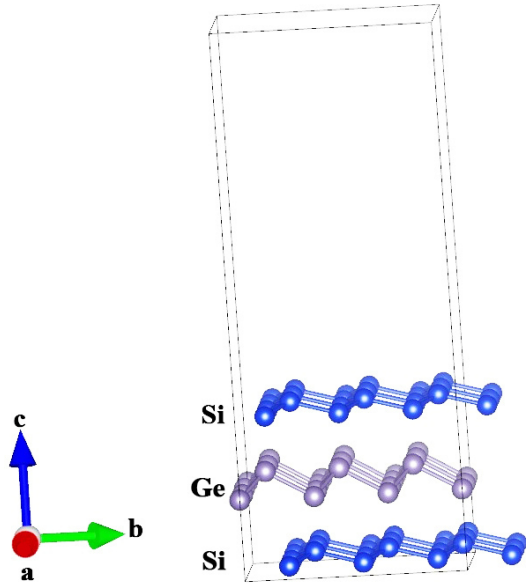


Fig. 2. Structural model of supercell of 2D Si/Ge/Si interface: the structure consists of 54 atoms, 18 of which are germanium atoms and 36 are silicon atoms

Next, a free valence bond (hole) was created in the Si/Ge/Si system and the initial magnetization was set. The hole was created by removing one electron from the system. To illustrate the contribution of the created electron vacancy to the electrostatic potential, we compared the dependences of electrostatic potential of the system on the concentration of holes and the given direction of initial magnetization (Fig. 3).

Evidently, when a hole is added to the system, the electrostatic potential decreases. The graphs are almost identical for the up (Fig. 3,*a*) and down (Fig. 3,*b*) magnetization directions. The only difference is that in the first case the distance between the first peaks is 0.670 eV (Fig. 3,*a*) and in the second case it is 0.642 eV (Fig. 3,*b*). This means that the sign of magnetization practically does not contribute to the distribution of the electrostatic potential in the system, while the larger contribution to the potential value is made by Si atoms.

The electrostatic potential was calculated to subsequently calculate the work function W for each case. The following formula was used for this purpose:

$$W = -e\phi - E_f,$$

where e is the electron charge, ϕ is the near-vacuum value of the electrostatic potential, E_f is the Fermi level.

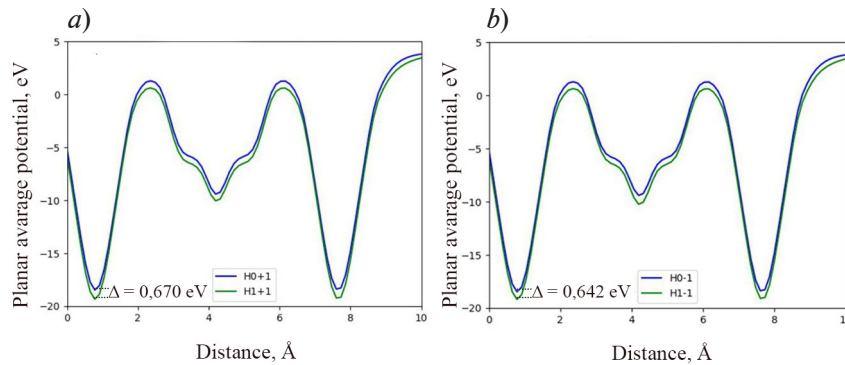


Fig. 3. Comparison of dependences of electrostatic potential of Si/Ge/Si system on concentration of holes with given magnetization directions of the system, +1 (up) and -1 (down): (a) and (b), respectively
Cases of systems without holes (blue curves) and with one hole (green curves) are compared

The results obtained are given in Table.

It follows from the data in Fig. 3 and Table that the value of the electrostatic potential decreases when a hole is added to the system, and the work function increases. In addition, it can be concluded that in the system with the magnetization direction of -1 (down), the work function in the absence of holes is greater than in a system with the magnetization of +1 (up). In the presence of holes, the work function becomes approximately the same for both cases.

Table

**Dependence of work functions for interface
on magnetization direction and presence of holes**

Magnetization direction	Work function W , eV	
	Absence of hole	Presence of holes
up	4.946	6.460
down	4.970	6.456

Conclusion

We calculated the band structure and density of states for a two-dimensional Si/Ge/Si layer. These calculations indicate that the main part of the electronic states is localized in the energy range from -2 to -4 eV. The changes in the Si/Ge/Si band structure, compared with the individual band structures of germanium and silicon, are due to the formation of interface states, causing new energy bands to appear. If a hole is added to the system, the electrostatic potential decreases due to a shift in the energy vacuum level, while the sign of the given initial magnetization makes an insignificant contribution to the change in the electrostatic potential of the system. We established that the work function is greater in the system with negative initial magnetization than in the system with a positive one, while adding a hole to systems with different magnetization equalizes the values of the work function.

In conclusion, it should be noted that the results obtained can be used to design quantum computers or quantum sensors for next-generation nanoelectronics.

The research was carried out using the resources of the Shared Facility Center “Data Center” of the Far Eastern Branch of the Russian Academy of Sciences, Khabarovsk.



REFERENCES

1. Chibisov A. N., Chibisova M. A., *Ab initio* calculation of the equilibrium quantum state for hole qubit and electrostatic characteristics of the B:Si system, J. Comput. Electron. 20 (5) (2021) 1959–1963.
2. Chibisov A. N., Aleshin M. S., Chibisova M. A., DFT analysis of hole qubits spin state in germanium thin layer, Nanomaterials. 12 (13) (2022) 2244.
3. Fang Y., Philippopoulos P., Culcer D., et al., Recent advances in hole-spin qubits, Mater. Quantum Technol. 3 (1) (2023) 012003.
4. Valentini M., Borovkov M., Prada E., et al., Majorana-like Coulomb spectroscopy in the absence of zero-bias peaks, Nature. 612 (7940) (2022) 442–447.
5. Watzinger H., Kukučka J., Vukušić L., et al., A germanium hole spin qubit, Nat. Commun. 9 (25 Sept) (2018) 3902.
6. Goncharov A. V., Chibisov A. N., Effect of external pressure and quantum state on the local magnetization of germanium layers: Ab initio calculation, Adv. Theory Simul. 6 (3) (2023) 2200816.
7. Chibisov A. N., Chibisova M. A., Prokhorenko A. V., et al., Possibilities of controlling the quantum states of hole qubits in an ultrathin germanium layer using a magnetic substrate: Results from ab initio calculations, Nanomaterials. 13 (23) (2023) 3070.
8. Watzinger H., Kloeffer C., Vukušić L., et al. Heavy-hole states in germanium hut wires, Nano Lett. 16 (11) (2016) 6879–6885.
9. Ueno N., Sacuraba M., Osakabe Y., et al., Electronic properties of Si/Si-Ge Alloy/Si(100) heterostructures formed by ECR Ar plasma CVD without substrate heating, Mater. Sci. Semicond. 70 (1 Nov) (2017) 55–62.
10. Antonova I. V., Kagan M. S., Polyakov V. I., et al., Effect of interface states on population of quantum wells in SiGe/Si structures, Phys. Status Solidi C. 2 (6) (2005) 1924–1928.
11. Žutić I., Fabian J., Erwin S. C., Spin injection and detection in silicon, Phys. Rev. Lett. 97 (2) (2006) 026602.
12. Gao F., Zhang J. Y., Wang J. H., et al. Ge/Si quantum wires for quantum computing, Proc. 5th IEEE Electron Devices Technology and Manufacturing Conf. (EDTM-2021). April 8–11, 2021. Chengdu, China, IEEE Inc. (2021) 9420817.
13. Ercan H. E., Friesen M., Coppersmith S. N., Charge-noise resilience of two-electron quantum dots in Si/SiGe heterostructures, Phys. Rev. Lett. 128 (24) (2022) 247701.
14. Paquelet Wuetz B., Loset M. P., Koelling S., et al., Atomic fluctuations lifting the energy degeneracy in Si/SiGe quantum dots, Nat. Commun. 13 (13 Dec) (2022) 7730.
15. Kresse G., Hafner J., Ab initio molecular dynamics for liquid metals, Phys. Rev. B. 47 (1) (1993) 558.
16. Kresse G., Furthmüller J., Efficiency of ab-initio total energy calculations for metals and semiconductors using a plane-wave basis set, Comput. Mater. Sci. 6 (1) (1996) 15–50.
17. Perdew J. P., Burke K., Ernzerhof M., Generalized gradient approximation made simple, Phys. Rev. Lett. 77 (18) (1996) 3865.
18. Monkhorst H. J., Pack J. D., Special points for Brillouin-zone integrations, Phys. Rev. B. 13 (12) (1976) 5188.

СПИСОК ЛИТЕРАТУРЫ

1. Chibisov A. N., Chibisova M. A. *Ab initio* calculation of the equilibrium quantum state for hole qubit and electrostatic characteristics of the B : Si system // Journal of Computational Electronics. 2021. Vol. 20. No. 5. Pp. 1959–1963
2. Chibisov A. N., Aleshin M. S., Chibisova M. A., DFT analysis of hole qubits spin state in germanium thin layer // Nanomaterials. 2022. Vol. 12. No. 13. P. 2244.
3. Fang Y., Philippopoulos P., Culcer D., Coish W. A., Chesi S. Recent advances in hole-spin qubits // Materials for Quantum Technology. 2023. Vol. 3. No. 1. P. 012003.
4. Valentini M., Borovkov M., Prada E., Martín-Sánchez S., Botifoll M., Hofmann A. C., Arbiol J., Aguado R., San-Jose P., Katsaros G. Majorana-like Coulomb spectroscopy in the absence of zero-bias peaks // Nature. 2022. Vol. 612. No. 7940. Pp. 442–447.
5. Watzinger H., Kukučka J., Vukušić L., Gao F., Wang T., Schaffler F., Zhang J.-J., Katsaros G. A germanium hole spin qubit // Nature Communications. 2018. Vol. 9. 25 September. P. 3902.
6. Goncharov A. V., Chibisov A. N. Effect of external pressure and quantum state on the local magnetization of germanium layers: Ab initio calculation // Advanced Theory and Simulations. 2023. Vol. 6. No. 3. P. 2200816.
7. Chibisov A. N., Chibisova M. A., Prokhorenko A. V., Obratcov K. V., Fedorov A. S., Yu Yang-Xin. Possibilities of controlling the quantum states of hole qubits in an ultrathin germanium layer using a magnetic substrate: Results from ab initio calculations // Nanomaterials. 2023. Vol. 13. No. 23. P. 3070.
8. Watzinger H., Kloeffer C., Vukušić L., et al. Heavy-hole states in germanium hut wires // Nano Letters. 2016. Vol. 16. No. 11. Pp. 6879–6885.
9. Ueno N., Sacuraba M., Osakabe Y., Akima H., Sato S. Electronic properties of Si/Si-Ge Alloy/Si(100) heterostructures formed by ECR Ar plasma CVD without substrate heating // Materials Science Semiconductor Processing. 2017. Vol. 70. 1 November. P. 55–62.
10. Antonova I. V., Kagan M. S., Polyakov V. I., Golik L. L., Kolodzey J. Effect of interface states on population of quantum wells in SiGe/Si structures // Physica Status Solidi C. 2005. Vol. 2. No. 6. Pp. 1924–1928.
11. Žutić I., Fabian J., Erwin S. C. Spin injection and detection in silicon // Physical Review Letters. 2006. Vol. 97. No. 2. P. 026602.
12. Gao F., Zhang J. Y., Wang J. H., et al. Ge/Si quantum wires for quantum computing // Proceedings of the 5th IEEE Electron Devices Technology and Manufacturing Conference (EDTM-2021). April 8–11, 2021. Chengdu, China, IEEE Inc. P. 9420817.
13. Ercan H. E., Friesen M., Coppersmith S. N. Charge-noise resilience of two-electron quantum dots in Si/SiGe heterostructures // Physical Review Letters. 2022. Vol. 128. No. 24. P. 247701.
14. Paquelet Wuetz B., Loset M. P., Koelling S., et al. Atomic fluctuations lifting the energy degeneracy in Si/SiGe quantum dots // Nature Communications. 2022. Vol. 13. 13 December. P. 7730.
15. Kresse G., Hafner J. Ab initio molecular dynamics for liquid metals // Physical Review B. 1993. Vol. 47. No. 1. P. 558.
16. Kresse G., Furthmüller J. Efficiency of ab-initio total energy calculations for metals and semiconductors using a plane-wave basis set // Computational Materials Science. 1996. Vol. 6. No. 1. Pp. 15–50.
17. Perdew J. P., Burke K., Ernzerhof M. Generalized gradient approximation made simple // Physical Review Letters. 1996. Vol. 77. No. 18. P. 3865.
18. Monkhorst H. J., Pack J. D. Special points for Brillouin-zone integrations // Physical Review B. 1976. Vol. 13. No. 12. P. 5188.



THE AUTHORS

OBRAZCOV Kirill V.*Pacific National University*

136 Tikhookeanskaya St., Khabarovsk, 680035, Russia

2018102293@pnu.edu.ru

ORCID: 0009-0001-6034-7757

CHIBISOV Andery N.*Computing Center of the Far Eastern Branch of the Russian Academy of Sciences*

65 Kim Yu Chen St., Khabarovsk, 680000, Russia

andreichibisov@yandex.ru

ORCID: 0000-0002-5410-8661

MAMONOVA Marina V.*Omsk State University Named after Dostoevsky*

55-A Mir Ave., Omsk, 644077, Russia

mamonovamv@omsu.ru

ORCID: 0000-0001-7466-086X

СВЕДЕНИЯ ОБ АВТОРАХ

ОБРАЗЦОВ Кирилл Владимирович — лаборант кафедры физики Тихоокеанского государственного университета.

680035, Россия, г. Хабаровск, Тихоокеанская ул., 136.

2018102293@pnu.edu.ru

ORCID: 0009-0001-6034-7757

ЧИБИСОВ Андрей Николаевич — доктор физико-математических наук, ведущий научный сотрудник Вычислительного центра Дальневосточного отделения Российской академии наук.

680000, Россия, г. Хабаровск, ул. Ким Ю Чена, 65

andreichibisov@yandex.ru

ORCID: 0000-0002-5410-8661

МАМОНОВА Марина Владимировна — кандидат физико-математических наук, доцент кафедры теоретической физики Омского государственного университета имени Ф. М. Достоевского.

644077, г. Омск, проспект Мира, д. 55-А

mamonovamv@omsu.ru

ORCID: 0000-0001-7466-086X

Received 09.12.2024. Approved after reviewing 16.01.2025. Accepted 16.01.2025.

Статья поступила в редакцию 09.12.2024. Одобрена после рецензирования 16.01.2025. Принята 16.01.2025.

SIMULATION OF PHYSICAL PROCESSES

Original article

DOI: <https://doi.org/10.18721/JPM.18203>

APPLICATION OF MATHEMATICAL MODELING FOR DESCRIBING THE BEHAVIOR OF LAYERED PANELS WITH A TETRAHEDRAL CORE

O. V. Antonova¹✉, M. V. Ivanov¹, A. A. Mikhailov¹, V. A. Kuzmin²

¹ Peter the Great St. Petersburg Polytechnic University, St. Petersburg, Russia

² LLC "Tetral", St. Petersburg, Russia

✉ antonova_ov@spbstu.ru

Abstract. In the paper, mathematical modeling methods for describing the behavior of sandwich panels with a tetrahedral core under various loads have been used, and a series of numerical calculations carrying out by the ANSYS software. In so doing the previously obtained effective elastic characteristics were taken, which made it possible to replace the direct modeling of the tetrahedral core structure with elements of a simple form using orthotropic material with equivalent characteristics. The problem of the plate's three-point bending was solved, and a deformed state and deflection character of the panel were analyzed. The necessity of applying the heteromodular elasticity theory when modeling such objects and of taking into account the effective elastic characteristics obtained by tension and compression of the periodicity cell was established. Recommendations were given for the use of periodicity cells when computing the iterative changes in material properties and effective characteristics obtained during tension and compression.

Keywords: tetrahedral core, layered panel, effective elastic characteristics, finite element method

Citation: Antonova O. V., Ivanov M. V., Mikhailov A. A., Kuzmin V. A., Application of mathematical modeling for describing the behavior of layered panels with a tetrahedral core, St. Petersburg State Polytechnical University Journal. Physics and Mathematics. 18 (2) (2025) 30–40. DOI: <https://doi.org/10.18721/JPM.18203>

This is an open access article under the CC BY-NC 4.0 license (<https://creativecommons.org/licenses/by-nc/4.0/>)



Научная статья

УДК 539.3

DOI: <https://doi.org/10.18721/JPM.18203>

ПРИМЕНЕНИЕ МАТЕМАТИЧЕСКОГО МОДЕЛИРОВАНИЯ ДЛЯ ОПИСАНИЯ ПОВЕДЕНИЯ СЛОИСТЫХ ПАНЕЛЕЙ С ТЕТРАЭДРАЛЬНЫМ ЗАПОЛНИТЕЛЕМ

*О. В. Антонова¹✉, М. В. Иванов¹, А. А. Михайлов¹, В. А. Кузьмин²*¹ Санкт-Петербургский политехнический университет Петра Великого, Санкт-Петербург, Россия;² ООО «Тетрал», Санкт-Петербург, Россия✉ antonova_ov@spbstu.ru

Аннотация. В работе выполнено математическое моделирование с целью описания поведения слоистых панелей с тетраэдральным заполнителем под действием различных нагрузок. При этом была реализована серия численных расчетов в программном комплексе конечно-элементного анализа ANSYS. При моделировании использованы полученные ранее эффективные упругие характеристики, что позволило заменить прямое моделирование структуры тетраэдрального заполнителя элементами простой формы с применением ортотропного материала, имеющего эквивалентные характеристики. Решена задача о трехточечном изгибе пластины, проанализировано деформированное состояние панели и характер ее прогиба. Установлена необходимость применения принципов разномодульной теории упругости при моделировании таких объектов и учета эффективных упругих характеристик, полученных при растяжении и сжатии ячейки периодичности. Даны рекомендации по использованию в расчетах итерационного изменения свойств материала и эффективных характеристик, полученных при растяжении и сжатии ячейки периодичности.

Ключевые слова: тетраэдральный заполнитель, слоистая панель, эффективные упругие характеристики, метод конечных элементов

Ссылка для цитирования: Антонова О. В., Иванов М. В., Михайлов А. А., Кузьмин В. А. Применение математического моделирования для описания поведения слоистых панелей с тетраэдральным заполнителем // Научно-технические ведомости СПбГПУ. Физико-математические науки. 2025. Т. 18. № 2. С. 30–40. DOI: <https://doi.org/10.18721/JPM.18203>

Статья открытого доступа, распространяемая по лицензии CC BY-NC 4.0 (<https://creativecommons.org/licenses/by-nc/4.0/>)

Introduction

Due to growing demand for composite panels with various types of cores in diverse industries, it is important to carry out analysis and computational validation of such structural elements using mathematical modeling methods with high-performance computing equipment and modern software [1, 2]. Close attention throughout design, preparation, testing and, consequently, simulation of such panels and products made from them [3–5] should be paid to the structure and shape of the core [6, 7]. Honeycomb core is currently most widely used in aviation, automotive industry and building structures [8–11]. We should note that honeycombs have a closed cell structure and are well suited for thermal insulation; in addition, they provide strength, reliability and load-bearing capacity under significant loads [12].

On the other hand, structures with truss cores have less effective load resistance [13], but they allow for ventilation. That is why such cores have proved to be a solution for extending the service life of building facades by protecting them from adverse climatic events [14–16]. One of the possible core configurations is tetrahedral, i.e., combining truncated tetrahedra [17, 18].

A composite panel with a honeycomb or truss core can be described in simulation as a composite material with a complex microstructure. The core can be considered a homogeneous material in computational continuum mechanics, and its effective properties can be both anisotropic and orthotropic [19, 20]. Panels with tetrahedral cores are regarded in numerical simulation as structurally orthotropic composite material [21, 22].

To correctly implement this approach, a unit cell is selected at the first stage and its effective elastic characteristics are set. The latter are often determined using the direct homogenization method [23], allowing to calculate the effective values of orthotropic physico-mechanical parameters of a composite material with a complex microstructure; the method is also applicable to doubly periodic structures.

The main goal of this study is to propose a calculation procedure substantiating the application of multimodular elasticity theory to simulation of composite panels with core.

The following objectives were posed and achieved for this purpose:

- calculate the stiffness parameters of a panel with tetrahedral core under tension and compression;
- determine the stress-strain state of the panel in the three-point bending problem.

Object of research

The general view of the panel and tetrahedral core with its geometric characteristics, considered in this case, are shown in Fig. 1. Panels of this type are predominantly used in the construction industry, specifically in ventilated facades and enclosures.

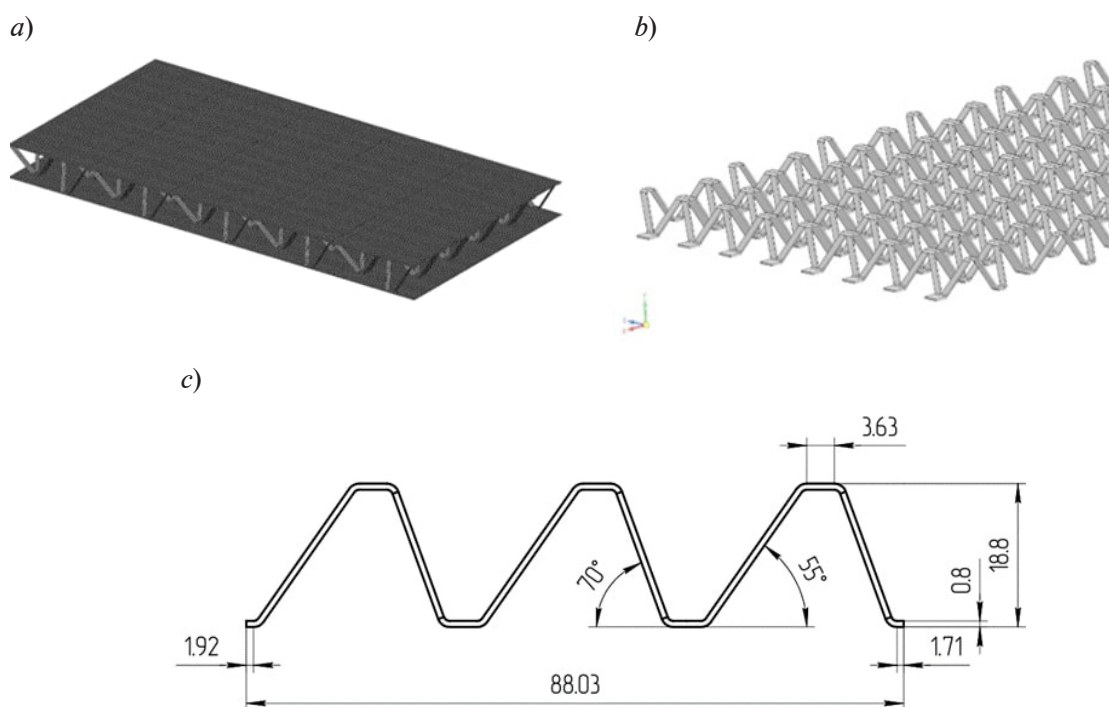


Fig. 1. General view of panel with tetrahedral core (a), its core (b) and its geometric characteristics (c)

The AMG2 material used has the following physico-mechanical parameters:

Density, kg/m^3	2,680;
Elastic modulus, GPa	71.0;
Ultimate tensile strength, MPa	190;
Yield strength, MPa	80;
Poisson's ratio	0.33.

It is assumed that the same material is used to manufacture the face sheets of the panel and the core.

The unit cell considered, measuring $28 \times 58 \times 19$ mm, is shown in Fig. 2.

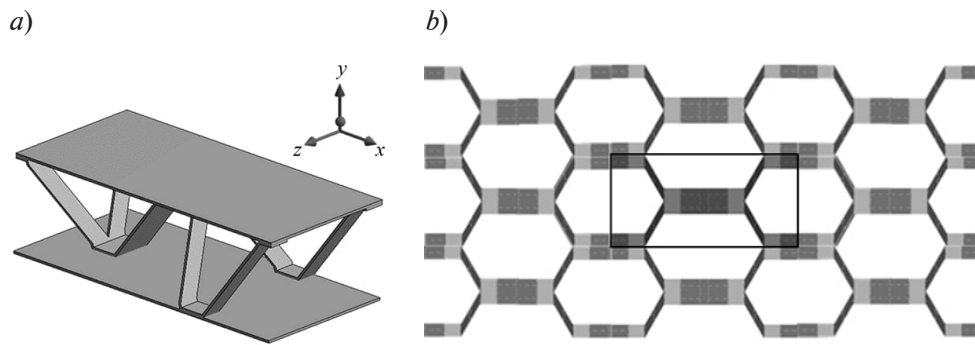


Fig. 2. Schematics of unit cell (a) and tetrahedral filler (top view) (b); the cell is marked by a rectangle

The values of the elastic parameters were determined by direct homogenization (the corresponding results and a detailed description of the method are given in [24]). The method of direct homogenization used is based on kinematic and static boundary conditions [25], allowing to determine the effective orthotropic physico-mechanical properties of a composite material with a complex microstructure.

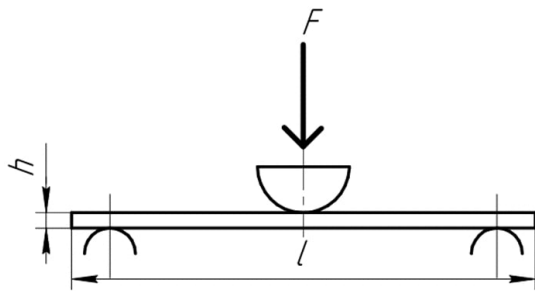


Fig. 3. Loading conditions for problem statement of three-point bending of the panel. Geometric parameters and the direction of the loading force F are shown

Problem of three-point bending of composite panel

This problem is of both scientific and practical interest [26–28]. Consider such a problem for a plate with a tetrahedral core, where the core structure is modeled without any simplifications and the structure is represented by a homogeneous medium with effective properties.

The loading conditions for the three-point bending problem of such a panel (its overall dimensions are $292 \times 140 \times 19$ mm) is shown in Fig. 3.

Nonlinear shell finite elements were used for numerical simulation. Conducting convergence analysis, we selected a model consisting of

156,050 elements and 532,325 nodes; the characteristic size of the element was 1 mm.

Based on the calculation performed, let us analyze the stress-strain state of the panel. Fig. 4 shows the vertical displacements of the panel under consideration and the dependence of its deflection in the central section along the length l .

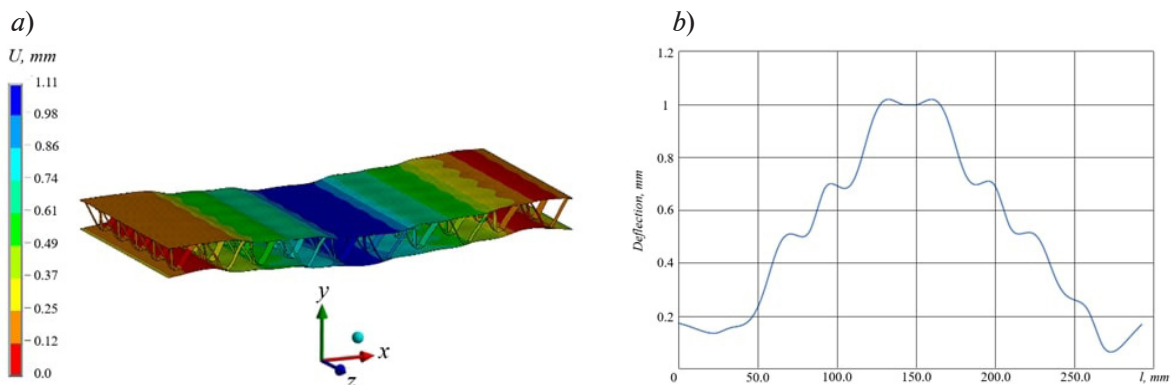


Fig. 4. Stress-strain state of sandwich panel: vertical displacements (a), color map, 10 : 1 scale; dependence of deflection of panel in its central section along the length l (b), see Fig. 3

It can be seen from the presented results that the location of the core affects the magnitude and behavior of the deflection for the plate with tetrahedral core. The deflection is smaller at the points where the core is attached.

The next stage in the simulation procedure is to establish a correspondence between the mean deflection of the panel with core and the deflection under bending in a similar panel but made of homogeneous, multimodular material with orthotropic characteristics. We emphasize that the loading behavior of two objects should be compared for this purpose:

panel with tetrahedral core,

panel made of homogeneous multimodular material with orthotropic characteristics.

For this comparison, we first consider two auxiliary problems:

evaluating the behavior of the unit cell under tension and compression,

analyzing the application of the principles of multimodular elasticity theory.

We should note that the formulation of these problems is of independent scientific interest.

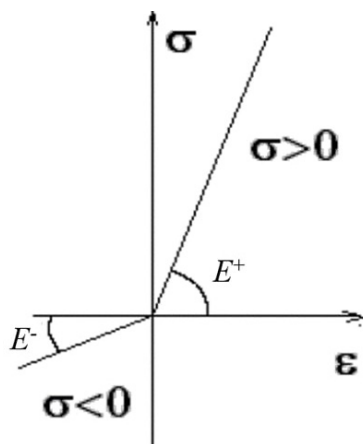


Fig. 5. Initial section of characteristic stress-strain curve (stress σ —strain ϵ) in accordance with multimodular elasticity theory: material has elastic modulus E^+ for uniaxial tension and E^- for uniaxial compression

According to multimodular elasticity theory, the stress-strain curve can be represented as two straight lines in the first approximation (Fig. 5).

To verify the applicability of this approach and validate it, in other words, to confirm the applicability of multimodular elasticity theory to design of sandwich panels with tetrahedral core, we carried out a series of numerical experiments on tension of the unit cell (see Fig. 2, b) in the directions of the x , y and z axes.

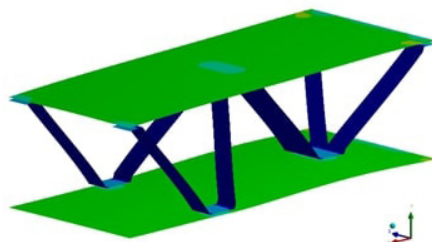
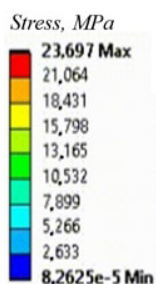
Application of principles of multimodular elasticity theory

In case of analysis at the macroscale, the geometric characteristics of the selected unit cell and its behavior under loading should be correctly described. Tetrahedral core with complex structure in layered composites behaves differently under tension and compression [25, 29–30], so approaches underlying the multimodular elasticity theory [31–33] can be reasonably applied.

The mechanical characteristics of homogeneous isotropic material in classical elasticity theory are described by two elastic constants: Young's modulus E and Poisson's ratio ν .

On the other hand, according to multimodular elasticity theory, the material has different Young's moduli for cases of uniaxial tension and uniaxial compression: E^+ and E^- , respectively, as well as different Poisson's ratios characterizing transverse contraction under tension and transverse expansion under compression: ν^+ and ν^- , respectively.

a)



b)

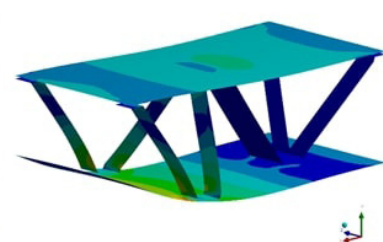
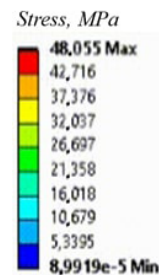


Fig. 6. Intensity of von Mises stresses (see color scale) for unit cell under tension (a) and compression (b) along the x axis

These simulations were performed using the ANSYS Mechanical software package. Nonlinear shell finite elements were used in numerical simulation. After conducting convergence analysis, we selected a model consisting of 4,148 elements and 13,177 nodes; the characteristic size of the element was 1 mm. The same finite element model was previously used in [24].

Fig. 6 shows the von Mises stress intensity distribution under tension and compression of the unit cell along the x axis.

Tensile and compressive behavior of the unit cell

The graph for the dependence of the reaction force on the maximum displacement U_{\max} in different loading directions is shown in Fig. 7. The dashed line shows the linear dependence of force on displacement in the compressive region with the stiffness equal to the tensile stiffness. The values of reactions upon load reversal are given in Table 1.

Thus, comparing the tensile and compressive behavior of the unit cell, we found a difference in the magnitude of reactions under loading in the x and y directions.

Notably, we used the values of effective elastic characteristics (Table 2) that we obtained in [24].

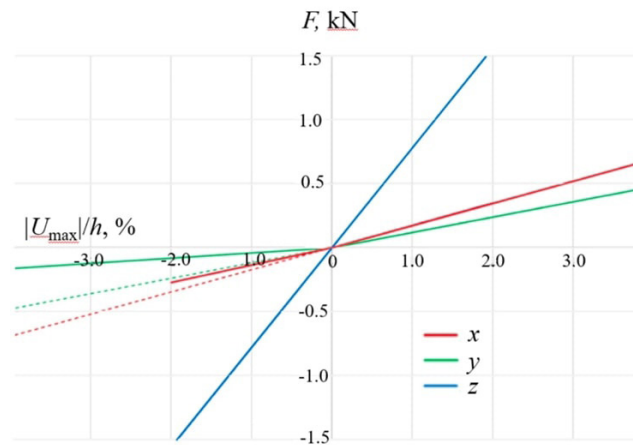


Fig. 7. Dependences of reaction force on normalized maximum displacement in different loading directions (along the axes x , y , z)

Dashed lines show the linear dependence of force on displacement in the compressive region with the stiffness equal to the tensile stiffness

Table 1

Comparison of reactions in unit cell
for varying direction and sign of load application

Loading direction	Parameter value		
	$+F_1$, kN	$-F_2$, kN	$ U_{\max} /h$, %
Axis x	0.347	0.271	2
Axis y	5.991	2.032	50
Axis z	1.561	1.562	2

Notations: $+F_1$, $-F_2$ are the reaction forces under tension and compression, respectively; $|U_{\max}|/h$ is the ratio of the maximum displacement along each axis to the thickness of the sheet.

The data in Fig. 7 and in Table 1 confirm that different values of reactions are observed in the x and y directions upon load reversal. This is especially pronounced for the y (vertical) direction. This result allows us to conclude that multimodular elasticity theory can be reasonably applied to describing the behavior of structures with the selected type of core. For more accurate description of the behavior of the unit cell, it is necessary to find effective characteristics for the case of compression as well.

Table 2

Effective elastic parameters used for simulations

Young's moduli, GPa	Poisson's ratios	Shear moduli, GPa
$E_1^* = 58.60$	$\nu_{12}^* = 0.31; \nu_{21}^* = 0.03$	$G_{12}^* = 1.030$
$E_2^* = 0.899$	$\nu_{23}^* = 0.01; \nu_{32}^* = 0.10$	$G_{23}^* = 0.113$
$E_3^* = 4.53$	$\nu_{13}^* = 0.29; \nu_{31}^* = 0.30$	$G_{13}^* = 0.832$

Note. The parameter values given in Table 2 were presented in our earlier study [24].

Conclusion

The results of numerical simulation indicate that the sandwich panel with the selected type of tetrahedral core has different stiffness characteristics under compression and tension.

We validated the application of the homogenization method combined with the principles of the multimodular elasticity theory to improve the simulation accuracy for the behavior of the plate at the macro level.

The obtained results open up opportunities for further research. The next stage is to confirm that the mean deflection of the panel with core corresponds to the same deflection under bending in a panel made of homogeneous multimodular material. The behavior of the panel with tetrahedral core should also be compared with the behavior of a panel made of homogeneous multimodular material with orthotropic characteristics. It should be noted separately that it is planned to describe the multimodular behavior of the structure by successive refinement of the equilibrium state for the current stress-strain state of the structure.

REFERENCES

1. Onyibo E. C., Safaei B., Application of finite element analysis to honeycomb sandwich structures: a review, Rep. Mech. Eng. 3 (1) (2022) 192–209.
2. Faidzi M. K., Abdullah S., Abdullah M. F., et al., Review of current trends for metal-based sandwich panel: Failure mechanisms and their contribution factors, Eng. Fail. Anal. 123 (May) (2021) 105302.
3. Makweche D., Morgan D., A review of the characteristics and structural behaviour of sandwich panels, Proc. Inst. Civil Eng.: Struct. Build. 175 (12) (2022) 965–979.
4. Catapano A., Montemurro M., A multi-scale approach for the optimum design of sandwich plates with honeycomb core. Part I: homogenization of core properties, Compos. Struct. 118 (Dec) (2014) 664–676.
5. Xu X. F., Qiao P., Homogenized elastic properties of honeycomb sandwich with skin effect, Int. J. Solids Struct. 39 (8) (2002) 2153–2188.
6. Paymushin V. R., Galimov N. K., Ob ustoychivosti trekhslonnykh plastin s legkim zapolnitem pri izgibe [On the bending stability of three-layer plates with light aggregate], Tr. seminara po teorii obolochek [Proc. of the Seminar on the Theory of Shells], Zavoisky Physical-Technical Institute, the USSR Academy of Sciences, Kazan. (5) (1974) 35–42 (in Russian).
7. Queheillalt D. T., Wadley H. N. G., Cellular metal lattices with hollow trusses, Acta Mater. 53 (2) (2005) 303–313.
8. Kreja I., A literature review on computational models for laminated composite and sandwich panels, Cent. Eur. J. Eng. 1(1) (2011) 59–80.
9. Wadley H. N. G., Fleck N. A., Evans A. G., Fabrication and structural performance of periodic cellular metal sandwich structures, Compos. Sci. Technol. 63 (16) (2003) 2331–2343.
10. Wadley H. N. G., Multifunctional periodic cellular metals, Phil. Trans. R. Soc. A. 364 (1838) (2006) 31–68.
11. Feng Y., Qiu H., Gao Y., et al., Creative design for sandwich structures: A review, Int. J. Adv. Robot. Syst. 17 (3) (2020) doi:10.1177/1729881420921327.
12. Paimushin V. N., Zakirov I. M., Lukankin S. A., et al., Averaged elastic and strength characteristics of honeycomb core and theoretical and experimental method for their determination, Mech. Compos. Mater. 48 (5) (2012) 511–524.



13. **Abdullin I. N., Gaynutdinov V. G.**, *Proyektirovaniye ratsionalnykh trekhsloynnykh konstruktsey so sterzhnevym zapolnitelem* [The design of rational three-layer structures with core filler], Tupolev Kazan National Research Technical University publishing, (KNITU-KAI), Kazan, Russia, 2017 (in Russian).
14. **Nayshut Yu. S.**, *Sotovyye stroitelnyye konstruktсии* [Honeycomb building structures], Publishing House of the Association of Construction Universities (ACU), Moscow, 1998 (in Russian).
15. **Panin V. F., Gladkov Yu. A.**, *Konstruktсии s zapolnitelem* [Constructions with core], Mashinostroyeniye Publishing, Moscow, 1991 (in Russian).
16. **Endogur A. I., Weinberg M. V., Ierusalimsky K. M.**, *Sotovyye konstruktсии. Vybor parametrov i proektirovaniye* [Honeycomb structures. Parameter selection and design], Mashinostroyeniye Publishing, Moscow, 1986 (in Russian).
17. **Kuzmin V. A.**, *Zapolnitel s fermennoy obyemnoy strukturoy mnogoslownoy kompozitnoy paneli* [A core with truss bulk structure of a sandwich composite panel], Pat. No. 2710157C1 Russian Federation, MPK B32B 7/00, B32B 15/00, B32B 3/12. Kuzmin Valeriy Anatolievich is a declarant and patentee. No. 2019106951; declar. 12.03.2019; publ. 25.02.2020.
18. **Kuzmin V. A.**, *Sposob izgotovleniya zapolnitelya s fermennoy obyemnoy strukturoy i mnogoslownykh paneley na yego osnove* [Method of producing a filler with a truss bulk structure and sandwich panels based on it], Pat. No. 2710177C1 Russian Federation, MPK B32B 7/00, B32B 15/00, B32B 3/12; Kuzmin Valeriy Anatolievich is a declarant and patentee. No. 2019106952: declar. 12.03.2019; publ. 24.12.2019.
19. **Lim J.-H., Kang K.-J.**, Mechanical behavior of sandwich panels with tetrahedral and Kagome truss cores fabricated from wires, *Int. J. Solids Struct.* 43 (17) (2006) 5228–5246.
20. **Dragoni E.**, Optimal mechanical design of tetrahedral truss cores for sandwich constructions, *J. Sandw. Struct. Mater.* 15 (4) (2013) 464–484.
21. **Joo J.-H., Kang K.-J.**, Modified metallic octet truss cellular cores for sandwich structures fabricated by an expanded metal forming process, *J. Sandw. Struct. Mater.* 12 (3) (2009) 327–349.
22. **Yang W., Xiong J., Feng L.-J., et al.**, Fabrication and mechanical properties of three-dimensional enhanced lattice truss sandwich structures, *J. Sandw. Struct. Mater.* 22 (5) (2018) 1594–1611.
23. **Borovkov A. I., Aleman Meza D.**, Homogenization of unidirectional fiber and granular elastic composites, *Nauchno-Tekhnicheskiye Vedomosti Sankt-Peterburgskogo Gosudarstvennogo Politekhnikeskogo Universiteta* [St. Petersburg Polytechnic State University Journal of Engineering Science and Technology]. (3(84)) (2009) 135–153 (in Russian).
24. **Ivanov M. V., Mikhailov A. A., Antonova O. V., Kuz'min V. A.**, *Analiz uprugogo povedeniya i opredelenie effektivnykh harakteristik sloistyh paneley s tetraedral'nym zapolnitelem* [An analysis of elastic behavior and determination of effective characteristics of laminated panels with tetrahedral core], *Proc. All-Russian Conf. "The Science Week at the Institute of Physics and Mechanics"*, April 3–7, 2023, St. Petersburg Peter the Great Polytechnic University (2023) 261–263 (in Russian).
25. **Borovkov A. I.**, *Effective physical and mechanic properties of fiber composites*, Publishing of Russian Institute for Scientific and Technical Information (VINITI RAS), Moscow, 1985 (in Russian).
26. **Borovkov A. I., Mamchits D. V., Nemov A. S., Novokshenov A. D.**, Problems of modeling and optimization of variable-hardness panels and structures made of layered composites, *Mechanics of Solids.* 53 (1) (2018) 93–100.
27. **Bukatny S. A., Osadchy N.V.**, Solution of the plane problem of the theory of elasticity on bending of an articulated fixed multilayer panel with a circular axis, *PNRPU Mechanics Bulletin.* (2) (2022) 49–57 (in Russian).
28. **Zhigun V. I., Plume E. Z., Kristone S. A., Krasnov L. L.**, Method for determining the shear moduli of composite materials from experiments in the three-point transverse bending, *Mech. Compos. Mater.* 2023. 58 (6) (2023) 811–822.
29. **Lomakin E. V., Rabotnov Yu. N.**, A theory of elasticity for an isotropic body with different moduli in tension and compression, *Mechanics of Solids.* 13 (6) (1978) 25–30.
30. **Gainutdinov V. G., Abdullin I. N., Musavi-Safavi S. M.**, Calculation of design relative density for rational sandwich structure with truss core, *Russian Aeronautics.* 59 (1) (2016) 64–68.
31. **Ambartsumyan S. A., Khachatryan A. A.**, The basic equations of the theory of elasticity for materials with different stiffness in tension and compression, *Mechanics of Solids.* 1 (2) (1966) 29–34.
32. **Ambartsumyan S. A.**, *Raznomodul'naya teoriya uprugosti* [Multi-module theory of elastisity], Nauka Publishing, Moscow, 1982 (in Russian).
33. **Tsvlodub I. Yu.**, Multimodulus elasticity theory, *J. Appl. Mech. Tech. Phys.* 49 (1) (2008) 129–135.

СПИСОК ЛИТЕРАТУРЫ

1. **Onyibo E. C., Safaei B.** Application of finite element analysis to honeycomb sandwich structures: a review // *Reports in Mechanical Engineering*. 2022. Vol. 3. No. 1. Pp. 192–209.
2. **Faidzi M. K., Abdullah S., Abdullah M. F., Azman A. H., Hui D., Singh S. S. K.** Review of current trends for metal-based sandwich panel: Failure mechanisms and their contribution factors // *Engineering Failure Analysis*. 2021. Vol. 123. May. P. 105302.
3. **Makweche D., Morgan D.** A review of the characteristics and structural behaviour of sandwich panels // *Proceedings of the Institution of Civil Engineers: Structures and Buildings*. 2022. Vol. 175. No.12. Pp. 965–979.
4. **Catapano A., Montemurro M.** A multi-scale approach for the optimum design of sandwich plates with honeycomb core. Part I: homogenization of core properties // *Composite Structures*. 2014. Vol. 118. December. Pp. 664–676.
5. **Xu X. F., Qiao P.** Homogenized elastic properties of honeycomb sandwich with skin effect // *International Journal of Solids and Structures*. 2002. Vol. 39. No. 8. Pp. 2153–2188.
6. **Паймушин В. Р., Галимов Н. К.** Об устойчивости трехслойных пластин с легким заполнителем при изгибе // *Труды семинара по теории оболочек*. Казань: Изд. Казанского физико-технического ин-та АН СССР, 1974. Вып. 5. С. 35–42.
7. **Queheillalt D. T., Wadley H. N. G.** Cellular metal lattices with hollow trusses // *Acta Materialia*. 2005. Vol. 53. No. 2. Pp. 303–313.
8. **Kreja I.** A literature review on computational models for laminated composite and sandwich panels // *Central European Journal of Engineering*. 2011. Vol. 1. No. 1. Pp. 59–80.
9. **Wadley H. N. G., Fleck N. A., Evans A. G.** Fabrication and structural performance of periodic cellular metal sandwich structures // *Composites Science and Technology*. 2003. Vol. 63. No. 16. Pp. 2331–2343.
10. **Wadley H. N. G.** Multifunctional periodic cellular metals // *Philosophical Transactions of the Royal Society A*. 2006. Vol. 364. No. 1838. Pp. 31–68.
11. **Feng Y, Qiu H, Gao Y, Zheng H, Tan J.** Creative design for sandwich structures: A review // *International Journal of Advanced Robotic Systems*. 2020. Vol. 17. No. 3 (May –June) doi:10.1177/1729881420921327.
12. **Паймушин В. Н., Закиров И. М., Луканкин С. А., Закиров И. И., Холмогоров С. А.** Усредненные упругие и прочностные характеристики сотового заполнителя и теоретико-экспериментальный метод их определения // *Механика композитных материалов*. 2012. Т. 48. № 5. С. 745–764.
13. **Абдуллин И. Н., Гайнутдинов В. Г.** Проектирование рациональных трехслойных конструкций со стержневым заполнителем. Изд. Казанского национального исследовательского технического университета им. А. Н. Туполева –КАИ (КНИТУ–КАИ), 2017. 31 с.
14. **Найштут Ю. С.** Сотовые строительные конструкции. М.: Изд-во Ассоциации строительных вузов (АСВ), 1998. 140 с.
15. **Панин В. Ф., Гладков Ю. А.** Конструкции с заполнителем. М.: Машиностроение, 1991. 272 с.
16. **Ендогур А. И., Вайнберг М. В., Иерусалимский К. М.** Сотовые конструкции. Выбор параметров и проектирование. М.: Машиностроение, 1986. 200 с.
17. **Кузьмин В. А.** Заполнитель с ферменной объемной структурой многослойной композитной панели. Пат. 2710157С1 Российская Федерация, МПК В32В 7/00, В32В 15/00, В32В 3/12. Заявитель и патентообладатель Кузьмин В. А. № 2019106951: заявл. 12.03.2019: опубл. 25.02.2020. Бюлл.
18. **Кузьмин В. А.** Способ изготовления заполнителя с ферменной объемной структурой и многослойных панелей на его основе. Пат. № 2710177С1 Российская Федерация, МПК В32В 7/00, В32В 15/00, В32В 3/12. Заявитель и патентообладатель Кузьмин В.А. № 2019106952: заявл. 12.03.2019: опубл. 24.12.2019. Бюлл.
19. **Lim J.-H., Kang K.-J.** Mechanical behavior of sandwich panels with tetrahedral and Kagome truss cores fabricated from wires // *International Journal of Solids and Structures*. 2006. Vol. 43. No. 17. Pp. 5228–5246.
20. **Dragoni E.** Optimal mechanical design of tetrahedral truss cores for sandwich constructions // *Journal of Sandwich Structures & Materials*. 2013. Vol. 15. No.4. Pp. 464–484.



21. Joo J.-H., Kang K.-J. Modified metallic octet truss cellular cores for sandwich structures fabricated by an expanded metal forming process // *Journal of Sandwich Structures & Materials*. 2009. Vol. 12. No. 3. Pp. 327–349.
22. Yang W., Xiong J., Feng L.-J., Pei Ch., Wu L.-Z. Fabrication and mechanical properties of three-dimensional enhanced lattice truss sandwich structures // *Journal of Sandwich Structures & Materials*. 2018. Vol. 22. No. 5. Pp. 1594–1611.
23. Боровков А. И., Меца Д. А. Гомогенизация однонаправленных волокнистых и гранулированных упругих композитов // *Научно-технические ведомости Санкт-Петербургского государственного политехнического университета*. 2009. № 3 (84). С. 135–153.
24. Иванов М. В., Михайлов А. А., Антонова О. В., Кузьмин В. А. Анализ упругого поведения и определение эффективных характеристик слоистых панелей с тетраэдральным наполнителем // *Неделя науки ФизМех: Сборник материалов Всероссийской научной конференции*. 3–7 апреля 2023 г. СПб.: ПОЛИТЕХ-ПРЕСС, 2023. С. 261–263.
25. Боровков А. И. Эффективные физико-механические свойства волокнистых композитов. М.: Изд-во ВИНТИ. 1985. 113 с.
26. Боровков А. И., Мамчиц Д. В., Немов А. С., Новокшенов А. Д. Задачи моделирования и оптимизации панелей переменной жесткости и конструкций из слоистых композитов // *Известия Российской академии наук. Механика твердого тела*. 2018. № 1. С. 113–122.
27. Букатый С. А., Осадчий Н. В. Решение плоской задачи теории упругости об изгибе шарнирно-закрепленной многослойной панели с круговой осью // *Вестник Пермского национального исследовательского политехнического университета. Механика*. 2022. № 2. С. 49–57.
28. Жигун В. И., Плюме Э. З., Кристоне С. А., Краснов Л. Л. Метод определения модуля сдвига композитных материалов из опытов на трехточечный поперечный изгиб // *Механика композитных материалов*. 2022. Т. 58. № 6. С. 1157–1174.
29. Ломакин Е. В., Работнов Ю. Н. Соотношения теории упругости для изотропного разномодульного тела // *Известия АН СССР. Механика твердого тела*. 1978. № 6. С. 29–34.
30. Гайнутдинов В. Г., Абдуллин И. Н., Мусави-Сафави С. М. О расчете проектных значений плотности рациональной трехслойной конструкции со стержневым наполнителем // *Известия вузов. Авиационная техника*. 2016. № 1. С. 59–63.
31. Амбарцумян С. А., Хачатрян А. А. Основные уравнения теории упругости для материалов, разносопротивляющихся растяжению и сжатию // *Известия АН СССР. Механика твердого тела*. 1966. № 2. С. 44–53.
32. Амбарцумян С. А. Разномодульная теория упругости М.: Наука, 1982. 320 с.
33. Цвелодуб И. Ю. О разномодульной теории упругости // *Прикладная механика и техническая физика*. 2008. Т. 49. № 1. С. 157–164.

THE AUTHORS

ANTONOVA Olga V.

Peter the Great St. Petersburg Polytechnic University
29 Politechnicheskaya St., St. Petersburg, 195251, Russia
antonova_ov@spbstu.ru
ORCID: 0000-0002-4318-7050

IVANOV Maksim V.

Peter the Great St. Petersburg Polytechnic University
29 Politechnicheskaya St., St. Petersburg, 195251, Russia
ivanov.m@compmechlab.ru
ORCID: 0009-0003-5702-2251

MIKHAILOV Aleksandr A.

Peter the Great St. Petersburg Polytechnic University
29 Politechnicheskaya St., St. Petersburg, 195251, Russia
mikhailov@compmechlab.com
ORCID: 0000-0002-1025-0148

KUZMIN Valerii A.

LLC “Tetral”

19, build 1, letter A, Lunacharsky Ave., St. Petersburg, 194354, Russia

valerkuzmin@yandex.ru

ORCID: 0009-0002-2129-1591

СВЕДЕНИЯ ОБ АВТОРАХ

АНТОНОВА Ольга Владимировна — кандидат технических наук, доцент Высшей школы механики и процессов управления Санкт-Петербургского политехнического университета Петра Великого.

195251, Россия, г. Санкт-Петербург, Политехническая ул., 29

antonova_ov@spbstu.ru

ORCID: 0000-0002-4318-7050

ИВАНОВ Максим Вячеславович — аспирант Физико-механического института Санкт-Петербургского политехнического университета Петра Великого.

195251, Россия, г. Санкт-Петербург, Политехническая ул., 29

ivanov.m@compmechlab.ru

ORCID: 0009-0003-5702-2251

МИХАЙЛОВ Александр Александрович — аспирант Физико-механического института Санкт-Петербургского политехнического университета Петра Великого.

195251, Россия, г. Санкт-Петербург, Политехническая ул., 29

michailov@compmechlab.com

ORCID: 0000-0002-1025-0148

КУЗЬМИН Валерий Анатольевич — генеральный директор ООО «Тетрал».

194354, Россия, г. Санкт-Петербург, пр. Луначарского, 19 (к. 1, лит. А).

valerkuzmin@yandex.ru

ORCID: 0009-0002-2129-1591

Received 26.12.2024. Approved after reviewing 20.02.2025. Accepted 20.02.2025.

Статья поступила в редакцию 26.12.2024. Одобрена после рецензирования 20.02.2025. Принята 20.02.2025.

EXPERIMENTAL TECHNIQUE AND DEVICES

Original article

DOI: <https://doi.org/10.18721/JPM.18108>

THE EFFECT OF THE MAGNETIC FIELD ON THE SHIELDING EFFICIENCY IN A RUBIDIUM ATOMIC CLOCK

S. V. Ermak[✉], V. V. Semenov, M. V. Sergeeva

Peter the Great St. Petersburg Polytechnic University, St. Petersburg, Russia

[✉] serge_ermak@mail.ru

Abstract. The paper presents the experimental study results of the dependence of the longitudinal shielding coefficient of a magnetic shield (in the direction of the shield axis) on the strengths and mutual orientation of the operational internal and additional external magnetic fields of a small-sized rubidium atomic clock (RAC). In this case, an additional field magnetizes the RAC's magnetic shield from the outside and penetrates inside it. The significant influence of these fields in their interrelation on the shielding properties of the magnetic shield of the RAC has been found. The obtained results allowed us to determine the longitudinal RAC-shielding coefficient at the effective values of the operational and additional magnetic fields and, as a consequence, to compensate for the effect of geomagnetic field variations on the frequency of the onboard RAC.

Keywords: rubidium atomic clock, magnetic field, magnetic screen, longitudinal shielding coefficient

Funding: The reported study was funded by Russian Science Foundation (Grant No. 20-19-00146), <https://rscf.ru/project/20-19-00146/>.

Citation: Ermak S. V., Semenov V. V., Sergeeva M. V., The effect of the magnetic field on the shielding efficiency in a rubidium atomic clock, St. Petersburg State Polytechnical University Journal. Physics and Mathematics. 18 (2) (2025) 41–48. DOI: <https://doi.org/10.18721/JPM.18108>

This is an open access article under the CC BY-NC 4.0 license (<https://creativecommons.org/licenses/by-nc/4.0/>)

Научная статья

УДК 53.098

DOI: <https://doi.org/10.18721/JPM.18108>

ВЛИЯНИЕ МАГНИТНОГО ПОЛЯ НА ЭФФЕКТИВНОСТЬ МАГНИТНОГО ЭКРАНИРОВАНИЯ В РУБИДИЕВЫХ АТОМНЫХ ЧАСАХ

С. В. Ермак[✉], В. В. Семенов, М. В. Сергеева

Санкт-Петербургский политехнический университет Петра Великого, Санкт-Петербург, Россия

[✉] serge_ermak@mail.ru

Аннотация. В работе представлены результаты экспериментальных исследований зависимости продольного коэффициента экранирования магнитного экрана (в направлении оси экрана) малогабаритных рубидиевых атомных часов (РАЧ) от напряженностей и взаимной ориентации их внутреннего рабочего и дополнительного внешнего магнитных полей. При этом дополнительное поле намагничивает извне магнитный экран РАЧ и проникает внутрь него. Установлено существенное влияние этих полей в их взаимосвязи на экранирующие свойства магнитного экрана РАЧ. Полученные результаты позволяют определять продольный коэффициент экранирования РАЧ при действующих значениях рабочего и дополнительного магнитных полей и, как следствие, компенсировать влияние вариаций геомагнитного поля на частоту бортовых РАЧ.

Ключевые слова: рубидиевые атомные часы, магнитное поле, магнитный экран, продольный коэффициент экранирования

Финансирование: Работа выполнена при финансовой поддержке Российского научного фонда, грант № 20-19-00146, <https://rscf.ru/project/20-19-00146/>.

Ссылка для цитирования: Ермак С. В., Семенов В. В., Сергеева М. В. Влияние магнитного поля на эффективность магнитного экранирования в рубидиевых атомных часах // Научно-технические ведомости СПбГПУ. Физико-математические науки. 2025. Т. 18. № 2. С. 41–48. DOI: <https://doi.org/10.18721/JPM.18108>

Статья открытого доступа, распространяемая по лицензии CC BY-NC 4.0 (<https://creativecommons.org/licenses/by-nc/4.0/>)

Introduction

Low-Earth satellite systems are crucial for navigation applications. The accuracy of such systems largely depends on the characteristics of onboard atomic clocks [1–3], which can be used for mini and nanosatellites using small-sized rubidium atomic clocks (RAC) [4]. The magnetic shield of the latter weakens the influence of variations in the external magnetic (geomagnetic) field on RAC frequency. However, due to unavoidable defects (for example, seams and communication ports), such shields do not allow to completely exclude the influence of field variations on the stability of RAC frequency [5]. These irregularities in the shield design lead to a sharp difference in the transverse and longitudinal (along the shield axis) shielding coefficients [6]. Such a difference in the shielding factors leads to a change in the magnitude and direction of the magnetic field penetrating the magnetic shield for RAC located, for example, on-board a satellite [7] moving in low-Earth orbit and leading to orientation dependence of the frequency of onboard RAC. Multilayer magnetic shields providing sufficiently high stability of RAC frequency are commonly used to weaken this dependence. For example, a five-layer magnetic shield was used in the onboard laser-pumped cesium-beam atomic clock described in [8] to obtain long-term relative frequency instability at the level of $3.5 \cdot 10^{-15}$ with short-term relative instability of 10^{-13} . The experimental value of the shielding factor was $3 \cdot 10^5$ in a magnetic field equal to ± 24 A/m.

A drawback of multilayer magnetic shields in onboard RAC (especially small-sized ones) is an increase in their total dimensions and weight. This is why there is a search for new design solutions ensuring the required stability of RAC frequency. It was shown in our earlier paper [9] that magnetization of a two-layer magnetic shield by an additional constant external field significantly increases its shielding factor, which reduces the influence of variations in the external magnetic field on the stability of RAC frequency. In particular, an eightfold increase in the shielding factor was observed for the additional constant magnetizing field of about 12.8 A/m, directed perpendicular to the RAC axis (the direction of the largest shielding factor of the RAC magnetic shield), with an amplitude of an external rotating magnetic field of about 2.5 A/m, simulating the geomagnetic field in the orbit of a navigation satellite.

Further experiments found that at the given values of the additional magnetizing and rotating magnetic fields, the shielding factor of the RAC magnetic shield depends both on the magnitude and on the orientation of the operating magnetic field \mathbf{H}_{op} (internal RAC field) generated in the vicinity of the gas cell by the magnetic system of the RAC.

In this paper, we analyze the details of this dependence based on the measurement results for shifts in RAC frequency at orthogonal and coaxial orientations of the additional constant external magnetic field \mathbf{H}_0 relative to the operating magnetic field \mathbf{H}_{op} .

This additional field \mathbf{H}_0 penetrates from the outside into the shield and is oriented along the longitudinal axis of this shield. A small value of the longitudinal (compared with the transverse) shielding factor S characterizes the degree of penetration of the field \mathbf{H}_0 inside the screen and, consequently, the sensitivity of RAC frequency to variations in the external magnetic field. Thus, measuring the RAC frequency shifts allows to extract information about the values of the longitudinal shielding factor S .



The goal of this study was to find methods for compensating for the influence of an external magnetic field on the frequency of a rubidium atomic clock. The primary objective was to understand the behavior of the key quantity that is the longitudinal shielding factor of the magnetic shield, whose values can be optimized and used for compensation.

The problem was solved by studying the influence of the operating (\mathbf{H}_{op}) and additional (\mathbf{H}_0) magnetic fields, as well as the influence of their mutual orientation on the value of S .

Procedure for measuring the longitudinal shielding coefficient of magnetic shield

The longitudinal shielding factor of a two-layer magnetic shield in a commercial small-sized RAC was evaluated using the experimental setup described in our study [10]. The setup contained a magnetic system of three pairs of Helmholtz coils, with small-sized RAC at the center, connected to a circuit for measuring variations in their frequency. The Helmholtz coils were used to completely compensate for the geomagnetic field in area where the RAC was placed (with an accuracy of tens of nT) and generate an additional constant magnetic field \mathbf{H}_0 of varying strengths. The vector \mathbf{H}_0 was oriented coaxial (orientation $\uparrow\uparrow$) or orthogonal (orientation $\uparrow\downarrow$) to the operating magnetic field \mathbf{H}_{op} . The shield was made of 79NM permalloy, a ferromagnetic Ni alloy. The longitudinal shielding factor S for both orientations ($\uparrow\uparrow$ and $\uparrow\downarrow$) of the operating and additional magnetic fields was determined by measuring the RAC frequency shift relative to the frequency reference at two fixed values of the current in the coil generating the operating magnetic field \mathbf{H}_{op} .

The magnitude of the quantity $|\mathbf{H}_{op}|$ was found by a well-known expression for the frequency of the lasing transition of RAC (see monograph [5]) with the addition of the component ΔH_{in} :

$$\nu = \nu_0 + \beta \cdot (H_{op} \pm \Delta H_{in})^2, \quad (1)$$

where ν_0 is the atomic transition frequency for ^{87}Rb atoms ($\nu_0 = 6.835$ MHz); β is the proportionality constant ($\beta = 90.5$ MHz $\cdot\text{m}^2/\text{A}^2$); ΔH_{in} is the component of the additional external field \mathbf{H}_0 penetrating inside the magnetic shield and oriented coaxially with the operating magnetic field \mathbf{H}_{op} . The value of the latter in RAC is typically on the order of 10 A/m [5].

In our experiments, the longitudinal shielding factor was measured at two values of H_{op} : 11.68 and 12.16 A/m.

The values of the field increments $\pm\Delta H_{in}$ (acting inside the shield and induced by field increments $\pm\Delta H_0$), necessary for subsequent calculations of the longitudinal shielding factor of the RAC screen, were determined by measuring the frequency difference between the RAC and the frequency reference by Eq. (1).

In contrast to the technique described in [9], this study did not use an external rotating magnetic field; it was unnecessary, since we considered the influence of the increments of the additional field ΔH_0 , simulating the geomagnetic field of the Earth, on RAC.

Measurements of longitudinal shielding factor

Fig. 1 shows example waveforms of the relative frequency shift of RAC in the range of magnetic field increments ΔH_0 from 5 to 30 A/m. Table 1 shows the corresponding values of the relative frequency shift of RAC.

Small-sized RAC of the same type as the one considered in the study was used as reference frequency for measuring the RAC frequency shift. This small-sized clock was located outside the magnetic system generating increments ΔH_0 .

The following expression was used to determine the longitudinal shielding coefficient S :

$$S = \Delta H_0 / \Delta H_{in}. \quad (2)$$

Based on the data in Table 1, using Eq. (2) (taking into account expression (1)), we calculated the values of the longitudinal shielding factor S for various combinations of the mutual orientation of the vectors \mathbf{H}_{op} and \mathbf{H}_0 . The results of these calculations are given in Table 1.

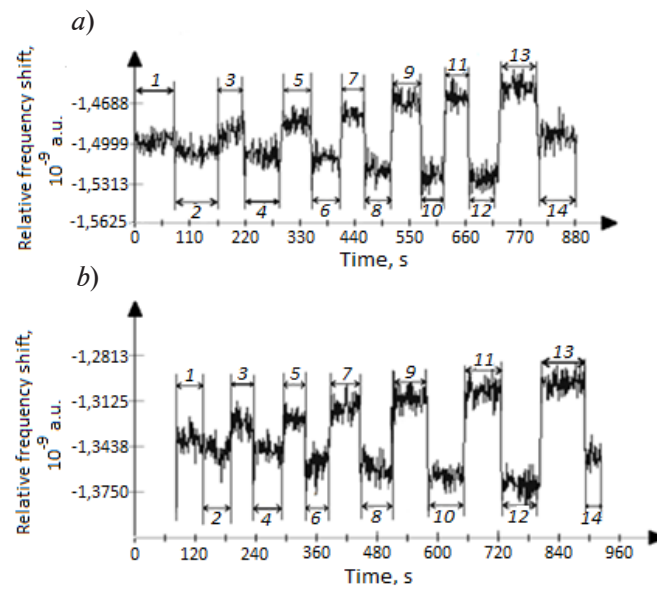


Fig. 1. Waveforms of relative frequency shift of RAC induced by increments ΔH_0 of additional constant external magnetic field H_0 of different orientation at two magnitudes of operating magnetic field H_{op} , A/m: 11.68 (a) and 12.16 (b)
Numbers above the segments correspond to the periods (see Table 1)

Table 1

**Relative frequency shifts of rubidium atomic clock
at different increments of external magnetic field
and two magnitudes of operating magnetic field H_{op}**

Period	External magnetic field increment ΔH_0 , A/m	Relative frequency shift, 10^{-9} rel. units	
		$H_{op} = 11.68$ A/m	$H_{op} = 12.16$ A/m
1	0	-1.4990	-1.3396
2	+5	-1.5047	-1.3449
3	-5	-1.4881	-1.3201
4	+10	-1.5083	-1.3463
5	-10	-1.4831	-1.3251
6	+15	-1.5113	-1.3539
7	-15	-1.4771	-1.3184
8	+20	-1.5196	-1.3576
9	-20	-1.4655	-1.3112
10	+25	-1.5259	-1.3645
11	-25	-1.4635	-1.3062
12	+30	-1.5262	-1.3707
13	-30	-1.4552	-1.3009
14	0	-1.4917	-1.3521



Table 2

**Summary table of longitudinal shielding factors
for two magnitudes of operating magnetic field H_{op}
and its orientation relative to external field H_0**

ΔH_0 , A/m	Longitudinal shielding factor S			
	$H_{op} = 11.68$ A/m		$H_{op} = 12.16$ A/m	
	$\uparrow\uparrow$	$\uparrow\downarrow$	$\uparrow\uparrow$	$\uparrow\downarrow$
5	128	329	89	294
10	181	366	219	294
15	200	398	225	323
20	178	310	250	351
25	665	293	240	320
30	205	352	250	305
40	294	265	305	234
60	288	290	307	209
80	313	290	260	173

Notations: ΔH_0 is the increment of the external magnetic field; $\uparrow\uparrow$ and $\uparrow\downarrow$ are the mutual orientations of the magnetic fields H_0 and H_{op} .

It follows from the data in Table 2 that the greatest discrepancy in the values of the shielding factor S for the orientations of the additional external (H_0) and operating (H_{op}) magnetic fields (denoted as $\uparrow\uparrow$ and $\uparrow\downarrow$) is observed in the range $\Delta H_0 = 5$ A/m, i.e., where the magnetic permeability of the material of the magnetic shield (permalloy) undergoes the most drastic change in the function of the constant external magnetic field [11] whose order of magnitude is comparable to the geomagnetic field intensity in the orbit of navigation satellites. The dynamics of the variations in the shielding factor as a function of the magnitudes of the vectors H_{op} and H_0 and the directions of their mutual orientation makes it possible to determine the value of the shielding factor for various combinations of both the values and the directions of these fields. Data for the shielding factor allows to determine the parameters of the magnetizing field directed orthogonally to the axis of the magnetic shield for the purpose of increasing its shielding factor [9] as well as compensating for the influence of variations in the external magnetic field on the frequency response.

Conclusion

Analysis of the results obtained in the study allows to draw the following conclusions.

1. The longitudinal shielding factor of the RAC magnetic shield significantly depends on both the operating magnetic field and additional magnetizing field as well as on their mutual orientation.
2. The maximum difference between the shielding factors for two opposite orientations of the additional magnetizing field H_0 and operating field H_{op} is observed for the field increment $\Delta H_0 \approx 5$ A/m, which approximately corresponds to the geomagnetic field in the orbit of navigation satellites.
3. The obtained dependence of the shielding factor is of fundamental importance for adjusting the RAC frequency based on the data on variation in the magnitude and direction of the external magnetic field during the satellite's orbital motion.

REFERENCES

1. Kurshin A. V., Improving the accuracy of GLONASS positioning consumers by increasing the refresh rate of satellite clock information, Trudy MAI. (57) (2012) 10 (in Russian).
2. Svehla D., Geometrical theory of satellite orbits and gravity field (Part of Book Series “Springer Theses”), Springer, Cham, Switzerland, 2018.
3. Bandura A. S., Evaluation of the accuracy of the data of navigation messages of spacecraft of satellite radio navigation systems, Sci. Tech. J. Inf. Technol. Mech. Opt. (6(29)) (2006) 215–221 (in Russian).
4. Dinkelaker A. N., Kaparthy A., Reher S. E., Krutzik M., Optical quantum technologies for compact rubidium vapor-cell frequency standards in space using small satellites, J. Br. Interplanet. Soc. 72 (3) (2019) 74–82.
5. Riehle F., Frequency standards: Basics and applications, Wiley–VCH Verlag GmbH & Co., Weinheim, Germany, 2004.
6. Donley E. A., Hodby E., Hollberg L., Kitching J., Demonstration of high-performance compact magnetic shields for chip-scale atomic devices, Rev. Sci. Instrum. 78 (8) (2007) 083102.
7. Ermak S., Semenov V., The influence of the operation magnetic field modulation on the short-term frequency stability of rubidium atomic clock at magnetic gradient, Proc. 2022 Int. Conf. on Electrical Engineering and Photonics (EExPolytech), 20–21 Oct. 2022., St. Petersburg. (2022) 347–350.
8. Dukhina N. G., Miryushchenko N. G., Pleshanov S. A., et al., The shielding efficiency investigation of precision airborne cesium atomic-beam tubes (ABT) with laser pumping (LP), Elektronnaya Tekhnika [Electronic Engineering], Series 1: Microwave Engineering. (4(547)) (2020) 37–52 (in Russian).
9. Ermak S. V., Semenov V. V., Baranov A. A., et al., Effect of shield magnetization on variations in the frequency of onboard rubidium atomic clocks, St. Petersburg State Polytechnical University Journal. Physics and Mathematics. 17 (1) (2024) 56–63 (in Russian).
10. Lozov R. K., Ermak S. V., Semenov V. V., Ermak O. V., Modeling the geomagnetic field influence on the atomic clock accuracy of the satellite navigation systems on-board equipment, J. Radioeng. 83 (12-2) (2019) 32–37 (in Russian).
11. Chikazumi S., Physics of ferromagnetism (Series of Monographs on Physics), Oxford University Press, Oxford, UK, 2009.

СПИСОК ЛИТЕРАТУРЫ

1. Куршин А. В. Повышение точности определения местоположения потребителей ГЛОНАСС путем увеличения частоты закладок временной информации на спутники // Труды МАИ. 2012. № 57. С. 1–7.
2. Svehla D. Geometrical theory of satellite orbits and gravity field. (Part of book series “Springer Theses”). Cham, Switzerland: Springer, 2018. 542 p.
3. Бандура А. С. Оценка точности данных навигационных сообщений космических аппаратов спутниковых радионавигационных систем // Научно-технический вестник информационных технологий, механики и оптики. 2006. № 6 (29). С. 215–221.
4. Dinkelaker A. N., Kaparthy A., Reher S. E., Krutzik M. Optical quantum technologies for compact rubidium vapor-cell frequency standards in space using small satellites // Journal of the British Interplanetary Society. 2019. Vol. 72. No. 3. Pp. 74–82.
5. Риле Ф. Стандарты частоты. Принципы и приложения. Пер. с англ. М.: Физматлит, 2009, 512 с.
6. Donley E. A., Hodby E., Hollberg L., Kitching J. Demonstration of high-performance compact magnetic shields for chip-scale atomic devices // Review of Scientific Instruments. 2007. Vol. 78. No. 8. P. 083102
7. Ermak S., Semenov V. The influence of the operation magnetic field modulation on the short-term frequency stability of rubidium atomic clock at magnetic gradient // Proceedings of 2022 International Conference on Electrical Engineering and Photonics (EExPolytech), 20–21 October, 2022. St. Petersburg. Pp. 347–350.
8. Дукина Н. Г., Мирюшенко Н. И., Плешанов С. А., Ревенко К. В., Чугунов В. В. Исследование эффективности экранирования прецизионных бортовых цезиевых АЛТ-ЛН // Электронная техника. Серия 1: СВЧ-техника. 2020. № 4 (547). С. 37–52.



9. Ермак С. В., Семенов В. В., Баранов А. А., Рогатин М. А., Сергеева М. В. Влияние намагничивания экрана на вариации частоты бортовых атомных часов // Научно-технические ведомости СПбГПУ. Физико-математические науки. 2024. Т. 17. № 1. С. 56–63.
10. Лозов Р. К., Ермак С. В., Семенов В. В., Ермак О. В. Моделирование влияния геомагнитного поля на точность атомных часов бортовой аппаратуры систем спутниковой навигации // Радиотехника. 2019 Т. 83 № 12 (20). С. 32–37.
11. Тикадзуми С. Физика ферромагнетизма. Магнитные характеристики и практические применения. М.: Мир, 1987. 420 с.

THE AUTHORS

ERMAK Sergey V.

Peter the Great St. Petersburg Polytechnic University
29 Politechnicheskaya St., St. Petersburg, 195251, Russia
serge_ermak@mail.ru
ORCID: 0000-0002-6210-4003

SEMENOV Vladimir V.

Peter the Great St. Petersburg Polytechnic University
29 Politechnicheskaya St., St. Petersburg, 195251, Russia
vladimir_semenov@mail.ru
ORCID: 0000-0003-0346-8349

SERGEEVA Maria V.

Peter the Great St. Petersburg Polytechnic University
29 Politechnicheskaya St., St. Petersburg, 195251, Russia
mamavel2001@mail.ru
ORCID: 0009-0005-8838-6845

СВЕДЕНИЯ ОБ АВТОРАХ

ЕРМАК Сергей Викторович — доктор физико-математических наук, профессор Высшей школы прикладной физики и космических технологий Санкт-Петербургского политехнического университета Петра Великого.

195251, Россия, г. Санкт-Петербург, Политехническая ул., 29

serge_ermak@mail.ru

ORCID: 0000-0002-6210-4003

СЕМЕНОВ Владимир Васильевич — доктор физико-математических наук, профессор Высшей школы прикладной физики и космических технологий Санкт-Петербургского политехнического университета Петра Великого.

195251, Россия, г. Санкт-Петербург, Политехническая ул., 29

vladimir_semenov@mail.ru

ORCID: 0000-0003-0346-8349

СЕРГЕЕВА Мария Вячеславовна — инженер Высшей школы прикладной физики и космических технологий Санкт-Петербургского политехнического университета Петра Великого.

195251, Россия, г. Санкт-Петербург, Политехническая ул., 29

mamavel2001@mail.ru

ORCID: 0009-0005-8838-6845

Received 09.07.2024. Approved after reviewing 28.11.2024. Accepted 28.11.2024.

Статья поступила в редакцию 09.07.2024. Одобрена после рецензирования 28.11.2024. Принята 28.11.2024.

Original article

DOI: <https://doi.org/10.18721/JPM.18205>

THE X-RAY ABSORPTION IMMERSION TECHNOLOGY FOR ENRICHMENT OF DIAMOND ORES: PHYSICAL FOUNDATIONS AND PRACTICAL IMPLEMENTATION

V. D. Kuptsov[✉]

Peter the Great St. Petersburg Polytechnic University, St. Petersburg, Russia

[✉] kuptsov@spbstu.ru

Abstract. The paper presents physical principles of X-ray absorption immersion technology (XRAIT) based on recording X-ray radiation passed through diamond-containing ore, pore spaces between the pieces of which are preliminarily filled with an immersion medium (IM). The energy range of X-ray photons where the diamond is more transparent than the ore components has been determined. Based on the proposed approximation of the mass attenuation coefficients of elements by the sum of two power functions, a justification for a conscious choice of the mass attenuation coefficient of the IM equal to the average value for all ore components was carried out taking into account their weight content. An optimal composition of the IM in the form of a bulk material, namely aluminum-zinc alloy powder, was proposed. Experiments conducted on a developed and manufactured prototype of the separator confirmed the possibility of using the XRAIT with significant advantages over analogues.

Keywords: X-ray absorption technology, immersion medium, mass attenuation coefficient, X-ray radiation, diamonds

Citation: Kuptsov V. D., The X-ray absorption immersion technology for enrichment of diamond ores: physical foundations and practical implementation, St. Petersburg State Polytechnical University Journal. Physics and Mathematics. 18 (2) (2025) 49–59. DOI: <https://doi.org/10.18721/JPM.18205>

This is an open access article under the CC BY-NC 4.0 license (<https://creativecommons.org/licenses/by-nc/4.0/>)

Научная статья

УДК 622.7

DOI: <https://doi.org/10.18721/JPM.18205>

РЕНТГЕНО-АБСОРБЦИОННАЯ ИММЕРСИОННАЯ ТЕХНОЛОГИЯ ОБОГАЩЕНИЯ АЛМАЗОСОДЕРЖАЩИХ РУД: ФИЗИЧЕСКИЕ ОСНОВЫ И ПРАКТИЧЕСКАЯ РЕАЛИЗАЦИЯ

В. Д. Купцов[✉]

Санкт-Петербургский политехнический университет Петра Великого, Санкт-Петербург, Россия

[✉] kuptsov@spbstu.ru

Аннотация. В работе представлены физические основы рентгено-абсорбционной иммерсионной технологии (РАИТ), основанной на регистрации рентгеновского излучения, прошедшего через алмазосодержащую руду, пустоты между кусками которой предварительно заполняются иммерсионной средой (ИС). При этом определен диапазон энергий рентгеновских фотонов, в котором алмаз более прозрачен, чем компоненты руды. На основе предложенной аппроксимации массовых коэффициентов ослабления элементов суммой двух степенных функций проведено обоснование осознанного выбора массового коэффициента ослабления ИС, равного среднему значению по всем компонентам руды с учетом их весового содержания. По результатам тестирования

предложен оптимальный состав ИС в виде сыпучего материала: порошок сплава алюминия с цинком. Эксперименты, проведенные на разработанном и изготовленном образце сепаратора, подтвердили возможность применения РАИТ, обладающей существенными преимуществами над аналогами.

Ключевые слова: рентгено-абсорбционная технология, иммерсионная среда, массовый коэффициент ослабления, рентгеновское излучение, алмазы

Ссылка для цитирования: Купцов В. Д. Рентгено-абсорбционная иммерсионная технология обогащения алмазосодержащих руд: физические основы и практическая реализация // Научно-технические ведомости СПбГПУ. Физико-математические науки. 2025. Т. 18. № 2. С. 49–59. DOI: <https://doi.org/10.18721/JPM.18205>

Статья открытого доступа, распространяемая по лицензии CC BY-NC 4.0 (<https://creativecommons.org/licenses/by-nc/4.0/>)

Introduction

The physical basis of the X-ray absorption technology for enrichment of minerals is the attenuation (absorption and scattering) of electromagnetic radiation in the X-ray spectrum passing through diamond-bearing ore. A distinguishing feature in separation of minerals is the difference in radiation intensities transmitted through the ore in its cross-sections with and without diamonds.

The advances in the X-ray absorption technology made recently allow to replace the common methods for processing diamond-bearing ores with this technology, not only during recovery but also in the main stages of enrichment [1].

Currently, X-ray fluorescence (XRF), gravity-based separation and techniques using grease tables are widely used in mining.

The physical basis of the XRF technique is the fluorescence of the diamond exposed to X-ray pulses. To analyze this fluorescence, two separation criteria are used: the autocorrelation function and the ratio of the components of the fluorescence lifetime [1]. The diamond must be located on the surface of a piece of kimberlite for such analysis, otherwise it will not be detected. Consequently, ore should be disintegrated in wet ball mills or jaw crushers, which causes damage (chipping) to the stones, significantly reducing their cost. In addition to chipping, losses due to uncharacteristic fluorescence kinetics typical for diamonds occur during XRF separation [2].

To overcome this drawback, research is underway on treating raw materials with organic luminophores to modify the X-ray fluorescent properties of weakly fluorescent diamonds and selectively identify them in XRF separators [3].

The physical basis of gravity (heavy-media) separation technology is the difference in the density of diamonds and gangue. The density of a diamond is 3.40–3.55 g/cm³, while that of gangue is about 2.5 g/cm³. In the process of such separation in a liquid medium with a density of about 3.0 g/cm³, diamond-bearing ore sinks to the bottom of the container and gangue floats to the surface. Rotating the liquid together with ore pieces in special hydrocyclones accelerates the separation process [4]. The advantage of gravity technology is that it allows to extract rough diamonds (located inside pieces of ore). Its disadvantages include the need for precision control of the density of heavy liquid, maintained at the level of 3.0 g/cm³, and most importantly, environmental damages.

The physical basis of the grease-based technology is the difference in the adhesion of diamond and kimberlite pieces to the grease table. Grease separation is mainly used in at the recovery stage.

Great efforts are made to improve the technologies for processing diamond ore. Recent advances include a dual-energy X-ray separation method using nanosecond pulses of two energy levels of an explosive electron emission-based X-ray tube [5], as well as complementing the X-ray fluorescence method with X-ray absorption [6, 7].

The above-mentioned drawbacks of diamond ore processing technologies can be significantly mitigated or even completely eliminated by introducing the X-ray absorption immersion technology (XRAIT) [8].

XRAIT is based on placing pieces of diamond ore into an immersion medium (IM) with a linear X-ray attenuation coefficient close to the linear attenuation coefficient of kimberlite. The IM is intended for filling all cavities between diamond ore pieces, ore with a constant thickness on the transporter [9].

IM allows to arrange pieces of diamond-bearing ore on a transporter as a parallelepiped made of kimberlite, inside which a diamond may be located. The schematic diagram for XRAIT is shown in Fig. 1.

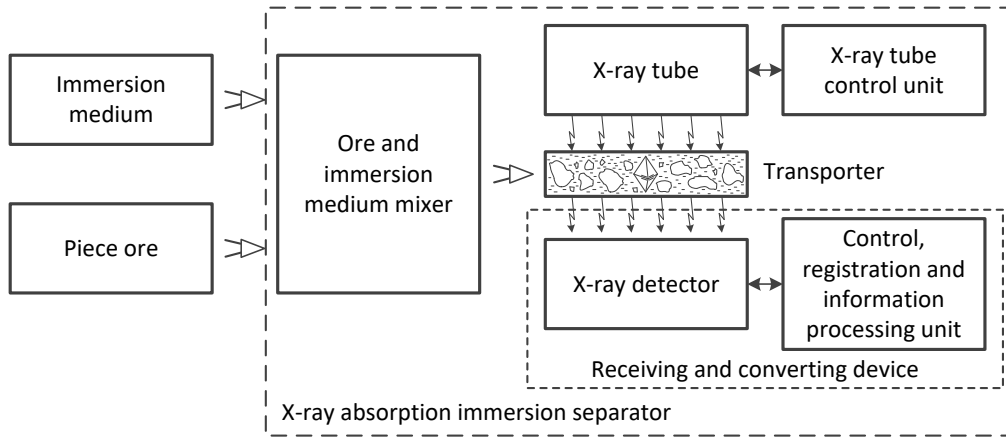


Fig. 1. Schematic diagram of X-ray absorption immersion technology: immersion medium; piece ore; X-ray tube control unit; receiving and converting device

The goals of this study consisted in theoretical analysis of the physical foundations of X-ray absorption immersion technology, aimed at resolving its main technological drawbacks.

To achieve these goals, we analyzed the attenuation of X-ray radiation in diamond and related minerals, conducting experimental tests to validate the proposed technology

Attenuation of X-ray radiation by different media

The penetrating radiation generated in the X-ray tube passes through a mixture of ore and IM, is converted into optical radiation in the scintillator, which, in turn, is converted into electrical signal in the receiving and converting device. The braking radiation of the X-ray tube is generated during the curvilinear motion of electrons in the Coulomb field of atoms in the tube's anode. In addition to braking radiation, X-ray tubes emit rather narrow spectral lines of characteristic X-ray radiation associated with the transition of electrons from one orbit to another. However, significantly lower energy is concentrated in the characteristic radiation compared to the braking radiation, which makes it possible not to neglect the characteristic radiation in calculations of intensity and transmitted radiation.

The XRAIT is based on the detecting radiation transmitted through ore placed in IM with a linear attenuation coefficient close to the linear attenuation coefficient of gangue of diamond-bearing ore. As a result, the intensity level of X-ray radiation after passing through diamond-bearing ore in IM is determined by the attenuation of radiation in kimberlite, diamond, IM and scintillator. A photocurrent proportional to the intensity of the transmitted X-ray radiation is formed in the receiving and converting device.

The X-ray radiation intensity I_x at the medium depth x is determined by the Bouguer–Lambert law:

$$I_x = I_0 \exp\{-\mu_x x\} = I_0 \exp\{-\mu_m \rho x\}, \quad (1)$$

where μ_x is the linear attenuation coefficient of X-ray radiation, μ_m is the mass attenuation coefficient, ρ is the density of absorbing substance, I_0 is the intensity of incident radiation.

The mass attenuation coefficient, unlike the linear one, does not depend on the aggregate state of the substance. The mass attenuation coefficients of the elements obtained experimentally can be found in reference tables in [10].

Approximations of the energy dependence of mass attenuation coefficients are used for analytical calculations of penetrating radiation. In contrast to the discrete range of energies given in the tables with experimental data [10], the approximated dependences allow to calculate X-ray attenuation continuously for all photon energies.

The smallest error of the approximations of mass attenuation coefficient considered is provided by the approximation in the form of a sum of two power functions:

$$\begin{cases} \mu_1 = a_{11}E^{-b_{11}} + a_{12}E^{-b_{12}} + c_1, & E < E_k, \\ \mu_2 = a_{21}E^{-b_{21}} + a_{22}E^{-b_{22}} + c_2, & E \geq E_k, \end{cases} \quad (2)$$

where E_k is the energy of the k -absorption edge.

The relative error of this approximation for elements with the atomic number Z lower than 26 in the energy range of 1–150 keV does not exceed 1% compared with experimental data [10]. The relative error does not exceed 2% for elements with the atomic number higher than 26 (^{26}Fe) in the range of 1–400 keV. Table 1 gives the approximations obtained for the mass attenuation coefficients of the elements of diamond-bearing ore, the materials of anodes of X-ray tubes, filters and scintillators. Characteristic radiation was not taken into account.

The mass attenuation coefficient of a complex molecule is

$$(\mu_m)_{mol} = \sum_i C_i \mu_{mi}, \quad (3)$$

where μ_{mi} is the mass attenuation coefficient of the i th element in the molecule, C_i is the mass fraction of the i th element in the molecule; summation is carried out for all elements in the molecule. The mass attenuation coefficients of mixtures of suspensions, alloys and solutions are determined similarly. In this case, C_i is the mass fraction of the i th substance in such medium [11].

The intensity of transmitted radiation is reduced by half in the so-called half-value layer (HVL) [11]:

$$d(E) = \frac{\ln 2}{\mu_m(E) \cdot \rho} = \frac{\ln 2}{\mu_x(E)}. \quad (4)$$

The chemical compositions of the main components of the diamond-bearing ore are given in Table 2. Based on the energy dependences obtained for the mass attenuation coefficients of the elements, in accordance with expressions (3) and (4), we calculated the HVL of the components of diamond-bearing ore depending on the energy of X-ray photons for the ranges of 10–100 and 100–1000 keV (Fig. 2).

The HVL of diamond significantly exceeds those of any components of the diamond-bearing ore in the photon energy range of 10–50 keV (see Fig. 2, *a*). At an energy of 30 keV, the HVL of diamond exceeds the HVL of the nearest component of the diamond-bearing ore, serpentine, by two times.

XRAIT is based on X-ray attenuation by the diamond in the photon energy range of 10–50 keV, where the half-value layer exceeds those for all other minerals in the ore. An additional factor is that the cavities between the ore pieces are filled with the immersion medium with a linear attenuation coefficient close to the average for all ore components taking into account their mass fraction.

Diamond is significantly more transparent than any of the other components of the diamond-bearing ore in the photon energy range of 10–50 keV. The IM is used to fill cavities between pieces of diamond-bearing ore. Then there is a significant increase in the intensity of transmitted X-ray radiation in the diamond cross-section. If the cavities are left unfilled, the intensity of the transmitted X-ray radiation in the cross-sections of the cavities increases as if this cross-section contained a large diamond. There are a lot of cavities between pieces of ore on the multilayer transporter, therefore XRAIT without the IM cannot be used to isolate pieces of ore containing diamonds.



Table 1

**Formulas of approximations obtained for mass attenuation coefficients
of elements by summation of two power functions (see Eq. (2))**

Element	Approximation formula for μ (E , keV), cm^2/g	Energy range E , keV
^6C	$2.781 \cdot 10^3 \cdot E^{-3.100} - 8.477 \cdot 10^{-4} \cdot E^{0.840} + 0.1930$	$1.0000 \leq E < 200.00$
^8O	$6.284 \cdot 10^3 \cdot E^{-3.032} - 3.403 \cdot 10^{-4} \cdot E^{0.977} + 0.1820$	$1.0000 \leq E < 200.00$
^{11}Na	$1.575 \cdot 10^4 \cdot E^{-3.010} - 7.884 \cdot 10^{-7} \cdot E^{2.044} + 0.1557$	$1.0000 \leq E < 200.00$
^{12}Mg	$2.130 \cdot 10^4 \cdot E^{-3.007} - 6.825 \cdot 10^{-6} \cdot E^{1.655} + 0.1640$	$1.0000 \leq E < 200.00$
^{13}Al	$1.955 \cdot 10^3 \cdot E^{-2.623} - 10.5560$	$1.0000 \leq E < 1.5596$
	$2.390 \cdot 10^4 \cdot E^{-2.961} - 1.880 \cdot 10^4 \cdot E^{-4.541} + 0.1430$	$1.5596 \leq E < 105.00$
^{14}Si	$1.582 \cdot 10^3 \cdot E^{-2.616} - 12.2000$	$1.0000 \leq E < 1.8389$
	$3.190 \cdot 10^4 \cdot E^{-2.967} - 3.020 \cdot 10^4 \cdot E^{-4.403} + 0.1480$	$1.8389 \leq E < 110.00$
^{19}K	$4.272 \cdot 10^3 \cdot E^{-2.684} - 2.100 \cdot 10^2 \cdot E^{-6.354} - 3.7300$	$1.0000 \leq E < 3.6074$
	$7.720 \cdot 10^4 \cdot E^{-2.949} - 1.080 \cdot 10^5 \cdot E^{-4.094} + 0.1350$	$3.6074 \leq E < 125.00$
^{20}Ca	$5.163 \cdot 10^3 \cdot E^{-2.677} - 2.900 \cdot 10^2 \cdot E^{-6.183} - 4.3500$	$1.0000 \leq E < 4.0381$
	$8.565 \cdot 10^4 \cdot E^{-2.930} - 1.855 \cdot 10^5 \cdot E^{-4.367} + 0.1365$	$4.0381 \leq E < 125.00$
^{25}Mn	$9.770 \cdot 10^3 \cdot E^{-2.716} - 1.680 \cdot 10^3 \cdot E^{-4.701} - 1.3000$	$1.0000 \leq E < 6.5390$
	$1.380 \cdot 10^5 \cdot E^{-2.902} - 7.830 \cdot 10^5 \cdot E^{-4.580} + 0.1185$	$6.5390 \leq E < 150.00$
^{26}Fe	$1.113 \cdot 10^4 \cdot E^{-2.709} - 2.050 \cdot 10^3 \cdot E^{-4.758} - 1.4000$	$1.0000 \leq E < 7.1120$
	$1.555 \cdot 10^5 \cdot E^{-2.897} - 10.45 \cdot 10^5 \cdot E^{-4.609} + 0.1204$	$7.1120 \leq E < 150.00$
^{29}Cu	$1.505 \cdot 10^4 \cdot E^{-2.709} - 3.700 \cdot 10^3 \cdot E^{-4.741} - 1.0000$	$1.0961 \leq E < 8.9789$
	$1.840 \cdot 10^5 \cdot E^{-2.864} - 8.300 \cdot 10^6 \cdot E^{-5.350} + 0.1120$	$8.9789 \leq E < 175.00$
^{30}Zn	$1.685 \cdot 10^4 \cdot E^{-2.710} - 4.600 \cdot 10^3 \cdot E^{-4.617} - 0.9000$	$1.1936 \leq E < 9.6586$
	$2.029 \cdot 10^5 \cdot E^{-2.859} - 3.600 \cdot 10^6 \cdot E^{-4.872} + 0.1100$	$9.6586 \leq E < 195.00$
^{39}Y	$3.210 \cdot 10^4 \cdot E^{-2.660} - 2.777 \cdot 10^4 \cdot E^{-5.381} - 0.9100$	$2.3725 \leq E < 17.0384$
	$3.131 \cdot 10^5 \cdot E^{-2.791} - 8.232 \cdot 10^7 \cdot E^{-5.558} + 0.0950$	$17.0384 \leq E < 220.00$
^{42}Mo	$4.007 \cdot 10^4 \cdot E^{-2.665} - 9.713 \cdot 10^4 \cdot E^{-5.978} - 0.6500$	$2.8655 \leq E < 19.9995$
	$3.852 \cdot 10^5 \cdot E^{-2.792} - 1.489 \cdot 10^8 \cdot E^{-5.533} + 0.0970$	$19.9995 \leq E < 220.00$
^{47}Ag	$5.557 \cdot 10^4 \cdot E^{-2.667} - 5.017 \cdot 10^5 \cdot E^{-6.354} - 0.3500$	$3.8058 \leq E < 25.5140$
	$4.413 \cdot 10^5 \cdot E^{-2.751} - 1.476 \cdot 10^9 \cdot E^{-6.066} + 0.0895$	$25.5140 \leq E < 280.00$
^{48}Cd	$5.733 \cdot 10^4 \cdot E^{-2.663} - 8.930 \cdot 10^5 \cdot E^{-6.629} - 0.3200$	$4.0180 \leq E < 26.7112$
	$4.439 \cdot 10^4 \cdot E^{-2.743} - 4.511 \cdot 10^8 \cdot E^{-5.663} + 0.0850$	$26.7112 \leq E < 320.00$
^{53}I	$8.091 \cdot 10^4 \cdot E^{-2.693} - 1.333 \cdot 10^6 \cdot E^{-5.932} + 0.0600$	$5.1881 \leq E < 33.1694$
	$5.245 \cdot 10^5 \cdot E^{-2.724} - 1.200 \cdot 10^9 \cdot E^{-5.790} + 0.0824$	$33.1694 \leq E < 320.00$
^{55}Cs	$8.757 \cdot 10^4 \cdot E^{-2.684} - 2.230 \cdot 10^6 \cdot E^{-6.050} + 0.0260$	$5.7143 \leq E < 35.9846$
	$5.920 \cdot 10^5 \cdot E^{-2.732} - 2.150 \cdot 10^{10} \cdot E^{-6.447} + 0.0860$	$35.9846 \leq E < 320.00$
^{56}Ba	$8.986 \cdot 10^4 \cdot E^{-2.679} - 2.253 \cdot 10^6 \cdot E^{-5.983} + 0.0210$	$5.9888 \leq E < 37.4406$
	$5.943 \cdot 10^5 \cdot E^{-2.725} - 1.631 \cdot 10^{10} \cdot E^{-6.368} + 0.0839$	$37.4406 \leq E < 320.00$
^{64}Gd	$1.294 \cdot 10^5 \cdot E^{-2.669} - 3.501 \cdot 10^5 \cdot E^{-6.639} + 0.0800$	$8.3756 \leq E < 50.2391$
	$7.300 \cdot 10^5 \cdot E^{-2.689} - 1.330 \cdot 10^8 \cdot E^{-4.800} + 0.0818$	$50.2391 \leq E < 320.00$
^{65}Tb	$1.341 \cdot 10^5 \cdot E^{-2.664} - 4.335 \cdot 10^7 \cdot E^{-6.673} + 0.0740$	$8.7080 \leq E < 51.9957$
	$7.520 \cdot 10^5 \cdot E^{-2.684} - 2.260 \cdot 10^7 \cdot E^{-4.300} + 0.0804$	$51.9957 \leq E < 320.00$
^{74}W	$1.959 \cdot 10^5 \cdot E^{-2.665} - 2.036 \cdot 10^7 \cdot E^{-5.619} + 0.1390$	$12.0998 \leq E < 69.5250$
	$7.715 \cdot 10^5 \cdot E^{-2.623} - 3.140 \cdot 10^8 \cdot E^{-4.981} + 0.0775$	$69.5250 \leq E < 400.00$
^{79}Au	$2.194 \cdot 10^5 \cdot E^{-2.642} - 3.200 \cdot 10^7 \cdot E^{-5.631} + 0.1290$	$14.3528 \leq E < 80.7249$
	$8.118 \cdot 10^5 \cdot E^{-2.600} - 2.784 \cdot 10^7 \cdot E^{-4.400} + 0.0795$	$80.7249 \leq E < 400.00$
^{82}Pb	$2.385 \cdot 10^5 \cdot E^{-2.636} - 3.226 \cdot 10^7 \cdot E^{-5.471} + 0.1250$	$15.8608 \leq E < 88.0045$
	$7.526 \cdot 10^5 \cdot E^{-2.569} + 0.0770$	$88.0045 \leq E < 400.00$

Table 2

Key characteristics of natural minerals of diamond-bearing ore			
Number	Mineral	Chemical formula	Density, kg/m ³
1	Serpentine	Mg ₆ Si ₄ O ₁₈ H ₈	2.52
2	Quartz	SiO ₂	2.60
3	Diamond	C	3.51
4	Calcite	CaCO ₃	2.65
5	Pyrope	Mg ₃ Al ₂ Si ₃ O ₁₂	3.55
6	Kyanite	Al ₂ O ₈ Si	3.58
7	Diopside	CaMgSiO ₂	3.28
8	Biotite	KMg ₃ Fe ₃ AlO ₁₂ H ₂ F ₂	3.00
9	Ilmenite	FeTiO ₃	4.73
10	Pyrite	FeS ₂	4.95
11	Magnetite	Fe ₃ O ₄	5.00
12	Zircon	SrSiO ₄	4.66
13	Scheelite	CaWO ₄	5.90

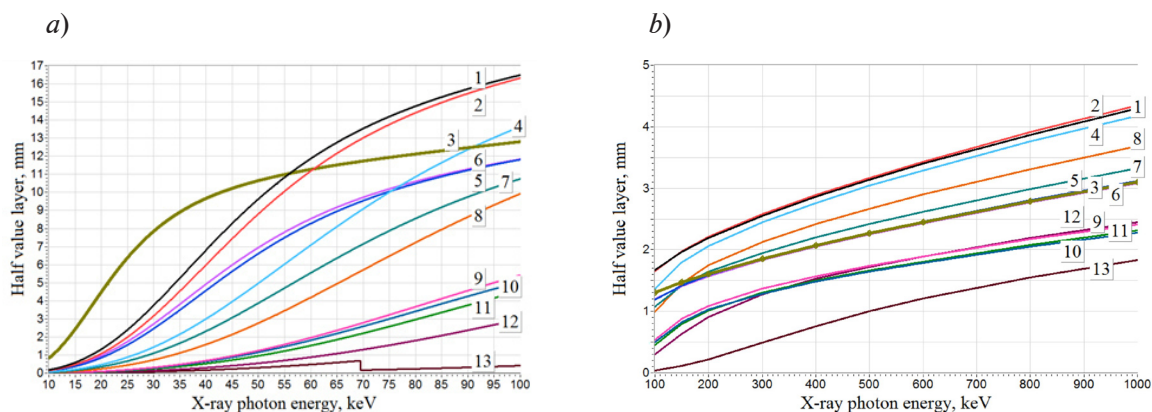


Fig. 2. Dependences of half-value layer for components of diamond-bearing ore on X-ray photon energies in range of 10–100 keV (a) and 100–1000 keV (b)
Curve numbers correspond to those in Table 2

In the case when the IM evenly fills all cavities between the ore pieces, X-ray radiation is guaranteed to pass through the same thickness of the component mixture: ore, diamond and IM. The characteristic differentiating the diamond from gangue is the transmitted X-ray radiation exceeding the threshold determined by fluctuations in the X-ray background associated with inhomogeneous composition of the ore.

The patent [5] proposes a method for dual-energy X-ray projection separation of mineral raw materials based on reducing the attenuation coefficient compared to the host rock at low X-ray radiation energy (values of 20–230 keV are given) and (conversely) increasing this coefficient at a high energy level (250–700 keV).



Notably, such ore components as serpentine, quartz, calcite, and biotite attenuate primary radiation to a smaller extent than diamond in the energy range of 250–700 keV (see Fig. 2,*b*). Therefore, these minerals fit the differentiation criterion proposed in the patent [5]. However, minerals such as diopside, pyrope, and kyanite are practically indistinguishable from diamonds in terms of attenuation of penetrating radiation. As for minerals such as ilmenite, pyrite, magnetite, zircon and scheelite, they have significantly lower transparency compared to diamond the same as in range of 10–50 keV. This means that these minerals do not fit the differentiation criterion proposed in the patent [5]. As a result, the method proposed by in the patent [5] is not always applicable for separating diamond from its ore.

Experimental results obtained with X-ray absorption immersion separator

The proposed technology is based on X-ray absorption immersion separators. We fabricated a prototype separator, using to detect rough diamonds in pieces of kimberlite. The separator consists of the following parts:

- X-ray tube with control unit and cooling system for tungsten anode with running water;
- vibratory feeder supplying ore;
- feeder supplying immersion medium;
- separation device;
- receiving and converting device.

The X-ray radiation transmitted through the ore in IM is converted into electrical signal in the receiving and converting device, which includes a position-sensitive scintillation detector based on gadolinium oxysulfide $\text{Gd}_2\text{O}_2\text{S}(\text{Tb})$ (0.3 mm thick), 256 photodiode-based integrated photodetectors and operational amplifiers with capacitive feedback and control unit for detection of penetrating X-ray radiation, information processing and control of separator actuators. The $\text{Gd}_2\text{O}_2\text{S}(\text{Tb})$ scintillator converts transmitted X-rays into green light (visible range), which is then transmitted to photodiodes. The electric charge from the photodiodes, proportional to the transmitted X-ray radiation, is supplied to the operational amplifier integrators. The control unit allows to visualize the intensity of the transmitted X-ray radiation in the cross-section of the transporter as graphs on a computer screen.

The IM can be liquid: both in the form of suspensions and aqueous solutions of salts. The experimental studies conducted confirmed the possibility of using suspensions of barium sulfate (BaSO_4) and ferrosilicon (FeSi). Testing of many aqueous solutions made it possible to isolate potassium iodide (KI), lead acetic acid ($\text{Pb}(\text{CH}_3\text{COO})_2 \cdot 3\text{H}_2\text{O}$) and sodium tungstate ($\text{Na}_2\text{WO}_4 \cdot 2\text{H}_2\text{O}$) for practical use. To achieve the required linear attenuation coefficient of the IM, it is necessary to select the appropriate concentration. Importantly, the required mass density of immersion suspensions and solutions turned out to be lower than the density of liquid media in gravity technology.

However, the following problem arose: when ore pieces and liquid IM were mixed, air bubbles were formed that were even more transparent to X-rays than diamonds; as a result, the bubbles were mistakenly detected as large diamonds. Despite attempts to remove the bubbles by flushing, it was not possible to obtain an effective solution to this problem.

The immersion medium in the form of bulk powder yielded much better results. In this case, uniform thickness of the bulk material layer had to be achieved, but this task was easily solved using a scraper mounted above the transporter. Experiments were conducted for milled ferrosilicon, iron oxide, separately for iron and aluminum powders, aluminum alloy powders with tin and copper, with zinc, with nickel and quartz sand.

Metal alloy powders are used in powder metallurgy, so they are more affordable, as they are produced industrially. In terms of X-ray absorption and consumer properties, aluminum alloy powder with zinc (94% Al + 6% Zn) with a fraction of 100–200 μm has proved to be the best option. This material has a number of advantages: it is completely non-hazardous, it has good flowability, it is dust-free, it separates perfectly from pieces of diamond-bearing ore, dries and does not clump. Due to these properties, it is comparatively easy to return the material to the circulation cycle of the immersion medium at mining facilities. The powder made it possible to completely solve the problem of air bubbles on the transporter.

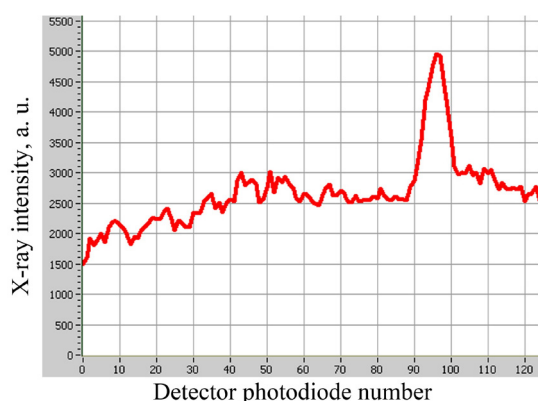


Fig. 3. Distribution of X-ray radiation intensity transmitted through ore with 4 mm diamond placed in immersion medium (Al + Zn alloy powder) along transporter cross-section
Photodiode numbers of the position-sensitive scintillation detector are plotted along the ordinate

Detection of rough diamonds using the proposed XRAIT was carried out on with an experimental prototype separator. The obtained results are presented in Fig. 3, showing the intensity distribution of the transmitted X-ray radiation through ore pieces in the cross section of the transporter at a 30 kV anode voltage of the X-ray tube and a layer thickness of 26 mm. The IM was an aluminum alloy powder with zinc (94% Al + 6% Zn), fraction of 100–200 μm , bulk density of 1.46 g/cm^3 .

The response amplitude of the 4 mm diamond was twice as high as the average level of the transmitted X-ray radiation. The ratio of useful signal depending on the presence of diamond to the fluctuation level associated with the inhomogeneity of fractions in kimberlite pieces exceeded a fivefold value. As a result, the probability of detecting diamond in a piece of diamond-bearing ore was 99%.

Conclusion

Studies of the physical foundations of X-ray absorption immersion technology provided insights into the propagation of X-rays in diamond-bearing ore containing many different minerals: serpentine, quartz, calcite, pyrope, kyanite, diopside, biotite, ilmenite, zircon and scheelite. We found and justified a convenient range of X-ray photon energies, 10–50 keV, where diamond is more transparent to penetrating X-rays compared with other natural minerals of diamond-bearing ore. It was established that serpentine is the closest in transparency to diamond in this range.

To mathematically describe the physical phenomenon of attenuation of penetrating X-ray radiation through objects, we constructed a model with an approximation of the mass attenuation coefficients by the sum of two power functions containing a set of key parameters. The proposed approximations give a relative error of 1–2% in the energy range of 1–400 keV and are suitable for calculating the energy dependences of penetrating X-ray radiation.

Based on the detected patterns of X-ray attenuation, we proposed an X-ray absorption immersion technology for extracting natural diamonds, which involves filling cavities between pieces of kimberlite with an immersion medium with a linear attenuation coefficient equal to the average for all ore components, taking into account their mass fractions. We established the advantages of using an immersion medium in the form of a bulk material (aluminum alloy powder with zinc) over liquid immersion media where the influence of air bubbles has to be eliminated.

The proposed X-ray absorption immersion method was validated with a prototype separator we developed and fabricated, used for experiments to detect rough diamonds in pieces of kimberlite. The experiments revealed that the response amplitude of a 4 mm diamond is twice as high as the average level of the transmitted X-ray radiation. Such an important indicator as the ratio of useful signal corresponding to the presence of diamond to the level of fluctuations associated with the inhomogeneity of fractions in the composition of kimberlite pieces was found to exceed a fivefold value. As a result, the presence of diamond in a piece of diamond-bearing ore is determined with a high probability of 99%.

The proposed X-ray absorption immersion technology for extracting natural diamonds offers significant advantages:

- possibility of extracting rough diamonds,
- reduced amount of chipping during ore disintegration,
- possibility of extracting weakly fluorescent diamonds,
- low environmental damage.



Naturally, such advantageous technology will require additional equipment at mining facilities to mix the immersion medium (dry powder) with disintegrated diamond-bearing ore and ensure a closed cycle reusing the immersion medium. The workflow of the facilities will also require restructuring.

However, such costs are undoubtedly justified and will pay off quickly: even saving only one 100-carat diamond from chipping generates revenue of up to tens of millions of dollars.

Adjusting the technical parameters of X-ray absorption immersion separators will make it possible to achieve diamond extraction in poor and remote deposits, and even mining of tailings in existing deposits with high economic efficiency.

Acknowledgment

The author expresses his sincere gratitude to V.P. Valyukhov (Doctor of Technical Sciences) for his support in conducting research on X-ray absorption immersion technology and a fruitful discussion of the results.

The author also owes a debt of gratitude to the late V.W. Novikov (Candidate of Technical Sciences), developer of the first industrial X-ray fluorescent separators, and V.A. Olkhov, both of whom were actively involved in the early stages of the work presented here.

REFERENCES

1. Zyryanov I. V., Yakovlev V. N., Ivanov A. V., Makalin I. A., *Istoriya i perspektivy razvitiya otechestvennoy tekhnologii radiometricheskogo obogashcheniya almazosoderzhashchikh rud* [History and prospects for the development of domestic technology for radiometric enrichment of diamond ores], *Gornyi Zhurnal* [Mining Magazine]. (2) (2024) 37–41 (in Russian).
2. Mironov V. P., Emelyanova A. S., Shabalin S. A., et al., X-ray luminescence in diamonds and its application in industry, *AIP Conf. Proc.* 2392 (1) (2021) 020010.
3. Morozov V. V., Chanturia V. A., Dvoichenkova G. P., et al., Selecting organic collectors for luminophore-bearing modifying agents to extract weakly fluorescent diamonds, *J. Min. Sci.* 59 (2) (2023) 292–301.
4. Karlina A., Mineral gravity separation hydrodynamics study, *Proc. Irkutsk State Techn. Univers.* (3(98)) (2015) 194–199 (in Russian).
5. Dvortsov M. A., Komarskii A. A., Korzhenevskii S. R., Korzhenevskii N. S., Method and device for X-ray projection separation of mineral raw materials, Pat. No. 2785068 Russian Federation, MPK B 07 C 5/34, G 01 N 23/083; OOO “IMPULS-U” is a declarant and patentee. No. 2022105162; declar. 26.02.2022; publ. 02.12.2022, Bull. No. 34.
6. Modise E. G., Zungeru A. M., Mtengi B., Ude A., A fast and noise rejecting Kolmogorov – Smirnov sorting algorithm in X-ray diamond sorting, *Proc. 2022 Int. Conf. Smart Appl., Commun. Networking (SmartNets)*. Nov.29th–Dec. 1st, 2022. Palapye, Botswana (Southern Africa) (2022) 1–5.
7. Modise E. G., Zungeru A. M., Chuma J. M., et al., The new paradox of dual modality X-ray diamond sorting, *IEEE Photonics J.* 13 (3) (2021) 3400124.
8. Kuptsov V. D., Valjukhov V. P., Novikov V. V., Olkhovoy V. A., The new natural diamonds extraction out of fragmented kimberlite technology, *Trudy SPbGTU* [Transactions of St. Petersburg State Technical University]. (507) (2008) 98–100 (in Russian).
9. Novikov V. V., Rudakov V. V., Zlobin M. N., et al., The method of separation of minerals, Pat. No. 2472595 Russian Federation, MPK B07C 5/346, Novikov Vladlen Vasilyevich is a declarant and patentee. No. 2011150666/12; declar. 14.12.2011; publ. 20.01.2013, Bull. No. 2.
10. Physical reference data. Tables of X-ray mass attenuation coefficients and mass energy-absorption coefficients. Access Mode: <http://physics.nist.gov/PhysRef Data/ XrayMassCoef /cover.html> (Date of Access is 15.06.2024).
11. Pavlinsky G. V., *Fundamentals of X-ray physics*, Cambridge International Science Publishing, Cambridge, UK, 2008.

СПИСОК ЛИТЕРАТУРЫ

1. Зырянов И. В., Яковлев В. Н., Иванов А. В., Макалин И. А. История и перспективы развития отечественной технологии радиометрического обогащения алмазосодержащих руд // Горный журнал. 2024. № 2. С. 37–41.
2. Mironov V. P., Emelyanova A. S., Shabalin S. A., Bubyr E. V., Kazakov L. V., Martynovich E. F. X-ray luminescence in diamonds and its application in industry // AIP Conference Proceedings. 2021. Vol. 2392. No. 1. P. 020010.
3. Морозов В. В., Чантурия В. А., Двойченкова Г. П., Чантурия В. А., Подкаменный Ю. А. Выбор органических коллекторов в составе люминофорсодержащих модификаторов для извлечения слабосветящихся алмазов // Физико-технические проблемы разработки полезных ископаемых. 2023. № 2. С. 122–133.
4. Карлина А. И. Изучение гидродинамики гравитационного обогащения полезных ископаемых // Вестник Иркутского государственного технического университета. 2015. № 3 (98). С. 194–199.
5. Дворцов М. А., Комарский А. А., Корженевский С. Р., Корженевский Н. С. Способ и устройство для рентгенопроекционной сепарации минерального сырья. Пат. 2785068 Российская Федерация, МПК В 07 С 5/34, G 01 N 23/083., заявитель и патентообладатель ООО «ИМПУЛЬС-У». № 2022105162; заявл. 26.02.2022; опубл. 02.12.2022, Бюл. № 34. 22 с.
6. Modise E. G., Zungeru A. M., Mtengi B., Ude A. A fast and noise rejecting Kolmogorov – Smirnov sorting algorithm in X-ray diamond sorting // Proceedings of the 2022 International Conference on Smart Applications, Communications and Networking (SmartNets). Nov. 29th–Dec 1st, 2022. Palapye, Botswana (Southern Africa), 2022. Pp. 1–5.
7. Modise E. G., Zungeru A. M., Chuma J. M., Prabakaran S. R. S., Mtengi B., Ude A., Nedev Z. The new paradox of dual modality X-ray diamond sorting // IEEE Photonics Journal. 2021. Vol. 13. No. 3. P. 3400124.
8. Купцов В. Д., Валюхов В. П., Новиков В. В., Ольховой В. А. Новая технология извлечения природных алмазов в кусках кимберлита // Труды СПбГТУ. 2008. № 507. С. 98–100.
9. Новиков В. В., Рудаков В. В., Злобин М. Н., Малаховский В. И., Купцов В. Д., Валюхов В. П., Купцов М. В., Ольховой В. А. Способ сепарации минералов. Пат. 2472595 Российская Федерация, МПК В07С 5/346, заявитель и патентообладатель Новиков Владлен Васильевич. № 2011150666/12; заявл. 14.12.2011; опубл. 20.01.2013, Бюл. № 2. 11 с.
10. Physical reference data. Tables of X-ray mass attenuation coefficients and mass energy-absorption coefficients. Режим доступа: <http://physics.nist.gov/PhysRefData/XrayMassCoef/cover.html> (дата обращения: 15.06.2024).
11. Павлинский Г. В. Основы физики рентгеновского излучения: Физматлит, 2007. 240 с.



THE AUTHOR

KUPTSOV Vladimir D.

Peter the Great St. Petersburg Polytechnic University

29 Politechnicheskaya St., St. Petersburg, 195251, Russia

kuptsov@spbstu.ru

ORCID: 0000-0001-8594-9423

СВЕДЕНИЯ ОБ АВТОРЕ

КУПЦОВ Владимир Дмитриевич — доктор технических наук, профессор Высшей школы прикладной физики и космических технологий Санкт-Петербургского политехнического университета Петра Великого.

195251, Россия, г. Санкт-Петербург, Политехническая ул., 29

kuptsov@spbstu.ru

ORCID: 0000-0001-8594-9423

Received 20.06.2024. Approved after reviewing 13.02.2025. Accepted 13.02.2025.

*Статья поступила в редакцию 20.06.2024. Одобрена после рецензирования 13.02.2025.
Принята 13.02.2025.*

Original article

DOI: <https://doi.org/10.18721/JPM.18206>

THE INFLUENCE OF FIELD MISALIGNMENT AND ELECTRIC FIELD ASYMMETRY ON THE STABILITY ZONES OF A COMBINED ION TRAP

*A. S. Berdnikov¹, A. V. Egorova², N. K. Krasnova²,
S. V. Masyukevich¹, K. V. Solovyev^{2,1✉}*

¹ Institute for Analytical Instrumentation of RAS, St. Petersburg, Russia;

² Peter the Great St. Petersburg Polytechnic University, St. Petersburg, Russia

✉ k-solovyev@mail.ru

Abstract. This study continues a series of articles devoted to the operating features of ion-optical devices with periodic electric power supply and constant homogenous magnetic field, used in mass spectrometers. It has been shown how the structure of combined ion trap stability diagram is changed when the trap configuration deviates from the ideal one. The influence of an angle between the electric field symmetry axis and a magnetic field direction as well as the influence of the electric field asymmetry on the pattern of stability zones were found. The results obtained are worthy of use both for estimating the impact of manufacturing defects and for designing new nonclassical ion traps.

Keywords: combined ion trap, stability zones, mass spectrometry, ion confinement

Funding: The research was funded in part within the framework of the FFZM-2022-0009 topic (State registration No. 122040600002-3) of the State Assignment No. 075-01157-23-00, dated 29.12.2022, of the Ministry of Science and Higher Education of the Russian Federation for Institute for Analytical Instrumentation of RAS (St. Petersburg).

Citation: Berdnikov A. S., Egorova A. V., Krasnova N. K., Masyukevich S. V., Solovyev K. V., The influence of field misalignment and electric field asymmetry on the stability zones of a combined ion trap, St. Petersburg State Polytechnical University Journal. Physics and Mathematics. 18 (2) (2025) 60–68. DOI: <https://doi.org/10.18721/JPM.18206>

This is an open access article under the CC BY-NC 4.0 license (<https://creativecommons.org/licenses/by-nc/4.0/>)



Научная статья
УДК 621.384.8
DOI: <https://doi.org/10.18721/JPM.18206>

ВЛИЯНИЕ НЕСООСНОСТИ ПОЛЕЙ И АСИММЕТРИИ ЭЛЕКТРИЧЕСКОГО ПОЛЯ НА ЗОНЫ УСТОЙЧИВОСТИ КОМБИНИРОВАННОЙ ИОННОЙ ЛОВУШКИ

А. С. Бердников¹, А. В. Егорова², Н. К. Краснова²,
С. В. Масюкевич¹, К. В. Соловьев^{2,1✉}

¹ Институт аналитического приборостроения РАН, Санкт-Петербург, Россия;

² Санкт-Петербургский политехнический университет Петра Великого, Санкт-Петербург, Россия

✉ k-solovyev@mail.ru

Аннотация. Данное исследование продолжает цикл статей, посвященных особенностям функционирования ионно-оптических устройств с периодическим электрическим питанием и постоянным однородным магнитным полем, применяемых в масс-спектрометрии. В статье показано, как диаграмма устойчивости комбинированной ионной ловушки меняет свою структуру при отклонении конфигурации ловушки от идеальной. Определено влияние величины угла между осью симметрии электрического поля и направлением магнитной индукции, а также влияние нарушения осевой симметрии электрического поля на картину зон устойчивости. Полученные результаты целесообразно использовать как для оценки влияния дефектов изготовления либо юстировки на работу классической комбинированной ловушки, так и для проектирования новых неклассических ионных ловушек.

Ключевые слова: комбинированная ионная ловушка, зона устойчивости, масс-спектрометрия, удержание ионов

Финансирование: Работа частично профинансирована в рамках темы FFZM-2022-0009 (номер гос. регистрации 122040600002-3) Государственного задания Министерства науки и высшего образования Российской Федерации № 00-23-01157-075 от 29.12.2022 для Института аналитического приборостроения Российской академии наук (Санкт-Петербург).

Ссылка для цитирования: Бердников А. С., Егорова А. В., Краснова Н. К., Масюкевич С. В., Соловьев К. В. Влияние несоосности полей и асимметрии электрического поля на зоны устойчивости комбинированной ионной ловушки // Научно-технические ведомости СПбГПУ. Физико-математические науки. 2025. Т. 18. № 2. С. 60–68. DOI: <https://doi.org/10.18721/JPM.18206>

Статья открытого доступа, распространяемая по лицензии CC BY-NC 4.0 (<https://creativecommons.org/licenses/by-nc/4.0/>)

Introduction

A combined ion trap is commonly understood as a Penning trap with oscillating voltages supplied to its electrodes. This trap is actually a combination of Penning and Paul traps [1, 2]. The combined ion trap, although it has the disadvantages of each of its components, has a number of advantages, in particular, an increased stability zone.

It is convenient to construct the stability zones of ions in a combined trap in a rotating coordinate system, which makes it possible to separate the variables and obtain a pair of independent Hill equations [3] (in the particular case, the Mathieu equations). The stability zone of the system is constructed in this case as the intersection region of the stability zones of the obtained Hill equations.

However, this technique is effective only for systems with axial symmetry. A number of configurations of the combined trap are not intended for an axisymmetric system but preserve linearity of the equations of ion motion. The latter makes it possible to study the nature of ion motion using the analytical tools of Floquet theory [4, 5]. We already adopted an approach based on this theory in our previous studies [6–8]. It allows to directly establish the conditions for stability of ion motion, facilitating the study of the system and allowing to draw conclusions about its possible operating modes.

This paper confirms that Floquet theory can be used to analyze ion traps based on non-axisymmetric hyperbolic electric fields with oscillating voltage immersed in a uniform magnetic field of arbitrary direction.

Stability of dimensionless trap model

For simplicity, we introduce dimensionless units of measurement [16], assuming that the dimensional coordinates $\mathbf{R} = (X, Y, Z)$ and time t are related as follows to the corresponding dimensionless coordinates $\mathbf{r} = (x, y, z)$ and time τ :

$$\mathbf{R} = \ell \mathbf{r}, t = T\tau, \quad (1)$$

where ℓ , T are linear and time scales chosen from physical considerations.

The motion of a particle with charge e and mass m in a trap occurs in a constant uniform magnetic field with the strength B_0 and the direction set by the polar and azimuthal angles (θ, φ) relative to the coordinate system associated with the geometry of the electric quadrupole:

$$\mathbf{B} = B_0 (\sin\theta \cdot \cos\varphi, \sin\theta \cdot \sin\varphi, \cos\theta) \quad (2)$$

and in an electric field (with oscillating voltage) quadratic with respect to the coordinates:

$$\begin{aligned} U &= (U_0 - U_1 f(\omega t)) \frac{\alpha X^2 + \beta Y^2 + \gamma Z^2}{\ell^2}, \\ f(\omega(t + \sigma)) &= f(\omega t), \\ \alpha + \beta + \gamma &= 0, \end{aligned} \quad (3)$$

where U_0 , U_1 are the amplitudes of the DC and AC components of the supply voltage; ω is the angular frequency of the latter, σ is its period; α , β , γ are the parameters defining the geometry of the field.

The dimensionless equations of motion in these fields form a system

$$\begin{aligned} \ddot{x} &= -2\alpha(a - 2q \cdot f(2\tau))x + \dot{y}b_z - \dot{z}b_y, \\ \ddot{y} &= -2\beta(a - 2q \cdot f(2\tau))y + \dot{z}b_x - \dot{x}b_z, \\ \ddot{z} &= -2\gamma(a - 2q \cdot f(2\tau))z + \dot{x}b_y - \dot{y}b_x, \end{aligned} \quad (4)$$

where the components of the dimensionless magnetic field are determined by the equality

$$\mathbf{b} = b(\sin\theta \cos\varphi, \sin\theta \sin\varphi, \cos\theta) = (b_x, b_y, b_z), \quad (5)$$

and the coefficients a , q , b for the given time scale $T = 2/\omega$ are determined by the relations

$$a = \frac{4eU_0}{\omega^2 m \ell^2}, \quad q = \frac{2eU_1}{\omega^2 m \ell^2}, \quad b = \frac{2eB_0}{\omega m}. \quad (6)$$

The dots above the variables in Eqs. (4) denote differentiation with respect to dimensionless time τ .



In the general case, system (4) has six independent parameters that affect stability: traditional ones, a and q ; new ones, b , θ , φ , related to the strength and direction of the magnetic field; two parameters of the geometry of the electric field, for example, α , β (taking into account the last equation in system (3)).

Evidently, the multidimensional region can only be visualized by sections whose dimensions do not exceed 3. Here we confine ourselves to traditional two-dimensional diagrams.

For a dimensionless magnetic field $\mathbf{b} = b(0, 0, 1)$ directed along the symmetry axis of the electric field, the form of equations (4) is simplified:

$$\begin{aligned}\ddot{x} &= 2\alpha(a - 2q \cdot f(2\tau))x + b\dot{y}, \\ \ddot{y} &= 2\beta(a - 2q \cdot f(2\tau))y - b\dot{x}, \\ \ddot{z} &= -2\gamma(a - 2q \cdot f(2\tau))z = -(a_z - 2q_z \cdot f(2\tau))z,\end{aligned}\tag{7}$$

The electric field with axial symmetry corresponds to a set of parameters

$$(\alpha, \beta, \gamma) = (-1/4, -1/4, 1/2).$$

The diagrams for the stability zones below are given in the coordinates $(q, a) = (q_z, a_z)$.

The stability of ion motion in the axisymmetric hyperbolic electric field and the longitudinal magnetic field is studied in a coordinate system rotating around the z axis. Recall that if we introduce a complex variable $\xi = x + iy$ for $\alpha = \beta = -1/4$, then we obtain the following equation from the first two equations in system (7):

$$\ddot{\xi} = \frac{1}{2}(a - 2q \cdot f(2\tau))\xi - ib\dot{\xi}.\tag{8}$$

Next, moving on to the rotating coordinate system $\eta = x^* + iy^*$, using the transformation

$$\xi = \eta \cdot \exp(-ib\tau/2),$$

Eq. (6) is converted to the following form:

$$\ddot{\eta} - \frac{1}{2}\left(a - \frac{b^2}{2} - 2q \cdot f(2\tau)\right)\eta = 0.\tag{9}$$

Thus, we obtain the Hill equation shifted with respect to the parameter a . Then the stability of the system including the third equation of system (7) and Eqs. (8), (9) can be easily analyzed by the traditional method of superposition of stability zones of the Hill equation [1, 2].

Case I. Consider the case where the electric field is axisymmetric, namely, $(\alpha, \beta, \gamma) = (-1/4, -1/4, 1/2)$, and the magnetic field is directed at an angle θ to the z axis, i.e., there is misalignment between the magnetic field and the symmetry axis of the electric field. There is no dependence on the azimuthal angle, the strength of the dimensionless magnetic field is $\mathbf{b} = b(\sin\theta, 0, \cos\theta)$. Then system (4) takes the following form:

$$\begin{aligned}\ddot{x} &= -2\alpha(a - 2q \cdot f(2\tau))x + b\dot{y}\cos\theta, \\ \ddot{y} &= -2\beta(a - 2q \cdot f(2\tau))y + b(\dot{z}\sin\theta - \dot{x}\cos\theta), \\ \ddot{z} &= -2\gamma(a - 2q \cdot f(2\tau))z - b\dot{y}\sin\theta.\end{aligned}\tag{10}$$

In turn, system (10) cannot be reduced to a set of Hill equations, but it remains linear with periodic coefficients and therefore is subject to analysis by the technique proposed in [6].

Let us rewrite Eq. (23) as follows:

$$\dot{\mathbf{x}} = \mathbf{A}(\tau)\mathbf{x}, \mathbf{A}(\tau + A) = \mathbf{A}(\tau),\tag{11}$$

where

$$\mathbf{x} = (x_1 \ x_2 \ x_3 \ x_4 \ x_5 \ x_6)^T = (x \ \dot{x} \ y \ \dot{y} \ z \ \dot{z})^T \quad (12)$$

(the superscript T denotes transposition);

$$\mathbf{A}(\tau) = \begin{pmatrix} 0 & 1 & 0 & 0 & 0 & 0 \\ -2\alpha(a - 2q \cdot f(2\tau)) & 0 & 0 & b_z & 0 & -b_y \\ 0 & 0 & 0 & 1 & 0 & 0 \\ 0 & -b_z & -2\beta(a - 2q \cdot f(2\tau)) & 0 & 0 & b_x \\ 0 & 0 & 0 & 0 & 0 & 1 \\ 0 & b_y & 0 & -b_x & -2\gamma(a - 2q \cdot f(2\tau)) & 0 \end{pmatrix}. \quad (13)$$

In accordance with Floquet theory [4, 5], the stability of solutions (13) is assessed through analysis of the monodromy matrix eigenvalues of system (11). The procedure for constructing stability diagrams of system (11)–(13) is described in sufficient detail in [6]; let us briefly recall its key points: the fundamental matrix of solutions $\mathbf{X}(\tau)$, $\mathbf{X}(0) = \mathbf{E}$ is constructed. Next, the spectrum of the monodromy matrix $\mathbf{X}(A)$ is analyzed. The spectral radius equal to unity corresponds to the values of the parameters representing stable motion.

Fig. 1 illustrates the evolution in the configuration of the first stability zone for $f(\tau) = \cos \tau$ at $b = 1$ with varying parameter θ .

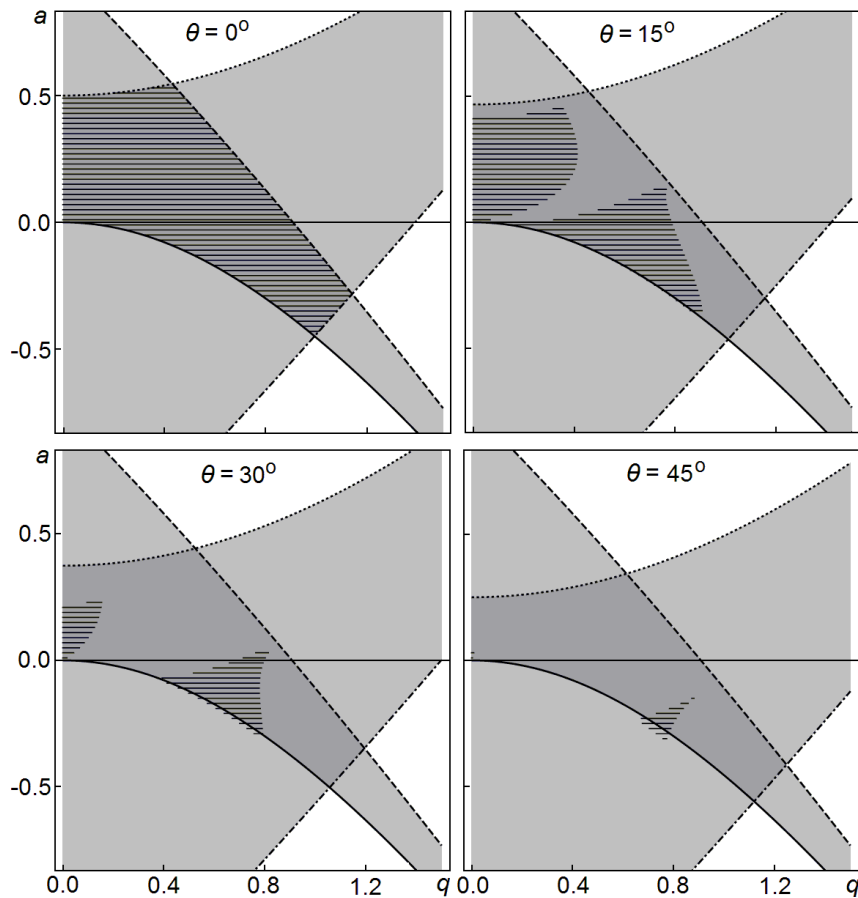


Fig. 1. Stability zones (hatched by horizontal lines) for different values of misalignment angle θ between the symmetry axis of the electric field and the direction of the magnetic field; $b = 1$; $f(\tau) = \cos \tau$ (Case I)

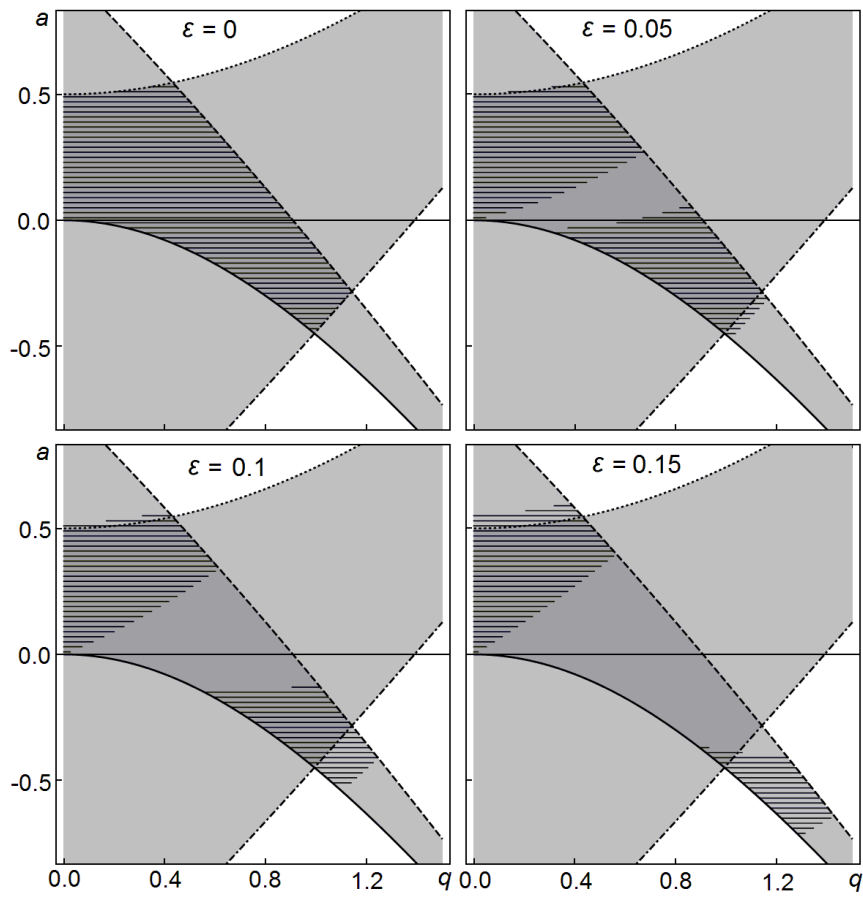


Fig. 2. Stability zones (hatched by horizontal lines) for different values of the electric field asymmetry parameter ε ; $b = 1$, $f(\tau) = \cos \tau$ (Case II)

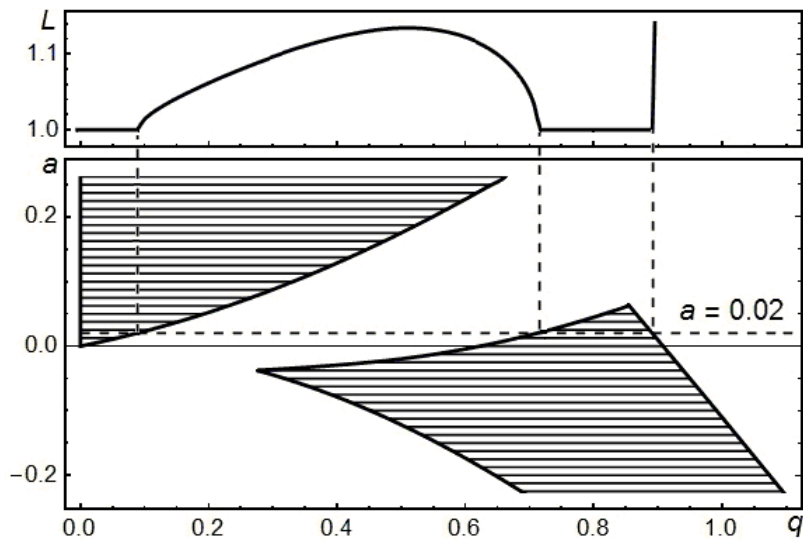


Fig. 3. Diagram (q, a) (lower part of figure) and dependence of $L(q)$ (upper part): the former shows the configuration of stability regions in coordinates (q, a) , the second shows the change in the spectral radius of the monodromy matrix L from identity to non-identity and vice versa at the boundaries of stability regions with the parameter q varying along the line $a = 0.02$ (horizontal dashed line)

Case II. Consider a situation where the axial symmetry of the electric field is broken. We introduce the parameter ε , lying in the range $0 < \varepsilon < \min(\alpha, \beta)$, and analyze the case of an electric field with geometric parameters $(\alpha, \beta, \gamma) = (-1/4 - \varepsilon, -1/4 + \varepsilon, 1/2)$. The condition that the sum of the parameters be equal to zero is satisfied, we have a field with equipotentials that are hyperboloids of revolution for $\varepsilon = 0$, a harmonic non-axisymmetric field for $\varepsilon \neq 0$. The system of equations of motion is the same: (11)–(13). Although all components (5) of the magnetic field strength \mathbf{b} are important in this case, for ease of visualization, we focus on the option $\mathbf{b} = b(0, 0, 1)$. The result presented below is obtained by performing the above sequence of steps. Fig. 2 shows a change in the configuration of the first stability zone of the combined trap for $f(\tau) = \cos \tau$ at $b = 1$ with varying ε .

Note that the diagrams (Figs. 1, 2) were obtained by a technique refining the boundary points as transition points to/from non-identity of the spectral radius of the monodromy matrix, previously used for a simpler system [7, 8]. This approach is illustrated in Fig. 3, where the upper part shows the dependence of the spectral radius of the monodromy matrix L on the parameter q of Eqs. (10) with the parameter $a = 0.02$ (option $b = 1, \varepsilon = 0.05$); the lower part of the figure shows the correspondence of q values for the variation in the spectral radius to the boundaries of the stability regions of system (10).

Conclusion

The misalignment of the electric and magnetic fields, as well as the non-axisymmetry of the electric field, significantly affect the structure of the stability diagram of a traditional (axisymmetric) combined ion trap and lead to a change in this diagram. The latter is divided into fragments, defining the behavior of the system in a new way depending on the values of the non-ideality factors.

The results and methodology obtained can be used both to assess the influence of manufacturing and alignment defects on the operation of a traditional ion trap and to design new traps without axial symmetry.

REFERENCES

1. Major F. G., Gheorghe V. N., Werth G., Charged particle traps, Springer-Verlag, Berlin–Heidelberg, 2005.
2. Vogel M., Particle Confinement in Penning Traps. – 2nd ed. – Cham, Switzerland: Springer Int. Pub. AG, part of Springer Nature, 2024.
3. Kamke E., Differentialgleichungen Lösungsmethoden und Lösungen, Band 1. 10 Ed. B. G. Teubner, Springer, Leipzig, 1977.
4. Floquet G., Sur les équations différentielles linéaires coefficients périodiques, Ann. Sci. Éc. Norm. Supér. 2e Serie, 12 (1883) 47–88.
5. Demidovich B. P., Lektsii po matematicheskoy teorii ustoychivosti [Lectures on the mathematical stability theory], Nauka, Moscow, 1967 (in Russian).
6. Golikov Yu. K., Krasnova N. K., Solovyev K. V., et al., Stability zones of quadrupole mass spectrometer in longitudinal magnetic field, Appl. Phys. (Prikladnaya fizika). (3) (2006) 78–81 (in Russian).
7. Berdnikov A., Kapralov V., Solovyev K., Krasnova N., Algorithm for constructing a multidimensional stability domain of a charged particle in an ion-optical system with periodic supply voltage, In: Proc. of 2021 IEEE Int. Conf. on Electrical Engineering and Photonics (EExPolytech-2021), Oct. 14–15, 2021. St. Petersburg, Russia. (2021) 51–54.
8. Berdnikov A. S., Krasnova N. K., Masyukevich S. V., Solovyev K. V., Visualization of the 3D stability zone of a quadrupole mass filter in the static longitudinal magnetic field, St. Petersburg State Polytechnical University Journal. Physics and Mathematics. 15 (2) (2022) 26–33 (in Russian).



СПИСОК ЛИТЕРАТУРЫ

1. Major F. G., Gheorghe V. N., Werth G. Charged particle traps. Berlin—Heidelberg: Springer-Verlag, 2005. 354 p.
2. Vogel M. Particle confinement in penning traps. 2nd ed. Cham, Switzerland: Springer Int. Pub. AG, part of Springer Nature, 2024. 467 p.
3. Камке Э. Справочник по обыкновенным дифференциальным уравнениям. М.: Наука, 1976. 576 с.
4. Floquet G. Sur les équations différentielles linéaires coefficients périodiques // Annales Scientifiques de l'École Normale Supérieure. 2e Serie, 1883. Tome 12. Pp. 47–88.
5. Демидович Б. П. Лекции по математической теории устойчивости. М.: Наука, 1967. 471 с.
6. Голиков Ю. К., Краснова Н. К., Соловьев К. В., Елохин В. А., Николаев В. И. Зоны устойчивости квадрупольного масс-спектрометра в продольном магнитном поле // Прикладная физика. 2006. № 3. С. 78–81.
7. Berdnikov A., Kapralov V., Solovyev K., Krasnova N. Algorithm for constructing a multidimensional stability domain of a charged particle in an ion-optical system with periodic supply voltage // Proc. of 2021 IEEE Int. Conference on Electrical Engineering and Photonics (EExPolytech-2021), Oct. 14–15, 2021. Pp. 51–54.
8. Бердников А. С., Краснова Н. К., Масюкевич С. В., Соловьев К. В. Визуализация трехмерной зоны устойчивости квадрупольного фильтра масс в постоянном продольном магнитном поле // Научно-технические ведомости СПбГПУ. Физико-математические науки. 2022. Т. 15. № 2. С. 26–33.

THE AUTHORS

BERDNIKOV Alexander S.*Institute for Analytical Instrumentation of RAS*

31–33, Ivan Chernykh St., St. Petersburg, 198095, Russia

asberd@yandex.ru

ORCID: 0000-0003-0985-5964

EGOROVA Anastasia V.*Peter the Great St. Petersburg Polytechnic University*

29 Politechnicheskaya St., St. Petersburg, 195251, Russia

e4av2abao@mail.ru

ORCID: 0009-0001-8247-6410

KRASNOVA Nadezhda K.*Peter the Great St. Petersburg Polytechnic University*

29 Politechnicheskaya St., St. Petersburg, 195251, Russia

n.k.krasnova@mail.ru

ORCID: 0000-0002-6162-9481

MASYUKEVICH Sergey V.*Institute for Analytical Instrumentation RAS*

31–33, Ivan Chernykh St., St. Petersburg, 198095, Russia

serg_08@mail.ru

ORCID: 0000-0002-0873-8849

SOLOVYEV Konstantin V.*Peter the Great St. Petersburg Polytechnic University*

29 Politechnicheskaya St., St. Petersburg, 195251, Russia

k-solovyev@mail.ru

ORCID: 0000-0003-3514-8577

СВЕДЕНИЯ ОБ АВТОРАХ

БЕРДНИКОВ Александр Сергеевич — доктор физико-математических наук, ведущий научный сотрудник *ФГБУН «Институт аналитического приборостроения Российской академии наук»*.

190103, Россия, г. Санкт-Петербург, ул. Ивана Черных, 33–31, лит. А.

asberd@yandex.ru

ORCID: 0000-0003-0985-5964

ЕГОРОВА Анастасия Васильевна — студентка *Института электроники и телекоммуникаций Санкт-Петербургского политехнического университета Петра Великого*.

195251, Россия, г. Санкт-Петербург, Политехническая ул., 29

e4av2abao@mail.ru

ORCID: 0009-0001-8247-6410

КРАСНОВА Надежда Константиновна — доктор физико-математических наук, профессор *Высшей инженерно-физической школы Санкт-Петербургского политехнического университета Петра Великого*.

195251, Россия, г. Санкт-Петербург, Политехническая ул., 29

n.k.krasnova@mail.ru

ORCID: 0000-0002-6162-9481

МАСЮКЕВИЧ Сергей Владимирович — старший научный сотрудник *ФГБУН «Институт аналитического приборостроения Российской академии наук»*.

198095, Россия, г. Санкт-Петербург, ул. Ивана Черных, 31–33, лит. А.

serg_08@mail.ru

ORCID: 0000-0002-0873-8849

СОЛОВЬЕВ Константин Вячеславович — кандидат физико-математических наук, доцент *Высшей инженерно-физической школы Санкт-Петербургского политехнического университета Петра Великого*.

195251, Россия, г. Санкт-Петербург, Политехническая ул., 29

k-solovyev@mail.ru

ORCID: 0000-0003-3514-8577

Received 03.11.2024. Approved after reviewing 05.12.2024. Accepted 05.12.2024.

Статья поступила в редакцию 03.11.2024. Одобрена после рецензирования 05.12.2024. Принята 05.12.2024.

Original article

DOI: <https://doi.org/10.18721/JPM.18207>

POLYCRYSTALLINE FILMS OF $\text{MA}_x\text{MEA}_{1-x}\text{PbI}_3$ HYBRID PEROVSKITES OBTAINED BY THE SOLUTION METHOD: CRYSTALLIZATION AND MORPHOLOGY

A. A. Ryabko¹, M. K. Ovezov¹✉, A. I. Maximov², N. V. Permiakov²,
A. K. Tuchkovskiy³, I. A. Vrublevskiy³, E. N. Muratova²,
A. N. Aleshin¹, V. A. Moshnikov²

¹ Ioffe Institute of RAS, St. Petersburg, Russia;

² St. Petersburg Electrotechnical University "LETI", St. Petersburg, Russia;

³ Belarusian State University of Informatics and Radioelectronics, Minsk, Republic of Belarus

✉ strontiumx94@gmail.com

Abstract. In this work, the morphological features of polycrystalline films of hybrid perovskites $\text{MA}_x\text{MEA}_{1-x}\text{PbI}_3$ formed by a single-stage centrifugation method from DMF and DMSO solutions (4:1) have been investigated. The results of the studies showed that an increase in the proportion of monoethanolammonium in $\text{MA}_x\text{MEA}_{1-x}\text{PbI}_3$ led not only to a change in the absorption spectra and an increase in the interplanar distances of the crystal lattice, but also to a significant change in the morphology of the films from elongated split crystallites to a uniform coating of nanocrystallites. An increase in the proportion of monoethanolammonium iodide in the solution also improved the wettability of solutions and the continuity of the coating of substrates with hybrid perovskite $\text{MA}_x\text{MEA}_{1-x}\text{PbI}_3$ without additional surface activation processes. The increased band gap of $\text{MA}_x\text{MEA}_{1-x}\text{PbI}_3$ compared to MAPbI_3 makes these hybrid perovskites attractive for use in tandem solar cells.

Keywords: hybrid perovskites, polycrystalline film, solar cell, split crystallite, morphology, crystallization

Funding: The work was carried out with the support of a grant from Russian Science Foundation No. 23-42-10029 dated 20 December 2022, <https://rscf.ru/en/project/23-42-10029/>. This research was funded by the Belarusian Republican Foundation for Fundamental Research grant number F23RNF-160.

Citation: Ryabko A. A., Ovezov M. K., Maximov A. I., Permiakov N. V., Tuchkovskiy A. K., Vrublevskiy I. A., Muratova E. N., Aleshin A. N., Moshnikov V. A., Polycrystalline films of $\text{MA}_x\text{MEA}_{1-x}\text{PbI}_3$ hybrid perovskites obtained by the solution method: Crystallization and morphology, St. Petersburg State Polytechnical University Journal. Physics and Mathematics. 18 (2) (2025) 69–81. DOI: <https://doi.org/10.18721/JPM.18207>

This is an open access article under the CC BY-NC 4.0 license (<https://creativecommons.org/licenses/by-nc/4.0/>)

Научная статья

УДК 538.91

DOI: <https://doi.org/10.18721/JPM.18207>

КРИСТАЛЛИЗАЦИЯ И МОРФОЛОГИЯ ПОЛИКРИСТАЛЛИЧЕСКИХ ПЛЕНОК ГИБРИДНЫХ ПЕРОВСКИТОВ $\text{MA}_x\text{MEA}_{1-x}\text{PbI}_3$, ПОЛУЧЕННЫХ РАСТВОРНЫМ МЕТОДОМ

А. А. Рябко¹, М. К. Овезов¹✉, А. И. Максимов², Н. В. Пермяков²,
А. К. Тучковский³, И. А. Врублевский³, Е. Н. Муратова²,
А. Н. Алешин¹, В. А. Мошников²

¹ Физико-технический институт имени А. Ф. Иоффе РАН, Санкт-Петербург, Россия;

² Санкт-Петербургский государственный электротехнический университет «ЛЭТИ» им. В. И. Ульянова (Ленина), Санкт-Петербург, Россия;

³ Белорусский государственный университет информатики и радиоэлектроники, Минск, Республика Беларусь

✉ strontiumx94@gmail.com

Аннотация. В работе были исследованы морфологические особенности поликристаллических пленок гибридных перовскитов $\text{MA}_x\text{MEA}_{1-x}\text{PbI}_3$, сформированных одностадийным методом центрифугирования из растворов ДМФ и ДМСО (4:1). Результаты исследований показали, что увеличение доли моноэтаноламония в $\text{MA}_x\text{MEA}_{1-x}\text{PbI}_3$ приводит не только к изменению спектров поглощения и увеличению межплоскостных расстояний кристаллической решетки, но также к существенному изменению морфологии пленок от вытянутых расщепленных кристаллитов до однородного покрытия из нанокристаллитов. Увеличение доли моноэтаноламония йодида в растворе также обеспечивает улучшение смачиваемости растворов и сплошность покрытия подложек гибридным перовскитом $\text{MA}_x\text{MEA}_{1-x}\text{PbI}_3$ без дополнительных процессов активации их поверхности. Увеличенная ширина запрещенной зоны $\text{MA}_x\text{MEA}_{1-x}\text{PbI}_3$, по сравнению с MAPbI_3 , делает эти гибридные перовскиты привлекательными для использования в tandemных солнечных элементах.

Ключевые слова: гибридные перовскиты, поликристаллическая пленка, солнечный элемент, расщепленный кристаллит, морфология, кристаллизация

Финансирование: Авторы благодарны аспиранту СПбГЭТУ «ЛЭТИ» Корепанову О.А. за измерения рентгенограмм образцов гибридных перовскитов $\text{MA}_x\text{MEA}_{1-x}\text{PbI}_3$. В части синтеза металлоорганических перовскитов работа выполнена при поддержке гранта Белорусского республиканского фонда фундаментальных исследований № Ф23РНФ-160 и Российского научного фонда № 10029-42-23 (<https://rscf.ru/project/10029-42-23/>) от 20.12.2022.

Ссылка для цитирования: Рябко А. А., Овезов М. К., Максимов А. И., Пермяков Н. В., Тучковский А. К., Врублевский И. А., Муратова Е. Н., Алешин А. Н., Мошников В. А. Кристаллизация и морфология поликристаллических пленок гибридных перовскитов $\text{MA}_x\text{MEA}_{1-x}\text{PbI}_3$, полученных раствором методом // Научно-технические ведомости СПбГПУ. Физико-математические науки. 2025. Т. 18. № 2. С. 69–81. DOI: <https://doi.org/10.18721/JPM.18207>

Статья открытого доступа, распространяемая по лицензии CC BY-NC 4.0 (<https://creativecommons.org/licenses/by-nc/4.0/>)

Introduction

Materials based on hybrid perovskites are of great interest for applications in photovoltaics and photodetectors, due to their direct-bandgap structure, tunable band gap, high absorption coefficient, high mobility and long mean free path [1, 2]. In addition, hybrid perovskites are promising for creating X-ray detectors, optically-controlled memristors and light-emitting devices [3–5].



A wide range of polycrystalline APbX_3 -based films is used to create photovoltaic structures, typically with varying proportions of formamidinium (FA^+ , $\text{CH}(\text{NH}_2)_2^+$) and methylammonium (MA^+ , CH_3NH_3^+) cations and I^- , Br^- , Cl^- anions, as well as by introducing inorganic cations or partial substitution of lead [6–9]. A wide range of hybrid perovskite compositions is also used to fabricate tandem solar cells [10, 11], which is particularly attractive for further development of heterostructure silicon solar cells, where hybrid perovskites with a wider band gap are used. Using complex compositions of hybrid perovskites is aimed at improving stability while ensuring optimal band gap and efficiency for the solar cell [12].

A transition is currently underway from nanotechnology to nanoarchitectonics, providing a synergistic effect from the contact of two nanomaterials [13]. To improve the stability of perovskite photovoltaic structures, molecular etching and growth of films from 3D/2D perovskites are widely used [14–17]. Long-chain amines are commonly used for this purpose, whose $-\text{NH}_2$ terminal groups interact with uncoordinated lead ions and passivate defects on the periphery of grains, or, like some short-chain amines, can serve as organic binders between inorganic octahedral frameworks in quasi-2D perovskites [15]. However, some short-chain amines, along with formamidinium and methylammonium cations, can integrate into the crystal lattice of hybrid perovskite with a change in the band gap [18].

The goal of this paper is to identify the effect of the proportion of monoethanolammonium in $\text{MA}_x\text{MEA}_{1-x}\text{PbI}_3$ hybrid perovskite on the crystallization, optical properties, and morphology of polycrystalline films produced by single-stage synthesis from solution.

Experimental

Preparation of solutions. A solution of $\text{MA}_x\text{MEA}_{1-x}\text{PbI}_3$ hybrid perovskite was obtained by mixing a solution of monoethanolammonium iodide $\text{HOCH}_2\text{CH}_2\text{NH}_3\text{I}$ (with the concentration of 0.645 mol/l) and lead iodide PbI_2 (with the same concentration, i.e., 0.645 mol/l) with a solution of hybrid perovskite MAPbI_3 of equimolar concentration with 1 : 3, 1 : 1 and 3 : 1 volume ratios for varying proportions of the monoethanolammonium cation $\text{HOCH}_2\text{CH}_2\text{NH}_3^+$ (MEA) in the range from 0.25 to 0.75, respectively.

A solution of dimethylformamide (DMFA) with dimethyl sulfoxide (DMSO) with a volume ratio of 4:1 was used as a solvent. DMSO increases the solubility limit of lead iodide [19]. The ratio of DMFA and DMSO was also chosen because the precipitator can be subsequently used successfully for one-step spin-coating [19, 20].

To obtain polycrystalline layers of $\text{MA}_x\text{MEA}_{1-x}\text{PbI}_3$, solutions with a mass concentration of about 400 mg/ml were deposited on glass substrates by spin-coating followed by heating on a laboratory hot plate at 110 °C for 10 minutes. The spin-coating rate was 3000 rpm (for 30 s) with spin-up at 1000 rpm (10 s). Before applying the perovskite films, the glass substrates were thoroughly washed in soap solution, distilled water, acetone and isopropyl alcohol using an ultrasonic bath (10 minutes each). To confirm the formation of the crystalline structure of hybrid perovskites, samples were deposited on glass substrates by drop-casting followed by annealing at 110 °C to obtain thick layers.

Methods. To study the contact angle of $\text{MA}_x\text{MEA}_{1-x}\text{PbI}_3$ solutions in DMFA and DMSO, solutions with a volume of about 5 μl were applied to clean glass substrates and then monitored using an optical microscope.

The morphology of $\text{MA}_x\text{MEA}_{1-x}\text{PbI}_3$ polycrystalline layers was studied using optical microscopy (POLAM-312 polarization microscope) and atomic force microscopy (Ntegra Therma system from NT-MDT).

Optical absorption spectra were measured using a PE-5400UF spectrophotometer. X-ray images were obtained using a Bruker D2 PHASER diffractometer (Bruker, USA) with a scan speed of 1 deg/min with a CuK_α X-ray source.

Results and discussion

Results of X-ray diffraction (XRD) analysis for MAPbI_3 and $\text{MA}_{0.75}\text{MEA}_{0.25}\text{PbI}_3$, $\text{MA}_{0.5}\text{MEA}_{0.5}\text{PbI}_3$, $\text{MA}_{0.25}\text{MEA}_{0.75}\text{PbI}_3$ solid solutions (Fig. 1) with intense peaks that were attributed to the (110), (220), (310), (224), (330) planes, and minor peaks of the (200), (202), and (312) planes confirmed the tetragonal structure of perovskite [21]. Furthermore, with an increase in the proportion of monoethanolammonium in the composition of hybrid perovskites, a shift of peaks towards a decrease in the 2θ angle is observed in the XRD patterns, indicating an increase in the interplanar distances of the crystal lattice.

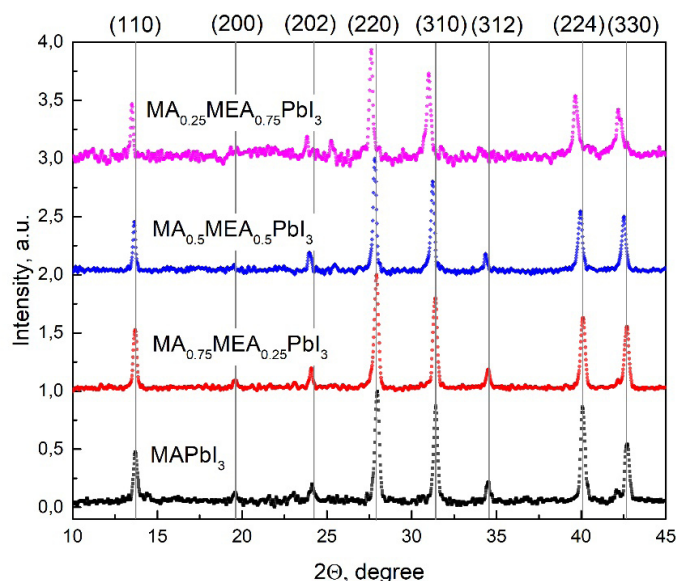


Fig. 1. XRD patterns of obtained materials: MAPbI_3 thick films and $\text{MA}_{0.75}\text{MEA}_{0.25}\text{PbI}_3$, $\text{MA}_{0.5}\text{MEA}_{0.5}\text{PbI}_3$, $\text{MA}_{0.25}\text{MEA}_{0.75}\text{PbI}_3$ solid solutions

An increase in the proportion of monoethanolammonium in the composition of $\text{MA}_x\text{MEA}_{1-x}\text{PbI}_3$ hybrid perovskites also leads to a change in the optical absorption spectra of the films. As follows from the spectra in Fig. 2, an increase in the proportion of monoethanolammonium in the composition leads to a shift in its absorption edge to the short-wavelength region, i.e., an increase in the band gap.

Results obtained by XRD analysis and spectrophotometry indicate the incorporation of monoethanolammonium cations into the crystal lattice, which leads to an increase in the interplanar distances in the crystal lattice, an increase in the optical band gap, and a change in absorption spectra with an increase in the proportion of monoethanolammonium in $\text{MA}_x\text{MEA}_{1-x}\text{PbI}_3$ solid solutions. The possibility of increasing the band gap with an increase in the proportion of monoethanolammonium makes $\text{MA}_x\text{MEA}_{1-x}\text{PbI}_3$ solid solutions attractive for use in tandem solar cells.

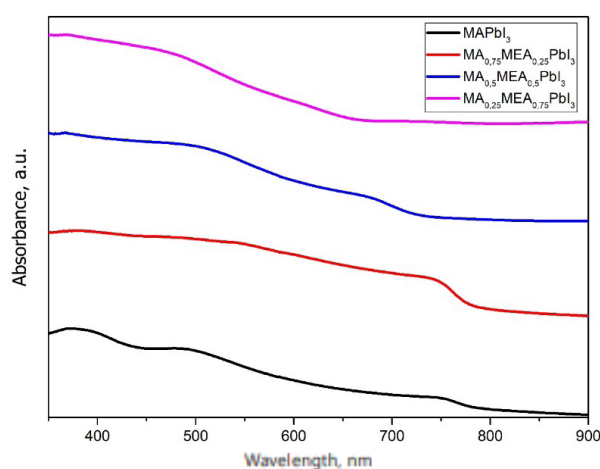


Fig. 2. Normalized optical absorption spectra of MAPbI_3 perovskite films and $\text{MA}_{0.75}\text{MEA}_{0.25}\text{PbI}_3$, $\text{MA}_{0.5}\text{MEA}_{0.5}\text{PbI}_3$, $\text{MA}_{0.25}\text{MEA}_{0.75}\text{PbI}_3$ solid solutions

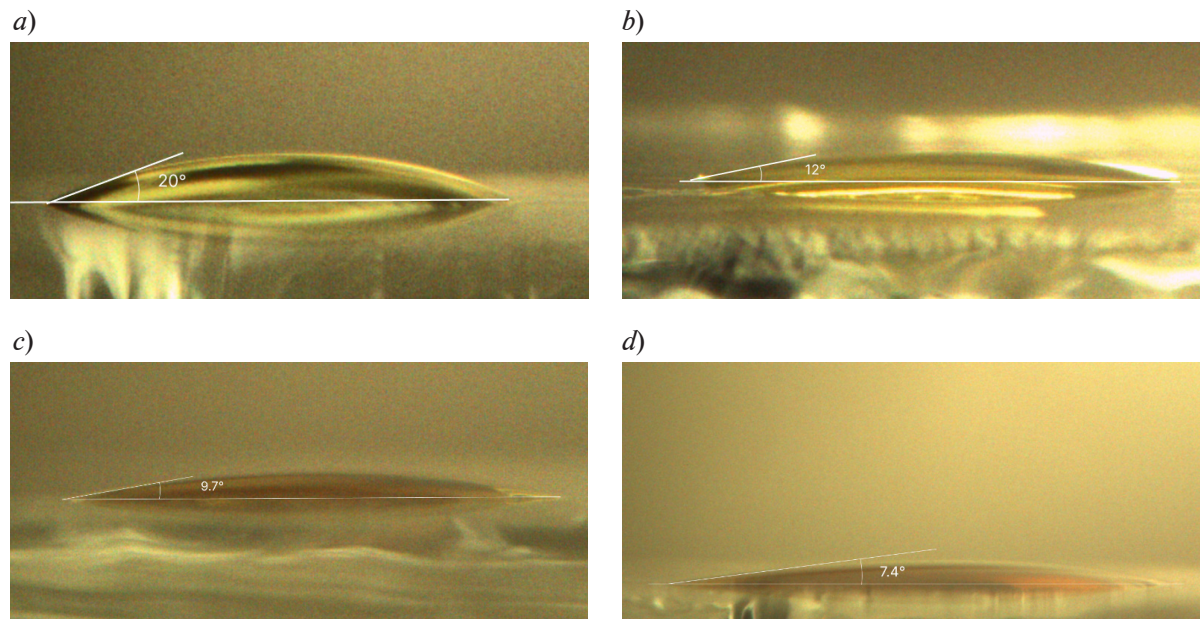


Fig. 3. Measurements of contact angle in hybrid perovskite solutions in DMFA with DMSO from photographs: MAPbI_3 (a), $\text{MA}_{0.75}\text{MEA}_{0.25}\text{PbI}_3$ (b), $\text{MA}_{0.5}\text{MEA}_{0.5}\text{PbI}_3$ (c), $\text{MA}_{0.25}\text{MEA}_{0.75}\text{PbI}_3$ (d)

The measurement results for contact angles of MAPbI_3 , $\text{MA}_{0.75}\text{MEA}_{0.25}\text{PbI}_3$, $\text{MA}_{0.5}\text{MEA}_{0.5}\text{PbI}_3$, $\text{MA}_{0.25}\text{MEA}_{0.75}\text{PbI}_3$ compounds in DMFA and DMSO solutions on the surface of glass substrates are shown in Fig. 3.

According to the data in Fig. 3, the MAPbI_3 solution shows the largest contact angle, and the 1 : 3 ratio of the MEAI and MAI components in the solution leads to a significant decrease in this angle from about 20° to 12° . Therefore, this ratio makes it possible to improve wettability without introducing significant distortions into the perovskite crystal lattice. A further increase in the proportion of MEAI relative to MAI to a 3 : 1 ratio ensures a further decrease in the contact angle (to about 7.4°). Better wettability of the substrate surface with the solution typically contributes to more uniform coating of the substrate, at both macro and microscale.

The results of optical microscopy studies of $\text{MA}_x\text{MEA}_{1-x}\text{PbI}_3$ perovskite films are shown in Fig. 4. Evidently, elongated split crystallites with a characteristic size of about $25\ \mu\text{m}$ are predominantly formed under these conditions for MAPbI_3 film synthesized from solution in DMFA and DMSO (see Fig. 4,a). Crystallization of $\text{MA}_{0.75}\text{MEA}_{0.25}\text{PbI}_3$ films leads to the formation of larger elongated split crystallites with characteristic sizes of $0.1\text{--}0.2\ \text{mm}$ (see Fig. 4,b). Such elongated crystallites may be promising for applications in planar structures, for example, photodetectors or X-ray detectors [22], since they likely contain fewer grain boundaries in the lateral direction than polycrystalline films with characteristic crystallite sizes in fractions of micrometers. However, such a crystallization process can be critical for vertical structures, since it can be accompanied by discontinuities in the coating of the substrate surface, uneven thickness and microcavities forming under split crystallites, which can lead to efficiency loss of the device or shunting of the perovskite layer.

As shown in [23], the formation of large elongated crystallites in hybrid perovskites may be associated with homogeneous nucleation in the near-surface region of the thin film of the solution. Evaporation of the solvent leads to an increase in the solute concentration in the near-surface region, and a lower temperature at the surface of the solution layer reduces the solubility of perovskite, providing supersaturation and homogeneous nucleation. A small concentration of nuclei in the near-surface layer and a long evaporation process lead to the formation of large elongated crystallites. Another nucleation region to be considered is the interface on the substrate surface, since the energy barrier for heterogeneous nucleation is lower than for homogeneous nucleation.

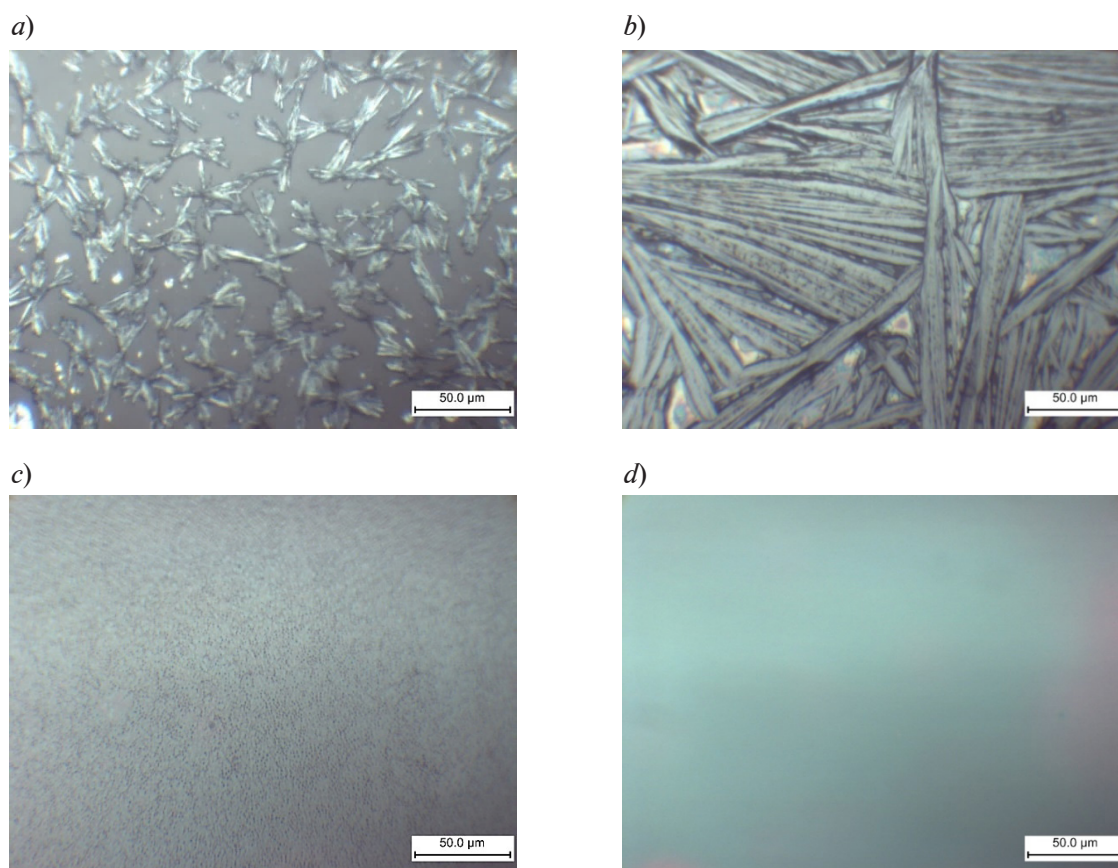


Fig. 4. Micrographs of $\text{MA}_x\text{MEA}_{1-x}\text{PbI}_3$ solid solutions obtained by one-step spin-coating from DMFA and DMSO solutions (1:4) on glass substrates: MAPbI_3 (a), $\text{MA}_{0.75}\text{MEA}_{0.25}\text{PbI}_3$ (b), $\text{MA}_{0.5}\text{MEA}_{0.5}\text{PbI}_3$ (c), $\text{MA}_{0.25}\text{MEA}_{0.75}\text{PbI}_3$ (d)

Analysis of AFM images of the MAPbI_3 coating (Fig. 5) shows the presence of small crystallites on the surface of the substrate.

For example, the observed small dark regions between large elongated crystallites in Fig. 5, *b* are crystallites formed under heterogeneous nucleation. It can be seen from Fig. 5, *c* and *d* that the size of these crystallites is tens and hundreds of nanometers. An increase in the solute concentration in the near-surface region during drying of the solution also leads to solute diffusion towards the substrate surface, while growth processes with homogeneous and heterogeneous nucleation are competing and are often observed simultaneously [23–25].

Figs. 4, *a* and 5 also show that the MAPbI_3 film layer contains uncoated regions of the substrate and, in general, a smaller volume of material on the substrate, while the $\text{MA}_{0.75}\text{MEA}_{0.25}\text{PbI}_3$ film completely covers the substrate even at the macroscale, and the elongated structures are much larger (see Fig. 4, *b*). This is probably due to poor wettability of the substrate surface with MAPbI_3 solution, which can lead to greater separation of solution droplets during spin-coating and a decrease in the volume of solution on the substrate [26]. Moreover, the lower wettability of the substrate with the solution can lead to nonuniform coating of the substrate with the formation of individual microdroplets during drying. On the other hand, a dramatic improvement in wettability of $\text{MA}_{0.75}\text{MEA}_{0.25}\text{PbI}_3$ solution with an almost twofold decrease in the contact angle by (from 20° to 12°) probably leads to an increase in the volume of the solution on the substrate during spin-coating. Nevertheless, the difference in the sizes of elongated crystallites may be related not only to the available volume of the solution, but also to a different crystallization kinetics of the $\text{MA}_{0.75}\text{MEA}_{0.25}\text{PbI}_3$ film.

As follows from the optical microscopy data for $\text{MA}_{0.5}\text{MEA}_{0.5}\text{PbI}_3$ and $\text{MA}_{0.25}\text{MEA}_{0.75}\text{PbI}_3$ films (see Fig. 4, *c*, *d*), a further decrease in the contact angle is correlated with the coating quality of the substrates with continuous and homogeneous polycrystalline layers. In this case, the

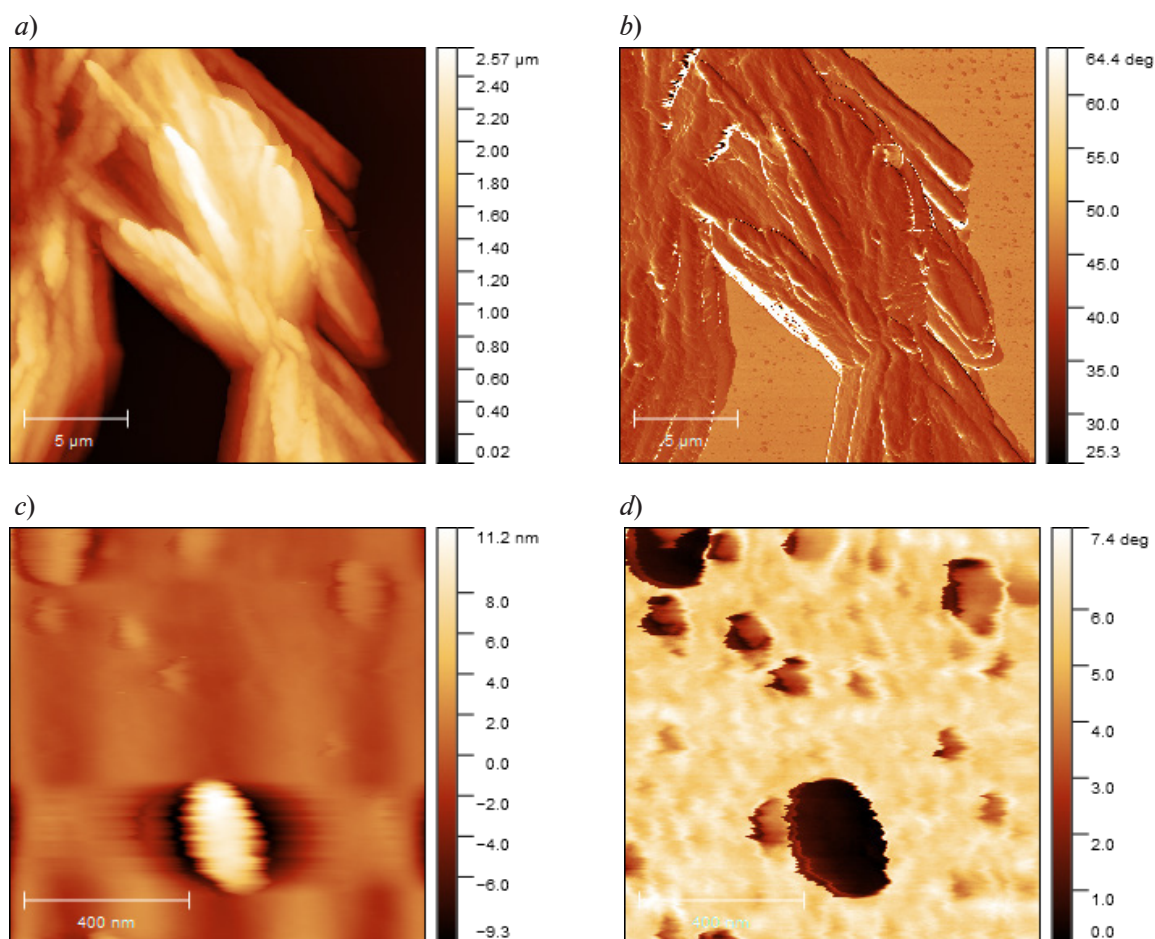


Fig. 5. AFM images of MAPbI₃ film: its topology (*a*, *b*) and phase contrast (*c*, *d*)

crystallization kinetics of the layer clearly changes dramatically when heterogeneous nucleation prevails, and the formation of elongated crystallites is not observed.

The contact angle for the MA_{0.25}MEA_{0.75}PbI₃ solution is also smaller than for the MA_{0.5}MEA_{0.5}PbI₃ solution. Optical microscopy studies revealed no grain boundaries or roughness for the MA_{0.25}MEA_{0.75}PbI₃ layer. As seen from the AFM images (Fig. 6, *a*, *b*), the MA_{0.5}MEA_{0.5}PbI₃ polycrystalline film demonstrates a hierarchical structure where larger grains with the approximate sizes of 0.5–1.0 μm consist of nanocrystallites with the characteristic sizes of about 50 nm. The film with a higher proportion of monoethanolammonium (MA_{0.25}MEA_{0.75}PbI₃) is a homogeneous coating of nanocrystallites about 50 nm in size, without forming larger grains (Fig. 6, *c*, *d*).

It was found in [27] that an increase in the wettability of the substrate surface with the solution (a decrease in the contact angle) leads to an increase in the grain concentration of the polycrystalline hybrid perovskite film. However, the change in the morphology of the films in our work cannot be explained solely by the change in the wettability of the surface with the solution, since the obtained MA_{0.5}MEA_{0.5}PbI₃ and MA_{0.25}MEA_{0.75}PbI₃ films consist of nanocrystallites of similar sizes at the nanoscale. The concentration of monoethanolammonium obviously affects the alignment of nanocrystallites in the film. This phenomenon may be related to the incorporation of monoethanolammonium not only into the crystal lattice, but also in the region at the boundaries of nanocrystallites, acting as ligand molecules limiting grain growth.

Thus, we assume that the change in the morphology of MA_{*x*}MEA_{1-*x*}PbI₃ films is due to both a change in the contact angle of the solutions (and, probably, the solvent evaporation and supersaturation rates) and to mutual alignment of the nanocrystallites of the film depending on the concentration of monoethanolammonium at the boundaries of the nanocrystallites. Thus, continuous coating of the substrate with elongated split crystallites ensures a significant change in the contact angle relative to the MAPbI₃ solution for the MA_{0.75}MEA_{0.25}PbI₃ film, in contrast to

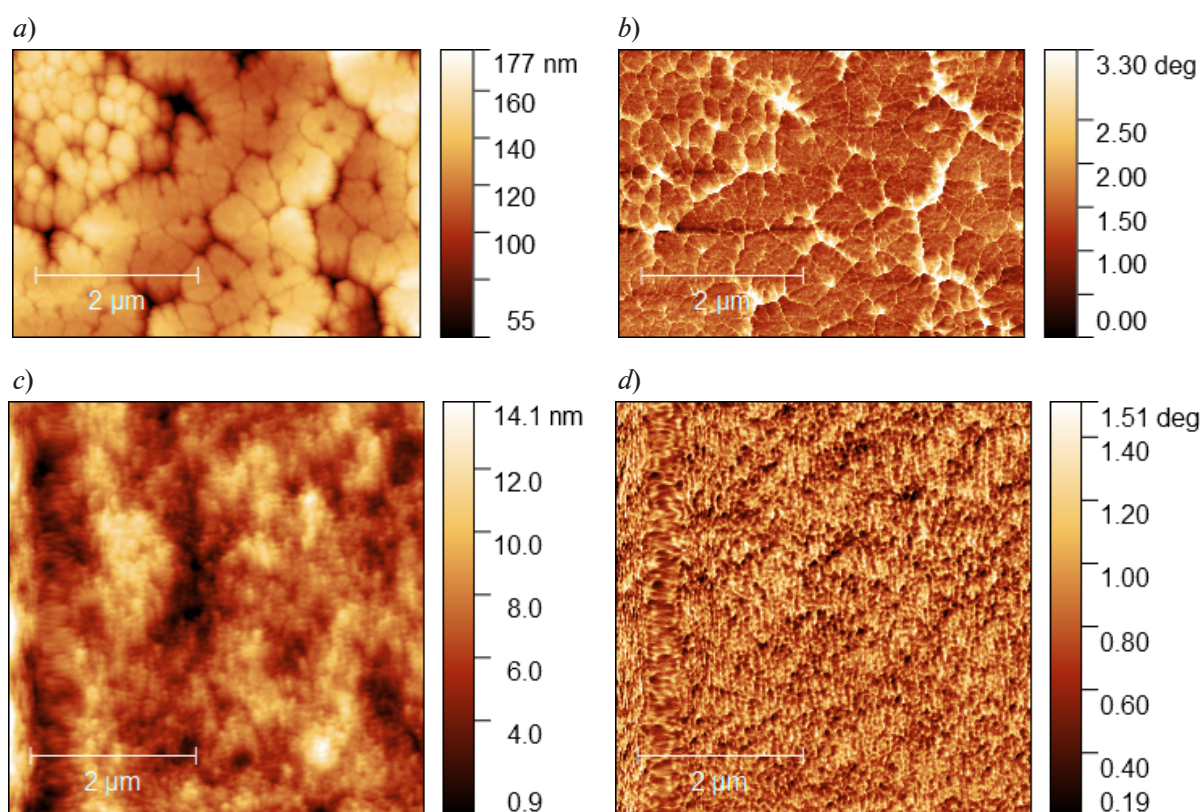


Fig. 6. AFM images of $\text{MA}_{0.5}\text{MEA}_{0.5}\text{PbI}_3$ (*a, b*) and $\text{MA}_{0.25}\text{MEA}_{0.75}\text{PbI}_3$ (*c, d*) films, showing their topology (*a, c*) and phase contrast (*b, d*)

discontinuous coating for the MAPbI_3 solution. However, the absence of elongated crystallites in $\text{MA}_{0.5}\text{MEA}_{0.5}\text{PbI}_3$ and $\text{MA}_{0.25}\text{MEA}_{0.75}\text{PbI}_3$ films may be due not only to violation of the conditions for homogeneous nucleation and growth of elongated crystallites due to a decrease in the contact angle, evaporation rate, and predominance of the heterogeneous nucleation mechanism, but also to a restriction of crystallite intergrowth during the incorporation of monoethanolammonium molecules at the boundaries of nanocrystallites. Nevertheless, good wettability of the substrates with $\text{MA}_{0.5}\text{MEA}_{0.5}\text{PbI}_3$ and $\text{MA}_{0.25}\text{MEA}_{0.75}\text{PbI}_3$ solutions obviously ensures good uniformity and continuity of the films without additional activation of the substrate surface.

A change in the optical absorption spectra with an increase in the band gap and a shift in XRD peaks clearly indicates the incorporation of monoethanolammonium cations into the crystal lattice in the entire range of compositions studied. Therefore, we assume that monoethanolammonium molecules are incorporated simultaneously both in the crystal lattice, forming a solid solution, and at the boundary of nanocrystallites. Notably, the MEAPbI_3 film did not exhibit a crystalline phase of perovskite according to XRD analysis. This indicates that the incorporation of monoethanolammonium into the crystal lattice is energetically unfavorable and indirectly confirms our assumption about the possible incorporation of monoethanolammonium at the boundaries of $\text{MA}_{0.25}\text{MEA}_{0.75}\text{PbI}_3$ nanocrystallites as well.

Conclusion

We considered the morphological features of polycrystalline films of hybrid perovskites $\text{MA}_x\text{MEA}_{1-x}\text{PbI}_3$, prepared by one-step spin-coating from DMF and DMSO (4:1) solutions.

The experiments indicate that an increase in the proportion of monoethanolammonium in $\text{MA}_x\text{MEA}_{1-x}\text{PbI}_3$ leads not only to a change in the absorption spectra with an increase in the band gap and interplanar distances of the crystal lattice, but also to a significant change in the morphology of the films, as well as to an improvement in wettability of $\text{MA}_x\text{MEA}_{1-x}\text{PbI}_3$ solutions. A decrease in the contact angle of $\text{MA}_x\text{MEA}_{1-x}\text{PbI}_3$ solutions with an increase in the proportion of MEA ensures the continuity of the substrate coating without additional surface activation.



Importantly, the increased band gap of $\text{MA}_x\text{MEA}_{1-x}\text{PbI}_3$ films, compared with MAPbI_3 , makes these hybrid perovskites attractive for use in tandem solar cells. It was found that films with the composition $\text{MA}_{0.75}\text{MEA}_{0.25}\text{PbI}_3$ form elongated split crystallites with characteristic sizes of 0.1–0.2 μm under these growth conditions, which promises new avenues for the creation of photodetectors or X-ray detectors.

A further increase in the proportion of monoethanolammonium in $\text{MA}_x\text{MEA}_{1-x}\text{PbI}_3$ hybrid perovskites leads to a change in the mechanisms of film crystallization, inhibiting the growth of elongated crystallites and yielding high-quality layers for use in vertical structures such as tandem solar cells. We assume that the change in crystallization mechanisms is due not so much to a change in wettability and the predominance of heterogeneous nucleation over homogeneous nucleation, but rather to incorporation of part of the monoethanolammonium molecules at the nanocrystallite boundaries of the film.

The nature of such a phenomenon as predominant incorporation of monoethanolammonium molecules into the crystal lattice or on nanocrystallite boundaries in the film requires further research, presenting not only practical but also purely scientific interest.

REFERENCES

1. Krishna B. G., Ghosh, D. S., Tiwari S., Progress in ambient air-processed perovskite solar cells: Insights into processing techniques and stability assessment, *Sol. Energy*. 224 (Aug) (2021) 1369–1395.
2. Lian Z., Yan Q., Lv Q., et al., High-performance planar-type photodetector on (100) facet of MAPbI_3 single crystal, *Sci. Rep.* 5 (13 Nov) (2015) 16563.
3. Kim Y. C., Kim K. H., Son D.-Y., et al., Printable organometallic perovskite enables large-area, low-dose X-ray imaging, *Nature*. 550 (7674) (2017) 87–91.
4. Zhao X., Xu H., Wang Z., et al., Memristors with organic-inorganic halide perovskites, *InfoMat.* 1 (2) (2019) 183–210.
5. Zhu X., Lee J., Lu W., Iodine vacancy redistribution in organic–inorganic halide perovskite films and resistive switching effects, *Adv. Mater.* 29 (29) (2017) 1700527.
6. Bencherif H., Meddour F., Elshorbagy M. H., et al., Performance enhancement of $(\text{FAPbI}_3)_{1-x}(\text{MAPbBr}_3)_x$ perovskite solar cell with an optimized design, *Micro Nanostructures*. 171 (Nov) (2022) 207403.
7. Gao B., Meng J., $\text{RbCs}(\text{MAFA})\text{PbI}_3$ perovskite solar cell with 22.81% efficiency using the precise ions cascade regulation, *Appl. Surf. Sci.* 530 (15 Nov) (2020) 147240.
8. Fan X., Advanced progress in metal halide perovskite solar cells: A review, *Mater. Today Sustain.* 24 (Dec) (2023) 100603.
9. Nenashv G. V., Aleshin A. N., Ryabko A. A., et al., Effect of barium doping on the behavior of conductivity and impedance of organic-inorganic perovskite films, *Solid State Commun.* 388 (15 Sept) (2024) 115554.
10. Khan F., Rezgui B. D., Khan M. T., Al-Sulaiman F. A., Perovskite-based tandem solar cells: Device architecture, stability, and economic perspectives, // *Renewable & Sustainable Energy Reviews*. 165 (Sept) (2022) 112553.
11. Li H., Zhang W., Perovskite tandem solar cells: From fundamentals to commercial deployment, *Chem. Rev.* 120 (18) (2020) 9835–9950.
12. Khatoon S., Yadav S. K., Chakraborty V., et al., Perovskite solar cell's efficiency, stability and scalability: A review, *Mater. Sci. Energy Technol.* 6 (1) (2023) 437–459.
13. Kozodayev D. A., Muratova E. N., Moshnikov V. A., Ot nanotekhnologii k nanoarkhitektonike [From nanotechnology to architektoniks], The 79-th Scientific and Technical Conference of St. Petersburg's STS REC named after Popov, dedicated to the Day of Radio, April 22–26, 2024; ETU “LETI”, Book of reports. St. Petersburg. Section 9. 1(79) (2024) 350–352.
14. Su K., Chen W., Huang Y., et al., In situ graded passivation via porphyrin derivative with enhanced photovoltage and fill factor in perovskite solar cells, *Solar RRL*. 6 (4) (2022) 2270041.
15. Feng W., Tan Y., Yang M., et al., Small amines bring big benefits to perovskite-based solar cells and light-emitting diodes, *Chem.* 8 (2) (2022) 351–383.
16. Azmi R., Ugur E., Seithkan A., et al., Damp heat-stable perovskite solar cells with tailored-dimensionality 2D/3D heterojunctions, *Science*. 376 (6588) (2022) 73–77.

17. **Leung T. L., Ahmad I., Syed A. A., et al.**, Stability of 2D and quasi-2D perovskite materials and devices, *Commun. Mater.* 3 (06 Sept) (2022) 63 (2022).
18. **Liu D., Li Q., Wu K.**, Ethylammonium as an alternative cation for efficient perovskite solar cells from first-principles calculations, *RSC Adv.* 9 (13) (2019) 7356–7361.
19. **Fan P., Gu D., Liang G., et al.**, High-performance perovskite $\text{CH}_3\text{NH}_3\text{PbI}_3$ thin films for solar cells prepared by single-source physical vapour deposition, *Sci. Rep.* 6 (18 July) (2016) 29910.
20. **Ryabko A. A., Ovezov M. K., Maksimov A. I., et al.**, Competing growth mechanisms during the formation of a MAPbI_3 polycrystalline film, *Vestnik of Yaroslav the Wise Novgorod State University.* (3(132)) (2023) 365–373 (in Russian).
21. **Li Y., Li X., Qianqian C., et al.**, Tuning nucleation sites to enable monolayer perovskite films for highly efficient perovskite solar cells, *Coatings.* 8 (11) (2018) 408.
22. **Kumar J., Srivastava P., Bag M.**, Advanced strategies to tailor the nucleation and crystal growth in hybrid halide perovskite thin films, *Front. Chem.* 10 (13 Apr) (2022) 842924.
23. **Moshnikov V., Muratova E., Aleshin A., et al.**, Controlled crystallization of hybrid perovskite films from solution using prepared crystal centers, *Crystals.* 14 (4) (2024) 376.
24. **Kim N. K., Kang D. H., Kang H. W.**, Unevenness of thin liquid layer by contact angle variation of substrate during coating process, *Coatings.* 9 (3) (2019) 162.
25. **Pylnev M., Barbisan A. M., Wei T.-C.**, Effect of wettability of substrate on metal halide perovskite growth, *Appl. Surf. Sci.* 541 (1 March) (2021) 148559.

СПИСОК ЛИТЕРАТУРЫ

1. **Krishna B. G., Ghosh, D. S., Tiwari S.** Progress in ambient air-processed perovskite solar cells: Insights into processing techniques and stability assessment // *Solar Energy.* 2021. Vol. 224. August. Pp. 1369–1395.
2. **Lian Z., Yan Q., Lv Q., Wang Y., Liu L., Zhang L., Pan S., Li Q., Wang L.-D., Sun J.-L.** High-performance planar-type photodetector on (100) facet of MAPbI_3 single crystal // *Scientific Reports.* 2015. Vol. 5. 13 November. P. 16563.
3. **Kim Y. C., Kim K. H., Son D.-Y., Jeong D.-N., Seo J.-Y., Choi Y. S., Han I. T., Lee S. Y., Park, N.-G.** Printable organometallic perovskite enables large-area, low-dose X-ray imaging // *Nature.* 2017. Vol. 550. No. 7674. Pp. 87–91.
4. **Zhao X., Xu H., Wang Z., Lin Y., Liu Y.** Memristors with organic-inorganic halide perovskites // *InfoMat.* 2019. Vol. 1. No. 2. Pp. 183–210.
5. **Zhu X., Lee J., Lu W.** Iodine vacancy redistribution in organic–inorganic halide perovskite films and resistive switching effects // *Advanced Materials.* 2017. Vol. 29. No. 29. P. 1700527.
6. **Bencherif H., Meddour F., Elshorbagy M. H., Hossain M. K., Cuadrado A., Abdi M. A., Bendib T., Kouda S., Alda J.** Performance enhancement of $(\text{FAPbI}_3)_{1-x}(\text{MAPbBr}_3)_x$ perovskite solar cell with an optimized design // *Micro and Nanostructures.* 2022. Vol. 171. November. P. 207403.
7. **Gao B., Meng J.** $\text{RbCs}(\text{MAFA})\text{PbI}_3$ perovskite solar cell with 22.81% efficiency using the precise ions cascade regulation // *Applied Surface Science.* 2020. Vol. 530. 15 November. P. 147240.
8. **Fan X.** Advanced progress in metal halide perovskite solar cells: A review // *Materials Today Sustainability.* 2023. Vol. 24. December. P. 100603.
9. **Nenashev G. V., Aleshin A. N., Ryabko A. A., Shcherbakov I. P., Moshnikov V. A., Muratova E. N., Kondratev V. M., Vrublevsky I. A.** Effect of barium doping on the behavior of conductivity and impedance of organic-inorganic perovskite films // *Solid State Communications.* 2024. Vol. 388. 15 September. P. 115554.
10. **Khan F., Rezgui B. D., Khan M. T., Al-Sulaiman F. A.** Perovskite-based tandem solar cells: Device architecture, stability, and economic perspectives // *Renewable & Sustainable Energy Reviews.* 2022. Vol. 165. September. P. 112553.
11. **Li H., Zhang W.** Perovskite tandem solar cells: From fundamentals to commercial deployment // *Chemical Reviews.* 2020. Vol. 120. No. 18. Pp. 9835–9950.
12. **Khatoon S., Yadav S. K., Chakraborty V., Singh J., Singh R. B., Hasnain M. S., Hasnain S. M. M.** Perovskite solar cell's efficiency, stability and scalability: A review // *Materials Science for Energy Technologies.* 2023. Vol. 6. No. 1. Pp. 437–459.



13. Козодаев Д. А., Муратова Е. Н., Мошников В. А. От нанотехнологии к наноархитектонике // 79-я Научно-техническая конференция Санкт-Петербургского НТО РЭС им. А. С. Попова, посвященная Дню радио. Сборник докладов. 22–26 апреля 2024 г., СПбГЭТУ «ЛЭТИ». Санкт-Петербург. Секция 9. № 1 (79). С. 350–352.
14. Su K., Chen W., Huang Y., Yang G., Brooks K. G., Zhang B., Feng Y., Nazeeruddin M. K., Zhang Y. In situ graded passivation via porphyrin derivative with enhanced photovoltage and fill factor in perovskite solar cells // *Solar RRL*. 2022. Vol. 6. No. 4. P. 2270041.
15. Feng W., Tan Y., Yang M., Jiang Y., Lei B.-X., Wang L. P., Wu W.-Q. Small amines bring big benefits to perovskite-based solar cells and light-emitting diodes // *Chem*. 2022. Vol. 8. No. 2. Pp. 351–383.
16. Azmi R., Ugur E., Seitkhan A., et al. Damp heat-stable perovskite solar cells with tailored-dimensionality 2D/3D heterojunctions // *Science*. 2022. Vol. 376. No. 6588. Pp. 73–77.
17. Leung T. L., Ahmad I., Syed A. A., Ng A. M. C., Popović J., Chen W. Stability of 2D and quasi-2D perovskite materials and devices // *Communications Materials*. 2022. Vol. 3. 06 September. P. 63 (2022).
18. Liu D., Li Q., Wu K. Ethylammonium as an alternative cation for efficient perovskite solar cells from first-principles calculations // *Royal Society of Chemistry (RSC) Advances*. 2019. Vol. 9. No. 13. Pp. 7356–7361.
19. Fan P., Gu D., Liang G., Luo J., Chen J.-L., Zheng Z., Zhang D. High-performance perovskite $\text{CH}_3\text{NH}_3\text{PbI}_3$ thin films for solar cells prepared by single-source physical vapour deposition // *Scientific Reports*. 2016. Vol. 6. 18 July. P. 29910.
20. Рябко А. А., Овезов М. К., Максимов А. И., Алешин А. М., Мошников В. А. Конкурирующие механизмы роста при формировании поликристаллической пленки MAPbI_3 // *Вестник Новгородского государственного университета*. 2023. № 3 (132) С. 365–373.
21. Li Y., Li X., Qianqian C., Dong H., Yao J.-T., Zhou Y., Yang G.-J. Tuning nucleation sites to enable monolayer perovskite films for highly efficient perovskite solar cells // *Coatings*. 2018. Vol. 8. No. 11. P. 408.
22. Kumar J., Srivastava P., Bag M. Advanced strategies to tailor the nucleation and crystal growth in hybrid halide perovskite thin films // *Frontiers in Chemistry*. 2022. Vol. 10. 13 April. P. 842924.
23. Moshnikov V., Muratova E., Aleshin A., Maksimov A., Nenashev G., Vrublevsky I., Lushpa N., Tuchkovsky A., Zhilenkov A., Kichigina O. Controlled crystallization of hybrid perovskite films from solution using prepared crystal centers // *Crystals*. 2024. Vol. 14. No. 4. P. 376.
24. Kim N. K., Kang D. H., Kang H. W. Unevenness of thin liquid layer by contact angle variation of substrate during coating process // *Coatings*. 2019. Vol. 9. No. 3. P. 162.
25. Pylnev M., Barbisan A. M., Wei T.-C. Effect of wettability of substrate on metal halide perovskite growth // *Applied Surface Science*. 2021. Vol. 541. 1 March. P. 148559.

THE AUTHORS

RYABKO Andrey A.

Ioffe Institute of RAS

26 Polytekhnicheskaya St., St. Petersburg, 194021, Russia

a.a.ryabko93@yandex.ru

ORCID: 0000-0001-9626-7612

OVEZOV Maksat K.

Ioffe Institute of RAS

26 Polytekhnicheskaya St., St. Petersburg, 194021, Russia

strontiumx94@gmail.com

ORCID: 0009-0009-6273-1478

MAXIMOV Alexander I.

St. Petersburg Electrotechnical University “LETI”

5 Professor Popov St., St. Petersburg, 197376, Russia

aimaximov@mail.ru

ORCID: 0000-0003-0195-8870

PERMIAKOV Nikita V.

St. Petersburg Electrotechnical University "LETI"
5 Professor Popov St., St. Petersburg, 197376, Russia
nvpermiakov@etu.ru
ORCID: 0000-0002-6953-9958

TUCHKOVSKIY Alexander K.

Belarusian State University of Informatics and Radioelectronics
6 Petrus Brovka St., Minsk, 220013, Republic of Belarus
a.tuchkovskij@bsuir.by

VRUBLEVSKIY Igor A.

Belarusian State University of Informatics and Radioelectronics
6 Petrus Brovka St., Minsk, 220013, Republic of Belarus
vrublevsky@bsuir.edu.by
ORCID: 0000-0002-6796-8994

MURATOVA Ekaterina N.

St. Petersburg Electrotechnical University "LETI"
5 Professor Popov St., St. Petersburg, 197376, Russia
sokolovaeknik@yandex.ru
ORCID: 0000-0002-4181-6669

ALESHIN Andrey N.

Ioffe Institute of RAS
26 Polytekhnicheskaya St., St. Petersburg, 194021, Russia
aleshin.transport@mail.ioffe.ru
ORCID: 0000-0001-5449-4446

MOSHNIKOV Vyacheslav A.

St. Petersburg Electrotechnical University "LETI"
5 Professor Popov St., St. Petersburg, 197376, Russia
vamoshnirov@mail.ru
ORCID: 0000-0001-6500-5492

СВЕДЕНИЯ ОБ АВТОРАХ

РЯБКО Андрей Андреевич — кандидат технических наук, младший научный сотрудник лаборатории неравновесных процессов в полупроводниках Физико-технического института имени А. Ф. Иоффе РАН.

194021, Россия, г. Санкт-Петербург, Политехническая ул., 26
a.a.ryabko93@yandex.ru
ORCID: 0000-0001-9626-7612

ОВЕЗОВ Максат Кемалович — младший научный сотрудник лаборатории неравновесных процессов в полупроводниках Физико-технического института имени А. Ф. Иоффе РАН.

194021, Россия, г. Санкт-Петербург, Политехническая ул., 26
strontiumx94@gmail.com
ORCID: 0009-0009-6273-1478

МАКСИМОВ Александр Иванович — кандидат физико-математических наук, доцент кафедры микро- и нанoeлектроники Санкт-Петербургского государственного электротехнического университета «ЛЭТИ» имени В. И. Ульянова (Ленина).

197376, Россия, г. Санкт Петербург, ул. Проф. Попова, 5
aimaximov@mail.ru
ORCID: 0000-0003-0195-8870



ПЕРМЯКОВ Никита Вадимович — доцент кафедры микро- и нанoeлектроники Санкт-Петербургского государственного электротехнического университета «ЛЭТИ» имени В. И. Ульянова (Ленина).

197376, Россия, г. Санкт Петербург, ул. Проф. Попова, 5

nvpermiakov@etu.ru

ORCID: 0000-0002-6953-9958

ТУЧКОВСКИЙ Александр Константинович — старший научный сотрудник Белорусского государственного университета информатики и радиоэлектроники.

220013, Республика Беларусь, г. Минск, ул. Петруся Бровки, 6

a.tuchkovskij@bsuir.by

ORCID: --

ВРУБЛЕВСКИЙ Игорь Альфонсович — доцент Белорусского государственного университета информатики и радиоэлектроники.

220013, Республика Беларусь, г. Минск, ул. Петруся Бровки, 6

vrublevsky@bsuir.edu.by

ORCID: 0000-0002-6796-8994

МУРАТОВА Екатерина Николаевна — доцент кафедры микро- и нанoeлектроники Санкт-Петербургского государственного электротехнического университета «ЛЭТИ» имени В. И. Ульянова (Ленина).

197376, Россия, г. Санкт Петербург, ул. Проф. Попова, 5

sokolovaeknik@yandex.ru

ORCID: 0000-0002-4181-6669

АЛЕШИН Андрей Николаевич — доктор физико-математических наук, заведующий лабораторией неравновесных процессов в полупроводниках Физико-технического института имени А. Ф. Иоффе РАН.

194021, Россия, г. Санкт-Петербург, Политехническая ул., 26

aleshin.transport@mail.ioffe.ru

ORCID: 0000-0001-5449-4446

МОШНИКОВ Вячеслав Алексеевич — доктор физико-математических наук, профессор кафедры микро- и нанoeлектроники Санкт-Петербургского государственного электротехнического университета «ЛЭТИ» имени В. И. Ульянова (Ленина).

197376, Россия, г. Санкт Петербург, ул. Проф. Попова, д. 5

vamoshnirov@mail.ru

ORCID: 0000-0001-6500-5492

Статья поступила в редакцию 28.09.2024. Одобрена после рецензирования 04.12.2024. Принята 04.12.2024.

Received 28.09.2024. Approved after reviewing 04.12.2024. Accepted 04.12.2024.

Original article

UDC 538.915


DOI: <https://doi.org/10.18721/JPM.18208>

THE EFFECT OF PLA-BASED COMPOSITE MATERIAL HISTORY ON ITS ELECTRET PROPERTIES

I. A. Zagidullina ¹, A. A. Guzhova ¹, E. A. Karulina ² , S. M. Kulemina ²

¹ Kazan National Research Technological University, the Republic of Tatarstan, Kazan, Russia;

² Herzen State Pedagogical University of Russia, St. Petersburg, Russia

 karulina@mail.ru

Abstract. This study reveals the effects of manufacturing methods and composition of the films based on polylactic acid (PLA) and fine fillers of different nature (aerosil, white silica and starch) and concentration on the electret properties (EP). The methods were solution casting (I) and compression molding (II). PLA films manufactured via method II exhibited a significantly higher electret effect when subjected to unipolar corona discharge than the films obtained by method I. The difference in the EP was proved to be attributed to the presence of polar liquid molecules (trichloromethane, water) within the samples produced using method I enhancing the electrical conductivity of the samples. The samples showed a tendency for the EP parameters to increase when the dispersed particles of fine fillers were added to the pure PLA. An explanation for this phenomenon has been proposed. The composition of PLA with 4% white silica had the best electret properties.

Keywords: electret, polylactic acid, polymer, dispersed filler, white silica, aerosil, starch

Funding: The research was carried out using a grant from Academy of Sciences of the Republic of Tatarstan provided to young candidates of science (postdocs) for the purpose of presentation of a doctoral thesis, carrying out research work, as well as performing labor functions in scientific and educational organizations of the Republic of Tatarstan within the framework of the State Program “Scientific and Technological Development of the Republic of Tatarstan” (Agreement No. 114/2024-PD).

For citation: Zagidullina I. A., Guzhova A. A., Karulina E. A., Kulemina S. M., The effect of PLA-based composite material history on its electret properties, St. Petersburg State Polytechnical University Journal. Physics and Mathematics. 18 (2) (2025) 82–92. DOI: <https://doi.org/10.18721/JPM.18208>

This is an open access article under the CC BY-NC 4.0 license (<https://creativecommons.org/licenses/by-nc/4.0/>)

Научная статья

УДК 538.915


DOI: <https://doi.org/10.18721/JPM.18208>

ВЛИЯНИЕ ПРЕДЫСТОРИИ КОМПОЗИЦИОННЫХ МАТЕРИАЛОВ НА ОСНОВЕ ПОЛИЛАКТИДА НА ИХ ЭЛЕКТРЕТНЫЕ СВОЙСТВА

И. А. Загидуллин ¹, А. А. Гужов ¹, Е. А. Карулин ² , С. М. Кулемин ²

¹ Казанский национальный исследовательский технологический университет,
г. Казань, Республика Татарстан, Россия

² Российский государственный педагогический университет им. А. И. Герцена,
Санкт-Петербург, Россия

 karulina@mail.ru



Аннотация. Исследовано влияние метода изготовления и состава пленок из композиций полилактида (ПЛА) с дисперсными наполнителями (белая сажа, аэросил и крахмал в разной концентрации) на их электретные свойства (ЭС). Это методы полива из раствора (I) и прессования (II). Установлено, что пленки ПЛА, полученные методом II, гораздо лучше электретируются в униполярном коронном разряде и сохраняют ЭС, чем изготовленные методом I. Доказано, что разница в ЭС различных образцов обусловлена содержанием в их объеме полярной жидкости (хлороформ, вода), молекулы которой повышают электропроводность объектов. У образцов прослеживалась тенденция повышения параметров ЭС при добавлении дисперсных частиц к чистому ПЛА. Предложено объяснение этого эффекта. Лучшими ЭС обладала композиция ПЛА с 4 %-м содержанием белой сажи.

Ключевые слова: электрет, полилактид, полимер, дисперсный наполнитель, белая сажа, аэросил, крахмал

Финансирование: Работа выполнена за счет гранта Академии наук Республики Татарстан, предоставленного молодым кандидатам наук (постдокторантам) с целью защиты докторской диссертации, выполнения научно-исследовательских работ, а также выполнения трудовых функций в научных и образовательных организациях Республики Татарстан в рамках Государственной программы Республики Татарстан «Научно-технологическое развитие Республики Татарстан» (Соглашение №114/2024-ПД).

Для цитирования: Загидуллина И. А., Гужова А. А., Карулина Е. А., Кулемина С. М. Влияние предыстории композиционных материалов на основе полилактида на их электретные свойства // Научно-технические ведомости СПбГПУ. Физико-математические науки. 2025. Т. 18. № 2. С. 82–92. DOI: <https://doi.org/10.18721/JPM.18208>

Статья открытого доступа, распространяемая по лицензии CC BY-NC 4.0 (<https://creativecommons.org/licenses/by-nc/4.0/>)

Introduction

Polylactic acid (PLA) is an aliphatic polyester derived from renewable sources such as corn starch or sugarcane. It has a number of valuable properties that determine its wide application: biodegradability, non-toxicity, relatively high tensile strength and elasticity modulus, easy processing by injection molding and extrusion, low hydrophilicity, ability to be modified physically and chemically, etc. [1]. It is a sustainable material that tends to reduce negative environmental impact, creating an alternative to traditional synthetic polymers. Due to this property, an application field of PLA is constantly expanding, which entails the growth of its global production volume. Traditional areas of PLA application are packaging (bags, containers, disposable tableware), 3D printing, medicine (surgical threads and pins, medical masks), textile industry (fibers and fabrics), agriculture (covering materials in the form of nonwoven fabrics), filtration and others [2 – 4]. Over the past decade PLA has been considered as a promising dielectric material with piezoelectric and electret properties for the production of elements of wearable electronics, highly sensitive sensors, ultrasonic transducers, sensors, etc. [5 – 7].

Electrets are dielectric materials that possess dipole polarization or quasi-constant electric charge ("quasi-constant" means that the lifetime of an electret is much longer than the time during which it is applied or studied) [8].

Electrets are often made of polymers or polymer composites, the advantages of which are ease of processing and manufacturing, although they have lower temperature stability compared to inorganic (ceramic) electret materials. The scientific world is taking a strong interest in study of the electret properties of PLA and its composites. This is due to the growing requirements for environmental friendliness and protection, as well as the need to produce biocompatible sensors and transducers. PLA is described as a promising dielectric material with electret properties, although data on their quality and stability vary. Research has shown that the charge stability of PLA depends on the form (L- or D-stereoisomer), supramolecular structure (degree of crystallinity), environmental conditions (temperature, humidity, pressure), the presence of impurities and chemical additives in its composition, geometric dimensions of samples, etc. [9 – 15].

At the same time, attention is drawn to the fact that PLA-based electrets are produced by different manufacturers in various forms (films, sheets, fibers, coatings) and using all kinds of methods (pressing, extrusion, melt-blown, 3D printing, solution casting). Various methods of charging (thermal polarization, corona discharge) are also applied. It is clear that it is not worth comparing the values of electret characteristics of polymer samples obtained by different authors, because the prehistory of samples excludes the possibility of adequate comparison of the level of electret charge, their behavior during storage, research and operation.

The goal of the present study was to find the optimal method for preparing the PLA composition and the optimal nature of the filler (and its concentration) in order to obtain an electret with the best properties.

To achieve this goal the task was to compare the values and stability of electret parameters of films made of PLA and its compositions with fine fillers by different manufacturing methods.

Materials and methods

The subjects of research were polylactic acid and different fine fillers: pyrogenic silicon dioxide (aerosil), precipitated silicon dioxide (white silica) and starch. Their chemical structure, grades and properties are presented in Table 1.

Table 1

Characteristics of the materials under study

Material	Grade, standard	Chemical formula	Parameter value	
			ρ , g/cm ³	D , nm
Polylactic acid	Nature Works 40320	$(C_3H_4O_2)_n$	1.24	–
Aerosil	A1V0-, GOST 14922-77	SiO ₂	2.15	5–40
White silica	BS-120, GOST18307-78			19–27
Starch	Corn starch GOST 32159-2013	$(C_6H_{10}O_5)_n$	1.5	$(5–20) \cdot 10^3$
Trichloromethane	GOST TU 20015-88	CHCl ₃	1.483	–

Notations: ρ is the density, D is the particle size.

Footnote: Polylactic acid has the melting temperature $T_m = 155 - 170^\circ\text{C}$, glass transition temperature $T_g = 54 - 58^\circ\text{C}$.

The polymer and the fillers were mixed in a Brabender Mixer W 50 EHT at 180°C for 300 s at a roller speed of 150 rpm. The fillers were brought in the polymer in the ratio of 2, 4 and 6 wt. %. After that, films were produced by two methods:

Method I. Films 50 μm thick were manufactured by solution casting. For this purpose, PLA compositions were dissolved in the chloroform in the ratio of 1:20 and thoroughly stirred for 60 min; then they were left for 24 hrs until completely dissolved. Then, after another thorough stirring for 10 min, the 5 % (by mass) solution of PLA and its compositions were poured into specially prepared glass molds, dried under a hood for 1 hour, then drying was carried out under ambient conditions for three days, after that the films were removed from the substrates.

Method II. Samples in the form of films 500 μm thick were produced on a Gotech GT-7014-H10C press in accordance with GOST 12019-66. Compression molding parameters were as follows:

the heating temperature 200 °C,
the pressure 35 MPa,
the preheating time 20 min,
the pressure holding time ... 5 min,
the cooling time 2 min.

The films were charged with a two-electrode corona discharge film processing unit (Fig. 1). Processing parameters were as follows:



the distance between the sample and the electrode ... 20 mm,
 the polarization voltage 30 kV,
 the polarization time 30 s.

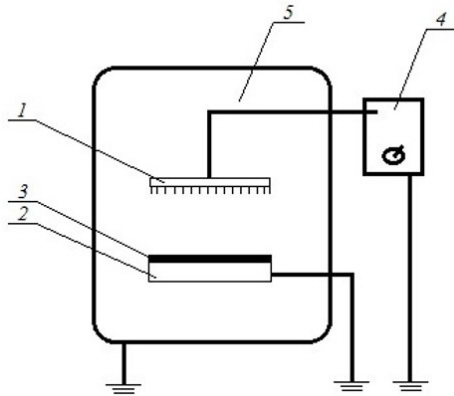


Fig. 1. Two-electrode charging unit with unipolar corona discharge:

a corona electrode (1), a grounded electrode (2), a sample (3), a power supply of the corona electrode (4), a heating chamber (5)

The electret properties of the samples, such as the surface potential V_s , the electric field strength E and the effective surface charge density σ_{eff} were measured with the IPEP-1 fieldmeter.

The FTIR spectrometer Agilent Cary 600 Series was used to record the infrared (IR) spectra of the samples.

Results and discussion

At the first stage of the study, PLA films were made from solution (casting) and melt (compression molding) of the polymer followed by the charging of the films in negative corona discharge to produce electrets. The results were quite unexpected. The PLA films obtained by solution casting had the following characteristics one hour after being charged:

$$V_s = 0.29 \text{ kV}, E = 9.7 \text{ kV/m}, \sigma_{eff} = 0.11 \text{ } \mu\text{C/m}^2,$$

while the compression-molded PLA films had the following characteristics:

$$V_s = 2.73 \text{ kV}, E = 170.3 \text{ kV/m}, \sigma_{eff} = 1.51 \text{ } \mu\text{C/m}^2,$$

i. e. by 10 times higher.

However, after 20 days of storage, the parameter values of electret properties of samples obtained by solution casting and compression molding became of the same order:

$$V_s = 0.14 \text{ kV}, E = 8.7 \text{ kV/m}, \sigma_{eff} = 0.09 \text{ } \mu\text{C/m}^2;$$

$$V_s = 0.19 \text{ kV}, E = 17.0 \text{ kV/m}, \sigma_{eff} = 0.08 \text{ } \mu\text{C/m}^2,$$

respectively.

However, the electret properties of the molded samples are still slightly higher than those of the samples cast from the solution.

The authors of Ref. [15] explained a great difference in the level of PLA properties by the presence of bound water in the samples: they showed that pre-annealing of PLA films led to a significant increase in the level and stability of their surface potential values.

To explain the observed difference in the properties of our samples obtained by different methods, their IR spectra were recorded, but no significant difference was found.

Notice that a range of $3700 - 3745 \text{ cm}^{-1}$ refers to isolated ("free") -OH groups, of $3650 - 3660 \text{ cm}^{-1}$ does to isolated pairs of neighboring OH-groups (vinyl-OH-groups) connected by hydrogen bonds, of $3650 - 3660 \text{ cm}^{-1}$ does to paired groupings of -OH-groups, with a hydrogen bond between. And so, judging by the absorption band group $3550 - 3750 \text{ cm}^{-1}$, water is present in both samples, but its amount is insignificant.

Migration of water molecules is known to occur into the polymer volume that during storage of PLA [1]. For the samples studied, this is evidenced by IR spectra of molded PLA films recorded immediately after preparation and after 90 days of storage (Fig. 2). It can be seen that the intensity of absorption bands at $3650 - 3660 \text{ cm}^{-1}$, corresponding to the vibration of water molecules, differ practically by a factor of 3, if calculated by the absolute value, and by a factor of 4, if calculated by the baseline. We suppose a significant drop in the values of V_s , E and σ_{eff} of electrets, which are inversely proportional to the values of electrical conductivity, to be related to this. The strong effect of polymer humidity on the value of its volume specific electrical conductivity (it can change by 1 – 3 orders of magnitude) is known [16], and it was shown that in this case water molecules were only a catalyst of electrical conductivity and did not participate directly in charge transfer [17].

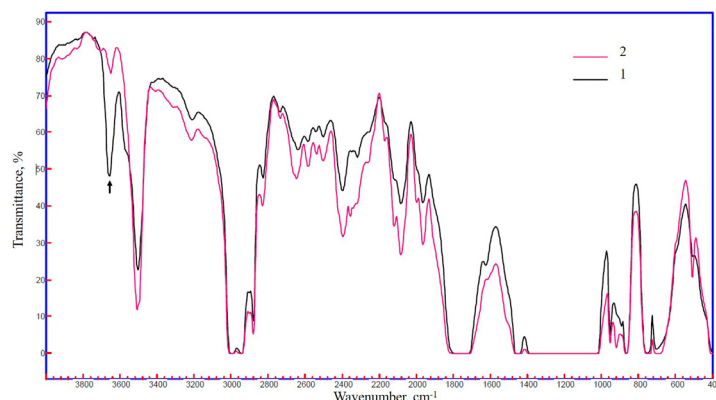


Fig. 2. IR spectrum of the PLA film obtained by compression molding, immediately after preparation (1) and after 90 days of storage (2).

The arrow indicates the position of the H_2O vibration

Probably, a similar process of charge transfer (relaxation of the electret state) is also observed for PLA films obtained by solution casting. However, it is not possible to prove it by IR spectroscopy, since the absorption bands characteristic of chloroform (2800 cm^{-1} refers to valence vibrations of CH, 1220 cm^{-1} does to deformation vibrations of CH, 630 cm^{-1} does to valence vibrations of CCl_3) overlap with the characteristic bands of PLA in this region (Fig. 3).

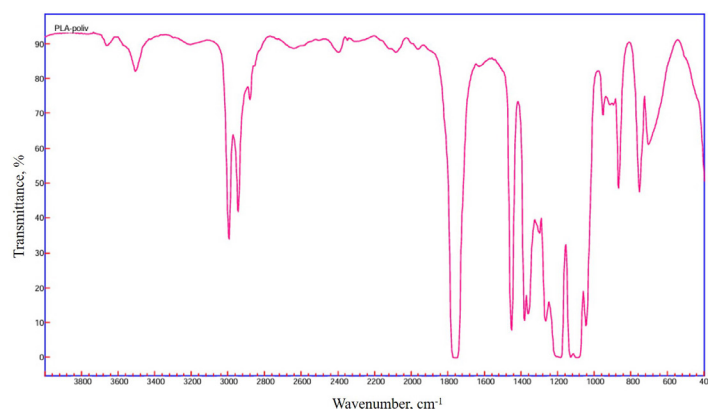


Fig. 3. IR spectrum of a solution-cast PLA film

Taking into account the results of the investigation aimed at increasing the charge stability of PLA by using fine fillers that cause structural defects in the polymer matrix and at the polymer – filler interface, which act as traps for charge carriers [12 – 14], at the second stage of study we created compositions of PLA with a number of dispersed fillers and studied their electret properties (see Fig. 4 and Table 2).

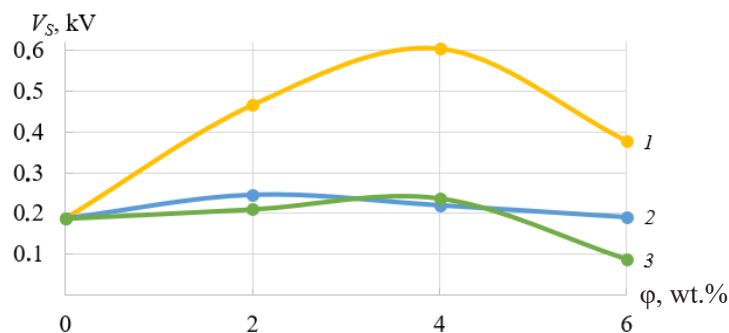


Fig. 4. A plot of surface potential values of PLA compositions with white silica (1), aerosil (2) and starch (3) versus the filler content after 20 days of storage

Table 2

Electret properties of PLA compositions (PLA + filler)

Filler	ϕ , wt. %	Method	Parameter value					
			Initial			After 20 days		
			V_s , kV	E , kV/m	σ_{eff} , $\mu\text{C}/\text{m}^2$	V_s , kV	E , kV/m	σ_{eff} , $\mu\text{C}/\text{m}^2$
No	0	I	0.29	9.7	0.11	0.14	10.9	0.07
		II	2.73	170.3	1.51	0.19	17.0	0.08
White silica	2	I	0.15	5.9	0.05	0.22	2.3	0.02
		II	2.42	153.7	1.37	0.47	22.4	0.09
	4	I	0.21	9.9	0.09	0.33	1.9	0.01
		II	2.45	153.3	1.36	0.61	28.4	0.12
	6	I	0.15	6.4	0.06	0.32	5.2	0.04
		II	3.86	241.0	2.13	0.38	18.3	0.10
Aerosil	2	I	0.13	5.3	0.05	0.28	2.2	0.01
		II	2.85	165.3	1.45	0.25	14.9	0.13
	4	I	0.08	1.6	0.01	0.30	2.3	0.08
		II	3.30	193.0	1.70	0.22	12.3	0.11
	6	I	0.06	6.2	0.05	0.21	2.5	0.02
		II	3.51	205.3	1.82	0.19	12.3	0.11
Starch	2	I	0.05	4.7	0.04	0.26	0.9	0.02
		II	3.35	197.3	1.73	0.21	10.6	0.10
	4	I	0.02	1.5	0.01	0.28	1.5	0.05
		II	2.51	143.7	1.27	0.24	12.6	0.11
	6	I	0.02	2.7	0.02	0.30	2.4	0.02
		II	2.81	164.3	1.43	0.09	4.8	0.05

Notations: ϕ is the filler content, V_s is the surface potential, E is the electric field strength, σ_{eff} is the effective surface charge density.

Footnote. Samples were manufactured either by solution casting (Method I) or by pressing (Method II).

If we consider compositions of PLA with fillers obtained by mixing filler with polymer melt, there is a tendency to increase the values of electret properties of PLA when adding fine particles. Composition of PLA with hydrated silicon dioxide has the best properties, and the highest values of V_s , E and σ_{eff} are observed at 4 % content of white silica (BS-120). If pyrogenic silicon dioxide is introduced into polylactide, then the optimal (for the manifestation of electret properties) formulation is a sample of polylactic acid with 2 % aerosil. The doping with starch, as well as aerosil, does not change the values of electret characteristics of the polymer significantly. An increase in the level of electret characteristics of PLA upon addition of dispersed particles is explained by the formation of structural defects acting as traps for charge carriers [12 – 14]. The solid surface of the filler reduces the segmental mobility of polylactic acid macromolecules due to the appearance of physical and hydrogen bonds between macromolecules and fillers. On one hand, this makes it difficult to polarize polylactide during corona discharge treatment. On the other hand, it complicates and even excludes the possibility of polarization relaxation. Especially it concerns dipole groups (for example, oxygen-containing), formed under the action of corona discharge and oriented along the field direction of corona discharge; the dipole appearing in the composition of macromolecule is fixed, the freedom of movement, oscillation of the macromolecule section in the areas adjacent to the surface is limited. That is, in filled polylactide near the surface of dispersed particles there is a layer of macromolecules with limited mobility,

which slows down (excludes) relaxation of dipole polarization in polylactide compositions. The following mechanism is also quite possible: dispersed particles act as macrodipoles, in which a dipole moment is induced when the sample is treated in the electric field of corona discharge. Applied to aerosil or white silica, this mechanism can be described as follows. A silicon atom has an unsaturated valence bond, which is saturated by the addition of a hydroxyl group OH [18]. The loss or gain of a proton leads to formation of a negatively ($[\text{OH}]^-$) or positively ($[\text{H}_2\text{O}]^+$) charged group, respectively. When such a dispersed particle enters an electric field, the charged groups move along the surface of the particle toward the opposite electrode. As a result, macrodipoles are formed in the structure of composites with increased concentration of charged hydroxyl groups on both sides of the filler particle. An increase in the number of charged particles and energy traps of charges in composites compared to the original polymer positively affects the ability of samples to be charged in the corona discharge and increases the stability of their surface potential, effective surface charge density and electric field strength.

It should be noted that annealing of the polymer before polarization is an effective way to preserve high level of electret properties. Fig. 5 compares the temperature curves of surface potential drop of PLA samples annealed and not annealed immediately before polarization. The annealing was carried out at 130° for 30 min.

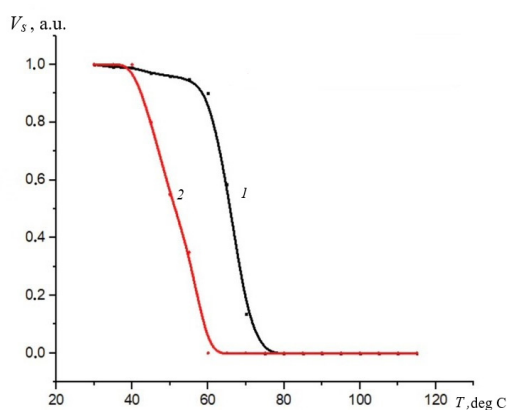


Fig. 5. A plot of surface potential versus temperature for the PLA samples with 4% starch polarized in the field of negative corona discharge. The samples were pre-annealed in a muffle furnace (1) or not annealed (2)

As can be seen from the presented graphs of the potential-temperature relation (see Fig. 5), the temperature and consequently the time stability of the surface potential increases significantly after pre-annealing.

Compositions of PLA with fillers manufactured via solution casting have a low level of electret characteristics. This result can be explained by poor dispersion of the filler and the presence of agglomerates with sizes exceeding the thickness of the samples. It is known that in production conditions polymer compositions cannot be obtained by simple addition of filler to the polymer solution, as this does not achieve a high degree of dispersion of filler agglomerates. Of course, it is possible to use special ball or bead mills, in which the filler agglomerates are grinded between hard surfaces (e.g., between the surface of metal balls), or ultrasonic dispersants. But the main limitation is due to the fact that polymer solutions have low concentration and solvents are very expensive. As a

rule, compositions of polymers with dispersed fillers are obtained by this method only when the solvent is a component thereof (paints, enamels, etc.).

At the same time, mixing of filler with polymer melt is the most common in the polymer composites industry. High quality of filler dispersion in the absence of any additional auxiliary additives levels out the disadvantages in the form of high energy consumption and expensive high-tech equipment.

Summary

Thus, polylactide films obtained by compression molding are an order of magnitude better charged in unipolar corona discharge than films obtained by the solution casting. After 20 days of storage, the values of electret characteristics of samples obtained by different methods become of the same order, but the electret properties of molded samples are still slightly higher than those of samples cast from solution.

The difference in the electret properties of different PLA samples is due to the presence of polar liquid molecules (chloroform, water) in its volume, the presence of which increases the values of electrical conductivity of the samples.

The compositions of PLA with fillers obtained by the method of mixing the filler with the polymer melt show a tendency to increase the values of electret parameters of PLA when dispersed



particles are added. The improvement in electret characteristics of PLA when bringing in the fine particles is explained by formation of structural defects acting as traps for charge carriers, decrease of segmental mobility of PLA macromolecules at the surface of filler particles and appearance of macrodipoles with increased concentration of charged hydroxyl groups, the role of which is played by dispersed filler particles.

The PLA-filler compositions obtained by solution casting generally exhibit low electret characteristics.

The PLA composition with 4 % content of hydrated silicon dioxide (white silica) exhibits the best electret properties. In order to create the preservation of high level of values of electret properties of polylactide, it is recommended to anneal the polymer before charging and to prevent the contact of the produced electrets from the action of air moisture during operation.

REFERENCES

1. Auras R. A., Lim L.-T., Selke S. E. M., Tsuji H. (Eds.), Poly (lactic acid): synthesis, structures, properties, processing, applications, and end of life (Wiley Series on Polymer Engineering and Technology), John Wiley & Sons, Inc., Hoboken, New Jersey, USA, 2022.
2. Zhang J., Chen G., Bhat G. S., et al., Electret characteristics of melt-blown polylactic acid fabrics for air filtration application, *J. Appl. Polym. Sci.* 137 (4) (2020) 48309.
3. Yu B., Han J., Sun H., et al., The preparation and property of poly (lactic acid)/tourmaline blends and melt-blown nonwoven, *Polym. Compos.* 36 (2) (2015) 264–271.
4. Swetha T. A., Bora A., Mohanrasu K., et al., A comprehensive review on polylactic acid (PLA) – Synthesis, processing and application in food packaging, *Int. J. Biolog. Macromol.* 234 (15 April) (2023) 123715.
5. Gong S., Zhang B., Zhang J., et al., Biocompatible poly(lactic acid)-based hybrid piezoelectric and electret nanogenerator for electronic skin applications, *Adv. Funct. Mater.* 30 (14) (2020) 1908724.
6. Dali O. B., Zhukov S., Chadda R., et al., Eco-friendly high-sensitive piezoelectrets for force myography, *IEEE Sens. J.* 23 (3) (2022) 1943–1951.
7. Qin Y., Ma X., Ruan Z., et al., Improvement of thermal stability of charges in polylactic acid electret films for biodegradable electromechanical sensors, *ACS Appl. Mater. Interfaces.* 16 (45) (2024) 62680–62692.
8. Sessler G. M., Electrets, 3rd ed., Laplacian Press, Morgan Hill, California, USA, 1999.
9. Viraneva A., Yovcheva T., Mekishev G., Pressure effect on the polymer electret films, *IEEE Trans. Dielectr. Electr. Insul.* 20 (5) (2013) 1882–1886.
10. Guzhova A. A., Galikhanov M. F., Kuznetsova N. V., et al., Effect of polylactic acid crystallinity on its electret properties, *AIP Conf. Proc.* 1767 (1) (2016) 020009.
11. Cai C., Tang G., Song G., et al., Preparation and properties of nano-SiO₂ electret/PLA composite melt-blown nonwovens, *Acta Mater. Compos. Sin.* 34 (3) (2017) 486–493.
12. Platko A., Sotova Yi., Gorokhovatskiy Ya., et al., Electret effect in biodecomposed polylactide films filled with nanoscale magnesia, *St. Petersburg State Polytechnical University Journal: Physics and Mathematics.* 11(1) (2018) 19 –24.
13. Galikhanov M., Guzhova A., Zagidullina I., Improvement of electret properties of polylactide by loading mineral fillers, *IEEE Dielectr. Electr. Insul.* 29 (3) (2022) 784–787.
14. Ma X., Zhukov S., von Seggern H., et al., Biodegradable and bioabsorbable polylactic acid ferroelectrets with prominent piezoelectric activity, *Adv. Electron. Mater.* 9 (3) (2023) 2201070.
15. Flachs D., Zhukov S., Zech I., et al., Enzymatic self-degradable PLA-based electrets, *J. Polym. Environm.* 32 (8) (2024) 3922–3932.
16. Sazhin B. I., Lobanov A. M., Romanovskaya O. S., et al., Elektricheskiye svoystva polimerov [Electrical properties of polymers] 3d ed., Khimiya Publishing, Leningrad, 1986 (in Russian).
17. Akhmedov F. I., Electrophysical properties of composites on the base of nonpolar polypropylene and polar polyvinylidene fluoride filled with alumina // *Physics and Chemistry of Materials Treatment.* (5) (2016) 71–76 (in Russian).
18. Sheka E. F., Markichev I. V., Natkaniec I., Khavryuchenko V. D., Technological polymorphism of dispersed amorphous silicas: neutron inelastic scattering on vibrations and computer modeling, *Phys. Part. Nuclei.* 27 (2) (1996) 204–233.

СПИСОК ЛИТЕРАТУРЫ

1. Auras R. A., Lim L.-T., Selke S. E. M., Tsuji H. (Eds.) Poly (lactic acid): synthesis, structures, properties, processing, applications, and end of life (Wiley Series on Polymer Engineering and Technology). Hoboken, New Jersey, USA: John Wiley & Sons, Inc., 2022. 688 p.
2. Zhang J., Chen G., Bhat G. S., Azari H., Pen H. Electret characteristics of melt-blown polylactic acid fabrics for air filtration application // *Journal of Applied Polymer Science*. 2020. Vol. 137. No. 4. P. 48309.
3. Yu B., Han J., Sun H., Zhu F., Zhang Q., Kong J. The preparation and property of poly (lactic acid)/tourmaline blends and melt-blown nonwoven // *Polymer Composites*. 2015. Vol. 36. No. 2. Pp. 264–271.
4. Swetha T. A., Bora A., Mohanrasu K., Balaji P., Raja R., Ponnuchamy K., Muthusamy G., Arun A. A comprehensive review on polylactic acid (PLA) – Synthesis, processing and application in food packaging // *International Journal of Biological Macromolecules*. 2023. Vol. 234. 15 April. P. 123715.
5. Gong S., Zhang B., Zhang J., Wang Z., Ren K. Biocompatible poly(lactic acid)-based hybrid piezoelectric and electret nanogenerator for electronic skin applications // *Advanced Functional Materials*. 2020. Vol. 30. No. 14. P. 1908724.
6. Dali O. B., Zhukov S., Chadda R., Kasanski A., von Seggern H., Zhang X., Sessler G. M., Kupnik M. Eco-friendly high-sensitive piezoelectrets for force myography // *IEEE Sensors Journal*. 2022. Vol. 23. No. 3. Pp. 1943–1951.
7. Qin Y., Ma X., Ruan Z., Xiang X., Shi Z., Zhou L., Hu Q., Zhang X. Improvement of thermal stability of charges in polylactic acid electret films for biodegradable electromechanical sensors // *ACS Applied Materials & Interfaces*. 2024. Vol. 16. No. 45. Pp. 62680–62692.
8. Электреты. Под ред. Сесслера Г. Пер. с англ. Серия: Проблемы прикладной физики. М.: Мир, 1983. 488 с.
9. Viraneva A., Yovcheva T., Mekishev G. Pressure effect on the polymer electret films // *IEEE Transactions on Dielectrics and Electrical Insulation*. 2013. Vol. 20. No. 5. Pp. 1882–1886.
10. Guzhova A. A., Galikhanov M. F., Kuznetsova N. V., Petrov V. A., Khairullin R. Z. Effect of polylactic acid crystallinity on its electret properties // *AIP Conference Proceedings*. 2016. Vol. 1767. No. 1. P. 020009.
11. Cai C., Tang G., Song G., Zhao L., Chen L. Preparation and properties of nano-SiO₂ electret/PLA composite melt-blown nonwovens // *Acta Materiae Compositae Sinica*. 2017. Vol. 34. No. 3. Pp. 486–493.
12. Платко А. П., Сотова Ю. И., Гороховатский Ю. А., Карулина Е. А., Галиханов М. Ф. Электретный эффект в биоразлагаемых полимерных пленках полилактида с наноразмерным оксидом магния в качестве наполнителя // *Научно-технические ведомости СПбГПУ. Физико-математические науки*. 2018. Т. 11. № 1. С. 26–33.
13. Galikhanov M., Guzhova A., Zagidullina I. Improvement of electret properties of polylactide by loading mineral fillers // *IEEE Transactions on Dielectrics and Electrical Insulation*. 2022. Vol. 29. No. 3. Pp. 784–787.
14. Ma X., Zhukov S., von Seggern H., Sessler G. M., Ben Dali O. B., Kupnik M., Dai Y., He P., Zhang X. Biodegradable and bioabsorbable polylactic acid ferroelectrets with prominent piezoelectric activity // *Advanced Electronic Materials*. 2023. Vol. 9. No. 3. P. 2201070.
15. Flachs D., Zhukov S., Zech I., Schreck T., Belle S., von Seggern H., Kupnik M., Altmann A. A., Thielemann C. Enzymatic self-degradable PLA-based electrets // *Journal of Polymers and the Environment*. 2024. Vol. 32. No. 8. Pp. 3922–3932.
16. Сажин Б. И., Лобанов А. М., Романовская О. С., Эйдельмант М. П., Койков С. Н., Шуваев В. П., Борисова М. Э. Электрические свойства полимеров. 3-е изд. Ленинград: Химия. Ленингр. отделение, 1986. 224 с.
17. Ахмедов Ф. И. Электрофизические свойства композитов на основе неполярного полипропилена и полярного поливинилиденфторида, наполненных оксидом алюминия // *Физика и химия обработки материалов*. 2016. № 5. С. 71–76.

18. Шека Е. Ф., Маркичев И. В., Натканец И., Хаврюченко В. Д. Технологический полиморфизм дисперсных аморфных кремнеземов: неупругое рассеяние нейтронов на колеблющихся атомах и компьютерное моделирование // Физика элементарных частиц и атомного ядра. 1996. Т. 27. № 2. С. 423–560.

THE AUTHOR

ZAGIDULLINA Inna A.

Kazan National Research Technological University
68 Karl Marx St., Kazan, the Republic of Tatarstan, 420015, Russia
zagidullina_inna@mail.ru
ORCID: 0000-0002-5736-6957

GUZHOVA Alina A.

Kazan National Research Technological University
68 Karl Marx St., Kazan, the Republic of Tatarstan, 420015, Russia
alina_guzhova@mail.ru
ORCID: 0000-0003-4354-8984

KARULINA Elena A.

Herzen State Pedagogical University of Russia
48 Moyka Emb., St. Petersburg, 191186, Russia
karulina@mail.ru
ORCID: 0000-0001-9604-4769

KULEMINA Sofya M.

Herzen State Pedagogical University of Russia
48 Moyka Emb., St. Petersburg, 191186, Russia,
sonia.kulemina@yandex.ru
ORCID: 0009-0002-3569-498

СВЕДЕНИЯ ОБ АВТОРЕ

ЗАГИДУЛЛИНА Инна Александровна — кандидат технических наук, доцент кафедры технологии переработки полимеров и композиционных материалов ФГБОУ ВО «Казанский национальный исследовательский технологический университет», г. Казань, Республика Татарстан, Россия. 420015, Россия, Республика Татарстан, г. Казань, ул. К. Маркса, 68
zagidullina_inna@mail.ru
ORCID: 0000-0002-5736-6957

ГУЖОВА Алина Альбертовна — кандидат технических наук, доцент кафедры иностранных языков для профессиональной коммуникации ФГБОУ ВО «Казанский национальный исследовательский технологический университет», г. Казань, Республика Татарстан, Россия. 420015, Россия, Республика Татарстан, г. Казань, ул. К. Маркса, 68
alina_guzhova@mail.ru
ORCID: 0000-0003-4354-8984

КАРУЛИНА Елена Анатольевна — кандидат физико-математических наук, доцент кафедры общей и экспериментальной физики Российского государственного педагогического университета имени А. И. Герцена, Санкт-Петербург, Россия. 191186, Россия, г. Санкт-Петербург, наб. р. Мойки, 48
karulina@mail.ru
ORCID: 0000-0001-9604-4769

КУЛЕМИНА Софья Михайловна — аспирантка кафедры общей и экспериментальной физики Российского государственного педагогического университета имени А. И. Герцена, Санкт-Петербург, Россия.

191186, Россия, г. Санкт-Петербург, наб. р. Мойки, 48

sonia.kulemina@yandex.ru

ORCID: 0009-0002-3569-498

Received 05.01.2025. Approved after reviewing 28.01.2025. Accepted 28.01.2025.

Статья поступила в редакцию 05.01.2025. Одобрена после рецензирования 28.01.2025. Принята 28.01.2025.

Original article

DOI: <https://doi.org/10.18721/JPM.18209>

AN ELECTRICAL LIFETIME OF POLYMERS IN TERMS OF THE CATASTROPHE THEORY

V. V. Kiselevich[✉]

Gomel State Technical University named after P. O. Sukhoi, Gomel, Belarus

[✉] valentinkis@list.ru

Abstract. The present study analyzes the known expressions establishing exponential and power relationships between the lifetime of polymer dielectrics and the strength of the electric field acting on them. The work notes the necessity of mathematical substantiation of the known power expression for the field dependence of electrical lifetime. We obtained the equation of dependence of the electrical lifetime of polymeric dielectrics on the value of the applied electric field strength within the framework of the mathematical catastrophe theory. The study has the performance of quantitative estimation of the parameters of this equation for paper, epoxy and polyethylene terephthalate electrical insulation. We established a good agreement between the literature experimental data and the field dependences of the electrical lifetime of polymers plotted by the proposed equation. The study analyses geometric images of the fold catastrophe function reflecting the nature of the change in the dimensionless parameter of the rate of damage accumulation in a polyethylene terephthalate film under varying electric field strength. The paper shows the prospect of using the mathematical apparatus of catastrophe theory to describe experimental regularities of changes in the electrical strength properties of polymer dielectrics in strong electric fields.

Keywords: polymer dielectric, electrical lifetime, electrical breakdown, electric field strength, catastrophe theory, fold catastrophe.

Citation: Kiselevich V. V., An electrical lifetime of polymers in terms of the catastrophe theory, St. Petersburg State Polytechnical University Journal. Physics and Mathematics. 18 (2) (2025) 93–108. DOI: <https://doi.org/10.18721/JPM.18209>

This is an open access article under the CC BY-NC 4.0 license (<https://creativecommons.org/licenses/by-nc/4.0/>)

Научная статья
УДК 621.315.61: 51-74
DOI: <https://doi.org/10.18721/JPM.18209>

ЭЛЕКТРИЧЕСКАЯ ДОЛГОВЕЧНОСТЬ ПОЛИМЕРОВ С ТОЧКИ ЗРЕНИЯ ТЕОРИИ КАТАСТРОФ

В. В. Киселевич[✉]

Гомельский государственный технический университет имени П. О. Сухого,
г. Гомель, Беларусь

[✉] valentinkis@list.ru

Аннотация. В рамках математической теории катастроф получено уравнение зависимости электрической долговечности полимерных диэлектриков от величины напряженности приложенного электрического поля. Выполнена количественная оценка параметров данного уравнения для бумажной, эпоксидной и полиэтилентерефталатной электроизоляции. Установлено хорошее согласие между опубликованными экспериментальными данными и полевыми зависимостями электрической долговечности полимеров, построенными по предложенному уравнению. Проанализированы геометрические образы функции катастрофы складки, отражающие характер изменения безразмерного параметра скорости накопления повреждений в пленке полиэтилентерефталата при варьировании напряженности электрического поля.

Ключевые слова: полимерный диэлектрик, электрическая долговечность, электрический пробой, напряженность электрического поля, теория катастроф, катастрофа складки.

Ссылка для цитирования: Киселевич В. В. Электрическая долговечность полимеров с точки зрения теории катастроф // Научно-технические ведомости СПбГПУ. Физико-математические науки. 2025. Т. 18. № 2. С. 93–108. DOI: <https://doi.org/10.18721/JPM.18209>

Статья открытого доступа, распространяемая по лицензии CC BY-NC 4.0 (<https://creativecommons.org/licenses/by-nc/4.0/>)

Introduction

Insulation of operating high-voltage electrical equipment is exposed to strong electric fields. The destructive effect of the field eventually leads to insulation breakdown, which is one of the main reasons for premature failure of most high-voltage electrical equipment [1–3]. Therefore, it is extremely important to understand the patterns of dielectric breakdown and find ways to prevent [4, 5], especially as increasingly stringent requirements are imposed on high-voltage equipment [6, 7].

It has been established that electrical degradation of polymer materials is kinetic in nature and is a process of gradual accumulation of damage to macromolecules, after which the material completely loses its insulating properties, i.e., electrical breakdown occurs [4, 8]. The main parameter characterizing the electrical strength properties of polymer dielectrics is the electrical lifetime, which is the time period from the beginning of voltage application to the dielectric until its breakdown [9, 10]. Studies on the behavior of dielectrics in strong electric fields focus closely on the variation in electrical lifetime for samples with different thickness [10, 11], ambient temperature [12–14] and applied field strength [3, 15, 16].

The field dependences of electrical lifetime are typically described using exponential [2, 9, 10, 16] and inverse power [1–3, 17] laws. Application of the exponential law to model the field dependence of the electrical lifetime in polymers is directly related to the physical process of damage accumulation in the polymers exposed to electric fields (thermally activated decomposition of molecular ions), since the speed of this process exponentially depends on the strength of this



field [8, 18]. In addition to providing a rigorous theoretical framework, exponential expressions ensure high accuracy of the obtained values of electrical lifetime [4, 10, 16].

Power laws have become widespread for evaluating the lifetime of polymer materials as part of technical tests [16]. However, despite the mathematical simplicity of the power expressions, their use for modeling the field dependences of the electrical lifetime of polymers has no physical justification. Some studies [19, 20] describe the experimental field dependences of electrical lifetime by relations representing a superposition of exponential and power laws. An increased number of significant parameters in such composite relations, on the one hand, contributes to increased accuracy of determining the electrical lifetime. On the other hand, this also complicates the form of these relations [21–23], consequently reducing their practical value.

Approaches from catastrophe theory [24] may provide a solution to this problem, as the phenomenological nature of this theory allows to obtain fairly simple mathematical expressions reflecting the behavior of physical and technical systems of different complexity with variable control parameters characterizing these systems. An important argument in favor of using methods of catastrophe theory to study the electrical properties of polymers is the sudden onset of breakdown in polymer dielectrics and its catastrophic nature [25]. Relatively few studies consider the degradation of polymer materials using the mathematical framework of catastrophe theory [26–29]; as a matter of fact, we have not managed to uncover any works applying this theory to describe the field dependence of electrical lifetime of polymers. We believe that filling this gap is of great scientific and practical importance.

The goal of this study is to better understand the influence of electric field strength on the lifetime of polymer dielectrics.

Catastrophe theory was used to achieve this goal. Our primary objective was to formulate an equation describing the dependence of electrical lifetime in polymer dielectrics on the strength of the applied electric field, determining the parameters of this equation for widely used dielectrics: paper, epoxy and polyethylene terephthalate (PET) insulation.

Problem statement

A key manifestation of the kinetic nature of electrical breakdown in polymers is that their lifetime t_{br} significantly depends on the strength E of the applied electric field [8, 10]. For this

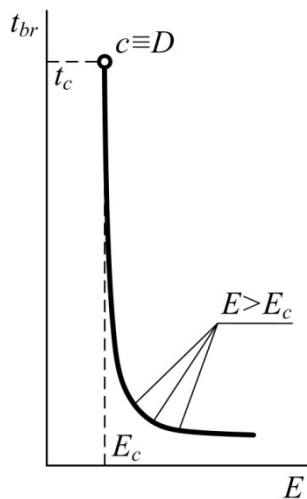


Fig. 1. Characteristic field dependence of electrical lifetime of polymer dielectrics t_{br} ; E_c is the value of E at which t_{br} significantly exceeds the experimental period; t_c is the value of t_{br} for $E = E_c$; the identity $c \equiv D$ expresses the correspondence between the physical critical point c and the degenerate mathematical point D (see the explanations in the text)

reason, a large number of studies on the electrical strength properties of polymer dielectrics are focused on obtaining the field dependence $t_{br} = f(E)$ of electrical lifetime.

In practice, the relationship $t_{br} = f(E)$ is established by conducting a series of experiments to measure the lifetime t_{br} at various fixed strengths $E = U/d$, where U is either a DC or AC voltage applied to a dielectric sample with a thickness D . In the case of tests in an AC electric field, the amplitude or RMS value of AC voltage is generally taken as the value of U [3, 4].

The lifetime of polymers placed in an AC electric field is approximately two orders of magnitude less than t_{br} for a DC field [4]. Meanwhile, experimental field dependences of electrical lifetime, measured in DC and AC electric fields, demonstrate almost identical behavior [2–4, 9, 10], which makes it possible to study the general patterns in their variation from a unified perspective. A typical dependence $t_{br} = f(E)$ whose behavior is consistent with known experimental data is shown in Fig. 1.

It can be seen that when the dielectric is in a field with the strength $E > E_c$, there is an inversely proportional relationship between t_{br} and E .

Fig. 1 shows the field strength E_c for which the estimated breakdown time t_{br} (the lifetime of the dielectric) significantly exceeds the duration of the experiment. Experiments to determine the lifetime are usually carried out at field strengths that ensure the detection of dielectric breakdown in the time range from 1 to 10^6 s [30]. In view of this, the value of E_c can range from a few to tens of MV/m, depending on the type and quality of the polymer dielectric sample, as well as its testing conditions [1–3]. The threshold strength of the working electric field [3, 31] corresponding to the given lifetime of the dielectric material can be used as E_c in a first approximation.

For small values of the applied field strength, when $E \approx E_c$ (see Fig. 1), we can observe a stronger field dependence for $t_{br} = f(E)$, so consequently, the lifetime $t_{br} = t_c$ becomes rather long, theoretically tending to infinity. The reason for this behavior of the function $t_{br} = f(E)$ is that the damage accumulation rate for $E \approx E_c$ is so low that a slight destructive effect of the electric field does not cause breakdown of the polymer dielectric at all and it retains its insulating properties for a long time.

Modeling the variation in the lifetime of dielectric materials with varying electric field strength accounting for the physical mechanism of damage accumulation in the dielectric produces an exponential field dependence $t_{br} = f(E)$. For polymer dielectrics, this dependence was obtained in the following form [18, 30]:

$$t_{br} = t_0 \exp\left(\frac{W^+ - el_0 qE}{k_B T}\right), \quad (1)$$

where t_0 , s, is a pre-exponential factor representing the vibrational frequency of atoms in solids, $t_0 \approx 10^{-13} - 10^{-12}$ s; W^+ , J, is the bond dissociation energy of molecular ions; e , C, is the electron charge; l_0 , m, is the activation length; q is the overvoltage factor characterizing the enhancement in field strength near irregularities on the electrodes; k_B , J/K, is the Boltzmann constant; T , K, is the temperature.

Accumulation of damage that can lead to dielectric breakdown is attributed in [18, 30] to a two-stage process of decomposition of polymer macromolecules in an electric field. At the first stage, field ionization of macromolecules occurs with the formation of positive molecular ions (macro-ions) with reduced bond dissociation energy [8, 18]. At the second stage, decomposition of macro-ions activated by thermal fluctuations occurs, accompanied by the formation of new macro-ions and chemically active free macroradicals [8, 18]. The gradual accumulation of defects (damage) during the decomposition of macromolecules leads to an increase in the concentration of charge carriers (quasi-free electrons and holes); reaching a critical concentration N_c is what causes breakdown [4, 8]. Varying the electric field strength allows to control the kinetics of accumulation of the concentration N_c , and consequently to vary the electrical lifetime of polymers [4, 8].

Exponential equation (1), obtained within the framework of the physical model [18], yields highly accurate theoretical values of the lifetime t_{br} agreeing well with the experimental data for a wide range of polymer dielectrics [9, 10].

Along with analytical expressions similar to Eq. (1), an empirical dependence of the form [2] is often used in practice to reflect the quantitative relationship between t_{br} and E observed in strong electric fields:

$$t_{br} = a(E - E_c)^{-b}, \quad (2)$$

where a , b are parameters depending on the type of insulation.

The simple mathematical form of power expression (2) was the main reason for its widespread use for estimating t_{br} during technical tests of polymer insulation [3, 16], which do not allow for accurate experimental design. It was found in [2, 3] that the use of the power dependence (2), firstly, is not physically justified, and, secondly, leads to a mathematical abstraction $t_{br} \rightarrow \infty$ at $E = E_c$, although in reality the period from the time when voltage is applied to the dielectric until the start of breakdown is finite.

Based on this, it is important to obtain an analytical equation for the field dependence $t_{br} = f(E)$, free from the above-mentioned disadvantages of expression (2). To solve it, we use the methods of catastrophe theory [24].



Fundamentals of catastrophe theory

To study physical systems in the theory of catastrophes, potential functions Φ (catastrophe functions) are used, whose type is determined by the number n of state variables x and the number k of control parameters A . The variables x characterizing the state of the system considered depend on the control parameters A . A smooth variation of A can correspond to both continuous and abrupt (catastrophic) variation of x . That is why the system's abrupt response to smooth variation in its control parameters is called a catastrophe.

At $k > 3$, mathematical description of catastrophes becomes rather cumbersome and it is difficult to visually represent the geometric characteristics of potential functions Φ . For many practical applications, it is sufficient to confine the consideration to considering catastrophe functions with one state variable and a number of control parameters not exceeding three. The well-known expression for the catastrophe function Φ with one state variable x has the following form [24]:

$$\Phi(x; A_i) = x^{k+2}/(k+2) + \sum_{i=1}^k A_i x^i/i, \quad (3)$$

where i is the number of the control parameter A , $i \in [1, k]$; $k = 1, 2$, and 3 for fold, cusp and swallowtail catastrophes, respectively.

Qualitative changes in the system considered are determined by the number and type of critical points of the catastrophe function. Therefore, the basis of catastrophe theory is analysis of the behavior of the function Φ in the vicinity of critical points. The positions of the critical points and the values of the function Φ at these points are determined by solving the equations obtained by equating its derivatives with respect to the state variable x to zero [24]:

$$\partial\Phi/\partial x = 0; \partial^2\Phi/\partial x^2 \neq 0; \quad (4)$$

$$\partial\Phi/\partial x = 0; \partial^m\Phi/\partial x^m = 0, \quad (5)$$

where m is the order of the derivative, $m \in [2, k+1]$.

The points found from conditions (4) are called non-degenerate critical points; in physical applications, the mathematical term 'non-degenerate critical point' corresponds to the definition of an equilibrium point. The solutions of Eqs. (5) correspond to degenerate critical points with the degree of degeneracy m , which are identical to physical critical points [24]. Degenerate critical points are more informative than non-degenerate ones, since it is in the vicinity of degenerate points that there is a high probability of a jump in the state of the system considered, i.e., the start of a catastrophe.

Catastrophe theory is concerned with variation in the equilibrium states $x(A_i)$ of the potential function $\Phi(x; A_i)$, given by Eq. (4), with varying control parameters A_i .

Catastrophe theory operates with dimensionless mathematical parameters, i.e., numbers that can take both positive and negative values. Therefore, to use this theory for physical applications, it is necessary to match the dimensionless mathematical parameters included in Eq. (3) with the dimensional quantities characterizing a particular physical process. The transition from dimensional physical quantities x' and A'_i to the corresponding dimensionless mathematical parameters x and A_i is carried out using normalization relations [24]:

$$x = x'/x_D - 1; A_i = A'_i/A'_{D(i)} - 1, \quad (6)$$

where x' is the physical state variable; A'_i is the i th physical control parameter; x_D , $A'_{D(i)}$ are the critical parameters of the catastrophe function, understood as the values of the quantities x' and A'_i at the physical critical point corresponding to the mathematical point D_{k+1} .

The point D_{k+1} is the point with the greatest degeneracy $m_{\max} = k + 1$ (for fold, cusp, and swallowtail catastrophes, the degree of degeneracy m_{\max} is 2, 3, and 4, respectively).

A bias term equal to unity is included in expressions (6), so consequently, when the physical quantities x' and A'_i reach the critical values x_D and $A_{D(i)}$, the mathematical parameters x and A_i take zero values. Because of this, the degenerate critical points D_2 , D_3 and D_4 , which are the germs of the fold, cusp and swallowtail catastrophes, are always located at the origin, greatly simplifying the analysis of these catastrophes.

It is advisable to analyze physical systems, processes or phenomena (referred to as systems from now on) in accordance with catastrophe theory by the following algorithm.

Step 1. Set the state variable x' and the control parameters A'_i , describing the physical system in question.

Step 2. Based on the known experimental and theoretical data describing the behavior of variable x' , determine the general trends in its variation with varying parameters A'_i .

Step 3. Identify the characteristic attributes, the so-called catastrophe flags [24], which can be used to conclude that a catastrophe has occurred in the given system.

Step 4. Establish the event identified as catastrophe and determine the critical parameters x_D and $A_{D(i)}$, upon reaching which the most characteristic transformations of the system are clearly detected.

Step 5. Based on the relationship between x and A_i resulting from Eqs. (3) and (4) and on analysis of the dependence of x' on A'_i performed in step 2, match the dimensionless parameters x and A_i with the dimensional physical quantities x' and A'_i .

Step 6. Applying relations (6), we reduce the quantities x' and A'_i to a dimensionless form and, starting from general expression (3), write the equation of the function Φ modeling the given system. Based on the correspondence between x , A_i and x' , A'_i , adopted in step 5, and considerations of algebraic convenience, multipliers can be introduced into the equation obtained for the catastrophe function to change the scale and reverse the sign of mathematical parameters.

Step 7. Determine the number and type of critical points of the catastrophe function Φ as well as analyze the geometric properties of the function Φ and its derivatives.

Step 8. Using conversion relations (6), represent the equation $\partial\Phi/\partial x = 0$ in physical terms and reduce it to the required dependence $x' = f(A'_i)$.

For consistency with the above algorithm, below we derive the equation describing the field dependence $t_{br} = f(E)$ of the electrical lifetime of polymer dielectrics.

Theoretical analysis of behavior of dielectric in strong electric field

First, we define the physical parameters of state and control that determine the electrical properties of the polymer dielectric at constant temperature. Initially, we take the electrical durability t_{br} as a state variable and the electric field strength E applied to the dielectric as a physical control parameter.

Next, we identify the flags indicating the possibility of a catastrophe in the dielectric exposed to a strong electric field.

The first flag for catastrophe is a critical charge concentration N_c accumulating in a time equivalent to the electrical lifetime t_{br} of the polymer dielectric. Experiments conducted in [4, 8], establishing this dependence found that $N_c \approx 10^{18} - 10^{19} \text{ cm}^{-3}$.

The second flag for catastrophe is the anomalous variance of experimental values of the electrical lifetime t_{br} , observed when low strengths comparable to E_c are applied to the dielectric. Indeed, as noted above, the field dependence $t_{br} = f(E)$ is considerably enhanced for $E \approx E_c$, in fact degenerating into an almost vertical straight line (see Fig. 1). Small variations in E near E_c lead to large variations in the lifetime t_{br} , so consequently, in practice, there is a large variance in the values of t_{br} measured at $E \approx E_c$ [1–3].

An event equivalent to the start of a mathematical catastrophe is the time when a critical concentration of damage is accumulated (which is equivalent to reaching N_c) in the polymer dielectric located in a field with the strength E_c . The point c in Fig. 1, in whose vicinity the field dependence of electrical lifetime becomes degenerate, is considered as the physical critical point. Then, following the above algorithm, we match the physical critical point c with the degenerate mathematical point D . Then the physical parameters t_c and E_c matched with point c become equivalent to the critical parameters of the catastrophe function: $t_c \equiv t_D$ and $E_c \equiv E_D$.

To describe the system considered (with one control parameter), we use equation for the fold catastrophe, which follows from the general expression (3) for $k = 1$ [24]:



$$\Phi(x; A_1) = x^3/3 + A_1 x. \quad (7)$$

It follows from Eq. (7) that the mathematical control parameter A_1 is proportional to the square of the state variable x : $A_1 \sim -x^2$. Therefore, in view of the proportionality $1/t_{br} \sim E^b$, characteristic for physical quantities t_{br} and E , it is convenient to take the field strength E as the state variable instead of the lifetime t_{br} . The quantity $\nu_{br} = 1/t_{br}$, inverse to electrical lifetime, is taken to be a physical control parameter in further analysis within the framework of catastrophe theory. The critical value ν_{br} in this case is determined by the equality $\nu_D = 1/t_D$. According to the definition in [9], the parameter ν_{br} characterizes the damage accumulation rate, i.e., the rate at which the polymer dielectric reaches breakdown.

The physical parameters of state x' and control A' can be interchangeable. As this may be necessary in situations such as ours (parameters t_{br} and E), when the parameters are substituted into the catastrophe equation, it is one of the advantage of the given approach. Moreover, such substitution is valid even when the physical quantity taken as a control parameter, i.e., an independent variable, cannot be directly varied in the real experiment (in this case, it is the electrical lifetime t_{br}), since mathematically, it makes little difference which dependence is considered in practice: $x' = f(A')$ or $A' = f(x')$.

Next, using normalization relations (6), we reduce the dimensional physical quantities E and ν_{br} to dimensionless form:

$$F_E = E/E_D - 1; \nu = \nu_{br}/\nu_D - 1 = t_D/t_{br} - 1, \quad (8)$$

where F_E is the dimensionless electric field strength (mathematical state variable); ν is the dimensionless damage accumulation rate (mathematical control parameter).

Taking $x = F_E$ and $A_1 = -a_i \nu$, we obtain from Eq. (7) an expression for the fold catastrophe function characterizing the state of the polymer dielectric in a strong electric field:

$$\Phi(F_E; \nu) = F_E^3/3 - a_i \nu F_E, \quad (9)$$

where a_i is the positive scale factor introduced for better visual representation of the geometric characteristics of the function Φ . The minus sign for a_i is taken for convenience of further analysis of the function Φ .

Equating the first and second derivatives of function (9) with respect to the variable F_E to zero, we write the equations determining the position of the critical points of this function:

$$\partial\Phi/\partial F_E = F_E^2 - a_i \nu = 0; \quad (10)$$

$$\partial^2\Phi/\partial F_E^2 = 2F_E = 0. \quad (11)$$

Since $a_i > 0$, Eq. (10) has no solutions for $\nu < 0$, and therefore, the catastrophe function $\Phi(F_E; \nu)$ has no critical points. Eq. (10) has one root $F_E = 0$ for $\nu = 0$ and the function $\Phi(F_E; \nu)$ has one critical point, a bifurcation point located at the origin. As Eqs. (10) and (11) are fulfilled simultaneously for $\nu = 0$, this critical point is doubly degenerate. If $\nu > 0$, Eq. (10) has two opposite roots: $F_E = \pm(a_i \nu)^{1/2}$, while the function $\Phi(F_E; \nu)$ has two non-degenerate critical points: a minimum point at $F_E > 0$ and a maximum point at $F_E < 0$.

Using conversion expressions (8), we write the relations that establish the correspondence between the characteristic values of dimensionless mathematical parameters (F_E , ν) and dimensional physical quantities (E , t_{br}):

$$\begin{aligned} F_E < 0 &\Leftrightarrow E < E_D; F_E = 0 \Leftrightarrow E = E_D; F_E > 0 \Leftrightarrow E > E_D; \\ \nu < 0 &\Leftrightarrow t_{br} > t_D; \nu = 0 \Leftrightarrow t_{br} = t_D; \nu > 0 \Leftrightarrow t_{br} < t_D. \end{aligned} \quad (12)$$

Accounting for relations (12) and analyzing the results of Eqs. (9)–(11), we reached the following conclusions.

In the case when the electric field with the strength $E < E_D$ is applied to the dielectric, no electrical breakdown occurs, since the damage accumulation rate is low ($\nu < 0$) and the time to reach the critical concentration N_c exceeds t_D . As the field strength increases to the level $E > E_D$, a noticeable increase in the dimensionless accumulation rate ($\nu > 0$) is observed, as a result of which electrical breakdown of the dielectric occurs in the time $t_{br} < t_D$. The equality $E = E_D$, for which the field dependence $t_{br} = f(E)$ becomes degenerate, corresponds to the condition for the beginning of a catastrophe, i.e., reaching a critical value of N_c and breakdown of the dielectric during the time $t_{br} = t_D$.

Substituting relations (8) into Eq. (10), we obtain the final expression for the field dependence of electrical lifetime of the polymer dielectric:

$$t_{br} = \frac{t_D}{1 + a_i^{-1}(E/E_D - 1)^2}. \quad (13)$$

Eq. (13) holds true for $E \geq E_D$, i.e., when electrical breakdown of the dielectric occurs in a time not exceeding t_D . An advantage of Eq. (13) is its structure, ensuring a finite value for the electrical lifetime t_{br} of a field with the strength $E_D = E_c$ is applied to the dielectric.

Geometry of fold catastrophe

The profiles $\Phi = f(F_E)$ of the fold catastrophe function corresponding to the cases of variations in the dimensionless parameter ν discussed above are shown in Fig. 2. The numbers $l \in [1, 5]$ of the profiles in Fig. 2 correspond to the characteristic values ν_l of this parameter. Since $\nu_1 < \nu_2 < 0$, curves 1 and 2 have no critical points. Curve 3, constructed for $\nu_3 = 0$, has a degenerate bifurcation point D_2 at the origin. Since $\nu_5 > \nu_4 > 0$, profiles 4 and 5 of the function Φ have minimum and maximum points characterizing stable and unstable equilibrium states of the system.

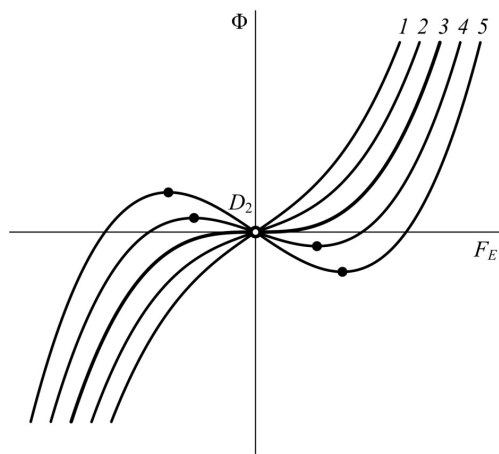


Fig. 2. Profiles of fold catastrophe function for different values of control parameter. Profile numbers correspond to the characteristic values of the parameter ν_1 – ν_5

Black dots mark the positions of minima and maxima, characterizing stable and unstable equilibrium states of the system; D_2 is a degenerate bifurcation point

As the mathematical control parameter increases from ν_1 to ν_5 , the profile of the function Φ gradually transforms, going through the following stages:

- curve is flattened near zero,
- degenerate point appears,
- degenerate point is split into a maximum and a minimum equidistant from it,
- amplitudes of these extrema further increase, the extrema keep diverging.

As the control parameter decreases from ν_5 to ν_1 , the maximum and minimum on the profile of the catastrophe function converge, merge, forming a degenerate critical point at the origin, and disappear. The doubly degenerate point D_2 in whose vicinity the bifurcation of solutions is detected, acts as the germ for the fold catastrophe.

The geometric locus of the critical points satisfying Eq. (10) is a parabola whose branches converge at point D_2 (Fig. 3,a). The set of critical values Φ_c of the catastrophe function, determined by substituting roots from Eq. (10) into Eq. (9), forms a wedge with the edge at D_2 (Fig. 3,b).

There is not a single equilibrium state to the left of the point D_2 and the branches of stable (1) and unstable (2) equilibrium states are located to its right, formed respectively by the minima and maxima of the catastrophe function Φ .

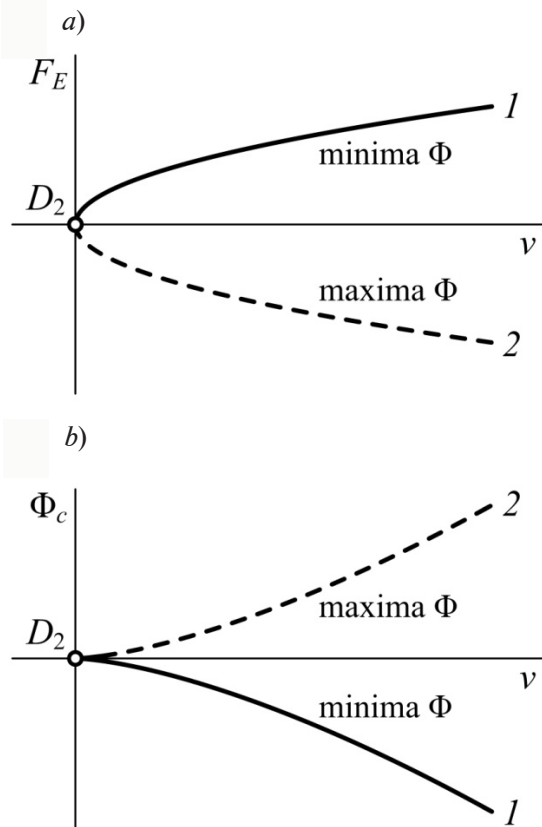


Fig. 3. Geometry of fold catastrophe: function of dimensionless damage accumulation rate (a) and critical value function (b). Branches of stable (1) and unstable (2) equilibrium states are shown, formed respectively by the minima and maxima of the catastrophe function Φ (see Fig. 2).

estimated electrical lifetime at a strength $E = E_D = 2.32$ MV/m turned out to be fairly long: $t_D = 29.23 \cdot 10^7$ s ≈ 9.27 years.

It follows from the profiles $\Phi = f(F_E)$ shown in Fig. 2 that an increase in the parameter ν causes a shift in the minimum/maximum of the function Φ to the region of larger positive/negative values of the state variable F_E and an increase in the amplitudes of these extrema. The result of this behavior of Φ is that when ν increases on stable branches of the dependences $F_E = f(\nu)$ and $\Phi_c = f(\nu)$ (see Fig. 3), F_E increases and Φ_c decreases. Conversely, F_E decreases and Φ_c increases on unstable branches of these dependences.

Results and discussion

The applicability of Eq. (13) was verified by processing the experimental data presented in [1–3, 31–33] for the field dependences of electrical lifetimes of insulating materials. The values of the parameters a_r , E_D and t_D obtained by this treatment are given in Table.

Analyzing the data in Table, we can conclude that insulators made of phenol formaldehyde laminate, oil-impregnated paper and PET film are characterized by much lower t_D values than those made of epoxy dielectrics. The reason for this is that the dependence $t_{br} = f(E)$ for epoxy samples was obtained in experiments performed at lower (compared to E_D) field strengths, resulting in slower defect accumulation in these dielectrics and, accordingly, longer electrical lifetime. For example, the field strength at which the test samples experienced breakdown in a time not exceeding the maximum test time (30,000 hours) was only 2.5 MV/m for the EZK-1 compound [33]. Therefore, the

Table

Parameter values of equation for field dependence of lifetime for several electrical insulators

Electrical insulator	Parameter of Eq. (13)		
	$a_r, 10^{-4}$	$E_D, \text{MV/m}$	$t_D, 10^7 \text{ s}$
Phenol formaldehyde laminate	2.3270	13.05	0.1094
Oil-impregnated paper	14.570	18.58	0.3507
PET film	22.180	24.16	0.0199
Epoxy resin	1.7910	4.59	1.0260
Epoxy compound EZK-1	0.9673	2.32	29.230

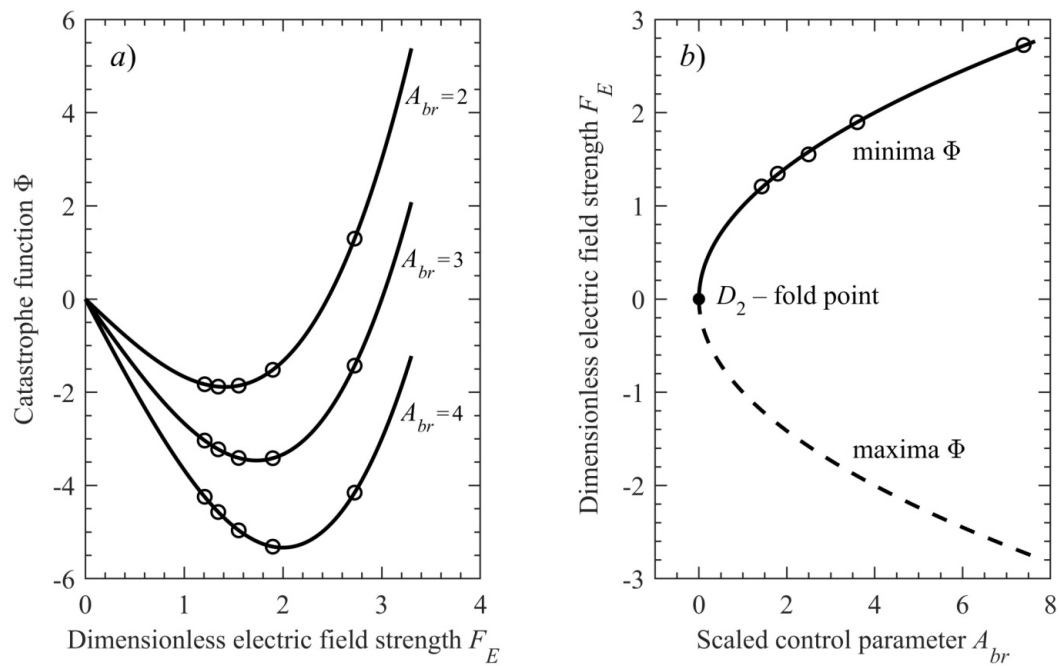


Fig. 4. Field dependences of fold catastrophe function $\Phi(a)$ and scaled damage accumulation rate $A_{br}(b)$ for PET film (experimental data (shown by symbols) are taken from [32]); approximating curves (solid lines) correspond to physically realizable states and the set of unstable states of the function Φ (dashed lines) does not appear in reality

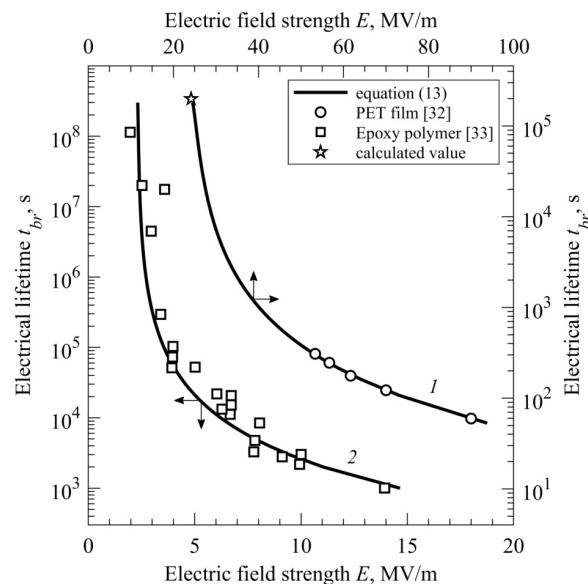


Fig. 5. Comparison of experimental (symbols) and theoretical (lines) field dependences of electrical lifetime of PET film (1) and epoxy compound (2)
 The asterisk indicates the calculated value of t_d for the PET film corresponding to the doubly degenerate mathematical point D_2 (see Fig. 4,b)



As an example, Fig. 4 shows the graphical dependences $\Phi = f(F_E)$ и $F_E = f(A_{br})$ for PET film, based on experimental data taken from [32]¹. A_{br} in Fig. 4 denotes a scaled control parameter equal to the product of dimensionless damage accumulation rate ν and the scale factor a_r , introduced earlier in Eq. (9): $A_{br} = a_r \nu$. The graphs constructed confirm an excellent agreement between the experimental data available in the literature and the approximating curve for the scaled damage accumulation rate A_{br} . The dashed line describing a decrease in the parameter A_{br} with an increase in the dimensionless strength F_E corresponds to a set of unstable states of the function Φ that does not occur in reality. The reason for this circumstance is that an increase in the field strength applied to the dielectric during the experiment leads to a decrease in the electrical lifetime t_{br} , equivalent to an increase in A_{br} .

The graph in Fig. 4, *a* clearly shows the trends in the behavior of the catastrophe function discussed above, namely: as the scaled parameter A_{br} increases, the minimum of the function Φ becomes deeper and shifts towards higher values of F_E . The decrease in A_{br} with a decrease in F_E (see Fig. 4, *b*) is consistent with the increase in electrical lifetime t_{br} observed in practice with a decrease in the strength E . The dimensionless parameter A_{br} becomes zero at point D_2 because t_{br} reaches the critical value t_D . Provided that $A_{br} < 0$, which is equivalent to the inequality $t_{br} > t_D$, the processes of electrical breakdown induced by the application of a weak electric field are slowed down and breakdown of the dielectric does not occur, even when the duration of the experiment significantly exceeds the critical value t_D .

The field dependences of electrical lifetime, constructed in accordance with Eq. (13) for PET film (curve 1) and epoxy compound EZK-1 (curve 2) in dimensional coordinates, are shown in Fig. 5. It can be seen that the solid curves 1 and 2 agree well with the experimental data [32, 33]. This confirms that Eq. (13) can be used to describe the field dependences $t_{br} = f(E)$ of polymer dielectrics. The asterisk in Fig. 5 indicates the calculated lifetime t_D for PET film corresponding to the doubly degenerate mathematical point D_2 .

Some discrepancies between curves 1 and 2 in Fig. 5 and the corresponding experimental points can be explained by the following reasons:

- large variance of experimental values of electrical lifetime determined for the same field strength;

- complicated procedures to account for the cumulative effect of various factors (for example, temperature, partial discharges, structural inhomogeneity, etc.) on electrical breakdown in real polymer dielectrics.

Finally, using analytical equation (1), we estimate the overvoltage factor q for PET film located in an electric field with the strength $E = E_D$. We take the following values of the physical parameters for the calculation:

$$t_0 = 10^{-13} \text{ s}, W^+ = 1.1 \text{ eV}, l_0 = 1.5 \text{ \AA} [8]; T = 293 \text{ K} [32];$$

$$E_D = 24.16 \text{ MV/m}, t_D = 0.0199 \cdot 10^7 \text{ s (see Table).}$$

As a result, we obtain the value of the factor $q \approx 9.7$, which suggests that the decomposition of molecular ions activated by thermal fluctuations is the mechanism prevailing over all other mechanisms behind electrical breakdown in PET films [32]. Two circumstances can serve to prove this hypothesis. First, according to the information in [18], at $q \approx 10$, favorable conditions are created in the polymer for field ionization of macromolecules, which (as noted above) is the first stage of the two-stage decomposition process of these macromolecules in a strong electric field [8, 18]. Secondly, the field dependence $t_{br} = f(E)$ was measured in [32] at a temperature of 293 K, when thermal breakdown is extremely unlikely to occur [34, 35].

¹ See also: Yemelyanov O. A. Efficiency of metal-film capacitors in accelerated condition: Ph.D. Thesis. St. Petersburg, 2004. 246 p.

Conclusion

We derived Eq. (13) from the standpoint of catastrophe theory to describe the dependence of electrical lifetime of polymer dielectrics on the strength of the applied electric field. A quantitative assessment of the parameters of this equation is given for widely used electrical insulators: phenol formaldehyde laminate, epoxy compounds, oil-impregnated paper and PET film.

PET film was used as an example for analysis of the basic geometric properties determining the behavior of the fold catastrophe function and the scale parameter for damage accumulation rate with varying dimensionless electric field strength. We plotted the the field dependences of electrical lifetime for polyethylene terephthalate and epoxy molding compound EZK-1. The published experimental data and the approximating curves corresponding to Eq. (13) were found to be in excellent agreement.

The results obtained can be used to explain the variations in electrical lifetime based on operational data and technical tests of polymer dielectrics as well as to predict breakdown phenomena.

The advantage of the approach used in the paper is that general expression (3) for the catastrophe function $\Phi(x;A)$ can be modified if it is necessary to replace or increase the number of physical control parameters governing the behavior of dielectric materials in strong electric fields.

As a direction for future research, we plan to account for the influence of the operating temperature of insulation on the breakdown strength of polymer dielectrics, which is possible with theoretical consideration of a higher-order catastrophe, a cusp catastrophe.

REFERENCES

1. **Borisova M. E., Koykov S. N.**, Fizika dielektrikov [Physics of dielectrics], Leningrad University Publishing, Leningrad, 1979 (in Russian).
2. **Dissado L. A., Fothergill J. C.**, Electrical degradation and breakdown in polymers (IEE Materials and Devices Ser. 9), Peter Peregrinus Ltd., London, UK, 1992.
3. **Ushakov V. Y.**, Insulation of high-voltage equipment, Springer, Berlin–Heidelberg, 2004.
4. **Zakrevskii V. A., Pakhotin V. A., Sudar' N. T.**, Dielectric aging and dielectric degradation (breakdown) of polymer films in AC electric fields, Phys. Solid State. 61 (10) (2019) 1915–1921.
5. **Semenov S. E., Kapralova V. M., Pakhotin V. A., Sudar' N. T.**, A mechanism of pulse breakdown evolution in polymeric films, Phys. Solid State. 64 (8) (2022) 954–960.
6. **Zhuravleva N. M., Kiesewetter D. V., Reznik A. S., et al.**, Electrophysical characteristics of paper-impregnated insulation by modifying the cellulose base with a biopolymer, St. Petersburg Polytechnic University Journal of Engineering Science and Technology. 24 (1) (2018) 75–86 (in Russian).
7. **Zhu M.-X., Song H.-G., Li J.-C., et al.**, Phase-field modeling of electric-thermal breakdown in polymers under alternating voltage, IEEE Trans. Dielectr. Electr. Insul. 27 (4) (2020) 1128–1135.
8. **Zakrevskii V. A., Sudar' N. T.**, Ionization mechanism of the electrical degradation (breakdown) of polymer dielectric films, Phys. Solid State. 55 (7) (2013) 1395–1400.
9. **Zakrevskii V. A., Sudar' N. T.**, Electrical breakdown of thin polymer films, Phys. Solid State. 47 (5) (2005) 961–967.
10. **Slutsker A. I., Polikarpov Yu. I., Gilyarov V. L.**, On elementary events in the electrical failure kinetics of polymers, Tech. Phys. 51 (12) (2006) 1591–1595.
11. **Bhutta M. S., Yang L., Ma Z., et al.**, Simulation of thickness controlled DC breakdown of XLPE regulated by space charge & molecular chain movement, IEEE Trans. Dielectr. Electr. Insul. 27 (4) (2020) 1143–1151.
12. **Borisova M. E., Marchenko M. S.**, Electric strength of polyimide films, Russ. Electr. Engin. 5 (1998) 4–6 (in Russian).
13. **Sudar' N. T.**, Vliyaniye temperatury na probivnuyu napryazhennost polimerov v postoyannom elektricheskom pole [Influence of temperature on breakdown strength polymers in the direct current], Trudy SPbGTU [Proceedings of St. Petersburg State Technical University]. 507 (2008) 275–279 (in Russian).
14. **Semenov S. E.**, The temperature effect on impulse dielectric strength of polymer films, St. Petersburg State Polytechnical University Journal. Physics and Mathematics. 17 (2) (2024) 141–149 (in Russian).



15. **Montanari G. C., Seri P., Dissado L. A.**, Aging mechanisms of polymeric materials under DC electrical stress: A new approach and similarities to mechanical aging, *IEEE Trans. Dielectr. Electr. Insul.* 26 (2) (2019) 634–641.
16. **Bian H., Yang L., Ma Z., et al.**, Improved physical model of electrical lifetime estimation for crosslinked polyethylene AC cable, *IEEE Trans. Dielectr. Electr. Insul.* 27 (1) (2020) 132–139.
17. **Hirose H.**, A method to estimate the lifetime of solid electrical insulation, *IEEE Trans. Electr. Insul.* EI-22 (6) (1987) 745–753.
18. **Zakrevskii V. A., Slutsker A. I.**, Possible mechanisms of degradation of macromolecules in mechanical and electrical fields, *Polym. Sci. U.S.S.R.* 26 (6) (1984) 1341–1348.
19. **Simoni L.**, A general phenomenological life model for insulating materials under combined stresses, *IEEE Trans. Dielectr. Electr. Insul.* 6 (2) (1999) 250–258.
20. **Mazzanti G., Montanari G. C., Civenni F.**, Model of inception and growth of damage from microvoids in polyethylene-based materials for HVDC cables. 2. Parametric investigation and data fitting, *IEEE Trans. Dielectr. Electr. Insul.* 14 (5) (2007) 1255–1263.
21. **Dissado L., Mazzanti G., Montanari G. C.**, The incorporation of space charge degradation in the life model for electrical insulating materials, *IEEE Trans. Dielectr. Electr. Insul.* 2 (6) (1995) 1147–1158.
22. **Mazzanti G., Montanari G. C., Civenni F.**, Model of inception and growth of damage from microvoids in polyethylene-based materials for HVDC cables. 1. Theoretical approach, *IEEE Trans. Dielectr. Electr. Insul.* 14 (5) (2007) 1242–1254.
23. **Mazzanti G.**, Life and reliability models for high voltage DC extruded cables, *IEEE Electr. Insul. Mag.* 33 (4) (2017) 42–52.
24. **Gilmore R.**, *Catastrophe theory for scientists and engineers*, Dover Publications, New York, 1993.
25. **Blythe T., Bloor D.**, *Electrical properties of polymers*, Cambridge University Press, Cambridge, UK, 2005.
26. **Rudskoi A. I., Baurova N. I.**, Technological heredity during the production and operation of structural materials, *Russ. Metall.* 2019 (13) (2019) 1378–1383.
27. **Baurova N. I., Zorin V. A., Prikhodko V. M.**, Determination of the synergetic effect of the damage accumulation process in polymer materials using catastrophe theory, *Theor. Found. Chem. Eng.* 50 (1) (2016) 119–125.
28. **Lu T., Cheng S., Li T., et al.**, Electromechanical catastrophe, *Int. J. Appl. Mech.* 8 (7) (2016) 1640005.
29. **Thete A., Geelen D., Van der Molen S. J., Tromp R. M.**, Charge catastrophe and dielectric breakdown during exposure of organic thin films to low-energy electron radiation, *Phys. Rev. Lett.* 119 (26) (2017) 266803.
30. **Zakrevskii V. A., Sudar' N. T.**, The effect of space charge on the electrical breakdown of polymers, *Tech. Phys.* 41 (4) (1996) 352–356.
31. **Kuchinskiy G. S., Nazarov N. I.**, *Silovyye elektricheskiye kondensatory* [Electrical power capacitors], 2nd edition, Energoatomizdat, Moscow, 1992 (in Russian).
32. **Emel'yanov O. A.**, Efficiency features of metal-film capacitors in accelerated conditions, *Russ. Electr. Engin.* 4 (2002) 6–10 (in Russian).
33. **Bobrovskaya L. D.**, Evaluating allowable field densities in epoxy insulation, *Electr. Technol. U.S.S.R.* 7 (1981) 43–45 (in Russian).
34. **Skanavi G. I.**, *Fizika dielektrikov (oblast' sil'nykh polei)* [Physics of dielectrics: Strong fields domain], GIFML Publishing, Moscow, 1958 (in Russian).
35. **Tsurimoto T., Nagao M., Kosaki M.**, Effect of oxidation on localized heat generation and dielectric breakdown of low-density polyethylene film, *Jpn. J. Appl. Phys.* 34 (12A) (1995) 6468–6472.

СПИСОК ЛИТЕРАТУРЫ

1. Борисова М. Э., Койков С. Н. Физика диэлектриков. Л.: Изд-во Ленинградского университета, 1979. 240 с.
2. Dissado L. A., Fothergill J. C. Electrical degradation and breakdown in polymers (IEE Materials and Devices Series 9). London, UK: Peter Peregrinus Ltd., 1992. 601 p.
3. Ушаков В. Я. Изоляция установок высокого напряжения. М.: Энергоатомиздат, 1994. 496 с.
4. Закревский В. А., Пахотин В. А., Сударь Н. Т. Старение и разрушение (пробой) полимерных пленок в переменном электрическом поле // Физика твердого тела. 2019. Т. 61. № 10. С. 1953–1959.
5. Семенов С. Е., Капралова В. М., Пахотин В. А., Сударь Н. Т. Механизм развития импульсного пробоя в полимерных пленках // Физика твердого тела. 2022. Т. 64. № 8. С. 948–954.
6. Журавлева Н. М., Кизеветтер Д. В., Резник А. С., Смирнова Е. Г., Хрипунов А. К. Электрофизические характеристики бумажно-пропитанной изоляции при модификации целлюлозной основы биополимером // Научно-технические ведомости СПбПУ. Естественные и инженерные науки. 2018. Т. 1 № 24. С. 86–75.
7. Zhu M.-X., Song H.-G., Li J.-C., Yu Q.-C., Chen J.-M. Phase-field modeling of electric-thermal breakdown in polymers under alternating voltage // IEEE Transactions on Dielectrics and Electrical Insulation. 2020. Vol. 27. No. 4. Pp. 1128–1135.
8. Закревский В. А., Сударь Н. Т. Ионизационный механизм электрического разрушения (пробоя) полимерных диэлектрических пленок // Физика твердого тела. 2013. Т. 55. № 7. С. 1298–1303.
9. Закревский В. А., Сударь Н. Т. Электрическое разрушение тонких полимерных пленок // Физика твердого тела. 2005. Т. 47. № 5. С. 931–936.
10. Слуцкер А. И., Поликарпов Ю. И., Гиляров В. Л. Об элементарных актах в кинетике электрического разрушения полимеров // Журнал технической физики. 2006. Т. 76. № 12. С. 52–56.
11. Bhutta M. S., Yang L., Ma Z., Nazir M. T., Akram S., Mehmood M. A., Faiz N. Simulation of thickness controlled DC breakdown of XLPE regulated by space charge & molecular chain movement // IEEE Transactions on Dielectrics and Electrical Insulation. 2020. Vol. 27. No. 4. Pp. 1143–1151.
12. Борисова М. Э., Марченко М. С. Электрическая прочность пленок полиимида // Электротехника. 1998. № 5. С. 4–6.
13. Сударь Н. Т. Влияние температуры на пробивную напряженность полимеров в постоянном электрическом поле // Труды СПбГТУ. 2008. № 507. С. 275–279.
14. Семенов С. Е. Влияние температуры на импульсную электрическую прочность полимерных пленок // Научно-технические ведомости СПбГПУ. Физико-математические науки. 2024. Т. 17. № 2. С. 149–141.
15. Montanari G. C., Seri P., Dissado L. A. Aging mechanisms of polymeric materials under DC electrical stress: A new approach and similarities to mechanical aging // IEEE Transactions on Dielectrics and Electrical Insulation. 2019. Vol. 26. No. 2. Pp. 634–641.
16. Bian H., Yang L., Ma Z., Deng B., Zhang H., Wu Z. Improved physical model of electrical lifetime estimation for crosslinked polyethylene AC cable // IEEE Transactions on Dielectrics and Electrical Insulation. 2020. Vol. 27. No. 1. Pp. 132–139.
17. Hirose H. A method to estimate the lifetime of solid electrical insulation // IEEE Transactions on Electrical Insulation. 1987. Vol. EI-22. No. 6. Pp. 745–753.
18. Закревский В. А., Слуцкер А. И. Возможные механизмы распада макромолекул в механическом и электрическом полях // Высокомолекулярные соединения. Серия А. 1984. Т. (A) 26. № 6. С. 1201–1206.
19. Simoni L. A general phenomenological life model for insulating materials under combined stresses // IEEE Transactions on Dielectrics and Electrical Insulation. 1999. Vol. 6. No. 2. Pp. 250–258.
20. Mazzanti G., Montanari G. C., Civenni F. Model of inception and growth of damage from microvoids in polyethylene-based materials for HVDC cables. 2. Parametric investigation and data fitting // IEEE Transactions on Dielectrics and Electrical Insulation. 2007. Vol. 14. No. 5. Pp. 1255–1263.
21. Dissado L., Mazzanti G., Montanari G. C. The incorporation of space charge degradation in the life model for electrical insulating materials // IEEE Transactions on Dielectrics and Electrical Insulation. 1995. Vol. 2. No. 6. Pp. 1147–1158.



22. **Mazzanti G., Montanari G. C., Civenni F.** Model of inception and growth of damage from microvoids in polyethylene-based materials for HVDC cables. 1. Theoretical approach // *IEEE Transactions on Dielectrics and Electrical Insulation*. 2007. Vol. 14. No. 5. Pp. 1242–1254.
23. **Mazzanti G.** Life and reliability models for high voltage DC extruded cables // *IEEE Electrical Insulation Magazine*. 2017. Vol. 33. No. 4. Pp. 42–52.
24. **Gilmore R.** Catastrophe theory for scientists and engineers. New York: Dover Publications, 1993. 666 p.
25. **Blythe T., Bloor D.** Electrical properties of polymers. Cambridge, UK: Cambridge University Press, 2005. 490 p.
26. **Рудской А. И., Баурова Н. И.** Технологическая наследственность при производстве и эксплуатации конструкционных материалов // *Технология металлов*. 2019. № 2. С. 2–10.
27. **Баурова Н. И., Зорин В. А., Приходько В. М.** Оценка синергетического эффекта процесса накопления повреждений в полимерных материалах с использованием теории катастроф // *Теоретические основы химической технологии*. 2016. Т. 50. № 1. С. 122–128.
28. **Lu T., Cheng S., Li T., Wang T., Suo Z.** Electromechanical catastrophe // *International Journal of Applied Mechanics*. 2016. Vol. 8. No. 7. P. 1640005.
29. **Thete A., Geelen D., Van der Molen S. J., Tromp R. M.** Charge catastrophe and dielectric breakdown during exposure of organic thin films to low-energy electron radiation // *Physical Review Letters*. 2017. Vol. 119. No. 26. P. 266803.
30. **Закревский В. А., Сударь Н. Т.** Влияние объемного заряда на закономерности электрического разрушения полимеров // *Журнал технической физики*. 1996. Т. 66. № 4. С. 105–113.
31. **Кучинский Г. С., Назаров Н. И.** Силовые электрические конденсаторы. 2-е изд. М.: Энергоатомиздат, 1992. 320 с.
32. **Емельянов О. А.** Особенности работоспособности металлопленочных конденсаторов в форсированных режимах // *Электротехника*. 2002. № 4. С. 6–10.
33. **Бобровская Л. Д.** Оценка допустимых напряженностей электрического поля в эпоксидной изоляции // *Электричество*. 1981. № 7. С. 43–45.
34. **Сканави Г. И.** Физика диэлектриков (область сильных полей). М.: Государственное издательство физико-математической литературы, 1958. 907 с.
35. **Tsurimoto T., Nagao M., Kosaki M.** Effect of oxidation on localized heat generation and dielectric breakdown of low-density polyethylene film // *Japanese Journal of Applied Physics*. 1995. Vol. 34. No. 12A. Pp. 6468–6472.

THE AUTHOR

KISELEVICH Valentin V.

Gomel State Technical University named after P. O. Sukhoi

48 October Ave., Gomel, 246029, Republic of Belarus

valentinkis@list.ru

ORCID: 0000-0003-0542-0939

СВЕДЕНИЯ ОБ АВТОРЕ

КИСЕЛЕВИЧ Валентин Владимирович — старший преподаватель кафедры «Промышленная теплоэнергетика и экология» Гомельского государственного технического университета имени П. О. Сухого.

246029, Республика Беларусь, г. Гомель, пр. Октября, 48

valentinkis@list.ru

ORCID: 0000-0003-0542-0939

Received 26.10.2024. Approved after reviewing 28.01.2025. Accepted 28.01.2025.

Статья поступила в редакцию 26.10.2024. Одобрена после рецензирования 28.01.2025. Принята 28.01.2025.

Original article

UDC 538.91; 548.74

DOI: <https://doi.org/10.18721/JPM.18210>

FORMATION OF BAINITE BELOW MARTENSITE START TEMPERATURE IN QUENCHING LOW CARBON STEEL

N. Yu. Zolotorevsky¹ , Yu. A. Belikova², S. N. Petrov^{2, 1}, A. A. Zisman^{2, 1}

¹ Peter the Great St. Petersburg Polytechnic University, St. Petersburg, Russia;

² NRC "Kurchatov Institute" – CRISM "Prometey", St. Petersburg, Russia

 zolotorevsky@phmf.spbstu.ru

Abstract. According to the phase transformation kinetics that we recorded by dilatometry in rapid cooling of low carbon steel, some amount of isothermal bainite appeared in the middle of martensitic temperature range. Presumably caused by adiabatic heating in the exothermal transformation, such an unexpected effect was confirmed by TEM data on the lath thickness, dislocation density and carbide particles. Furthermore, to assess a volume fraction of the detected bainite, statistics of crystal curvature (orientation gradient) was analyzed in terms of EBSD data. The combined analysis of results obtained using those three techniques suggests that certain amount of lath type bainite is formed not only below the martensite start temperature but also slightly above it.

Keywords: microstructure, martensite, bainite, isothermal transformation, quenching, low carbon steel

Funding: The reported study was funded by Russian Science Foundation (Grant No. 22-19-00627 on the topic "An analysis of the crystallographic structure of steels undergoing shear-type transformations upon cooling, and reconstruction of the structural state of their high-temperature phase").

For citation: Zolotorevsky N. Yu., Belikova Yu. A., Petrov S. N., Zisman A. A., Formation of bainite below martensite start temperature in quenching low carbon steel, St. Petersburg State Polytechnical University Journal. Physics and Mathematics. 18 (2) (2025) 109–118. DOI: <https://doi.org/10.18721/JPM.18210>


This is an open access article under the CC BY-NC 4.0 license (<https://creativecommons.org/licenses/by-nc/4.0/>)

Научная статья

УДК 538.91; 548.74

DOI: <https://doi.org/10.18721/JPM.18210>

ОБРАЗОВАНИЕ БЕЙНИТА В ТЕМПЕРАТУРНОМ ИНТЕРВАЛЕ МАРТЕНСИТНОГО ПРЕВРАЩЕНИЯ ПРИ ЗАКАЛКЕ НИЗКОУГЛЕРОДИСТОЙ СТАЛИ

Н. Ю. Золоторевский¹ , Ю. А. Беликов²,
С. Н. Петров^{2, 1}, А. А. Зисман^{2, 1}

¹ Санкт-Петербургский политехнический университет Петра Великого,
Санкт-Петербург, Россия;

² НИЦ «Курчатовский институт» – ЦНИИ КМ «Прометей», Санкт-Петербург, Россия

 zolotorevsky@phmf.spbstu.ru

Аннотация. В соответствии с кинетикой фазового превращения, зарегистрированной методом дилатометрии при быстром охлаждении низкоуглеродистой стали, в середине температурного диапазона мартенситного превращения образуется некоторое количество изотермического бейнита. Такой неожиданный эффект, предположительно вызванный

адиабатическим нагревом при неизотермическом превращении, подтверждается данными просвечивающей электронной микроскопии о толщине реек, плотности дислокаций и частицах карбидов. Кроме того, для оценки объемной доли обнаруженного бейнита на основе данных метода дифракции отраженных электронов проанализирована статистика кривизны кристаллической решетки (градиент ориентации). Совместный анализ результатов, полученных с помощью этих трех методов, позволяет заключить, что определенное количество бейнита реечного типа образуется не только ниже температуры начала мартенситного превращения, но и немного выше нее.

Ключевые слова: микроструктура, мартенсит, бейнит, изотермическое превращение, закалка, низкоуглеродистая сталь

Финансирование: Исследование выполнено при финансовой поддержке Российского научного фонда (грант на тему «Анализ кристаллографического строения сталей, испытывающих превращения сдвигового типа при охлаждении, и реконструкция структурного состояния их высокотемпературной фазы», № 22-19-00627).

Для цитирования: Золоторевский Н. Ю., Беликова Ю. А., Петров С. Н., Зисман А. А. Образование бейнита в температурном интервале мартенситного превращения при закалке низкоуглеродистой стали // Научно-технические ведомости СПбГПУ. Физико-математические науки. 2025. Т. 18. № 2. С. 109–118. DOI: <https://doi.org/10.18721/JPM.18210>

Статья открытого доступа, распространяемая по лицензии CC BY-NC 4.0 (<https://creativecommons.org/licenses/by-nc/4.0/>)

Introduction

In order to control the proportion of martensite and bainite microstructures in high-strength steels, isothermal treatments [1 – 3] or decelerated cooling [4] inside the martensitic temperature range attract an increasing researchers' attention. In principle, with allowance for adiabatic heating due to the exothermal transformation and for numerous nucleation sites at the α - γ boundaries of preformed martensite, appearance of bainite seems possible even in case of rapid cooling. However, to the authors' knowledge, such effects have never been reported, except for Ref. [5] where dilatometry data on low carbon steel indicated a short near-isothermal stage of bainitic transformation after a notable martensite amount accumulates.

To verify this uncommon behavior, the present work analyzes the underlying microstructures by independent Transmission Electron Microscopy (TEM) and Electron Backscatter Diffraction (EBSD) methods. The former evaluates local dislocation densities and lath thickness as well as images fine carbide particles if any; the latter technique reveals the distribution of crystal curvature indicative of martensite and bainite fractions.

Material and methods

Chemical composition of the studied steel (wt. %: 0.09C, 0.35Mn, 0.30Si, 5.50[Ni+Cu], 1.50[Mo+Cr], 0.15V) ensured its mostly martensitic microstructures after quenching in a wide range of cooling rates. Start and finish temperatures of the underlying transformation slightly increase when the slower cooling and hence deviate from the athermal nature of martensite expressed by the Koistinen – Marburger equation [6]. It remains a subject of dispute whether similar effects are due to specific (thermally activated) martensite embryos or a minor fraction of preformed lath bainite [7].

Reheated to 950°C and hold for 100 s, small specimens (Diam5×10 mm) of the steel have been quenched in DII 805 A/D dilatometer at 60°C/s cooling rate. To confirm their somewhat unexpected response considered below in this work, such experiments were repeated several times. Following Ref. [8], to properly evaluate the transformation degree in terms of the specimen length, we allow for the temperature dependence of thermal expansion coefficients in both the parent and product phases. When neglecting this issue, the martensite start temperature would be overestimated by ~20 to 40°C.



To analyze obtained microstructures by TEM FEI Tecnai G2 30 S-TWIN at an accelerating voltage of 200 kV, disks of 1 mm thickness cut from the quenched specimen were conventionally thinned by mechanical and electrolytic polishing. Surface oxide films were then removed from prepared foils by ion milling system Fischione 1010. The lath thickness, dislocation density and morphology of carbide particles, if any, were analyzed in various microstructure constituents. Owing to the apparent width of linear defects and their mutual screening through the foil thickness, reliable estimates of the dislocation density were limited to about $6.5 \cdot 10^{10} \text{ cm}^{-2}$. Nonetheless, the revealed types of martensite and bainite can be discriminated. Since the TEM technique is essentially local, the analysis of each foil was repeated on twenty domains of $6 \times 6 \text{ }\mu\text{m}$ randomly distributed over an area of $720 \text{ }\mu\text{m}^2$. Though the eventual averaging hardly ensures true representativeness, it still enables recognition and comparison of coexisting microstructural types. Fractions of them are approximately assessed by counting related pixels of digitized images.

A planar section prepared by usual metallographic procedures and additionally subjected to electrolytic polishing has been analyzed by EBSD on SEM Lyra 3-XM at an accelerating voltage of 20 kV. An area having a width and height of $100 \text{ }\mu\text{m}$ was scanned with a step of $0.05 \text{ }\mu\text{m}$, and crystal orientations at periodically arranged points were determined by means of Chamel 5 software. A subsequent analysis of the EBSD maps was carried out using MTEX software [9]. Respective levels of crystal curvature were assessed by the kernel average misorientation (KAM), that is, an average angle of lattice rotations at next neighbors of the considered data point with respect to the latter. Then a rather noisy KAM was averaged in microstructural elements separated by closed boundaries with tolerance angle $\theta_i = 4^\circ$. The resulting “grain average” misorientation (GAM) characterizes each martensite or bainite block as a whole since the employed θ_i is a lower bound for misorientations between admitted variants of orientation relationship (OR) peculiar to shear transformations in steels [10].

Treatment of experimental data

A temperature dependence of the transformed fraction in quenching was conventionally evaluated in terms of the thermal expansions, and the considered near-isothermal origination of bainite was verified by TEM and EBSD as follows.

Recognition of microstructures by TEM. Various microstructural constituents in quenched steel have been discriminated by TEM; they are lath martensite (LM) and bainite (LB), auto-tempered martensite (AM) and granular bainite (GB). The first and second of them are ascribed to domains of near-parallel laths whose thickness does not exceed $0.8 \text{ }\mu\text{m}$; then LM is separated owing to its relatively high dislocation densities ($\rho > 6.5 \cdot 10^{10} \text{ cm}^{-2}$) and usually finer ($< 0.3 \text{ }\mu\text{m}$) laths. It is kept in mind as well that bainitic domains usually contain more amounts of retained austenite.

Close dislocation densities diminished with respect to harder constituents are peculiar to both AM and GB, where domains of the former are recognizable owing to large (several microns) dimensions. Besides, this phase contains characteristic rod-like particles of cementite oriented along three crystallographic directions. Such precipitations remain thin because of relatively slow carbon diffusion at the transformation temperature.

Analysis of crystal curvature statistics. Determined by EBSD, the GAM measure of crystal curvature is due to both the dislocation density in structural elements and inhomogeneous phase stresses. Thus, there are two characteristic scales corresponding to the dislocation spacing and lath thickness. To extract each of the related contributions is problematic [11]; at the same time, their integral effect enables a rough discrimination between various constituents of the transformation product [12 – 15]. As neighboring crystals may have overlapping ranges of curvature, an analysis of its overall statistics (spectrum) rather than local data is preferable as shown in Ref. [5, 16]. Making use of this expedient, we will fit to a right tail (higher curvature range) of the experimental GAM spectrum a virtual lognormal part presumably involving martensite constituents: the LM and AM fractions. Although the latter have lower dislocation densities, its GAM keeps high according to strong phase stresses of martensite. Thus, the fraction of bainite constituents can be evaluated by subtracting the fitted spectrum from the experimental one. Relevance of this approach will be confirmed by TEM results and independent dilatometry data on the transformation kinetics.

Results and discussion

Transformation kinetics. A temperature dependence of the transformation degree F according to dilatometry data is represented in Fig. 1, *a*. In general, it fits perfectly with the Koistinen – Marburger equation [6] with nucleation temperature T_{KM} of about 300°C, though above the latter a minor part of transformed phase deviates from the athermal model. Besides, a near-isothermal (presumably bainitic) segment appears at the maximum slope of this curve after a notable amount of the preformed martensite. This particular effect is supported by Fig. 1, *b* showing a rather smooth time dependence of the transformed fraction that excludes experimental artifacts. The most plausible explanation of the considered finding is intensive adiabatic heating due to the exothermal transformation. According to the diagram in Fig. 1, *a*, the portions of about 13% and 8% of the transformed matter are not due to athermal martensite [6] but contain alternative phases thermally activated, at $T > T_{KM}$ and during the above-considered stage, respectively.

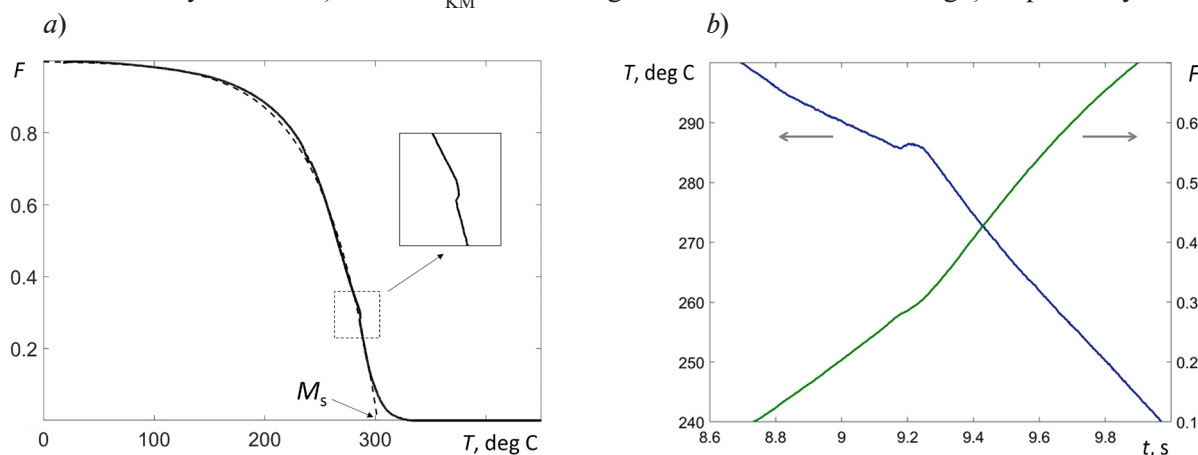


Fig. 1. Transformation kinetics in quenching low carbon martensitic steel: (*a*) the whole diagram where the insert indicates an isothermal stage; (*b*) time dependence of the temperature and the transformed fraction within the period that includes the isothermal stage.

A dashed line in (*a*) corresponds to the athermal transformation according to the Koistinen – Marburger equation (see Ref. [6])

TEM data. TEM results for microstructures of LM and AM, as well as of LB and GB, are presented respectively from Fig. 2 to Fig. 5. As previously described, these results enable assessment of the considered constituent fractions. Dislocation densities in each of them were determined on several fields under identical diffraction conditions while the foil thickness was evaluated by the electron energy loss spectroscopy. Foils were oriented to get (110) planes very slightly deviated from the reflecting (“two-beam”) position. Thus, high orientation gradients near dislocation cores result in dark traces of dislocation lines on the light field images with a high magnification. Besides, lower magnifications were applied to show a general appearance of transformation microstructures.

The light field image with a typical LM microstructure is represented in Fig. 2, *a* and the diffraction pattern in Fig. 2, *b* confirms a specific orientation of (110) planes. The LM occupying about 33% of the analyzed foil has thin and straight inter-lath boundaries where streaks of retained austenite and, sometimes, fine carbides are observed. The lath thickness varies from 50 to 290 nm and its average value is 160 nm. The average dislocation density of $7.0 \cdot 10^{10} \text{ cm}^{-2}$ evaluated in this most hard constituent exceeds the above-mentioned limit of $6.5 \cdot 10^{10} \text{ cm}^{-2}$ that would ensure accurate assessments by TEM.

Fig. 3, *a–c* represents corresponding TEM results for AM that is a type of martensite formed at higher temperatures. Moreover, Fig. 3, *d* images thin elongated particles of cementite oriented along three crystallographic directions and peculiar to this microstructure type. Its measured volume fraction equals 37% and structural units reaching 2–3 μm in width are rather large for the whole analyzed area of $720 \mu\text{m}^2$. As expected, their evaluated dislocation density of $5.4 \cdot 10^{10} \text{ cm}^{-2}$ proved to be reduced relative to that of LM.

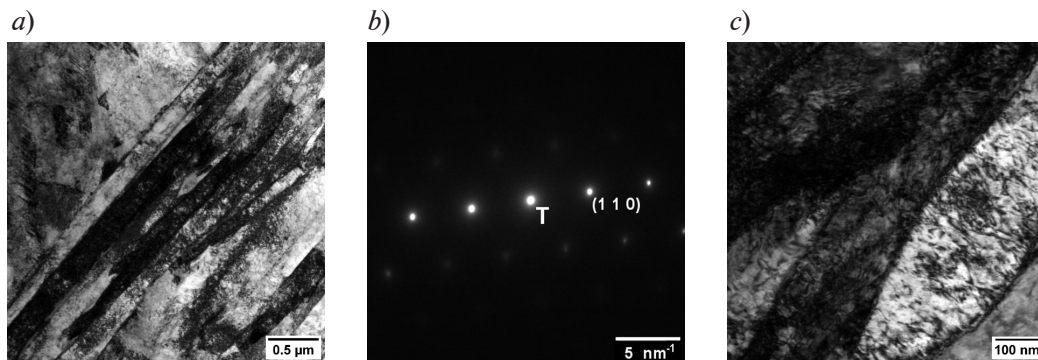


Fig. 2. TEM images of lath martensite: (a) general appearance by a light field image, (b) a diffraction pattern at (110) planes in the reflecting orientation, (c) dislocation traces imaged by dark streaks within the laths

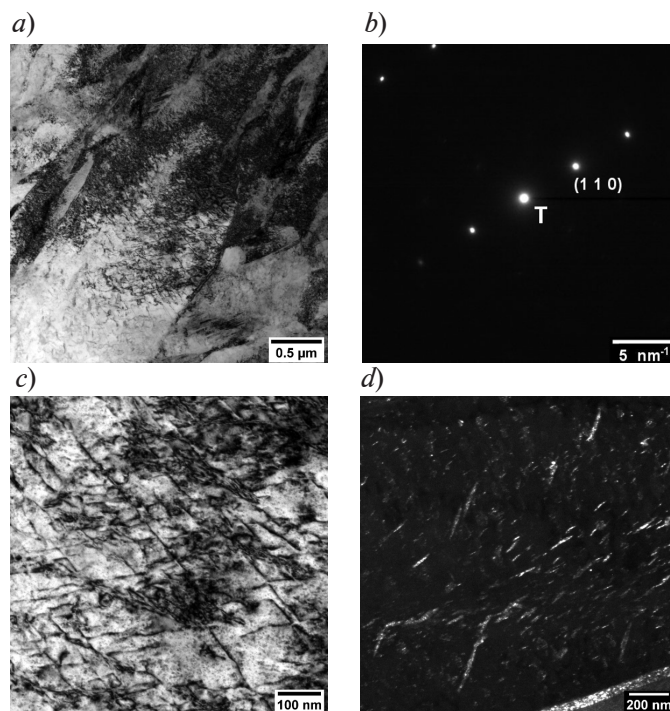


Fig. 3. TEM images of auto-tempered martensite: (a) general appearance by a light field image, (b) a diffraction pattern at (110) planes in the reflecting orientation, (c) dislocation traces imaged by dark streaks, (d) a dark field image of oriented carbide particles

According to the above-considered data, a martensite fraction of nominally martensitic steel quenched at very high cooling rate of 60°C/s reaches only 70% so that a notable residual fraction is presumably due to LB or/and GB phases. The following TEM and EBSD results represented in Figs. 4, 5 and 6, respectively, should verify this uncommon finding and then enable evaluation of the LB-to-GB proportion.

It is very hard to recognize LB and separate the latter from LM based only on morphological signs. Indeed, the thickness of GB laths varies from 80 to 900 nm and often approach values of up to 250 – 300 nm that is close to an upper bound for martensite laths. The average dislocation density of LB is $6.5 \cdot 10^{10} \text{ cm}^{-2}$ rather close to measured $7.0 \cdot 10^{10}$ of LM though still enabling discrimination between the two microstructures. Besides, as previously mentioned, their recognition is facilitated by more perfect and straight inter-lath boundaries in LM. As to the conventional discrimination between bainite and martensite in terms of carbide distributions, this way is hardly applicable to the considered steel since its carbon content is too low. TEM results for LB are shown in Fig. 4, and the fraction of this phase is 17%.

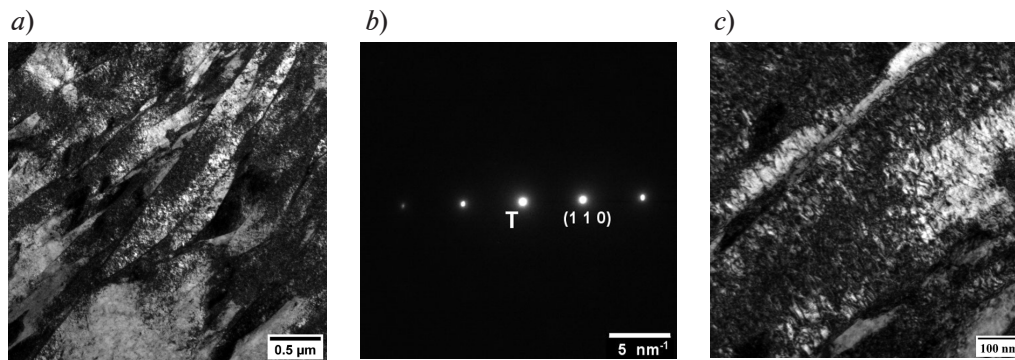


Fig. 4. TEM images of lath bainite microstructure: (a) general appearance by a light field image, (b) a diffraction pattern at (110) planes in the reflecting orientation, (c) dislocation traces imaged by dark streaks

GB elements have sizes from 0.5 to 0.7 μm and occupy a 13% fraction of the analyzed foil area; their average dislocation density is $5.2 \cdot 10^{10} \text{ cm}^{-2}$. TEM results for this phase are shown in Fig. 5.

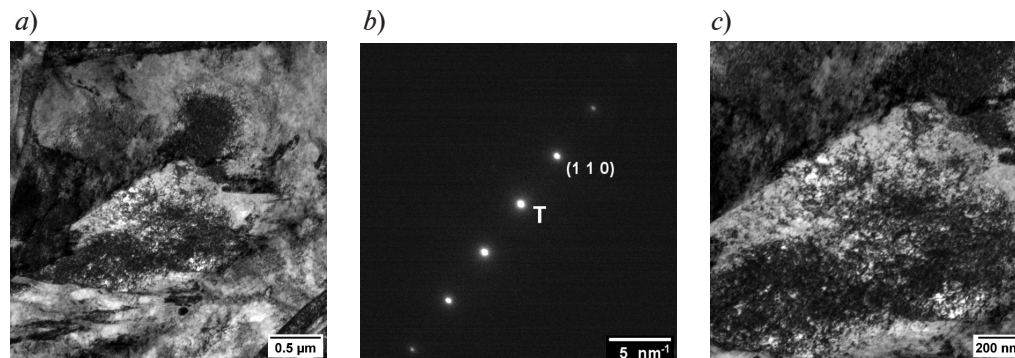


Fig. 5. TEM images of granular bainite microstructure: (a) general appearance by a light field image, (b) a diffraction pattern at (110) planes in the reflecting orientation, (c) dislocation traces imaged by dark streaks

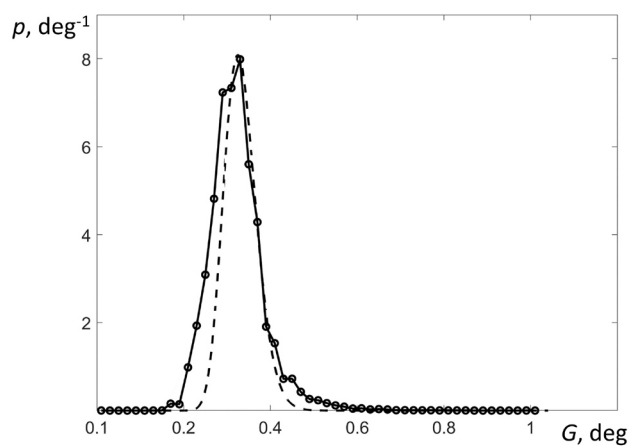


Fig. 6. A plot of probability density p versus crystal curvature G expressed by GAM function in low carbon martensitic steel quenched at the cooling rate of 60 deg C/s. A lognormal distribution is given by a dashed curve

Crystal curvature by EBSD. The fractions of steel constituents were evaluated using EBSD from the distribution of crystal curvature by a method suggested in our earlier study [5]. GAM spectrum derived by EBSD on the analyzed section is shown in Fig. 6, where a lognormal distribution (dashed curve) fitted to its right tail according to Ref. [5] corresponds to martensite constituents. To allow properly for the latter, deviations of fitted values from the lower right part of this plot are neglected, so that a remaining sum of LB and GB constituents is attributed to the spectrum part situated left from the lognormal approximation. Thus, assessed fractions of martensite (LM plus AM) and bainite (LB plus GB) equal 80% and 20%, respectively.



Combined analysis. In order to compare results provided by the three independent techniques, they are listed in Table. The martensite fraction of 79% derived from the transformation kinetics (see Fig. 1) fits 80% according to EBSD analysis much better than this could be expected. However, the TEM data, the representativeness of which is limited, should be analyzed with a special care. On the one hand, the corresponding 70% of martensite fraction could be accepted as satisfactorily close to the previous estimates of 79% and 80%. On the other hand, the difference is still notable and hence, suggests plausible corrections of the TEM results as follows. To comply with dilatometry and EBSD data, the martensite fraction should be increased by about 10% at the expense of bainite constituents. Specifically, it would be reasonable to reduce the GB rather than LB fraction as far as the former usually appears in the considered steel at much higher temperatures. As shown on the same specimens [5], this regularity agrees well with the statistics of paring of the transformation variants admitted by the inter-phase orientation relationship. In general, taking these reasons and Fig. 1 into account, both the deviation from the athermal transformation at $T > T_{KM}$ and the near-isothermal stage at $T \approx 280^\circ\text{C}$ are mostly due to the lath type of bainite.

Table

A comparison of results obtained by independent methods

Method	Volume fraction (%) of phase constituents			
	Martensite		Bainite	
	Lath	Auto-tempered	Lath	Granular
Transmission Electron Microscopy	37	33	17	13
Dilatometry	79 in sum*		21 in sum	
Electron Backscatter Diffraction	80 in sum		20 in sum	

* An immediate result of the athermal transformation regardless of subsequent auto-tempering.

Summary

A combined analysis of dilatometry, TEM and EBSD results confirms the near-isothermal formation of lath bainite in the middle of martensitic temperature range when quenching low carbon steel. Besides, a comparison of this independent data suggests the appearance of mostly the same bainite type at temperatures slightly above T_{KM} that leads to deviations of the transformation kinetics from the athermal martensite model [6].

REFERENCES

1. Wei Z., Hu H., Liu M., et al., Effect of austempering below Ms on the microstructure and wear performance of a low-carbon bainitic steel, *Metals*. 12 (1) (2022) 104.
2. Qian L., Li Z., Wang T., et al., Roles of pre-formed martensite in below-Ms bainite formation, microstructure, strain partitioning and impact absorption energies of low-carbon bainitic steel, *J. Mater. Sci. Technol.* 96 (1) (2022) 69–84.
3. Rampelberg C., Allain S. Y. P., Geandier G., et al., Carbide-free bainite transformations above and below martensite start temperature investigated by *in-situ* high-energy X-ray diffraction, *JOM*. 73 (11) (2021) 3181–3194.
4. Zhang X., Yu H., Li Q., Song C., Yang S., Study of microstructural evolution and mechanical properties of 1000 MPa low-carbon micro-alloyed steel prepared by multiple quenching strategies near Ms, *Mater. Sci. Eng. A*. 840 (4) (2022) 142968.
5. Zisman A. A., Zolotarevsky N. Y., Petrov S. N., Ermakova N. Y., Effect of cooling rate on the bainite fraction in low carbon martensitic steel: combined analysis of transformation kinetics and crystal curvature, *Lett. Mater.* 13 (1) (2023) 67–72.

6. Koistinen D. P., Marburger R. E., A general equation prescribing the extent of austenite-martensite transformation in pure iron-carbon alloys and plain carbon steels, *Acta Metall.* 7 (1) (1959) 59–60.
7. Jeyabalan K., Catteau S. D., Teixeira J., et al., Modeling of the austenite decomposition kinetics in a low-alloyed steel enriched in carbon and nitrogen, *Materialia*. 9 (March) (2020) 100582.
8. Choi S., Model for estimation of transformation kinetics from the dilatation data during a cooling of hypoeutectoid steels, *Mater. Sci. Eng. A*. 363 (1–2) (2003) 72–80.
9. Hielscher R., Silberman C. B., Schmidl E., Ihlemann J., Denoising of crystal orientation maps, *J. Appl. Cryst.* 52 (5) (2019) 984–996.
10. Takayama N., Miyamoto G., Furuhashi T., Effect of transformation temperature on variant pairing of bainitic ferrite in low carbon steel, *Acta Mater.* 60 (5) (2012) 2387–2396.
11. Zisman A., Choice of scalar measure for crystal curvature to image dislocation substructure in terms of discrete orientation data, *J. Mech. Behav. Mater.* 25 (1–2) (2016) 15–22.
12. Wright S. I., Nowell M. M., Field D. P., A review of strain analysis using electron backscatter diffraction, *Microsc. Microanal.* 17 (3) (2011) 316–329.
13. Gazder A. A., Al-Harbi F., Spanke H. Th., et al., A correlative approach to segmenting phases and ferrite morphologies in transformation-induced plasticity steel using electron back-scattering diffraction and energy dispersive X-ray spectroscopy, *Ultramicroscopy*. 147 (Dec) (2014) 114–132.
14. Breumier S., Martinez Ostormujof T., Frincu B., et al., Leveraging EBSD data by deep learning for bainite, ferrite and martensite segmentation, *Mater. Charact.* 186 (April) (2022) 111805.
15. Santos D. B., Camey K., Barbosa R., et al., Complex phase quantification methodology using electron backscatter diffraction (EBSD) on low manganese high temperature processed (HTP) microalloyed steel, *J. Mater. Res. Technol.* 8 (2) (2022) 2423–2431.
16. Zisman A. A., Petrov S. N., Zolotarevsky N. Y., Ermakova N. Y., Spectra of crystal curvature in terms of EBSD data to assess martensite fraction in bainitic steel, *Mater. Phys. Mech.* 51 (2) (2023) 227–234.

СПИСОК ЛИТЕРАТУРЫ

1. Wei Z., Hu H., Liu M., Tian J., Xu G. Effect of austempering below Ms on the microstructure and wear performance of a low-carbon bainitic steel // *Metals*. 2022. Vol. 12. No. 1. P. 104.
2. Qian L., Li Z., Wang T., Li D., Zhang F., Meng J. Roles of pre-formed martensite in below-Ms bainite formation, microstructure, strain partitioning and impact absorption energies of low-carbon bainitic steel // *Journal of Materials Science and Technology*. 2022. Vol. 96. No. 1. Pp. 69–84.
3. Rampelberg C., Allain S. Y. P., Geandier G., Teixeira J., Lebel F., Sourmail T. Carbide-free bainite transformations above and below martensite start temperature investigated by *in-situ* high-energy X-ray diffraction // *JOM*. 2021. Vol. 73. No. 11. Pp. 3181–3194.
4. Zhang X., Yu H., Li Q., Song C., Yang S. Study of microstructural evolution and mechanical properties of 1000 MPa low-carbon micro-alloyed steel prepared by multiple quenching strategies near Ms // *Materials Science and Engineering: A*. 2022. Vol. 840. 18 April. P. 142968.
5. Zisman A. A., Zolotarevsky N. Y., Petrov S. N., Ermakova N. Y. Effect of cooling rate on the bainite fraction in low carbon martensitic steel: combined analysis of transformation kinetics and crystal curvature // *Письма о материалах*. 2023. Т. 13. № 1. С. 67–72.
6. Koistinen D. P., Marburger R. E. A general equation prescribing the extent of austenite-martensite transformation in pure iron-carbon alloys and plain carbon steels // *Acta Metallurgica*. 1959. Vol. 7. No. 1. Pp. 59–60.
7. Jeyabalan K., Catteau S. D., Teixeira J., Geandier G., Denand B., Dulcy J., Denis S., Michel G., Courteaux M. Modeling of the austenite decomposition kinetics in a low-alloyed steel enriched in carbon and nitrogen // *Materialia*. 2020. Vol. 9. March. P. 100582.
8. Choi S. Model for estimation of transformation kinetics from the dilatation data during a cooling of hypoeutectoid steels // *Materials Science and Engineering: A*. 2003. Vol. 363. No.1–2. Pp. 72–80.
9. Hielscher R., Silberman C. B., Schmidl E., Ihlemann J. Denoising of crystal orientation maps // *Journal of Applied Crystallography*. 2019. Vol. 52. Part 5. Pp. 984–996.
10. Takayama N., Miyamoto G., Furuhashi T. Effect of transformation temperature on variant pairing of bainitic ferrite in low carbon steel // *Acta Materialia*. 2012. Vol. 60. No. 5. Pp. 2387–2396.



11. **Zisman A.** Choice of scalar measure for crystal curvature to image dislocation substructure in terms of discrete orientation data // *Journal of the Mechanic Behavior of Materials*. 2016. Vol. 25. No. 1–2. Pp. 15–22.
12. **Wright S. I., Nowell M. M., Field D. P.** A review of strain analysis using electron backscatter diffraction // *Microscopy and Microanalysis*. 2011. Vol. 17. No. 3. Pp. 316–329.
13. **Gazder A. A., Al-Harbi F., Spanke H. Th., Mitchel D. R. G., Pereloma E. V.** A correlative approach to segmenting phases and ferrite morphologies in transformation-induced plasticity steel using electron back-scattering diffraction and energy dispersive X-ray spectroscopy // *Ultramicroscopy*. 2014. Vol. 147. December. Pp. 114–132.
14. **Breumier S., Martinez Ostormujof T., Frincu B., Gey N., Couturier A., Loukachenko N., Abaperea P.E., Germain L.** Leveraging EBSD data by deep learning for bainite, ferrite and martensite segmentation // *Materials Characterization*. 2022. Vol. 186. April. P. 111805.
15. **Santos D. B., Camey K., Barbosa R., Andrade M. S., Escobar D. P.** Complex phase quantification methodology using electron backscatter diffraction (EBSD) on low manganese high temperature processed (HTP) microalloyed steel // *Journal of Materials Research and Technology*. 2022. Vol. 8. No. 2. Pp. 2423–2431.
16. **Zisman A. A., Petrov S. N., Zolotarevsky N. Y., Ermakova N. Y.,** Spectra of crystal curvature in terms of EBSD data to assess martensite fraction in bainitic steel // *Materials Physics and Mechanics*. 2023. Vol. 51. No. 2. Pp. 50–57.

THE AUTHOR

ZOLOTOREVSKY Nikolay Yu.

Peter the Great St. Petersburg Polytechnic University
29 Politechnicheskaya St., St. Petersburg, 195251, Russia
zolotarevsky@phmf.spbstu.ru
ORCID: 0000-0002-0185-5452

BELIKOVA Yulia A.

NRC “Kurchatov Institute” – CRISM “Prometey”
49 Shpalernaya St., St. Petersburg, 191015, Russia
belikjul@ya.ru

PETROV Sergey N.

NRC “Kurchatov Institute” – CRISM “Prometey”
Peter the Great St. Petersburg Polytechnic University
49 Shpalernaya St., St. Petersburg, 191015, Russia
petrov.epma@mail.ru
ORCID: 0000-0001-6732-7217

ZISMAN Alexander A.

NRC “Kurchatov Institute” – CRISM “Prometey”
Peter the Great St. Petersburg Polytechnic University
49 Shpalernaya St., St. Petersburg, 191015, Russia
crism_ru@yahoo.co.uk
ORCID: 0000-0002-9431-7097

СВЕДЕНИЯ ОБ АВТОРЕ

ЗОЛОТОРЕВСКИЙ Николай Юльевич – доктор физико-математических наук, профессор Высшей школы механики и процессов управления Санкт-Петербургского политехнического университета Петра Великого, Санкт-Петербург, Россия.

195251, Россия, г. Санкт-Петербург, Политехническая ул., 29
zolotarevsky@phmf.spbstu.ru
ORCID: 0000-0002-0185-5452

БЕЛИКОВА Юлия Александровна — научный сотрудник ФГУП «Центральный научно-исследовательский институт конструкционных материалов «Прометей» имени И. В. Горынина» Национального исследовательского центра «Курчатовский институт», Санкт-Петербург, Россия.

191015, Россия, г. Санкт-Петербург, Шпалерная ул., 49
belikjul@ya.ru

ПЕТРОВ Сергей Николаевич — доктор технических наук, кандидат химических наук, старший научный сотрудник ФГУП «Центральный научно-исследовательский институт конструкционных материалов «Прометей» имени И. В. Горынина» Национального исследовательского центра «Курчатовский институт», профессор базовой кафедры «Функциональные материалы и технологии» Санкт-Петербургского политехнического университета Петра Великого, Санкт-Петербург, Россия.

191015, Россия, г. Санкт-Петербург, Шпалерная ул., 49
petrov.epma@mail.ru
ORCID: 0000-0001-6732-7217

ЗИСМАН Александр Абрамович — доктор физико-математических наук, главный научный сотрудник ФГУП «Центральный научно-исследовательский институт конструкционных материалов «Прометей» имени И. В. Горынина» Национального исследовательского центра «Курчатовский институт», профессор Высшей школы механики и процессов управления Санкт-Петербургского политехнического университета Петра Великого, Санкт-Петербург, Россия.

191015, Россия, г. Санкт-Петербург, Шпалерная ул., 49
crism_ru@yahoo.co.uk
ORCID: 0000-0002-9431-7097

Received 14.10.2024. Approved after reviewing 29.11.2024. Accepted 29.11.2024.

Статья поступила в редакцию 14.10.2024. Одобрена после рецензирования 29.11.2024. Принята 29.11.2024.

NUCLEAR PHYSICS

Original article

DOI: <https://doi.org/10.18721/JPM.18211>

FEASIBILITY TO MEASURE THE PROPERTIES OF CHARGED $K^*(892)$ MESONS AND $\Sigma(1385)$ BARYONS IN COLLISIONS OF BISMUTH NUCLEI AT AN ENERGY OF 9.2 GeV IN THE NICA COLLIDER USING THE MPD EXPERIMENTAL SETUP

*Ya. A. Berdnikov¹, D. A. Ivanishchev^{1✉}, D. O. Kotov¹,
M. V. Malaev¹, A. Yu. Riabov²*

¹ Peter the Great St. Petersburg Polytechnic University, St. Petersburg, Russia;

² Petersburg Nuclear Physics Institute named after B. P. Konstantinov
of NRC Kurchatov Institute, St. Petersburg, Russia

✉ ivanishchev_da@pnpi.nrcki.ru

Abstract. We report results on a feasibility study of measuring the properties of $K^*(892)^\pm$ and $\Sigma(1385)^\pm$ resonances in collisions of bismuth nuclei (Bi) at an energy of 9.2 GeV using the MPD detector at the NICA collider. The dependencies of the processes key parameters on the transverse momentum for different intervals of centrality of Bi + Bi collisions were obtained in the rapidity range from -0.5 to $+0.5$ using model calculations. The evaluations of the mass resolution, detection efficiency of the MPD detector and the transverse momentum spectra for the $K^*(892)^\pm$ and $\Sigma(1385)^\pm$ resonances were made. The sample size of Bi + Bi collision data that allowed the $K^*(892)^\pm$ and $\Sigma(1385)^\pm$ resonances properties to be reconstructed with a sufficiently good accuracy to conduct a study of the $K^*(892)^\pm$ and $\Sigma(1385)^\pm$ resonances production was estimated.

Keywords: bismuth nuclei collisions, production, resonance, NICA collider, MPD detector

Funding: The reported study was carried out within the framework of the State Assignment for Fundamental Research (Subject Code FSEG-2025-0009).

Citation: Berdnikov Ya. A., Ivanishchev D. A., Kotov D. O., Malaev M. V., Riabov A. Yu., Feasibility to measure the properties of charged $K^*(892)$ mesons and $\Sigma(1385)$ baryons in collisions of bismuth nuclei at an energy of 9.2 GeV in the NICA collider using the MPD experimental setup, St. Petersburg State Polytechnical University Journal. Physics and Mathematics. 18 (2) (2025) 119–131. DOI: <https://doi.org/10.18721/JPM.18211>

This is an open access article under the CC BY-NC 4.0 license (<https://creativecommons.org/licenses/by-nc/4.0/>)

Научная статья
УДК 539.126.3, 539.126.6
DOI: <https://doi.org/10.18721/JPM.18211>

ВОЗМОЖНОСТИ ИЗМЕРЯТЬ СВОЙСТВА ЗАРЯЖЕННЫХ $K^*(892)$ -МЕЗОНОВ И $\Sigma(1385)$ -БАРИОНОВ В СТОЛКНОВЕНИЯХ ЯДЕР ВИСМУТА ПРИ ЭНЕРГИИ 9,2 ГэВ В УСКОРИТЕЛЕ NICA НА ЭКСПЕРИМЕНТАЛЬНОЙ УСТАНОВКЕ MPD

Я. А. Бердников¹, Д. А. Иванищев^{1✉}, Д. О. Котов¹,
М. В. Малаев¹, А. Ю. Рябов²

¹ Санкт-Петербургский политехнический университет Петра Великого, Санкт-Петербург, Россия;

² Петербургский институт ядерной физики им. Б. П. Константинова

НИЦ «Курчатовский институт», Санкт-Петербург, Россия

✉ ivanishchev_da@pnpi.nrcki.ru

Аннотация. В статье представлены результаты исследования возможности измерять свойства $K^*(892)^\pm$ - и $\Sigma(1385)^\pm$ -резонансов в столкновениях ядер висмута Bi при энергии 9,2 ГэВ с помощью экспериментальной установки (ЭУ) MPD на ускорителе NICA. Прослежены зависимости ключевых параметров процессов от поперечного импульса для различных интервалов по центральности столкновений $Bi + Bi$ в области быстрот от $-0,5$ до $0,5+$ посредством модельных расчетов. Получены оценки массового разрешения ЭУ MPD, эффективности регистрации в ЭУ MPD и спектров по поперечному импульсу для $K^*(892)^\pm$ - и $\Sigma(1385)^\pm$ -резонансов. Проведена оценка объема выборки данных ($Bi + Bi$)-столкновений, позволяющей восстановить свойства $K^*(892)^\pm$ и $\Sigma(1385)^\pm$ с достаточно хорошей точностью для исследования рождения этих резонансов.

Ключевые слова: столкновение ядер висмута, рождение, резонанс, ускоритель NICA, детектор MPD

Финансирование: Работа выполнена в рамках Государственного задания на проведение фундаментальных исследований (код темы FSEG-2025-0009).

Ссылка для цитирования: Бердников Я. А., Иванищев Д. А., Котов Д. О., Малаев М. В., Рябов А. Ю. Возможности измерять свойства заряженных $K^*(892)$ -мезонов и $\Sigma(1385)$ -барионов в столкновениях ядер висмута при энергии 9,2 ГэВ в ускорителе NICA на экспериментальной установке MPD // Научно-технические ведомости СПбГПУ. Физико-математические науки. 2025. Т. 18. № 2. С. 119–131. DOI: <https://doi.org/10.18721/JPM.18211>

Статья открытого доступа, распространяемая по лицензии CC BY-NC 4.0 (<https://creativecommons.org/licenses/by-nc/4.0/>)

Introduction

One of the main goals of experiments on collisions of relativistic heavy nuclei is to construct a phase diagram of quantum chromodynamic (QCD) matter and to study the properties of such matter at high temperatures and baryon densities. Convincing evidence for production of strongly interacting quark-gluon plasma (QGP) has been obtained in collisions of heavy nuclei at energies achieved at the Relativistic Heavy Ion Collider (RHIC) at Brookhaven National Laboratory (BNL, USA), the Super Proton Synchrotron (SPS) and the Large Hadron Collider (LHC) at the European Organization for Nuclear Research (CERN, Switzerland) [1, 2].



The evolution of the QGP is successfully described by hydrodynamic models assuming the presence of local thermal equilibrium and a number of specific initial conditions [3, 4]. The collision of relativistic heavy nuclei begins with primary nucleon-nucleon interactions. This is followed by the pre-equilibrium phase and production of QGP. As the system formed in collisions of relativistic heavy nuclei expands and cools, the process of hadronization begins, with the QGP subsequently transforming into colorless hadrons. Quarks and gluons are trapped inside hadrons. A dense and hot gas is produced from stable hadrons and resonances. The system reaches chemical freeze-out, at which inelastic collisions among hadrons cease, and the yields of stable particles are extracted [5].

After chemical freeze-out, the hadrons continue to interact with each other through elastic or pseudo-elastic (scattering through an intermediate state) scattering, exchanging momentum. The system reaches a stage when the mean free path of hadrons becomes significantly larger than the size of the system, i.e., the so-called kinetic freeze-out occurs. At this stage, a momentum distribution of hadrons is formed, their composition no longer changes and the hadrons move freely towards the detector devices. Since the temperatures of chemical freeze-out and the quark-hadron transition are close to each other, the phase between chemical and kinetic freezing is called hadronic [6]. The late hadronic phase of collision between relativistic heavy nuclei is a unique medium for studying the hadron system at high temperatures and densities. Understanding the processes occurring in excited hadronic gas is of paramount importance for interpreting the observables used to characterize chemical and kinetic freeze-out, the hadronic phase, and, more broadly, the time evolution of a system formed in collisions of relativistic heavy ions. The properties of the hadronic phase are investigated by measuring hadron decays of short-lived resonances [7]. The lifetime τ of short-lived hadronic resonances is rather short and comparable to the duration of the hadronic phase (about 10 fm/c [8]). In this context, short-lived hadronic resonances are sensitive probes for studying the hadronic phase. Hadronic resonances with the shortest lifetime, such as $\rho(770)$ meson ($\tau \approx 1$ fm/c [9]), decay during the hadronic phase. Their daughter particles can be scattered by the surrounding hadrons in dense hadronic matter, changing the momentum and direction of motion. As a result, the initial information about the resonance from which they originated is lost.

Due to the lack of correlation between the daughter particles, the resonance cannot be reconstructed by the standard invariant mass analysis, and the measured yield appears to be suppressed compared to the expected value [8]. Other observables of the resonances also change, such as the shape of the transverse momentum spectrum, mass, width, etc. The situation is further complicated by recombination effects, where hadrons in the hadronic gas recombine to produce new resonances, leading to an increase in the yield compared to its initial value. The intensity of these two processes depends on the lifetime of the hadronic phase, the density of the hadronic medium, the cross section of interactions between resonance decay products and other hadrons, and the lifetime of the resonances themselves.

The predominance of one effect over another can be investigated by studying the ratio of the resonance yields to the yields of long-lived hadrons with the same quark composition as a function of collision centrality. Hadronic resonances with a long lifetime, such as the $\phi(1020)$ meson ($\tau \approx 45$ fm/c [9]), most likely ‘survive’ the hadronic phase and decay in vacuum after kinetic freeze-out. This feature of such resonances is used for comparison with the production of shorter-lived resonances in reference measurements [10].

In addition to different lifetimes, hadronic resonances have different quark composition, mass, baryon number and strangeness. Therefore, comprehensive analysis of resonance production allows to understand not only the properties of the hadronic phase and its evolution, but also other effects peculiar to dense and hot nuclear matter. These are, for example, the mechanisms of hadronization in the region of intermediate and large transverse momenta, the dynamics of processes and reactions forming the transverse momentum spectra of particles, the excess yield of baryons relative to mesons, the excess yield of strangeness, etc. [10]. Hadronic resonances are produced in sufficient numbers. Daughter particles of their hadronic decays can be detected using detector setups, and their properties can be easily reconstructed by the invariant mass method even for cascade resonance decays.

The following resonances with dominant hadronic cascade decays play a special role for systematic study of hadronic resonances [9]:

Elementary particle	Lifetime τ , fm/c
$\Sigma(1385)^-$ baryon	≈ 5.01 ,
$\Sigma(1385)^+$ baryon	≈ 5.45 ,
$K^*(892)^+$ meson	≈ 3.84 ,
$K^*(892)^-$ meson	≈ 3.83 .

These resonances have lifetimes comparable to the lifetime of the hadronic phase. Similar to $K^*(892)^0$ and $\rho(770)$ mesons, they decay during the hadronic phase. Depending on the pre-dominance of rescattering or recombination effects, their yield may be suppressed or excessive, compared with the reference measurements of the yield of quasi-stable particles with a similar quark composition. Experimental observation of the predominance of a specific effect for a wide range of resonances allows to more accurately define the cross sections of hadronic interactions to describe the known hadronic processes for simulation of the hadronic phase.

The quark compositions of $\Sigma(1385)^-(uss)$, $\Sigma(1385)^+(dds)$ baryons as well as $K^*(892)^+-(s\bar{u})$ and $K^*(892)^--(u\bar{s})$ mesons include strange quarks; unlike the ϕ meson, they are open-strange. This property of these resonances allows to explore the production of strangeness more comprehensively by measuring their production together with the production of ϕ mesons. The different number of quarks included in the resonances under consideration also makes it possible to use them to study the excess yield of baryons relative to mesons, the mechanisms of hadronization, etc.

In the near future, after the Nuclotron-based Ion Collider (NICA) at the Joint Institute for Nuclear Research (Dubna, Russia) is commissioned, an experiment on studying the processes during collisions of heavy nuclei (Multi-Purpose Detector (MPD)) will begin at the collider facility [11]. It is expected that the first colliding systems at the NICA will be the nuclei of bismuth ($\text{Bi} + \text{Bi}$) and xenon ($\text{Xe} + \text{Xe}$) atoms at a center-of-mass energy (per nucleon pair) $\sqrt{s_{NN}} = 7.0\text{--}9.2$ GeV.

Systematic study of the production of resonances in collisions of relativistic nuclei at the energy of NICA is one of the main objectives of the MPD experiment, continuing the research on the production of resonances at the SPS, RHIC and LHC accelerators.

Preparations are currently underway for the launch of the collider facility. Measurement techniques are developed and potential observables are estimated based on model calculations. Special attention is paid to the development of complex algorithms, validated based on model calculations.

The goal of this study is to determine the possibility of measuring the properties of hadronic resonances of $\Sigma(1385)^-$ and $\Sigma(1385)^+$ baryons as well as $K^*(892)^+-(s\bar{u})$ and $K^*(892)^--(u\bar{s})$ mesons using the MPD setup in the NICA accelerator in collisions of bismuth nuclei at $\sqrt{s_{NN}} = 9.2$ GeV in hadron cascade decay channels

$$\Sigma(1385)^- \rightarrow \Lambda + \pi^-,$$

$$\Sigma(1385)^+ \rightarrow \Lambda + \pi^+ (\Lambda \rightarrow p + \pi^-),$$

$$K^*(892)^+ \rightarrow K_S + \pi^+,$$

$$K^*(892)^- \rightarrow K_S + \pi^- (K_S \rightarrow \pi^+ + \pi^-)$$

in the rapidity range $|\eta| < 0.5$ and depending on the collision centrality.

Experimental setup of the MPD and computational procedure

This facility is one of the two large detector systems at the NICA accelerator, optimized for studying dense and hot matter formed in collisions of relativistic heavy ions. The facility includes a central part, which has a large time projection chamber, a time-of-flight detector and an electromagnetic calorimeter (located inside a superconducting solenoid). Detectors are connected to the central part from the front and back, which are used to select events, measure the vertex and time of interaction, as well as collision centrality of heavy ions. The most detailed information about the detectors of the experimental MPD setup, their parameters and efficiency evaluation can be found [11]. The paper describes the capabilities of the Time Projection Chamber (TPC) for reconstructing charged particle tracks and particle detection, as well as the Time-Of-Flight (TOF) detector for particle detection.



The MPD experiment, like the entire NICA facility, is under construction and is scheduled to be launched in the coming years. In view of this, efforts are underway to reliably simulate collisions of heavy ions at energies expected at the NICA accelerator in both the collider configuration and the configuration with fixed-target collisions. Detailed modeling of the responses of various detector subsystems included in the MPD experimental setup is also carried out in order to evaluate the capabilities of the experimental setup to recover signals from various kinds of physical processes that are supposed to be studied in the MPD experiment, in particular, those occurring during collisions of different systems at different collision energies.

In this paper, we analyze data obtained by simulating collisions of Bi nuclei at energy $\sqrt{s_{NN}} = 9.2$ GeV. The UrQMD event generator, one of the most well-known and popular software packages for reliable simulation of heavy ion interactions in the energy range expected at the NICA accelerator, was used to simulate Bi + Bi collisions in a wide range of target parameter values. The studied resonances were declared stable particles in the input settings of the event generator.

Since the goal of this work was to explore the possibilities of a future MPD setup for reconstructing signals from cascade resonance decays, this setting was used to minimize distortion of the results obtained. The distortions are caused by the effects of the late hadronic phase in the interaction of heavy relativistic ions (rescattering and regeneration of daughter particles in hadronic gas). The simulated (Bi + Bi) collision events obtained by the UrQMD generator were then used to simulate the response of the MPD using the MpdRoot software package [11]. This package serves as the main tool for both simulating and processing the results obtained by the MPD setup. It contains the most up-to-date, accurate and detailed geometry of all detector subsystems, described using the GEANT software package, as well as tools for reconstructing charged particle tracks, signal processing of electromagnetic and hadronic calorimeters, particle detection, etc. The MpdRoot package was also applied to simulate the decay of the studied resonances in accordance with their tabulated parameters using the GEANT software package [9].

In this paper, we studied the decays of the following resonances in cascade modes (with the presence of a secondary vertex):

$$K^*(892)^\pm \rightarrow K_S + \pi^\pm (K_S \rightarrow \pi^+ + \pi^-),$$

$$\Sigma(1385)^\pm \rightarrow \Lambda + \pi^\pm (\Lambda \rightarrow p + \pi^-).$$

Analysis of such decays is peculiar in that the secondary vertex of the decay of K_S mesons and Λ baryons must be reconstructed before reconstructing the signal from the decay of the studied resonance. Since the inner tracking system will not be assembled at the first stage of experiments with the MPD setup (in the future it will allow more accurate reconstruction of secondary vertices), this study was aimed at optimizing the selection of candidates (by the required criteria) for secondary vertex from the decay of K_S mesons and Λ baryons (in particular, using tools from the MpdRoot software package). It was necessary to minimize the background level in the resulting distributions without significant loss of useful signal. More efficient algorithms were used for reconstructing charged particle tracks, and the data sample for (Bi + Bi) collisions was increased to 50 million collisions, compared with those described in [12, 13] (where it was 5 million), considering the capabilities of the MPD setup for measuring the properties of $K^*(892)^\pm$ and $\Sigma(1385)^\pm$ resonances in (Au + Au) collisions at energies $\sqrt{s_{NN}} = 4.0, 7.7$ and 11.0 GeV [12] and Bi + Bi collisions at energies $\sqrt{s_{NN}} = 9.2$ GeV [13]. In addition, the detector subsystems of the MPD setup were described in more detail based on new information.

Thanks to the application of new optimized algorithms and a larger-scale study, we obtained for the first time new interesting results reflecting the dependence on the collision centrality (which is the most important).

The properties of $K^*(892)^+$ and $K^*(892)^-$ resonances as well as $\Sigma(1385)^+$ and $\Sigma(1385)^-$ resonances are close, while their hadronic decays differ by the pion charge. This paper considered averaged sums to expand statistics and facilitate the reconstruction of the properties of the studied resonances.

$$[K^*(892)^+ + K^*(892)^-]/2 \text{ and } [\Sigma(1385)^+ + \Sigma(1385)^-]/2.$$

Events with a reconstructed interaction vertex within 130 cm along the z axis from the geometric center of the experimental setup were selected from the total sample. This requirement is imposed because constant trigger efficiency must be maintained along the z -coordinate of the interaction vertex. We estimated the centrality of events based on information about the multiplicity of charged particles reconstructed in the TPC detector [10].

A comprehensive technique was developed and improved to reconstruct the signal from the decays of the studied resonances taking into account the topology of the decays, the parameters and capabilities of the MPD, as well as possible background processes distorting the reconstructed signal. For each event, all the analyzed tracks of charged particles were tested for several criteria to select the tracks to be used to reconstruct the signal from the decays of the studied resonances. All tracks should be identified either as pions or as protons (depending on which type of particles were selected at this stage) using information from the TPC and TOF detectors. Only the most accurately reconstructed tracks were considered for selection; the selection criteria used were the minimal number of points in the TPC used to reconstruct the track and the maximum pseudorapidity of the reconstructed charged particle track.

To select pions from direct decay of $K^*(895)^\pm$ and $\Sigma(1385)^\pm$ resonances, the distance of the closest approach between the reconstructed track and the primary interaction vertex was also checked.

A separate stage was the selection of candidates and the reconstruction of the secondary decay vertex of K_S mesons and Λ baryons. In addition to the track selection criteria described above, the criterion of the minimal value of the parameter χ^2 was used for the selection of pions (protons) for matching the reconstructed track to the primary vertex of the interaction. The tracks selected in this way were combined into various $\pi^+\pi^-$ ($p\pi^-$) pairs in the case of reconstruction of the secondary vertex from the decay of K_S mesons (Λ baryons). Each analyzed pair was checked against the criteria for daughter particles from the decay of K_S mesons or Λ baryons:

- maximum distance between two tracks at the secondary decay vertex;
- reconstruction quality of the secondary vertex (maximum value of χ^2);
- minimum distance between the primary and secondary decay vertices;
- maximum angle between the vector connecting the primary and secondary vertices and the vector of the reconstructed momentum of K_S meson (Λ baryon).

As a result, only pairs that passed all the selection criteria were used to reconstruct the invariant mass of the $\pi^+\pi^-$ ($p\pi^-$) pair to isolate the signal from the decay of K_S mesons (Λ baryons).

Fig. 1 shows examples of the distributions of the reconstructed invariant masses for $\pi^+\pi^-$ and $p\pi^-$ pairs before and after applying the selection criteria. Evidently, applying these selection criteria significantly suppresses the background component of the distributions, which makes it possible to isolate signals with minimal background fraction from the decays of K_S mesons and Λ baryons for further analysis.

For the purpose of further analysis, candidates for decay of K_S mesons and Λ baryons in the range of ± 2 standard deviations from the tabulated mass of the K_S meson or Λ baryon were selected from the distributions shown in Fig. 1, *b*, *d*. Candidates for K_S mesons (Λ -baryons) selected in this way were combined with charged pions that passed all the selection criteria, generating the distributions of invariant masses for πK_S ($\pi\Lambda$) pairs. The obtained distributions contained, in addition to the signal from the decays of the studied resonances, a significant combinatorial background, which was evaluated by the event mixing method. Close values of the z -coordinate of the collision vertex position and the multiplicity of reconstructed event particles were selected for each analyzed event to evaluate the combinatorial background. The method described above was used to reconstruct the invariant mass of πK_S ($\pi\Lambda$) pairs, however, the pions for this pair were taken from the analyzed event, and candidates for K_S mesons (Λ baryons) were taken from selected similar events. The distribution of invariant masses obtained by event mixing was normalized by the analyzed distribution in the invariant mass region, where no useful signal was expected; then this distribution was subtracted from the analyzed distribution. Fig. 2 shows examples of the distributions of invariant masses for πK_S and $\pi\Lambda$ pairs before and after subtracting the combinatorial background.

The distribution formed after subtracting the combinatorial background was fitted to a composite function to calculate the yields of $K^*(892)^\pm$ and $\Sigma(1385)^\pm$ resonances in (Bi + Bi) collisions at $\sqrt{s_{NN}} = 9.2$ GeV, obtained after applying all selection criteria.

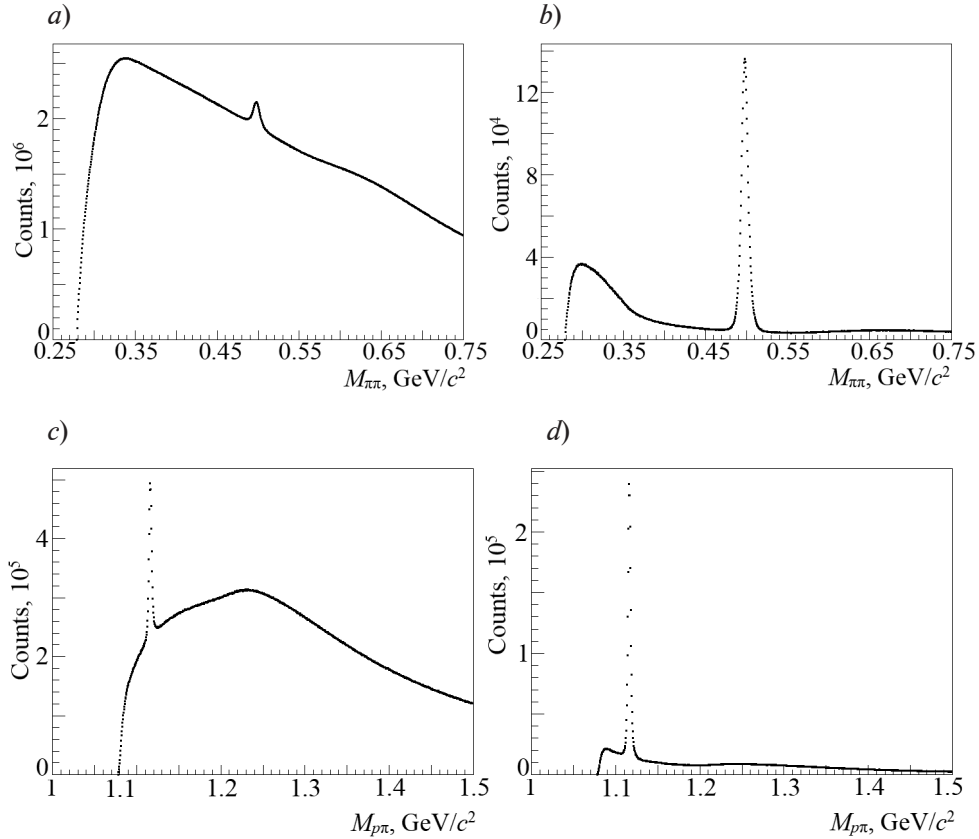


Fig. 1. Invariant mass spectra for pair of oppositely charged pions $\pi\pi$ (a, b) and proton- π^- pair (c, d) in collisions of bismuth (Bi + Bi) nuclei at $\sqrt{s_{NN}} = 9.2$ GeV before (a, c) and after (b, d) applying the selection criteria. Spectra were reconstructed in the transverse momentum range $0.4 < p_T < 0.6$ GeV/c for both pairs.

The fitting function includes a convolution of the Breit–Wigner function (to describe the spectral shape of the resonance) and a Gaussian (to account for the mass resolution of the MPD), as well as a polynomial to account for the residual background. The integral of the Breit–Wigner function convolved with the Gaussian was taken as the yield.

The mass resolution for each analyzed transverse momentum range was estimated by constructing the distribution of the difference between the values of the generated and reconstructed mass of the studied resonance. This distribution was fitted to the Gaussian, and the width obtained from the fit was taken as the mass resolution [10]. Fig. 3 shows the dependences of mass resolution of the MPD setup on the transverse momentum value in the case of decay reconstruction.

$$K^*(892)^\pm \rightarrow K_S + \pi^\pm \text{ (a) and } \Sigma(1385)^\pm \rightarrow \Lambda + \pi^\pm \text{ (b)}.$$

Fig. 4 shows the distributions of decay reconstruction efficiency.

$$K^*(892)^\pm \rightarrow K_S + \pi^\pm \text{ and } \Sigma(1385)^\pm \rightarrow \Lambda + \pi^\pm \text{ (b)}$$

in (Bi + Bi) collisions at $\sqrt{s_{NN}} = 9.2$ GeV in different centrality bins. The distributions were obtained as a function of the transverse momentum value. Although the reconstruction efficiency is small at low transverse momenta in the case of $K^*(892)^\pm$ mesons, it still exceeds zero, while in the case of $\Sigma(1385)^\pm$ baryons, the efficiency drops to zero, imposing restrictions on the transverse momenta that are minimally achievable for signal reconstruction from baryon decays. As the transverse momentum increases, the reconstruction efficiencies of $K^*(892)^\pm$ and $\Sigma(1385)^\pm$ resonances increase, reaching a value of 0.2, after which they remain stable. This means that the maximum achievable values of the transverse momentum are limited only by the statistical sample collected.

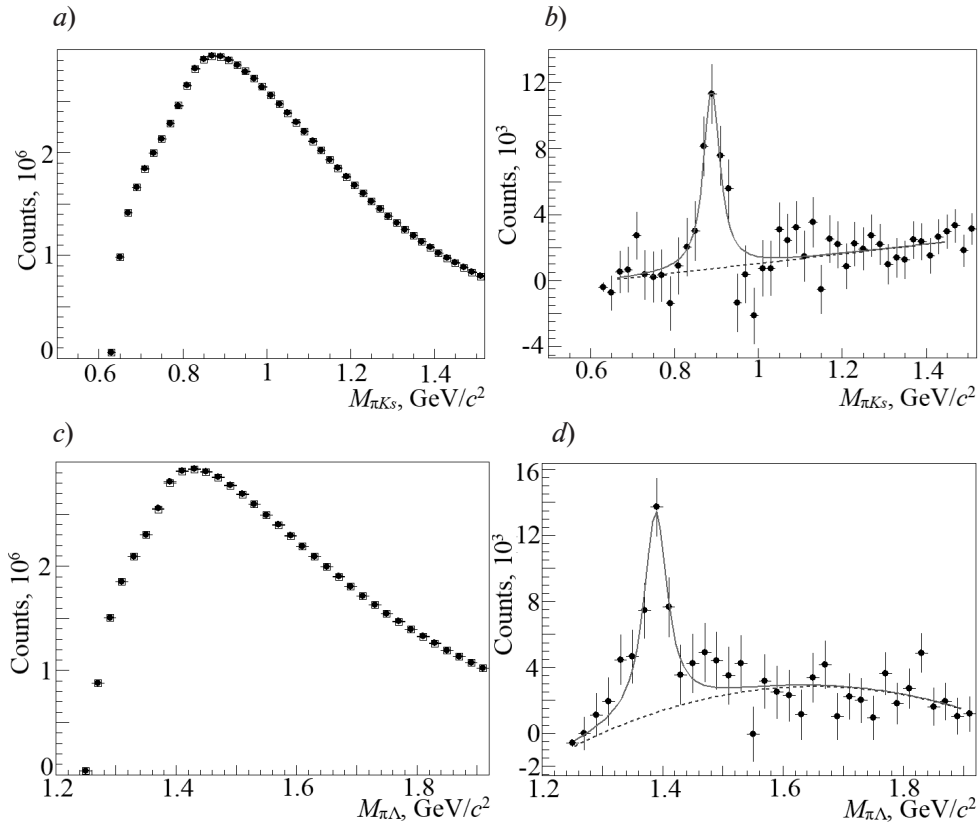


Fig. 2. Invariant mass spectra for πK_S (a, b) and $\pi \Lambda$ (c, d) pairs (black symbols) in (Bi + Bi) collisions at $\sqrt{s_{NN}} = 9.2$ GeV before (a, c) and after (b, d) subtraction of the combinatorial background (squares).

Spectra were reconstructed in the transverse momentum ranges $0.4 < p_T^{\pi K_S} < 0.6$ GeV/c and $0.4 < p_T^{\pi \Lambda} < 0.6$ GeV/c for πK_S and $\pi \Lambda$ pairs, respectively. Breit-Wigner function convolved with a Gaussian is used to reconstruct the peak (solid line); second-degree polynomial is used for the correlated background (dashed line).

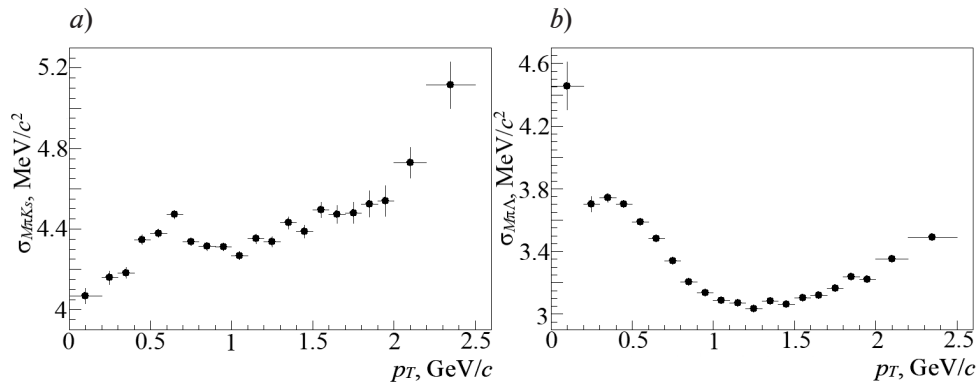


Fig. 3. Dependences of mass resolution of MPD ($\sigma_{M\pi K_S}$ and $\sigma_{M\pi \Lambda}$) on transverse momentum p_T of πK_S (a) and $\pi \Lambda$ (b) pairs for $K^*(892)^\pm \rightarrow K_S + \pi^\pm$ (a) and $\Sigma(1385)^\pm \rightarrow \Lambda + \pi^\pm$ (b) decay channels in (Bi + Bi) collisions at $\sqrt{s_{NN}} = 9.2$ GeV.

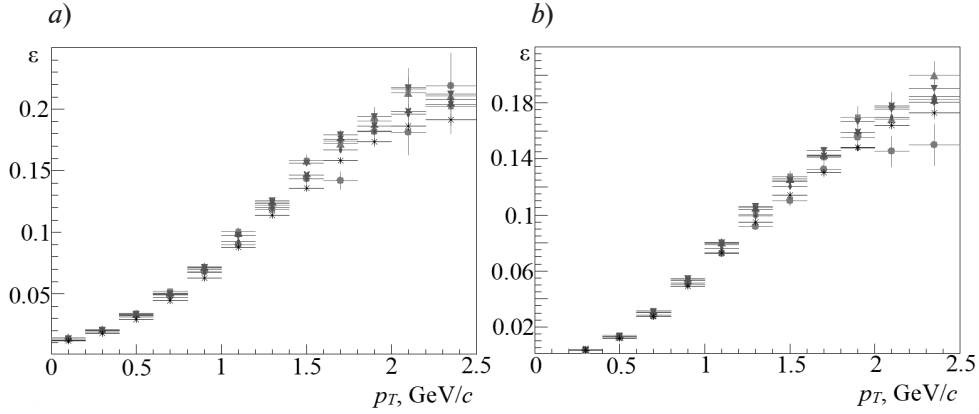


Fig. 4. Dependences of detection efficiency ε for $K^*(892)^\pm$ and $\Sigma(1385)^\pm$ resonances on transverse momentum in $K^*(892)^\pm \rightarrow K_S + \pi^\pm$ (a) and $\Sigma(1385)^\pm \rightarrow \Lambda + \pi^\pm$ (b) decay channels, extracted using MPD
Efficiency was calculated for (Bi + Bi) collisions at $\sqrt{s_{NN}} = 9.2$ GeV for 7 centrality bins, %: 0–10 (*), 10–20 (♦), 20–30 (*), 30–40 (▼), 40–50 (▲), 50–60 (■) and 60–90 (•)

Computational results

To construct the dependence of invariant yields on the transverse momentum (the so-called transverse momentum spectrum), the differential yields were calculated for each of the considered transverse momentum ranges and centrality bins of (Bi + Bi) collisions using the following formula [10]:

$$\frac{d^2 N}{dp_T dy} = \frac{N(p_T)}{N_{ev} \varepsilon(p_T) \Delta p_T \Delta y}, \quad (1)$$

where $N(p_T)$ are the yields of $K^*(892)^\pm$ - and $\Sigma(1385)^\pm$ -resonances; N_{ev} is the number of collisions analyzed; p_T , GeV/c, is the transverse momentum of $K^*(892)^\pm$ - and $\Sigma(1385)^\pm$ -resonances; Δp_T , GeV/c, is the transverse momentum range within which the yields of these resonances are determined; Δy is the rapidity range from -0.5 до 0.5 ; $\varepsilon(p_T)$ is the detection efficiency of $K^*(892)^\pm$ - and $\Sigma(1385)^\pm$ -resonances, equal to the geometric acceptance of the MPD for the studied hadronic resonance decays multiplied by the average decay probabilities for each channel

$$K^*(892)^\pm \rightarrow K_S + \pi^\pm \text{ and } \Sigma(1385)^\pm \rightarrow \Lambda + \pi^\pm.$$

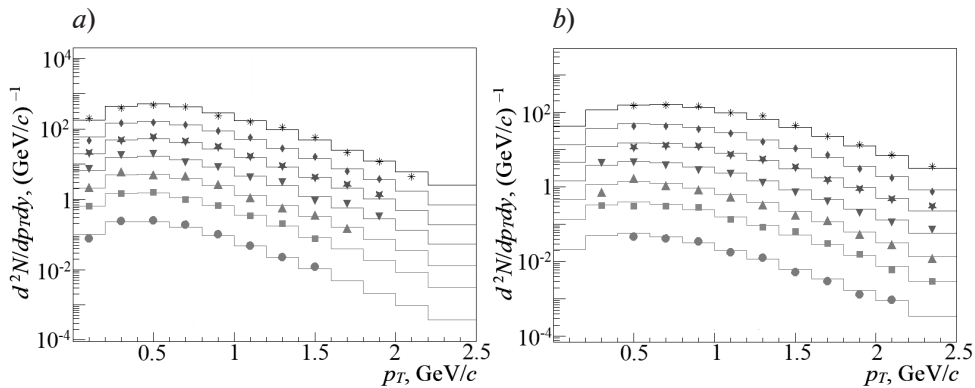


Fig. 5. Reconstructed transverse momentum spectra (symbols) and similar spectra initially generated by event generator (lines) for $K^*(892)^\pm$ (a) and $\Sigma(1385)^\pm$ (b) resonances in the rapidity range $|y| < 0.5$

These data correspond to the same collisions and energies, for the same centrality bins and notations as in Fig. 4. For clarity, the enlarged spectra are shown in one graph

The transverse momentum spectra for $K^*(892)^\pm$ and $\Sigma(1385)^\pm$ resonances are shown in Fig. 5. The spectra were obtained for various centrality bins of (Bi + Bi) collisions at $\sqrt{s_{NN}} = 9.2$ GeV in the rapidity range $|y| < 0.5$. The real transverse momentum spectra of $K^*(892)^\pm$ and $\Sigma(1385)^\pm$ resonances generated by the event generator are also shown for comparison. Evidently, the spectra are similar, which confirms the adequacy of the analytical procedure we developed. It can also be seen from the obtained transverse momentum spectra that for measuring the properties of $K^*(892)^\pm$ and $\Sigma(1385)^\pm$ resonances in hadron cascade decay channels

$$K^*(892)^\pm \rightarrow K_S + \pi^\pm \text{ and } \Sigma(1385)^\pm \rightarrow \Lambda + \pi^\pm,$$

depending on the transverse momentum and collision centrality, a sample exceeding 50 million (Bi + Bi) collisions is sufficient.

Conclusion

The paper reports on the feasibility of measuring the properties of $K^*(892)^\pm$ and $\Sigma(1385)^\pm$ resonances in collisions of bismuth nuclei at energy $\sqrt{s_{NN}} = 9.2$ GeV at the MPD experimental facility that is part of the NICA accelerator complex. The study was performed by simulating the collisions of bismuth nuclei and reconstructing the following hadronic cascade decays:

$$\Sigma(1385)^- \rightarrow \Lambda + \pi^-,$$

$$\Sigma(1385)^+ \rightarrow \Lambda + \pi^+ (\Lambda \rightarrow p + \pi^-),$$

$$K^*(892)^+ \rightarrow K_S + \pi^+,$$

$$K^*(892)^- \rightarrow K_S + \pi^- (K_S \rightarrow \pi^+ + \pi^-).$$

The dependences of the main process parameters on the transverse momentum were obtained in these decays, for various centrality bins of (Bi + Bi) collisions in the rapidity range from -0.5 to 0.5 . It was established that the accumulation of over 50 million of these collisions is sufficient for reconstructing the properties of $K^*(892)^\pm$ and $\Sigma(1385)^\pm$ resonances with satisfactory accuracy to study the production of $K^*(892)^\pm$ and $\Sigma(1385)^\pm$ resonances in a wide range of transverse momenta: from 0 for $K^*(892)^\pm$ mesons and from 0.2 for $\Sigma(1385)^\pm$ baryons to 2.5 GeV/c for both resonances and centralities of (Bi + Bi) collisions with a 10% bin for central and semi-central collisions, as well as with a 30% bin for peripheral ones.

REFERENCES

1. Adcox K., Adler S. S., Afanasiev S. V., et al. (PHENIX Collaboration), Formation of dense partonic matter in relativistic nucleus–nucleus collisions at RHIC: Experimental evaluation by the PHENIX Collaboration, Nucl. Phys. A. 757 (1–2) (2005) 184 – 283.
2. Aamodt K., Abelev B., Quintana A. A., et al. (ALICE Collaboration), Higher harmonic anisotropic flow measurements of charged particles in Pb–Pb collisions at $\sqrt{s_{NN}} = 2.76$ TeV, Phys. Rev. Lett. 107 (3) (2011) 032301.
3. Schenke B., Shen C., Tribedy P., Hybrid color glass condensate and hydrodynamic description of the relativistic heavy ion collider small system scan, Phys. Lett. B. 803 (10 April) (2020) 135322.
4. Andronic A., Braun-Munzinger P., Redlich K., Stachel J., Decoding the phase structure of QCD via particle production at high energy, Nature. 561 (7723) (2018) 321 – 330.
5. Heinz U. W., Kestin G., Jozso's legacy: Chemical and kinetic freeze-out in heavy-ion collisions. Eur. Phys. J. Spec. Top. 155 (1) (2008) 75 – 87.
6. Steinheimer J., Aichelin J., Bleicher M., Stucker H., Influence of the hadronic phase on observables in ultrarelativistic heavy ion collisions, Phys. Rev. C. 95 (6) (2017) 064902.
7. Riabov V., Short-lived resonances as probes of the medium produced in heavy-ion collisions, Particles. 4 (1) (2021) 1–10.
8. Acharya S., Adamovč D., Adler A., et al. (ALICE Collaboration), Evidence of rescattering effect in Pb–Pb collisions at the LHC through production of $K^*(892)^0$ and $\phi(1020)$ mesons, Phys. Lett. B. 802 (10 March) (2020) 135225.

9. **Workman R. L., Burkert V. D., Crede V., et al.** (Particle Data Group and Others), Review of particle physics, *Prog. Theor. Exp. Phys.* 2022 (8) (2022) 083C01.
10. **Berdnikov Ya. A., Ivanishchev D. A., Kotov D. O., et al.**, Feasibility to measure the properties of $\phi(1020)$ meson in collisions of bismuth nuclei at an energy of 9.2 GeV in the NICA collider using the MPD experimental setup, *St. Petersburg State Polytechnical University Journal. Physics and Mathematics.* 18 (1) (2025) 129–141. (in Russian).
11. **Abgaryan V., Acevedo Kado R., Afanasyev S. V., et al.**, Status and initial physics performance studies of the MPD experiment at NICA, *Eur. Phys. J. A.* 58 (7) (2022) 140.
12. **Ivanishchev D., Kotov D., Malaev M., et al.**, Resonance reconstruction in the MPD, *Particles.* 4 (1) (2021) 29–36.
13. **Ivanishchev D. A., Kotov D. O., Kryshen E. L., et al.**, Hadronic resonances as probes of late hadronic phase in heavy-ion collisions at NICA energies, *PEPAN.* 54 (3) (2023) 461–472.

СПИСОК ЛИТЕРАТУРЫ

1. **Adcox K., Adler S. S., Afanasiev S., et al.** (PHENIX Collaboration). Formation of dense partonic matter in relativistic nucleus–nucleus collisions at RHIC: Experimental evaluation by the PHENIX Collaboration // *Nuclear Physics A.* 2005. Vol. 757. No. 1–2. Pp. 184 – 283.
2. **Aamodt K., Abelev B., Quintana A. A., et al.** (ALICE Collaboration). Higher harmonic anisotropic flow measurements of charged particles in Pb-Pb collisions at $\sqrt{s_{NN}} = 2.76$ TeV // *Physical Review Letters.* 2011. Vol. 107. No. 3. P. 032301.
3. **Schenke B., Shen C., Tribedy P.** Hybrid color glass condensate and hydrodynamic description of the relativistic heavy ion collider small system scan // *Physics Letters B.* 2020. Vol. 803 (10 April) P. 135322.
4. **Andronic A., Braun-Munzinger P., Redlich K., Stachel J.** Decoding the phase structure of QCD via particle production at high energy // *Nature.* 2018. Vol. 561. No. 7723. Pp. 321 – 330.
5. **Heinz U. W., Kestin G.** Jozso’s legacy: Chemical and kinetic freeze-out in heavy-ion collisions // *The European Physical Journal Special Topics.* 2008. Vol. 155. No. 1. Pp. 75 – 87.
6. **Steinheimer J., Aichelin J., Bleicher M., Stucker H.** Influence of the hadronic phase on observables in ultrarelativistic heavy ion collisions // *Physical Review C.* 2017. Vol. 95. No. 6. P. 064902.
7. **Riabov V.** Short-lived resonances as probes of the medium produced in heavy-ion collisions // *Particles.* 2021. Vol. 4. No. 1. Pp. 1–10.
8. **Acharya S., Adamovč D., Adler A., et al.** (ALICE Collaboration). Evidence of rescattering effect in Pb–Pb collisions at the LHC through production of $K^*(892)^0$ and $\phi(1020)$ mesons // *Physics Letters B.* 2020. Vol. 802 (10 March) P. 135225.
9. **Workman R. L., Burkert V. D., Crede V., et al.** (Particle Data Group and Others). Review of particle physics // *Progress of Theoretical and Experimental Physics.* 2022. Vol. 2022. No. 8. P. 083C01.
10. **Бердников Я. А., Иванищев Д. А., Котов Д. О., Малаев М. В., Рябов А. Ю.** Возможности измерять свойства $\phi(1020)$ -мезона в столкновениях ядер висмута при энергии 9,2 ГэВ в ускорителе NICA на экспериментальной установке MPD // *Научно-технические ведомости СПбГПУ. Физико-математические науки.* 2025. Т. 18. № 1. С. 129–141.
11. **Abgaryan V., Acevedo Kado R., Afanasyev S. V., et al.** Status and initial physics performance studies of the MPD experiment at NICA // *The European Physical Journal A.* 2022. Vol. 58. No. 7. P. 140.
12. **Ivanishchev D., Kotov D., Malaev M., Riabov V., Riabov Y.** Resonance reconstruction in the MPD // *Particles.* 2021. Vol. 4. No. 1. Pp. 29–36.
13. **Иванищев Д. А., Котов Д. О., Крышень Е. Л., Малаев М. В., Рябов В. Г., Рябов Ю. Г.** Адронные резонансы как пробники поздней адронной фазы в столкновениях тяжелых ионов при энергиях ускорителя NICA // *Физика элементарных частиц и атомного ядра.* 2023. Т. 54. № 3. С. 461–472.

THE AUTHORS

BERDNIKOV Yaroslav A.

Peter the Great St. Petersburg Polytechnic University
29 Politechnicheskaya St., St. Petersburg, 195251, Russia
yberdnikov1947@gmail.com
ORCID: 0000-0003-0309-5917

IVANISHCHEV Dmitry A.

Peter the Great St. Petersburg Polytechnic University
29 Politechnicheskaya St., St. Petersburg, 195251, Russia
ivanishchev_da@pnpi.nrcki.ru
ORCID: 0000-0003-3298-3702

KOTOV Dmitry O.

Peter the Great St. Petersburg Polytechnic University
29 Politechnicheskaya St., St. Petersburg, 195251, Russia
Dmitriy.kotov@gmail.com
ORCID: 0000-0002-3395-0454

MALAEV Mikhail V.

Peter the Great St. Petersburg Polytechnic University
29 Politechnicheskaya St., St. Petersburg, 195251, Russia
Mmalayev@gmail.com
ORCID: 0009-0001-9974-0169

RIABOV Andrei Yu.

Petersburg Nuclear Physics Institute named by B. P. Konstantinov of NRC “Kurchatov Institute”
1, Orlova Roshcha (Mcr.), Gatchina, Leningrad Region, 188300, Russia
andrei.riabov@cern.ch
ORCID: 0009-0007-9874-9819

СВЕДЕНИЯ ОБ АВТОРАХ

БЕРДНИКОВ Ярослав Александрович — доктор физико-математических наук, профессор Высшей школы фундаментальных физических исследований Санкт-Петербургского политехнического университета Петра Великого.

195251, Россия, г. Санкт-Петербург, Политехническая ул., 29
yberdnikov1947@gmail.com
ORCID: 0000-0003-0309-5917

ИВАНИЩЕВ Дмитрий Александрович — кандидат физико-математических наук, старший научный сотрудник Высшей школы фундаментальных физических исследований Санкт-Петербургского политехнического университета Петра Великого.

195251, Россия, г. Санкт-Петербург, Политехническая ул., 29
ivanishchev_da@pnpi.nrcki.ru
ORCID: 0000-0003-3298-3702

КОТОВ Дмитрий Олегович — кандидат физико-математических наук, доцент Высшей школы фундаментальных физических исследований Санкт-Петербургского политехнического университета Петра Великого.

195251, Россия, г. Санкт-Петербург, Политехническая ул., 29
Dmitriy.kotov@gmail.com
ORCID: 0000-0002-3395-0454



МАЛАЕВ Михаил Владимирович — кандидат физико-математических наук, старший научный сотрудник Высшей школы фундаментальных физических исследований Санкт-Петербургского политехнического университета Петра Великого.

195251, Россия, г. Санкт-Петербург, Политехническая ул., 29

Mmalayev@gmail.com

ORCID: 0009-0001-9974-0169

РЯБОВ Андрей Юрьевич — аспирант Петербургского института ядерной физики имени Б. П. Константинова НИЦ «Курчатовский институт».

188300, Россия, Ленинградская область, г. Гатчина, микрорайон Орлова Роща, 1

andrei.riabov@cern.ch

ORCID: 0009-0007-9874-9819

Received 16.02.2025. Approved after reviewing 19.02.2025. Accepted 19.02.2025.

Статья поступила в редакцию 16.02.2025. Одобрена после рецензирования 19.02.2025. Принята 19.02.2025.

APPLIED AND COMPUTATIONAL MATHEMATICS

Original article

DOI: <https://doi.org/10.18721/JPM.18212>

AN INVERSE PROBLEM OF DIFFERENTIAL EQUATION SYSTEMS IN CONNECTION WITH THE STUDY OF SEMICONDUCTOR MATERIALS AND BIOMEDICINAL PROCESSES

A. P. Golovitskii[✉]

Peter the Great St. Petersburg Polytechnic University, St. Petersburg, Russia

[✉] alexandergolovitski@yahoo.com

Abstract. This paper puts forward a new method of solving the problem for calculating the unknown and non-measurable parameters, that are included in a system of differential equations, whose solution adequately reproduces the given experimental data, but has no analytical form. The problems of this kind are often found in physical research of semiconductor materials, biomedical processes and in electronics. The novelty lies in the proposed idea of numerical calculations of partial derivatives which has made it possible to adapt the Levenberg – Marquardt method of non-linear approximations for solving the said problem. Our specific examples showed that calculation errors of the parameter values were not more than the experimental errors.

Keywords: inverse problem, differential equation system, indirect measurements, Levenberg–Marquardt method

Funding: The reported study was carried out within the framework of the State Assignment for Fundamental Research (Subject Code FSEG-2023-0016).

Citation: Golovitskii A. P., An inverse problem of differential equation systems in connection with the study of semiconductor materials and biomedical processes, St. Petersburg State Polytechnical University Journal. Physics and Mathematics. 18 (2) (2025) 132–143. DOI: <https://doi.org/10.18721/JPM.18212>

This is an open access article under the CC BY-NC 4.0 license (<https://creativecommons.org/licenses/by-nc/4.0/>)

Научная статья

УДК 519.65, 53.088

DOI: <https://doi.org/10.18721/JPM.18212>

ОБРАТНАЯ ЗАДАЧА СИСТЕМ ДИФФЕРЕНЦИАЛЬНЫХ УРАВНЕНИЙ В СВЯЗИ С ИЗУЧЕНИЕМ ПОЛУПРОВОДНИКОВЫХ МАТЕРИАЛОВ И БИМЕДИЦИНСКИХ ПРОЦЕССОВ

А. П. Головицкий[✉]

Санкт-Петербургский политехнический университет Петра Великого, Санкт-Петербург, Россия

[✉] alexandergolovitski@yahoo.com

Аннотация. В работе представлен новый метод решения задачи вычисления априори неизвестных и не поддающихся прямым измерениям параметров, входящих в состав систем дифференциальных уравнений, адекватно описывающих имеющиеся экспериментальные данные, но не имеющих аналитической формы решения. Задачи такого рода нередко встречаются при физических исследованиях полупроводниковых материалов, а также в электронике, биофизике и медицинской физике. Новизна заключается в предложенной идее численного расчета частных производных, что позволило применить для решения такой задачи метод нелинейной аппроксимации Левенберга – Марквардта. На



конкретных примерах показано, что погрешность вычисления значений параметров оказывается не больше погрешности экспериментальных данных.

Ключевые слова: обратная задача, система дифференциальных уравнений, косвенные измерения, метод Левенберга –Марквардта

Финансирование: Работа выполнена в рамках Государственного задания на проведение фундаментальных исследований (код темы FSEG-2023-0016).

Ссылка для цитирования: Головицкий А. П. Обратная задача систем дифференциальных уравнений в связи с изучением полупроводниковых материалов и биомедицинских процессов // Научно-технические ведомости СПбГПУ. Физико-математические науки. 2025. Т. 18. № 2. С. 132–143. DOI: <https://doi.org/10.18721/JPM.18212>

Статья открытого доступа, распространяемая по лицензии CC BY-NC 4.0 (<https://creativecommons.org/licenses/by-nc/4.0/>)

Introduction

Systems of ordinary differential equations (ODEs) with solutions in the form of periodic nonlinear undamped oscillations are widely used for mathematical modeling of physical, chemical and biological self-oscillatory processes [1–4, 10]. Generally, the argument in these solutions is the time t .

Real processes in living and nonliving matter commonly include a large number of separate subprocesses or stages, often incredibly complex, especially in complex processes of current flow in semiconductor materials [10] or biological processes [3–6, 13]. Ideally, their model description should include a large number of related variables, which complicates the analysis, leads to ill-posedness of models and instability of model solutions, typically obtained numerically, since it often turns out that analytical solutions to such models do not exist.

In view of the above, models have to be simplified for clarity and stability, the number of variables is reduced; some unimportant reactions (as judged by the researchers) are neglected and others are combined into sets to quantify (albeit incompletely) the influence of those numerous reactions that do not determine the overall qualitative course of the given process.

To preserve the quantitative adequacy of simplified models that include such combined reaction sets, it is necessary to correctly define their rate coefficients acting as de-facto fitting parameters.

Notably, even the rates of individual biochemical reactions or the values of some parameters of new semiconductor materials are also known quite approximately; the data from different authors vary greatly.

Models can include unknown or ill-known parameters. It would be optimal to be able to calculate and refine their values to obtain new quantitative physical information.

If the variables that make up the solution of the ODE system are measured experimentally, it becomes possible to calculate unknown parameters to compare computational and experimental model results. Such an inverse problem of the ODE system can become the basis for indirect experimental measurements, when unknown parameters cannot be measured directly but can be calculated through a known relationship (model) with other measurable quantities and/or variables.

The goal of this paper is to develop a procedure for solving such an inverse problem and test it.

Problem statement

In general, the problem is formulated as follows. Experimental data are available about the variables $u(t_i)$, $v(t_i)$, $w(t_i)$, ... , measured (with an error) at k points in time t_i . There is also a system of ODE:

$$\left. \begin{aligned} \dot{u} &= f(t, \tilde{u}, \tilde{v}, \tilde{w}, \dots, a, b, c, \dots) \\ \dot{v} &= g(t, \tilde{u}, \tilde{v}, \tilde{w}, \dots, a, b, c, \dots) \\ \dot{w} &= h(t, \tilde{u}, \tilde{v}, \tilde{w}, \dots, a, b, c, \dots) \\ &\dots\dots\dots \end{aligned} \right\}, \quad (1)$$

with N components of the solution

$$\tilde{u}(t_i, a, b, c, \dots), \tilde{v}(t_i, a, b, c, \dots), \tilde{w}(t_i, a, b, c, \dots), \dots$$

It is assumed that system (1) has no analytical solution and that the components of solution (1) can only be found numerically.

Let us also assume that these components can adequately match the experimental data, denoted below as

$$u_i \equiv u(t_i), v_i \equiv v(t_i), w_i \equiv w(t_i), \dots$$

Let the initial conditions of all equations (1) be set at the conditional time origin t_0 ; then the ODE system (1) is the Cauchy problem. It is required to find unknown numerical values of the parameters a, b, c, \dots included in system (1), minimizing the functional of sums of square deviations of the solution components in system (1) from the corresponding experimental data:

$$S = \sum_{i=1}^k [\tilde{u}(t_i, a, b, c, \dots) - u_i]^2 + \sum_{i=1}^k [\tilde{v}(t_i, a, b, c, \dots) - v_i]^2 + \sum_{i=1}^k [\tilde{w}(t_i, a, b, c, \dots) - w_i]^2 + \dots \rightarrow \min_{a, b, c, \dots} \quad (2)$$

The number of sums in the functional S is equal to n , the number of those variables of system (1) for which experimental data were obtained.

Notably, it was found in the course of this study that it is unnecessary to obtain the experimental data for all N variables of system (1). Data on a smaller number of variables $n < N$, and often only on a single variable is sufficient to calculate the parameters with acceptable accuracy.

A problem similar to the one formulated in this section was posed earlier in [5] for the model of the Belousov–Zhabotinsky reaction [6]. The experimental data in [5] were modeled by solving a direct problem; no additional model error was introduced in these data. The parametric search for the minimum S was carried out in [5] using the Hooke–Jeeves method [7], which is a variant of the coordinate descent method [9]. The method is direct, so that inverse problem (2) was actually solved by searching over solutions to direct problem (1). For such methods of solving inverse problems, convergence is guaranteed only in a very small neighborhood of the minimum; it is also characterized by long calculation times and low accuracy of the results. The calculation accuracy for three reaction rates given in [5] turned out to be rather unsatisfactory: 12, 14, and 420%.

Algorithm for solving the problem

An alternative method is proposed in this paper to find the parameters minimizing functional (2), which is close in theory to the Levenberg–Marquardt nonlinear approximation method [11], including elements of gradient descent along with preconditioning and regularization.

Since solution (1) exists but the analytical form of its components

$$\tilde{u}(t_i, a, b, c, \dots), \tilde{v}(t_i, a, b, c, \dots), \tilde{w}(t_i, a, b, c, \dots), \dots$$

remains unknown, we are forced to assume a nonlinear dependence of the components on the parameters a, b, c, \dots . Therefore, to find the latter, it is advisable to apply one of the methods for nonlinear minimization of the functional S .

All such methods are based on linearization of deviations

$$\tilde{u}(t_i, a, b, c, \dots) - u_i; \tilde{v}(t_i, a, b, c, \dots) - v_i; \tilde{w}(t_i, a, b, c, \dots) - w_i; \dots, \text{ etc.}$$

of relatively small increments of the parameters da, db, dc, \dots .

Let us assume that a certain initial set of parameters is known from physical considerations:



$$a_0, b_0, c_0, \dots \equiv \mathbf{p}_0.$$

Here it makes sense to immediately try to solve system (1) with the initial parameter set \mathbf{p}_0 , calculate the relative residual of the form

$$\rho_0 = \frac{1}{n} \left\{ \frac{\sum_{i=1}^k [\tilde{u}(t_i, a_0, b_0, c_0, \dots) - u_i]^2}{\sum_{i=1}^k u_i^2} + \frac{\sum_{i=1}^k [\tilde{v}(t_i, a_0, b_0, c_0, \dots) - v_i]^2}{\sum_{i=1}^k v_i^2} + \right. \\ \left. + \frac{\sum_{i=1}^k [\tilde{w}(t_i, a_0, b_0, c_0, \dots) - w_i]^2}{\sum_{i=1}^k w_i^2} + \dots \right\}^{1/2} \quad (3)$$

and compare it with the relative experimental error ρ .

If it turns out that $\rho_0 \approx \rho$, we can assume that the required parameters were found. However, this is generally not the case, and $\rho_0 > \rho$. If the value of ρ_0 is excessively higher than the value of ρ , it is worthwhile to refine the initial set by trial and error, varying a_0, b_0, c_0, \dots , finding ρ_0 from expression (3) and comparing the values of ρ_0 and ρ .

We should note that the time dependences of some components of solution (1) often take the form of a sequence of narrow pulses with a large duty cycle. Practice shows that reliable convergence is guaranteed when the pulses of solution (1) overlap with the corresponding experimental data by at least 10%.

Next, we expand the deviation in the i th position:

$$\tilde{u}(t_i, a_0, b_0, c_0, \dots) - u_i; \tilde{v}(t_i, a_0, b_0, c_0, \dots) - v_i; \tilde{w}(t_i, a_0, b_0, c_0, \dots) - w_i; \quad (4)$$

in the vicinity of a_0, b_0, c_0, \dots into a Taylor series with respect to increments of parameters da, db, dc, \dots , retaining only the linear terms of the expansion:

$$S = \sum_{i=1}^k \left\{ \left[\tilde{u}(t_i, a_0, b_0, c_0, \dots) - u_i + \frac{\partial \tilde{u}(t_i)}{\partial a} \Big|_{\mathbf{p}_0} da + \frac{\partial \tilde{u}(t_i)}{\partial b} \Big|_{\mathbf{p}_0} db + \dots \right]^2 + \right. \\ \left. + \left[\tilde{v}(t_i, a_0, b_0, c_0, \dots) - v_i + \frac{\partial \tilde{v}(t_i)}{\partial a} \Big|_{\mathbf{p}_0} da + \frac{\partial \tilde{v}(t_i)}{\partial b} \Big|_{\mathbf{p}_0} db + \dots \right]^2 + \dots \right\} \\ + \left\{ \left[\tilde{w}(t_i, a_0, b_0, c_0, \dots) - w_i + \frac{\partial \tilde{w}(t_i)}{\partial a} \Big|_{\mathbf{p}_0} da + \frac{\partial \tilde{w}(t_i)}{\partial b} \Big|_{\mathbf{p}_0} db + \dots \right]^2 + \dots \right\}. \quad (5)$$

Thus, problem (2) turns out to be linearized with respect to the increments da, db, dc, \dots .

Then, as in the linear least squares method, we should find the partial derivatives

$$\frac{\partial S}{\partial[da]}, \frac{\partial S}{\partial[db]}, \frac{\partial S}{\partial[dc]}, \dots,$$

equate them to zero and obtain a system of linear algebraic equations (SLAE) with respect to the unknowns da, db, dc, \dots :

$$\begin{cases} A_{aa}[da] + A_{ab}[db] + A_{ac}[dc] + \dots = A_{a0}, \\ A_{ba}[da] + A_{bb}[db] + A_{bc}[dc] + \dots = A_{b0}, \\ A_{ca}[da] + A_{cb}[db] + A_{cc}[dc] + \dots = A_{c0}, \\ \dots\dots\dots \end{cases} \quad (6)$$

$$\begin{aligned} A_{ab} &= \sum_{i=1}^k \left[\frac{\partial \tilde{u}(t_i)}{\partial a} \Big|_{p_0} \frac{\partial \tilde{u}(t_i)}{\partial b} \Big|_{p_0} + \frac{\partial \tilde{v}(t_i)}{\partial a} \Big|_{p_0} \frac{\partial \tilde{v}(t_i)}{\partial b} \Big|_{p_0} + \frac{\partial \tilde{w}(t_i)}{\partial a} \Big|_{p_0} \frac{\partial \tilde{w}(t_i)}{\partial b} \Big|_{p_0} + \dots \right]; \\ A_{a0} &= - \sum_{i=1}^k \left\{ \frac{\partial \tilde{u}(t_i)}{\partial a} \Big|_{p_0} [\tilde{u}(t_i, a_0, b_0, c_0, \dots) - u_i] + \frac{\partial \tilde{v}(t_i)}{\partial a} \Big|_{p_0} [\tilde{v}(t_i, a_0, b_0, c_0, \dots) - v_i] + \dots \right\}. \end{aligned} \quad (7)$$

The main problem with applying the linearization method to find the parameters of control systems is that, unlike other nonlinear minimization methods (including the Levenberg–Marquardt method), it is impossible to calculate partial derivatives in (7) analytically, since it was initially assumed that system (1) does not have an analytical solution.

In this paper, it is proposed to find derivatives numerically.

Let us define an initial set $\mathbf{p}_0 \equiv a_0, b_0, c_0, \dots$, and initial conditions of system (1) from the experimental data. We solve system (1) numerically and find the components of the solution

$$\tilde{u}(t_i, a_0, b_0, c_0, \dots), \tilde{v}(t_i, a_0, b_0, c_0, \dots), \dots, \text{etc.}$$

After that, we define a small increment to parameter a_0 , such that $|\delta a| < |a_0|$, and leave all other parameters unchanged. Substituting $a_0 + \delta a$ into system (1) instead of a_0 , we solve it with the same initial conditions and find

$$\tilde{u}(t_i, a_0 + \delta a, b_0, c_0, \dots), \tilde{v}(t_i, a_0 + \delta a, b_0, c_0, \dots) \dots, \text{etc.}$$

Next, calculating the relation

$$\frac{\tilde{u}(t_i, a_0 + \delta a, b_0, c_0, \dots) - \tilde{u}(t_i, a_0, b_0, c_0, \dots)}{\delta a} = \frac{\partial \tilde{u}(t_i, a_0, b_0, c_0, \dots)}{\partial a}, \quad (8)$$

we obtain a numerical equivalent of the partial derivative

$$\frac{\partial \tilde{u}(t_i, a, b, c, \dots)}{\partial a} \Big|_{p_0}.$$

Partial derivatives $\frac{\partial}{\partial a} \Big|_{p_0}$ for the remaining components of solution (1) are found similarly.

Then a small increment is given to the parameter b_0 and numerical analogues $\frac{\partial}{\partial b} \Big|_{p_0}$, etc., are found similarly.

As a result, the problem of calculating all the elements of SLAE (6) is successfully solved.

The solution to SLAE (6) is a vector

$$d\mathbf{p} \equiv [da, db, dc, \dots].$$

Ostensibly, problem (2) should be solved iteratively, defining an initial parameter set \mathbf{p}_0 , constructing and solving a SLAE (6), finding $d\mathbf{p}$ and then $\mathbf{p}_1 = \mathbf{p}_0 + d\mathbf{p}$. After that, it is necessary to check whether the quantity S in Eq. (2) decreases when \mathbf{p}_1 is substituted instead of \mathbf{p}_0 . If it decreases, then \mathbf{p}_1 is taken for \mathbf{p}_0 and the next iteration begins: system (1) is solved again, SLAE (6) is composed, and so on, until the value of S is stabilized as it decreases monotonically.



So far, everything seems logical, since we describe the well-known Gauss–Newton method for finding the minimum. However, we found in this study that this method is basically unsuitable for solving inverse problems of ODE systems in practice. If this method is used, the value of S often does not decrease at all when the initial approximation is not sufficiently close to the set of parameters giving the minimum, and/or when the matrix A from SLAE (6) is ill-conditioned [12].

Solving inverse problems of ODE systems by the Gauss–Newton method, generally yields $S(\mathbf{p}_1) > S(\mathbf{p}_0)$ instead of $S(\mathbf{p}_1) < S(\mathbf{p}_0)$ at first iteration, and $S(\mathbf{p}_1)$ often turns out to be much larger than $S(\mathbf{p}_0)$. This is because physical considerations often give such a set a_0, b_0, c_0, \dots that neither the increments of the parameters da, db, dc, \dots , nor the deviations (4) are sufficiently small to neglect the higher terms of series (5). Then all expressions starting from (5) are, strictly speaking, incorrect, i.e., do not correspond to the problem. However, all these expressions would correspond to it if the increments da, db, dc, \dots were small.

Therefore, we propose, firstly, the same preconditioning procedure with matrix A as in the Levenberg–Marquardt method [11], called scaling, where matrix A is transformed into matrix R :

$$R = \begin{pmatrix} 1 & r_{ab} & r_{ac} & \cdots \\ r_{ba} & 1 & r_{bc} & \cdots \\ r_{ca} & r_{cb} & 1 & \vdots \\ \vdots & \vdots & \cdots & \ddots \end{pmatrix}, \text{ where } \forall m, n > 0 \ r_{mn} = \frac{A_{mn}}{\sqrt{A_{mm}A_{nn}}}. \quad (9)$$

It is also necessary to recalculate the elements in the column of free terms of SLAE (6):

$$\forall m > 0 \ r_{m0} = A_{m0} / \sqrt{A_{mm}}. \quad (10)$$

The scaled SLAE replacing SLAE (6) takes the following matrix form

$$Rz = R_0, \quad (11)$$

and the components of its solution z_m (their number is equal to the number of required parameters) are related to the components of the solution of SLAE (6) by

$$\forall m > 0 \ [d\mathbf{p}]_m = z_m / \sqrt{A_{mm}}. \quad (12)$$

SLAE (11) turns out to be much better-posed, and its solution is more stable than that of SLAE (6).

Secondly, to further improve the well-posedness of SLAE and accelerate the convergence of the method, we propose, based on the results from [11], to introduce additional regularization: a positive number μ should be added to the diagonal elements of the matrix R (which is positive definite and whose eigenvalues are all positive). In addition to reducing the condition number of SLAE (12), introducing the coefficient μ , according to Levenberg [11], forcibly makes the increments of the parameters small.

As a result, instead of SLAE (6), we need to solve the following SLAE:

$$(R + I\mu)z = R_0, \quad (13)$$

where I is the identity matrix.

The quantity μ must be refined during the solution of the problem. In the first iteration, it is recommended to take $\mu \approx 0.1\text{--}0.3$.

After composing SLAE (6), converting it to form (13) and finding a solution, we should perform inverse scaling of Eq. (12), thus calculating the increments of the required parameters da, db, dc, \dots . Next, we find

$$\mathbf{p}_1 = \mathbf{p}_0 + d\mathbf{p} \equiv a_0 + da, b_0 + db, c_0 + dc, \dots = a_1, b_1, c_1, \dots$$

Next, the found values of the parameters a_1, b_1, c_1, \dots are inserted into system (1), solved, and the residual ρ_1 is calculated:

$$\rho_1 = \frac{1}{n} \left\{ \frac{\sum_{i=1}^k [\tilde{u}(t_i, a_1, b_1, c_1, \dots) - u_i]^2}{\sum_{i=1}^k u_i^2} + \frac{\sum_{i=1}^k [\tilde{v}(t_i, a_1, b_1, c_1, \dots) - v_i]^2}{\sum_{i=1}^k v_i^2} + \frac{\sum_{i=1}^k [\tilde{w}(t_i, a_1, b_1, c_1, \dots) - w_i]^2}{\sum_{i=1}^k w_i^2} + \dots \right\}^{1/2}. \quad (14)$$

Now we should check whether there will be $\rho_1 \approx \rho$. If that is the case, then the required parameters were found (these are a_1, b_1, c_1, \dots), and the problem was successfully solved.

End of calculations.

If $\rho_1 > \rho_0$, the iteration is not counted, the value of μ should be increased (approximately by 1.5 times) and it is necessary to return to the beginning of solution (13). Occasionally, the ratio $\rho_1 > \rho_0$ suddenly appears in the course of calculations after the first iteration. Then the procedure for increasing μ can help restore convergence and stability. If μ has reached an excessively large value (exceeding 2), this indicates an error in the formulation of the problem.

End of calculations.

On the other hand, if $\rho_1 < \rho_0$, but still $\rho_1 > \rho$, then \mathbf{p}_1 is taken as \mathbf{p}_0 and ρ_1 as ρ_0 . Then it is necessary to reduce the quantity μ (multiplying it by 0.6–0.9) and start the next iteration: construct SLAE (6) again, etc.

Iterations are carried out until S stabilizes and ρ_1 becomes approximately equal to ρ .

Example solutions of inverse problems of ODE systems

In this section, two well-known models that can be called classical are considered as examples. The fourth-order Runge–Kutta method with a posteriori error estimation [8, 9] was used in this work to numerically solve system (1).

Brusselator model of autocatalytic reaction (Model I). The Brusselator model [13] was initially created by Prigogine and Lefever as a computational experiment, i.e., to find and establish a reasonable physico-chemical mechanism of periodic biochemical reactions. Subsequently, the model made it possible to study the properties of dissipative structures in various nonlinear systems, including those of a non-chemical nature. The model does not relate to any specific reaction, therefore, the values of all rates of the hypothetical intermediate stages of the reaction were fitting parameters, selected so that the solutions of the model equations exhibited an oscillatory behavior.

The ODE system proposed in the [13] has the following form:

$$\begin{cases} \dot{x} = a - (b+1)x + x^2 y; \\ \dot{y} = bx - x^2 y \end{cases}.$$

The variables $x(t)$ and $y(t)$ are proportional to the concentrations of the substances participating in the reaction and can be measured experimentally. The values of parameters a and b were assumed to be unknown.

The error of the model experimental data for the time functions $x(t)$ and $y(t)$ was taken as about 5% for this example. The starting approximations for the values of parameters a_0 and b_0 were selected by trial and error. As a result, $a_0 = 1.0$; $b_0 = 2.5$ were taken. The deviation of $x_0(t)$ and $y_0(t)$ from the experimental data amounted to 97% (Fig. 1, a, b).

The results of the algorithm after 18 iterations are shown in Fig. 1, c, d : the found parameter values were $a = 1.09$; $b = 3.16$; the error did not exceed 1.3% (model values of 1.1 and 3.2), which can be accepted as a good result.

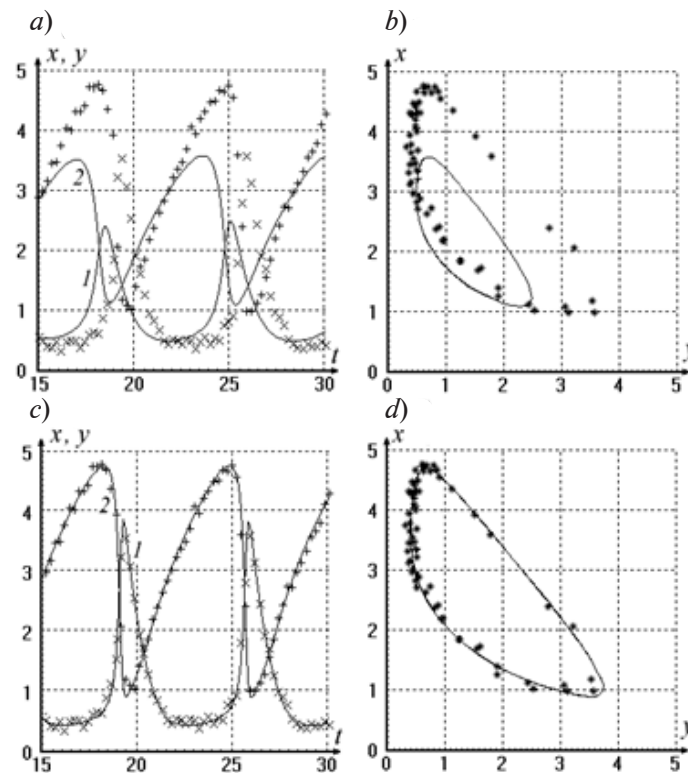


Fig. 1. Solution of inverse problem of ODE system for model I with respect to $x(t)$ (curves 1) and $y(t)$ (curves 2); the graphs show the experimental data (symbols) and calculation results (lines): variables calculated from the initial parameter approximations (a); limit cycle plotted from the experimental data and from the initial approximations (b); variables with optimal values of parameters and experimental data (c); limit cycles plotted from variables with optimal values of parameters and from the experimental data (d)

The above example shows that if there is experimental data on the time dependence of the concentrations of reagents and products of a particular reaction, it is possible to quantify the rates of the intermediate stages of this reaction (which is the essence of an indirect experiment), establishing the mechanism of their course based on this.

Oregonator model of periodic reaction (Model III). This model was proposed by Field and Noyes in [6] and is a good example of the simplified models mentioned in Introduction. It describes the mechanism of an entire class of reactions such as the Belousov–Zhabotinsky reaction including about 80 different stages. Reducing such a complex reaction to a system of only three equations for the concentrations of the principal reagents, the authors inevitably had to subdivide the entire range of intermediate reactions into a small number of complexes with some effective rates; attempts to refine these reaction rates are still made with varying success [5]. However, the purpose of this example was not to study the reaction itself but to identify the advantages of the algorithm proposed in this paper compared with algorithms used by other authors to solve the inverse problem of the same ODE system.

The corresponding system of equations takes the following form [6]:

$$\left. \begin{aligned} \dot{x} &= a(x + y - qx^2 - xy); \\ \dot{y} &= 2hz - y - xy; \\ \dot{z} &= (x - z) / 2 \end{aligned} \right\}. \quad (15)$$

The initial values of the parameters, selected by trial and error, were:

$$a_0 = 30.0; q_0 = 0.005; h_0 = 1.0.$$

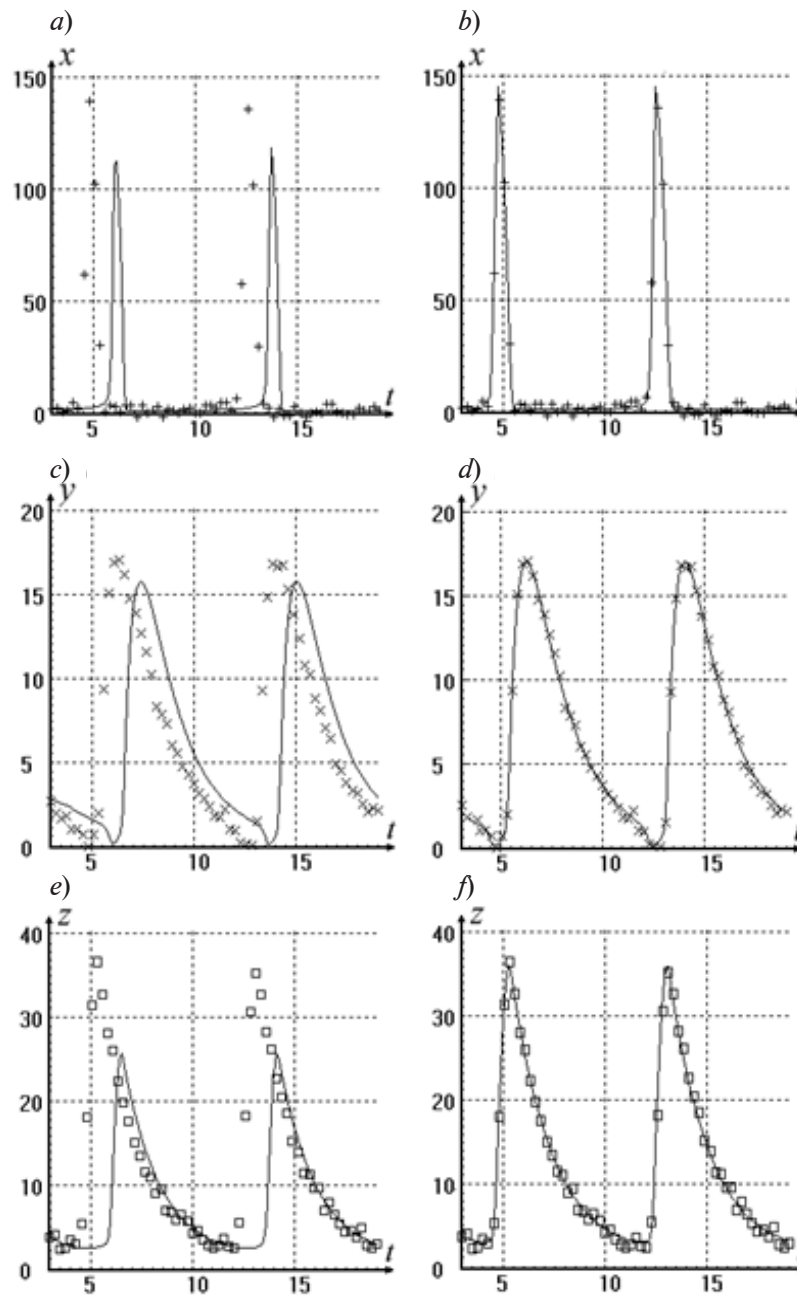


Fig. 2. Example solutions of inverse problem of ODE system (model II): experimental values (symbols) and components of solution of system (15) with initial approximations of parameters (lines) (a, c, e); comparison of components of solution of system (15) with optimal values of parameters (lines) found with experimental data (symbols) (b, d, f)

The input error of the experimental data was about 5%. The deviation of the initial variables $x_0(t)$, $y_0(t)$ and $z_0(t)$ from the experimental data was 84% (Fig. 2, a, c, e). The results of the algorithm are shown in Fig. 2, b, d, f. After 21 iterations, we obtained:

$$\rho_1 = 5.17\%; a = 34.6; q = 0.0059; h = 0.758;$$

the deviations of the parameters from the model values ($a = 33.3$; $q = 0.006$; $h = 0.75$) are no more than 3.9%, which can be accepted as a good result.

It is important to note that the accuracy of the results obtained by the method for solving the inverse problem of ODE systems proposed in this paper turned out to be of the same order as

the experimental data (this is also true for Model I) and significantly exceeds the accuracy of the above-mentioned results obtained by the direct Hooke–Jeeves method used in [5] for the same Oregonator model.

Both examples given here show that the presented algorithm for solving the inverse problem of ODE systems without analytical solutions can yield satisfactory accuracy for indirect measurements of the values of the parameters included in these ODE systems.

Results and discussion

If only one parameter a is unknown in the inverse problem of ODE system, then instead of the (rather complex) linearization algorithm presented above, it is advisable to minimize the quantity

$$S = \sum_{i=1}^k [\tilde{u}(t_i, a) - u_i]^2 + \sum_{i=1}^k [\tilde{v}(t_i, a) - v_i]^2 + \sum_{i=1}^k [\tilde{w}(t_i, a) - w_i]^2 + \dots \rightarrow \min_a,$$

using a simpler golden ratio algorithm [9], which, of course, should include the algorithm for solving system (1). It is common to try to avoid iterative solution of the direction problem by searching in the solution of inverse problems, due to the duration of the calculation and the unsatisfactory accuracy of the solutions obtained. However, in the case of a single unknown parameter, the golden ratio method combines fast convergence with good accuracy of the parameter value. On the other hand, the approach proposed in this paper is preferable for two or more parameters, since the golden ratio method turns out to be unsuitable, and other methods for solving inverse problems based on repeatedly solving the direct problem by searching over a multidimensional grid require much time while the accuracy of the results remains mediocre.

There are problems where it is required to calculate not the constant values of the parameters included in the ODE system but an unknown function $f(t)$, which is also part of ODE system (1) not related to the components of its solution. Then, if it is possible (for example, for physical considerations) to represent this function as a dependence on a finite number of parameters $f(t, a, b, \dots)$, then the proposed method for solving the inverse problem of ODE system can be applied and the numerical values of these parameters can be determined as described above.

It should also be noted that the solutions of ODE systems are very sensitive to parameter values. On the one hand, this complicates the choice of initial parameter values guaranteeing reliable convergence of the method (however, the preconditioning and regularization included in the proposed method significantly improve its convergence). On the other hand, such sensitivity makes it possible to consequently achieve good accuracy in calculating the required parameters even with noticeable errors in the experimental data.

REFERENCES

1. **Frame M.**, Mathematical models in the biosciences. Vol. I, CT, Yale University Press, New Haven, USA, 2021.
2. **Viana M., Espinar J. M.**, Differential equations: A dynamical systems approach to theory and practice (Book Ser. "Graduate Studies in Mathematics". Vol. 212). The American Mathematical Society, Providence, USA, 2021.
3. **Alvey Ch., Alvey D.**, Mathematical biology discrete and differential equations, CRC Press, Boca Raton, FL, USA, 2024.
4. **De Maria E. (Ed.)**, Systems biology modelling and analysis: Formal bioinformatics methods and tools, John Wiley & Sons, Inc., Hoboken, New Jersey, USA, 2022.
5. **Ikramov R. D., Mustafina S. A.**, The algorithm of search of rate constants of oscillating reaction to the example of the Belousov–Zhabotinsky reaction, Bashkirskiy Khimicheskiy Zhurnal [Bashkir Chemical Journal]. 22 (1) (2015) 87–91 (in Russian).
6. **Field R. J., Noyes R. M.**, Oscillations in chemical systems. IV. Limit cycle behavior in a model of a real chemical reaction, J. Chem. Phys. 60 (5) (1974) 1877–1884.
7. **Hooke R., Jeeves T. A.**, Direct search solution of numerical and statistical problems, Journal of the ACM. 8 (2) (1961) 212–229.

8. Städter Ph., Schälte Y., Schmiester L., et al., Benchmarking of numerical integration methods for ODE models of biological systems, Sci. Rep. 11 (1; Jan. 29) (2021) 2696.
9. Kalitkin N. N., Chislennyye metody [Numerical methods], Publ. BHV-Petersburg, St. Petersburg, 2011 (in Russian).
10. Sun Z. Z., Sun Y., Wang X. R., et al., Self-sustained current oscillations in superlattices and the van der Pol equation, Appl. Phys. Lett. 87 (18) (2005) 1821100–1821102.
11. Marquardt D. W., An algorithm for least-squares estimation of nonlinear parameters, J. Soc. Indust. Appl. Math. 11 (2) (1963) 431–441.
12. Yudin N. E., Modified Gauss–Newton method for solving a smooth system of nonlinear equations, Comput. Res. Model. 13 (4) (2021) 697–723 (in Russian).
13. Prigogine I., Lefever R., Symmetry breaking instabilities in dissipative systems. J. Chem. Phys. 48 (4) (1968) 1695–1700.

СПИСОК ЛИТЕРАТУРЫ

1. Frame M. Mathematical models in the biosciences. Vol. I. New Haven, CT, USA: Yale University Press, 2021. 544 p.
2. Viana M., Espinar J. M. Differential equations: A dynamical systems approach to theory and practice. Book series: “Graduate Studies in Mathematics”. Vol. 212. Providence, USA: American Mathematical Society, 2021. 536 p.
3. Alvey Ch., Alvey D. Mathematical biology discrete and differential equations. Boca Raton, FL, USA: CRC Press, 2024. 378 p.
4. De Maria E. (Ed.) Systems biology modeling and analysis: Formal bioinformatics methods and tools. Hoboken, New Jersey, USA: John Wiley & Sons, Inc., 2022. 464 p.
5. Икрамов Р. Д., Мустафина С. А. Алгоритм поиска констант скоростей колебательной реакции на примере реакции Белоусова – Жаботинского // Башкирский химический журнал. 2015. Т. 22. № 1. С. 87–91.
6. Field R. J., Noyes R. M. Oscillations in chemical systems. IV. Limit cycle behavior in a model of a real chemical reaction // The Journal of Chemical Physics. 1974. Vol. 60. No. 5. Pp. 1877–1884.
7. Hooke R., Jeeves T. A. Direct search solution of numerical and statistical problems // Journal of the Association for Computing Machinery (JACM). 1961. Vol. 8. No. 2. Pp. 212–229.
8. Städter Ph., Schälte Y., Schmiester L., Hasenauer J., Stapor P. L. Benchmarking of numerical integration methods for ODE models of biological systems // Scientific Reports. 2021. Vol. 11. No. 1. January 29. P. 2696.
9. Калиткин Н. Н. Численные методы. Серия: «Учебная литература для вузов (BHV)» СПб.: Изд-во БХВ-Петербург, 2011. 592 с.
10. Sun Z. Z., Sun Y., Wang X. R., Cao J. P., Wang Y. P., Wang Y. Q. Self-sustained current oscillations in superlattices and the van der Pol equation // Applied Physics Letters. 2005. Vol. 87. No. 18. Pp. 1821100–1821102.
11. Marquardt D. W. An algorithm for least-squares estimation of nonlinear parameters // Journal of the Society for Industrial and Applied Mathematics. 1963. Vol. 11. No. 2. Pp. 431–441.
12. Юдин Н. Е. Модифицированный метод Гаусса–Ньютона для решения гладкой системы нелинейных уравнений // Компьютерные исследования и моделирование. 2021. Т. 13. № 4. С. 697–723.
13. Prigogine I., Lefever R. Symmetry breaking instabilities in dissipative systems // The Journal of Chemical Physics. 1968. Vol. 48. No. 4. Pp. 1695–1700.



THE AUTHOR

GOLOVITSKII Alexander P.

Peter the Great St. Petersburg Polytechnic University

29 Politechnicheskaya St., St. Petersburg, 195251, Russia

alexandergolovitski@yahoo.com

ORCID: 0000-0003-4292-0959

СВЕДЕНИЯ ОБ АВТОРЕ

ГОЛОВИЦКИЙ Александр Петрович — доктор физико-математических наук, профессор Высшей инженерно-физической школы Санкт-Петербургского политехнического университета Петра Великого.

195251, Россия, г. Санкт-Петербург, Политехническая ул., 29

alexandergolovitski@yahoo.com

ORCID: 0000-0003-4292-0959

Received 25.02.2025. Approved after reviewing 04.03.2025. Accepted 04.03.2025.

Статья поступила в редакцию 25.02.2025. Одобрена после рецензирования 04.03.2025. Принята 04.03.2025.

THEORETICAL PHYSICS

Original article

DOI: <https://doi.org/10.18721/JPM.18213>

COLLECTIVE EXCITATIONS IN THE BULK DOPED SEMICONDUCTOR CADMIUM SULFIDE NANOCRYSTALS

A. N. Ipatov^{1,2}, G. A. Kupriianov¹

¹ Peter the Great St. Petersburg Polytechnic University, St. Petersburg, Russia;

² Alferov University of RAS, St. Petersburg, Russia

✉ henryweis3@gmail.com

Abstract. The excited states of nanosized CdS semiconductor crystals with bulk doping have been studied. It was demonstrated that the giant dipole resonance dominated in their photoabsorption spectra. Varying the potential barrier height at the nanoparticle boundary was shown to be able to cause a change in the character of the collective mode from the plasmonic-type electron density fluctuations to the dimensional quantization mode depending on the particle size and the number of free charge carriers.

Keywords: semiconductor nanocrystal, cadmium sulfide, doping, plasmon resonance, multiparticle excitation

Citation: Ipatov A. N., Kupriianov G. A., Collective excitations in the bulk doped semiconductor cadmium sulfide nanocrystals, St. Petersburg State Polytechnical University Journal. Physics and Mathematics. 18 (2) (2025) 144–161. DOI: <https://doi.org/10.18721/JPM.18213>

This is an open access article under the CC BY-NC 4.0 license (<https://creativecommons.org/licenses/by-nc/4.0/>)

Научная статья

УДК 538.9

DOI: <https://doi.org/10.18721/JPM.18213>

КОЛЛЕКТИВНЫЕ ВОЗБУЖДЕНИЯ В ОБЪЕМНО-ЛЕГИРОВАННЫХ ПОЛУПРОВОДНИКОВЫХ НАНОКРИСТАЛЛАХ СУЛЬФИДА КАДМИЯ

А. Н. Ипатов^{1,2}, Г. А. Куприянов¹

¹ Санкт-Петербургский политехнический университет Петра Великого, Санкт-Петербург, Россия;

² Академический университет имени Ж. И. Алфёрова РАН, Санкт-Петербург, Россия

✉ henryweis3@gmail.com

Аннотация. Исследованы возбужденные состояния наноразмерных полупроводниковых кристаллов CdS с объемным типом легирования. Продemonстрировано, что в их спектрах фотопоглощения доминирует гигантский дипольный резонанс. Показано, что варьирование высоты потенциального барьера на границах наночастиц может приводить к изменению характера коллективной моды от колебаний электронной плотности плазмонного типа к режиму размерного квантования, в зависимости от размера частицы и числа свободных носителей заряда.

Ключевые слова: полупроводниковый нанокристалл, сульфид кадмия, легирование, плазмонный резонанс, многочастичное возбуждение



Ссылка для цитирования: Ипатов А. Н., Куприянов Г. А. Коллективные возбуждения в объемно-легированных полупроводниковых нанокристаллах сульфида кадмия // Научно-технические ведомости СПбГПУ. Физико-математические науки. 2025. Т. 18. № 2. С. 144–161. DOI: <https://doi.org/10.18721/JPM.18213>

Статья открытого доступа, распространяемая по лицензии CC BY-NC 4.0 (<https://creativecommons.org/licenses/by-nc/4.0/>)

Introduction

The advances in nanoelectronics in recent decades have led to an interest in creating fundamentally new materials, whose properties differ from those of the corresponding bulk components. A burgeoning field is quantum plasmonics, which includes the study of interaction between electromagnetic radiation with matter at the nanoscale [1–7]. Doped semiconductor nanocrystals show promise in this field [4, 8–13].

A characteristic feature of such nanoscale systems is the presence of dipole resonances in their optical spectra. The position of the resonance line in the spectra of semiconductor nanoparticles depends on a number of parameters, in particular, on carrier density, properties of the medium and doping type, which can be generally defined as surface or bulk [8, 14–17]. In the first case, free carriers are injected into the bulk of the semiconductor nanoparticle by donors located on its surface [18, 19], and in the second case, the charge density of free carriers is distributed over the entire bulk of the crystal and is neutralized by the dopant charge [8, 10, 14, 17]. The difference in doping methods produces a significant difference in the behavior of the dipole resonance mode excited in semiconductor nanoparticles.

As shown in [20–22], the specifics of the electronic configuration of nanocrystals with surface doping [18, 19] is that only angular degrees of freedom are excited in the collective dipole mode upon interaction with an external electromagnetic field, while the electron motion in the radial direction does not occur and the electrons oscillate tangentially relative to the boundary of the system inside a relatively thin spherical layer.

In the case of bulk-doped semiconductor nanoparticles [12, 15–17], the dipole plasmon can be described in the adiabatic approximation [23, 24] by a model of harmonic oscillations of an entire system of delocalized electrons relative to the center of the positively charged core, in the direction normal to its surface.

It was found in [20, 21] that due to the peculiarities of the electronic structure of surface-doped nanocrystals, the frequencies and oscillator strengths of their plasmon modes are almost completely determined by the contribution of correlated excitations from a single dipole transition between single-particle HOMO and LUMO levels, which made it possible to describe the optical properties of such systems within a simple two-level model [21, 25].

The situation is different for bulk doping. Evidently, for theoretical description of the collective excited state, it is necessary to take into account the contributions of at least two single-particle channels connected by correlation interaction. On the other hand, the interaction of the harmonic mode with the surface of the nanocrystal in the presence of a potential barrier between the semiconductor particle and its dielectric medium leads to splitting of the resonance line into several separate modes [25].

The optical characteristics of nanoscale semiconductor crystals with various types of doping are considered in [17], demonstrating that the spectra of dipole excitations in such systems show a transition from size quantization with a small number of free carriers to plasmon oscillations with an increased number of free charge carriers. Additionally, it is also established in [25] that regardless of the doping approach used, the optical spectrum of nanoparticles is dominated by the resonant dipole mode whose nature depends both on the dimensions of the system itself and by the type of doping and its degree, i.e., the number of delocalized charge carriers. In this case, the transition from the size quantization mode to classical plasmon oscillations of the electronic system occurs both as the number of electrons increases and as the geometric dimensions of the system increase. The very nature of plasmon oscillations, depending on the degrees of freedom involved, can vary from the translational type, where the electron cloud moves in the direction normal to the surface of the system, to the collective rotational mode, where only angular degrees of freedom are excited, while motion in the radial direction practically does not occur.

The goal of this study is to investigate the dependence of many-particle excited states in the electronic system of bulk-doped semiconductor nanocrystals on the height of the potential barrier at the boundary and on the geometric dimensions of the system, considering the example of cadmium sulfide (CdS) crystals.

Our approach is based on a self-consistent quantum mechanical description of many-particle excitations in a system of delocalized charge carriers.

Calculations of the ground state of the system were carried out in the local density approximation (LDA) taking into account the local interparticle exchange interaction by numerically solving the self-consistent Kohn–Sham equations [26].

The photoabsorption spectra of nanocrystals of various dimensions were obtained using the random phase approximation (RPA) with local exchange interaction (RPAX) [27, 28]. The system of atomic units $|e| = \hbar = m_e = 1$ is used in the study.

Theoretical approach

We consider n -doped CdS nanocrystals with bulk-type doping in a dielectric medium. Let us consider an electrically neutral system of fermions coupled by the Coulomb interaction. We define negative particles as electrons with an effective mass in the conduction band m_e^* . In the case considered in this paper, the full Hamiltonian \hat{H} is the operator of the total energy of a system of N electrons interacting with each other via the Coulomb potential V in an external field with the potential $U_{ext}(\mathbf{r})$:

$$\hat{H} = \sum_i^N \frac{\hat{\mathbf{p}}_i^2}{2m_e^*} + \sum_i^N U_{ext}(\mathbf{r}_i) + \frac{1}{2} \sum_{i,j}^N V(\mathbf{r}_i, \mathbf{r}_j). \quad (1)$$

The motion of delocalized electrons within the bulk of the nanoparticle is restricted by the boundary of the conduction band near the surface. The external potential $U_{ext}(\mathbf{r})$ restricting the motion of delocalized electrons is described as a spherically symmetric potential well whose geometric parameter R is determined by the given dimensions of the nanocrystal, while the positive charge under bulk doping is assumed to be evenly distributed throughout the entire volume of the system. Thus, the external potential generated by this charge within the framework of the model used takes the form of the potential of a uniformly charged sphere with the charge $Z = Ne$ in a dielectric medium [17, 25]:

$$U_{ext}(r) = \begin{cases} \frac{Ne^2}{2\varepsilon_1 R^3} \left(r^2 - \left(1 + \frac{2\varepsilon_1}{\varepsilon_2} \right) R^2 \right), & 0 < r < R, \\ -\frac{Ne^2}{\varepsilon_2 r} + U, & r > R, \end{cases} \quad (2)$$

where U is the phenomenological parameter characterizing the height of the potential barrier at the interface between the nanocrystal and the dielectric medium (this height is commensurate in order of magnitude with the electron work function from the bulk material of the semiconductor); $\varepsilon_1, \varepsilon_2$ are the dielectric constants of the CdS nanocrystal and its dielectric medium, respectively; e is the elementary charge.

The Coulomb pair interaction between electrons at points \mathbf{r}_a and \mathbf{r}_b is screened as a result of polarization of both the semiconductor material itself (indicated by the subscript 1) and the medium (subscript 2), so that multipole decomposition of the interparticle interaction potential at $r_i, r_j < R$ can be written as follows:

$$V(\mathbf{r}_i, \mathbf{r}_j) = \sum_{LM} \frac{V_L}{2L+1} Y_{LM}(\mathbf{n}_i) Y_{LM}^*(\mathbf{n}_j),$$

$$V_L = \frac{4\pi e^2}{\varepsilon_1} \left(\frac{r_{<}^L}{r_{>}^{L+1}} + \frac{(\varepsilon_1 - \varepsilon_2)(L+1)(r_i r_j)^L}{(L\varepsilon_1 + (L+1)\varepsilon_2)R^{2L+1}} \right), \quad (3)$$



where $r_{>,<}$ are, respectively, the largest and smallest of the radii r_{ij} ; $Y_{LM}(\mathbf{n}_{ij})$ are the spherical components of the electron wave function whose position in space is determined by the position vectors \mathbf{r}_i and \mathbf{r}_j , respectively; L is the total orbital momentum of the system.

The interparticle interaction in the ground state of the system is described using the Local Density Approximation (LDA) where the single-particle wave functions of electrons $\phi_i(\mathbf{r})$ satisfy the self-consistent Kohn–Sham equations [26]:

$$-\frac{\hbar^2 \Delta_i}{2m_e^*} \phi_i(\mathbf{r}_i) + (U_{ext}(\mathbf{r}_i) + U_H(\mathbf{r}_i) + U_x(\mathbf{r}_i)) \phi_i(\mathbf{r}_i) = E_i \phi_i(\mathbf{r}_i), \quad (4)$$

where E_i are the single-particle electron energies; $U_H(\mathbf{r})$ is the corresponding Hartree potential; $U_x(\mathbf{r})$ is the local exchange potential.

In the case of the system with filled shells, the Hartree potential is written as

$$U_H(\mathbf{r}) = \int V(\mathbf{r}, \mathbf{r}') \rho_e(\mathbf{r}') d\mathbf{r}', \quad (5)$$

where the bulk density of electrons $\rho_e(\mathbf{r})$ is calculated by summation over all filled single-particle states:

$$\rho_e(\mathbf{r}) = 2 \sum_i \phi_i^*(\mathbf{r}) \phi_i(\mathbf{r}).$$

The local exchange potentials in the Dirac–Slater approximation $U_x(\mathbf{r})$ were defined as

$$U_x(\mathbf{r}) = -\left(e^2 / \epsilon_1\right) (3\rho_e(\mathbf{r}) / \pi)^{1/3}. \quad (6)$$

For spherically symmetric systems with closed electron shells and isotropic angular dependences $\rho_e(\mathbf{r})$ and $U(\mathbf{r})$, the cumulative index i denotes

$$i = (n, l, m, \sigma),$$

where n is the radial quantum number; l, m are the angular momentum and its projection; σ is the spin projection.

Single-particle wave functions for such systems are written as the product of radial, angular, and spin components [29]:

$$\phi_{nlm\sigma}(\mathbf{r}) = \frac{P_{nl}(r)}{r} Y_{lm}(\theta, \varphi) \chi_\sigma. \quad (7)$$

RPAX was used to describe many-electron correlations.

In this approach, the wave function of the excited state $|\Phi_k\rangle$ is represented as a superposition of single-particle excitations of the particle–vacancy type [28]:

$$|\Phi_k\rangle = \sum_{im} \left(X_{im}^{(k)} \hat{a}_m^+ \hat{a}_i + Y_{im}^{(k)} \hat{a}_i^+ \hat{a}_m \right) |\Phi_0\rangle, \quad (8)$$

where $|\Phi_0\rangle$ is the ground state of the system; \hat{a}^+, \hat{a} are single-particle creation and annihilation operators; $X_{im}^{(k)}, Y_{im}^{(k)}$ are the amplitude coefficients for forward-in-time and backward-in-time amplitudes, respectively (characterizing the contribution of the corresponding particle–vacancy pair to the many-particle excited state $|\Phi_k\rangle$); the subscripts i, m here and below to denote filled and unfilled single-particle states of the electronic subsystem.

The excited states of the many-particle system with filled shells possessing spherical symmetry are characterized in the spin-orbit (LS) coupling approximation by the total angular momentum L and its projection M , therefore, all single-particle particle–vacancy excitations in superposition (8) have the same multipole. To describe the optical properties of the systems considered, it is sufficient to consider only dipole transitions from the ground state $|\Phi_0\rangle$ to excited multiparticle states $|\Phi_k\rangle$ with $L = 1, M = 0$.

The amplitude coefficients $\mathbf{X}^{(k)}$ and $\mathbf{Y}^{(k)}$ in superposition (8) are determined by solving the matrix equation of RPAX:

$$\mathbf{U}\mathbf{Z}^{(k)} = \hbar\Omega_k\mathbf{Z}^{(k)}, \quad (9)$$

where Ω_k are the eigenvalues of the matrix \mathbf{U} :

$$\mathbf{U} = \begin{pmatrix} \mathbf{A} & \mathbf{B} \\ -\mathbf{B}^* & -\mathbf{A}^* \end{pmatrix}, \quad \mathbf{Z}^{(k)} = \begin{pmatrix} \mathbf{X}^{(k)} \\ \mathbf{Y}^{(k)} \end{pmatrix}. \quad (10)$$

The elements of Hermitian matrices \mathbf{A} , \mathbf{B} are expressed in terms of single-particle energies E_i and Coulomb matrix elements of interparticle pair interaction taking the form

$$\langle \alpha\beta | V | \gamma\eta \rangle = \delta_{\sigma_\alpha\sigma_\gamma} \delta_{\sigma_\beta\sigma_\eta} \int \phi_\alpha^*(\mathbf{r})\phi_\beta^*(\mathbf{r}')V(\mathbf{r},\mathbf{r}')\phi_\gamma(\mathbf{r})\phi_\eta(\mathbf{r}')d\mathbf{r}d\mathbf{r}' \quad (11)$$

with single-particle functions obtained by solving Eqs. (4), where the potential $V(\mathbf{r},\mathbf{r}')$ is determined from expression (3).

Matrices \mathbf{A} and \mathbf{B} relate the single-particle excitations within the electron system:

$$\begin{aligned} A_{im,jn} &= \delta_{ij}\delta_{mn}\omega_{in} + \langle in | U | mj \rangle, \\ B_{im,jn} &= \langle ij | U | mn \rangle, \end{aligned} \quad (12)$$

where $\omega_{im} = E_m - E_i$, including both direct (Hartree) and local exchange interactions within RPAX:

$$\langle \alpha\beta | U | \gamma\eta \rangle = 2\langle \alpha\beta | V | \gamma\eta \rangle + \langle \alpha\beta | V_x | \gamma\eta \rangle, \quad (13)$$

where

$$V_x(\mathbf{r},\mathbf{r}') = \frac{\delta U_x[\rho(\mathbf{r})]}{\delta \rho(\mathbf{r})} \delta(\mathbf{r} - \mathbf{r}'), \quad (14)$$

while the local exchange potential U_x is determined in accordance with expression (6).

The positive eigenvalues Ω_k are the transition energies between the ground state $|\Phi_0\rangle$ and the correlated excited states $|\Phi_k\rangle$ (8). The energy spectra of excited states obtained by solving Eqs. (9) and (10) and the corresponding wave functions allow to describe the processes associated with excitation of the system by various external perturbations. In particular, the response of the system to an external electromagnetic field is determined by the spectrum of dipole excitations. The oscillator strengths f_k for dipole transitions between the ground and the k th excited state are described by the formula

$$f_k = 2m_m^* D_k^2 \Omega_k, \quad (15)$$

and satisfy the Thomas–Reich–Kuhn sum rule, i.e., $\sum_k f_k = N$.

The dipole matrix elements D_k (in the length calibration) are calculated by summation over all single-particle excitations:

$$D_k = \sum_{im} (X_{im}^{(k)} d_{im} + Y_{im}^{(k)} d_{mi}), \quad (16)$$

where $d_{im} = \langle i | z | m \rangle$ are the single-particle dipole amplitudes for the particle–vacancy pair, and the amplitude coefficients $\mathbf{X}^{(k)}$ and $\mathbf{Y}^{(k)}$ are normalized by the condition



$$\sum_{im} \left(|X_{im}^{(k)}|^2 - |Y_{im}^{(k)}|^2 \right) = 1. \quad (17)$$

Results and discussion

This section discusses the calculation results for dipole excitation spectra of spherically symmetric bulk-doped nanoscale CdS quantum dots containing 8 delocalized electrons, forming two closed shells with the configuration $1s^2 2p^6$ in the ground state in the central field approximation, characteristic for such systems. Such a simple system was chosen as an example for illustrating the main factors associated with the influence of the potential barrier at its boundary on the spectral characteristics of the nanoparticle, aiming to minimize the number of independent parameters in the model used. Calculations were performed for different radii R of the nanocrystal and potential barrier heights U at its boundary.

Fig. 1 shows the distributions of oscillator strengths calculated by Eqs. (9) and (16), or (which is the equivalent for the local exchange potential) by Eqs. (A9) and (A18) (see Appendix It can be seen from the graphs for radii $R = 1$ and 6 nm that spectrum in the limit of ‘free’ systems (at $U = 0$) for both values of R consists of one dominant plasmonic line containing from 90% (at $R = 1$ nm) to 100% (at $R = 6$ nm) oscillator strengths, which is typical for harmonic oscillations of electron density as a whole. It turned out that the results obtained using the complete basis of single-particle excitations (denoted as RPAX in the graph) are almost identical to the results taking

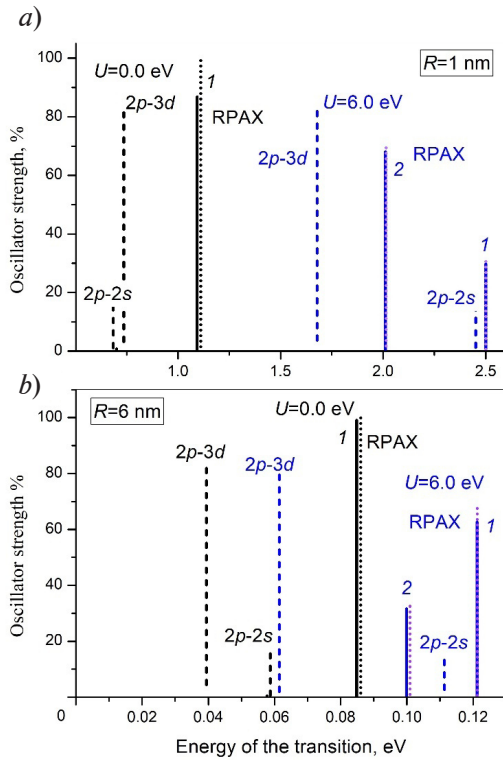


Fig. 1. Energy distribution of oscillator strengths for CdS quantum dots with $N = 8$ electrons, nanocrystal radii $R = 1$ nm (a) and 6 nm (b), at different potential barrier heights ($U = 0.0$ and 6.0 eV)

Results of exact RPAX calculation (see Eq. (9)) are shown by solid lines, results accounting for only two ground-state transitions (see Eq. (A19) in Appendix) are shown by dotted lines; oscillator strengths for these transitions are shown in single-particle approximation (dashed lines)

into account only two ground-state transitions: $2p \rightarrow 3d$ and $2p \rightarrow 2s$ (see Eq. (A19) of Appendix) over the entire variation range of the barrier height. There is a noticeable difference between the RPAX spectra, for which each excited state is described by linear combination (8) and the line distributions of single-particle transitions. This indicates a significant contribution of many-particle correlations to the formation of dipole modes $|\Phi_k\rangle$ (see Fig. 1), which have a collective nature.

It was important to establish the influence of potential barrier height on the distribution of oscillator strengths in the studied spectra. We found that as this height increases, the dominant line of the collective mode splits into two distinct components and the relative distribution of oscillator strengths between them depends on the geometric dimensions of the system. Moreover, as discussed below, when a harmonic mode interacts with a potential barrier at the nanocrystal boundary, the contributions of single-particle channels $2p \rightarrow 3d$ and $2p \rightarrow 2s$ are redistributed between the two observed lines of collective modes as the potential barrier height increases. In other words, there is a significant dependence of the corresponding amplitudes $X_{im}^{(k)}$ and $Y_{im}^{(k)}$ on the height of the barrier.

As seen from Fig. 2, the distribution of electron density in the ground state of the system at different radii depends on the height of the potential barrier. This naturally leads not only to a noticeable shift of the resonant frequencies to the right as the height of the barrier increases (see Fig. 1), but also to a transformation in the radial dependence of the transition density $\rho_r^{(k)}(\mathbf{r})$. The latter is defined for the k th collective mode (8) as

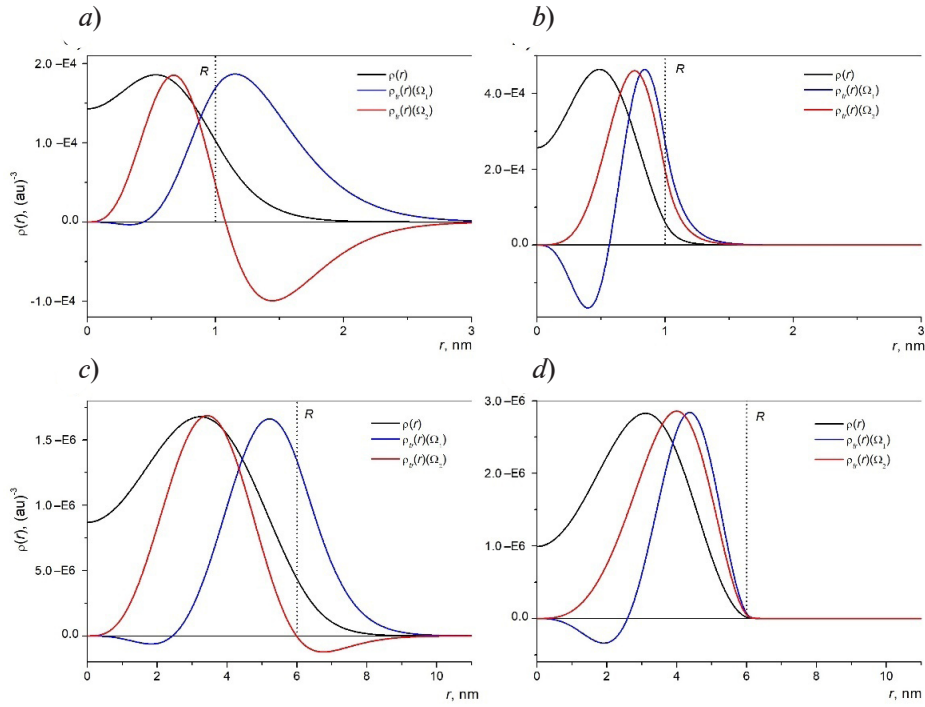


Fig. 2. Spatial distributions of electron density for ground state of CdS quantum dots with $N = 8$ electrons, nanocrystal radii $R = 1$ nm (*a*, *b*) and 6 nm (*c*, *d*), at potential barrier heights $U = 0.0$ eV (*a*, *c*) and 6.0 eV (*b*, *d*)
Radial density distributions of dipole transitions corresponding to RPAX spectral lines with frequencies Ω_1 and Ω_2 are also shown

$$\rho_{tr}^{(k)}(\mathbf{r}) = \langle \Phi_k | \delta \rho(\mathbf{r}) | \Phi_0 \rangle = \sum_{h < F, p > F} (X_{ph}^{(k)} \phi_p^*(\mathbf{r}) \phi_h(\mathbf{r}) + Y_{ph}^{(v)} \phi_p(\mathbf{r}) \phi_h^*(\mathbf{r})), \quad (18)$$

where F is the Fermi level energy of the system, and $\phi(\mathbf{r})$ are single-particle wave functions (7).

In this case, there is not only a shift in the transition densities following the shift of the electron density itself to the center of the system, but also a qualitative transformation in their radial dependencies. This is most noticeable for a smaller nanocrystal (see Fig. 2, *a*, *b*). It follows therefore that a change in the barrier height causes a redistribution between the contributions of single-particle channels during the formation of the corresponding excited state (8), i.e., the ratios between the amplitudes $X^{(k)}$ and $Y^{(k)}$ change significantly. Clearly, this concerns the redistribution between the contributions of single-particle channels $2p \rightarrow 3d$ and $2p \rightarrow 2s$. Importantly, in the absence of a barrier for modes with the frequency Ω_1 , the maximum transition density is observed near the interface. This is typical for surface plasmon modes where electron density fluctuations occur in the direction normal to the boundary. On the other hand, a significant part of radial density of the transitions is distributed over the bulk of the system for oscillations with the frequency Ω_2 , which is typical for excited states in which rotational degrees of freedom make the main contribution [21, 22, 25].

As seen from Fig. 1, these modes are practically absent in the spectrum of excited states at $U = 0$ and the dominant line corresponds to almost 100% of the oscillator-strength sum. This indicates that electron density fluctuations in free nanoparticles exhibit the behavior of a surface plasmon harmonic mode. On the contrary, as follows from the graphs in Figs. 1 and 2, *b*, *d*, two dominant lines with the frequencies Ω_1 and Ω_2 are clearly observed in the presence of a potential barrier at the nanoparticle boundary in the spectrum of its dipole excitations, where almost the entire sum of the oscillator strengths is also concentrated. The maximum distribution of the transition density near the surface, characteristic for surface plasmon oscillations, is already observed for the frequency Ω_2 , while a significant part of the transition density for Ω_1 falls on the internal volume of the system; this is especially pronounced for particles with smaller radii (at $R = 1$ nm).



For more detailed analysis of the influence of potential barrier on the dipole spectrum of the nanoparticles studied, we considered the dependences of oscillator strengths (8), frequencies, and amplitudes $X_{im}^{(k)}$ and $Y_{im}^{(k)}$ of collective modes, determining the contributions of individual single-particle excitations to the correlated excited state within of RPAX, on the magnitude of U at different geometric dimensions of the system. The absolute value of the backward-in-time amplitude $Y_{im}^{(k)}$ for the single-particle ground-state transition, describing the contribution of correlations in the ground state and generally comparable in order of magnitude to the corresponding forward-in-time amplitude $X_{im}^{(k)}$ for collective modes, was chosen as one of the criteria for evaluating the plasmonic behavior of the excited state considered [25, 30].

Figs. 3–6 show the results of calculations performed for nanoparticles with radii $R = 1, 4, 6$ and 8 nm.

Excited states in nanocrystals of radius $R = 1$ nm. The graphs in Fig. 3 show that the oscillator strength of the excited state oscillator with the transition frequency Ω_1 ranges from 88 to 96% of the sum rule for relatively small heights of the potential barrier U , while the contribution of the mode with the transition frequency Ω_2 remains negligible up to $U = 2$ eV, which is consistent with

the data in Fig. 1, *a*, where a single line is observed in the RPAX spectrum. Rapid growth of the second spectral component begins above 2 eV; the oscillator strength of this component reaches the magnitude of the first one at $U \approx 3.5$ eV, after which the line with the frequency Ω_2 starts to dominate. At $U \approx 8$ eV, oscillator strengths of the two dominant modes are virtually unchanged and correlate as

$$f(\Omega_1) / f(\Omega_2) \approx 70 / 30,$$

which is typical for excitations with dominant angular and radial degrees of freedom, respectively [21, 22]. The frequencies of both dipole excitations Ω_1 и Ω_2 , as well as the energy differences of single-particle levels, increase with increasing barrier height, which is observed in Fig. 1, *b*. At the same time, the oscillator strengths of single-particle transitions $2p \rightarrow 3d$ and $2p \rightarrow 2s$ remain virtually unchanged over the entire range of U values considered, suggesting that the redistribution of oscillator strengths (16) is related to the correlation interaction between these channels. This conclusion is confirmed by the behavior of the dependences of the amplitudes $X_{im}^{(k)}$ and $X_{2p-2s}^{(k)}$ for modes Ω_1 and Ω_2 (respectively) with increasing barrier height. It turned out that the main contribution to the excited state with a higher frequency Ω_1 is made primarily by the $2p \rightarrow 3d$ channel at $U \approx 0$, while the contribution of the $2p \rightarrow 2s$ channel 2 is relatively small. As the potential barrier increases, the amplitude ratio begins to change rapidly, so that correlation mixing of channels occurs, their contributions become equal at $U \approx 2.5$ eV, after which the component $2p \rightarrow 2s$ dominates.

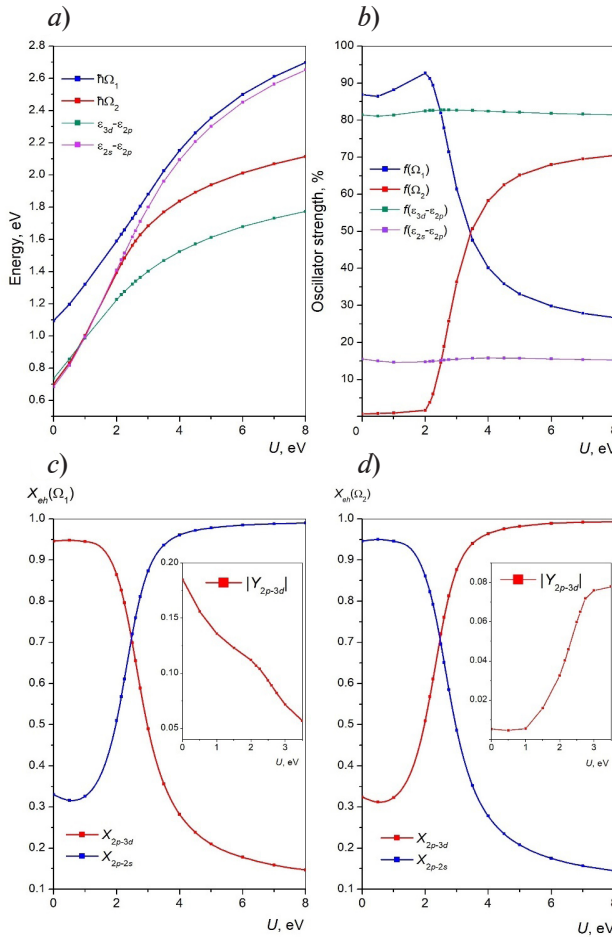


Fig. 3. Dependences of main quantities on potential barrier height U for CdS quantum dots with $N = 8$ electrons, radius $R = 1$ nm:

frequencies of main collective excitations and energies of single-particle transitions (*a*); oscillator strengths (*b*); forward-in-time amplitudes X_{im} for dominant single-particle components for excited states with frequencies Ω_1 (*c*) and Ω_2 (*d*).

Insets: dependences of backward-in-time amplitudes Y_{im} on U

The situation is reversed in the case of low-frequency excitation (with Ω_2): at first, the main contribution to the oscillator strength is made by the $2p \rightarrow 2s$ channel, but these oscillations still remain practically unexcited at $U \approx 0$, followed by rapid increase in both the oscillator strength and the amplitude of the $2p \rightarrow 3d$ component, whose contribution begins to dominate at $U \geq 2.5$ eV. Ultimately, at $U \geq 4.0$ eV, it turns out that the modes are reversed with respect to the two single-particle channels dominant in sum (8) compared to the situation with a free system.

This redistribution of contributions between the main single-particle channels can be explained by the example of radial dependences of transition density (see Fig. 2). In the absence of the potential barrier, the surface plasmon-type mode is effectively excited, characterized by the distribution $\rho_{tr}(r)$ corresponding to the line with the frequency Ω_1 and the $2p \rightarrow 3d$ channel, where the radial component of the wave function $P_{3d}(r)$ has no roots in the bulk of the system. The surface plasmon behavior of this excited state is also confirmed by the relatively large absolute values of the backward-in-time amplitude $Y_{2p-3d}^{(1)} \approx 0.20-0.15$, characteristic for plasmon modes at small barrier heights, as can be seen in the inset to Fig. 3, *a*. As the barrier further increases, the excitation of electron density fluctuations in the near-surface region becomes less effective, and they are replaced by fluctuations with the dominant $2p \rightarrow 2s$ channel, where the radial component of the wave function $P_{2s}(r)$ has a root and the electron density is more uniformly distributed over the volume. The absolute value of the amplitude $Y_{2p-3d}^{(1)}$ decreases rapidly, which indicates a transition to a size-quantization mode where the electron density is localized inside a region bounded by the surface potential barrier.

Notably, the frequency Ω_1 takes values very close to the single-particle energy difference of the $2p \rightarrow 2s$ channel, while its oscillator strength tends to the corresponding single-particle value in the limit of large U (see Fig. 3, *a*, *b*). These features of frequency behavior confirm the transition of this mode from collective plasmon excitations to almost single-particle in nature.

For the second mode, where the oscillator strength begins to dominate the spectrum at $U \geq 4$ eV (see Fig. 3, *b*), its frequency Ω_2 retains, with increasing U , a noticeable difference from the energy difference of the channel $E_{3d} - E_{2p}$, which becomes the main one for this mode. This suggests that the excitation is correlated, but also localized in a potential well with the barrier U at its boundary. The absolute value of the amplitude $Y_{2p-3d}^{(2)}$ increases markedly with an increase in U although it remains smaller than 0.1. Thus, a state with the frequency Ω_2 can be described as collective excitation with dominant rotational degrees of freedom.

Excited states in nanocrystals of radius $R = 4$ nm. An increase in the radius of the system to 4 nm leads to some changes in its spectral characteristics. First, the scale of all energies decreases by an order of magnitude (see Fig. 4, *a*). At the same time, both the frequencies of collective modes and the differences of single-particle energies of the same single-particle channels $E_{2s} - E_{2p}$ and $E_{3d} - E_{2p}$, making the main contribution at $R = 1$ nm, practically cease to depend on the barrier height at $U \approx 4-6$ eV. In other words,

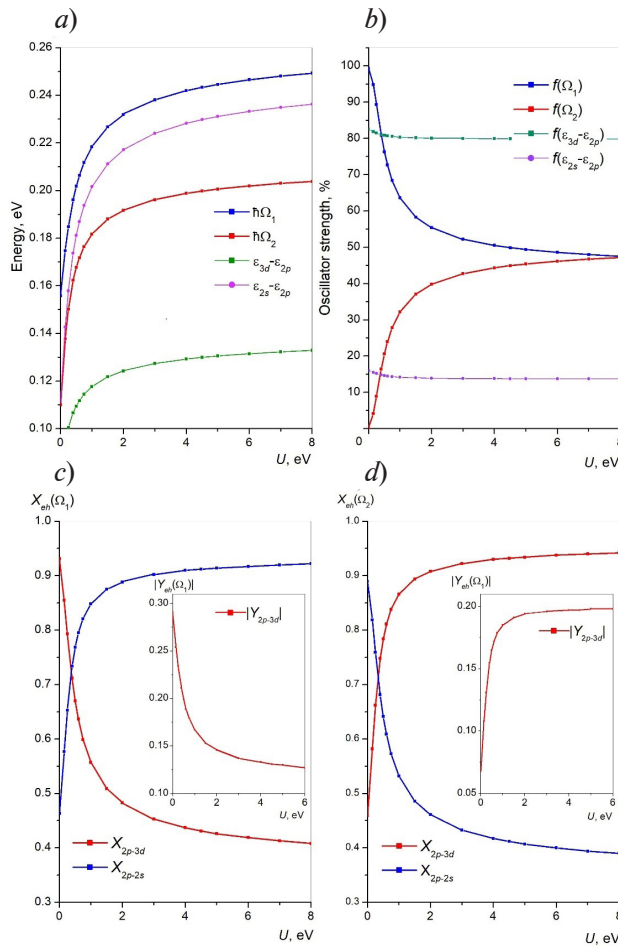


Fig. 4. Same dependences as in Fig. 3 but for nanocrystal radius $R = 4$ nm

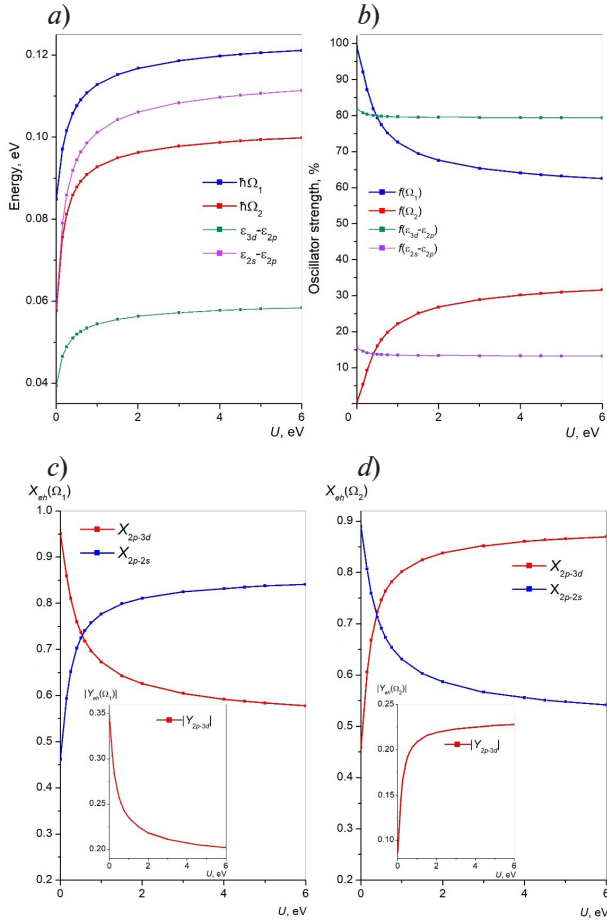


Fig. 5. Same dependences as in Figs. 3 and 4 but for nanocrystal radius $R = 6$ nm

approximately 50% of the total value in the sum rule, becoming commensurate. Thus, for the case $R = 4$ nm, the effect of the potential barrier at $U \approx 7-8$ eV leads to the disappearance of the clearly dominant line in the dipole spectrum of the nanoparticle.

Analyzing the graphs in Fig. 4, *c*, *d* allows to draw some conclusions about the distribution of contributions of single-particle channels to correlated RPAX states (8). The same as at $R = 1$ nm, the forward-in-time amplitude of the dominant component $X_{2p-3d}^{(1)}$ exceeds 0.9 for the line with the frequency Ω_1 in the free system, but when a potential barrier appears, it decreases sharply, and the amplitude $X_{2p-2s}^{(1)}$ starts to dominate at $U \approx 0.5$ eV. In this case, the component $X_{2p-3d}^{(1)}$ does not tend to zero (as was the case at $R = 1$ nm), but retains a finite value of about 0.4, and thus the excited state turns out to be mixed based on two channels coupled by correlation interaction. The situation is reversed for the other mode with the frequency Ω_2 : an increase in the barrier height leads to an increase in the contribution of the $2p \rightarrow 3d$ channel while the finite value of the amplitude $X_{2p-2s}^{(1)}$ is retained.

Let us focus more closely on the dependences for the absolute values of the backward-in-time amplitude for the more correlated $2p \rightarrow 3d$ channel (see the insets in Fig. 4, *c*, *d*). For spectral line 1, the absolute value of the amplitude $Y_{2p-3d}^{(1)}$ in the absence of potential barrier reaches about 0.3, i.e., it turns out to be of the same order as $X_{2p-3d}^{(1)}$. This makes it possible to define this mode as surface dipole plasmon with the harmonic frequency Ω_1 . As the barrier height increases, both amplitudes of the $2p \rightarrow 3d$ channel begin to decrease rapidly, and mode 1 becomes close to size quantization with dominant $2p \rightarrow 2s$ component, but with significant correlations between the channels.

the barrier more than an order of magnitude higher than the maximum energy of a single-particle dipole transition practically becomes infinitely high for this system. Thus, it turns out that the frequencies Ω_1 and Ω_2 of both RPAX modes differ significantly from the single-particle energy differences over the entire variation range of the barrier height, which means that interparticle correlations play a significant role in the formation of both excited states.

It can be seen from the dependence of oscillator strengths on the barrier height (Fig. 4, *b*) that the oscillator strengths of single-particle transitions remain virtually unchanged both at $R = 4$ nm and at $R = 1$ nm over the entire range of barrier heights U . As for collective modes, in the case of the free system at $U = 0$, there is also a single line with the frequency Ω_1 in the spectrum, including almost 100% of the sum rule, which is typical for excitations of the classical surface plasmon type. As in the previous case, oscillations with the frequency Ω_2 are practically not excited and their oscillator strength begins to manifest only with the appearance of the potential barrier. What is more, unlike the situation at $R = 1$ nm, the oscillator strength begins to markedly increase at small values ($U < 0.1$ eV) and upon reaching $U \approx 7-8$ eV, the oscillator strengths of both modes take a value of

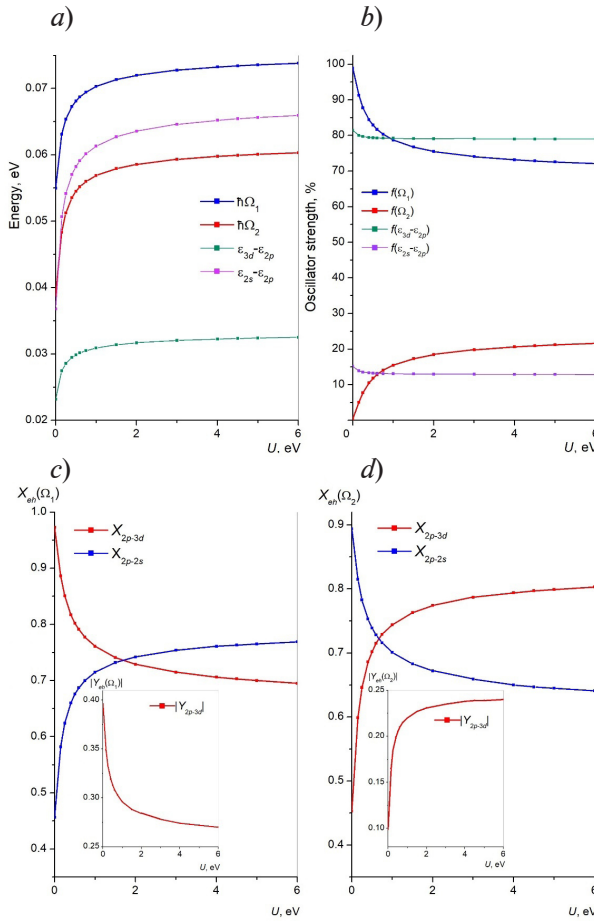


Fig. 6. Same dependences as in Figs. 3–5 but for nanocrystal radius $R = 8$ nm

the oscillator strengths of collective modes, the situation turns out to be different compared to the results shown in Fig. 3. As seen from Figs. 5, *b* and 6, *b*, the potential barrier appearing at the system boundary no longer leads to significant redistribution of oscillator strengths of dipole modes. Despite the appearance of the spectral line with the frequency Ω_2 , the contribution of the mode with Ω_1 (as follows from the data in Figs. 5, *b* and 6, *b*) remains dominant, further gaining dominance with increasing radius R and reaching large values of U in the limit (about 75% of the total value in the sum rule) at $R = 8$ nm.

On the other hand, as in the situations discussed above, the interaction of the electron system with the potential barrier leads to redistribution of the contributions of single-particle channels to the collective excited state. The increase in the potential on the surface of the nanoparticle still causes a redistribution of amplitudes of single-particle channels $X_{im}^{(k)}$ in collective excitations. However, the contributions of the transitions $2p \rightarrow 3d$ and $2p \rightarrow 2s$ remain of the same order over most of the entire variation range of U (see Figs. 5, *c*, *d* and 6, *c*, *d*). Thus, significant interchannel correlations in both excited states ensure their many-particle nature both in the absence of the barrier and in its presence. Furthermore, it follows from the dependences for the absolute value of backward-in-time amplitudes $Y_{im}^{(k)}(U)$ shown in the insets that the ratio of the coefficients $|Y|/X$ turns out to be smaller than or approximately equal to 0.2 for all values of the barrier height U , which serves as an indicator of plasmonic nature of both collective modes.

Thus, it can be concluded for the considered system with eight delocalized electrons ($N = 8$) that the appearance of a potential barrier at its boundary at $R > 4$ nm does not lead to a transition to the size quantization for any of the modes, while electron density fluctuations retain the character of dipole surface plasmons. The same conclusion is can be drawn by analyzing the

The absolute value of the amplitude $Y_{2p \rightarrow 3d}^{(2)}$ for mode 2, whose oscillator strength increases considerably at $U \approx 2$ eV, also increases to about 0.2, and since the $2p \rightarrow 3d$ channel is the main one for this excitation at $U \geq 2$ eV, then, as with $R = 1$ nm, this mode also becomes a correlated many-particle state. The relative contributions of both excitations to the sum of oscillator strengths turn out to be equal, and thus none of the modes can be described as purely radial or purely rotational oscillations.

Excited states in nanocrystals with radii $R = 6$ and 8 nm. Calculations indicate that a further increase in the geometric dimensions of the system leads to a number of changes in the spectral characteristics of the nanocrystal under study. As the radius R of the system increases, the energy of the single-particle levels further decreases (Figs. 5, *a* and 6, *a*), but the corresponding oscillator strengths for the ground-state transitions $2p \rightarrow 3d$ and $2p \rightarrow 2s$ virtually do not change compared with the cases $R = 1$ and 4 nm (see Figs. 5, *b* and 6, *b*). The relative increase in the energy difference between excited states in RPAX, the frequencies Ω_1 and Ω_2 as well as the energy differences between single-particle levels continues, which indicates a further increase in the role of interparticle correlations in the formation of collective modes (8). As for



radial dependence of transition density for the system with $R = 6$ nm (see Fig. 2,d), which has a maximum at the outer boundary of the electron density for both excited states in the presence of the potential barrier with the height $U = 6$ eV at the nanocrystal boundary.

Conclusion

We considered the excited states in spherical cadmium sulfide nanocrystals of various dimensions containing 8 delocalized electrons. The interparticle interaction of electrons with each other is described by the Dirac–Slater local exchange potential. To account for the correlation effects, the random phase approximation with exchange (RPAX) was used to describe the wave functions of collective excited states.

It was found for the limit of free systems in the absence of a potential barrier at the boundary that a dominant plasmon line with a frequency Ω_1 is present in the excitation spectrum. In addition, there are two ground-state transitions in the considered systems; accounting for them within RPAX yielded results virtually identical to the results obtained accounting for full basis of single-particle excitations. The dominant line turned out to be significantly correlated, i.e., it has a many-particle nature.

The appearance of a potential barrier at the nanocrystal boundary leads to an increase in the second resonant mode with the frequency Ω_2 . For nanocrystals with the radius $R = 1$ nm, as the barrier height increases, the modes change places and the second mode starts to dominate. This effect disappears as the system's dimensions increase. In particular, for nanocrystals with the radius $R = 4$ nm, with sufficiently large heights of the potential barrier, there is clearly no predominant mode, while the first line continues to dominate for larger systems at any height of the barrier.

Furthermore, as the dimensions of the system increase, interparticle correlations gain a more prominent role in the formation of the dominant dipole modes.

As for the nature of the excitations, when the system's radius is less than 4 nm, a transition to size quantization occurs for the mode Ω_1 with increasing height of the potential barrier. For nanocrystals with larger radii, such a transition does not occur for any modes or at any height of the potential barrier.

To summarize, we considered the influence of potential barrier height at the boundary and the influence of the geometric dimensions of nanocrystals on the nature of excited states in CdS nanocrystals containing 8 delocalized electrons and located in a dielectric medium.

However, to validate the obtained dependences and properties of spectral characteristics for any such systems, it is necessary to study the excited states of nanocrystals containing a larger number of free carriers.

Appendix

Application of two-level model within RPAX

If we assume that matrix elements (12) are real, Eqs. (9) and (10) can generally be rewritten in matrix form

$$\begin{pmatrix} \mathbf{A} & \mathbf{B} \\ \mathbf{B} & \mathbf{A} \end{pmatrix} \begin{pmatrix} \mathbf{X}^{(k)} \\ \mathbf{Y}^{(k)} \end{pmatrix} = \Omega_k \begin{pmatrix} \mathbf{X}^{(k)} \\ -\mathbf{Y}^{(k)} \end{pmatrix}, \quad (\text{A1})$$

and as a system of linear equations:

$$\begin{cases} \mathbf{A}\mathbf{X}^{(k)} + \mathbf{B}\mathbf{Y}^{(k)} = \Omega_k \mathbf{X}^{(k)} \\ \mathbf{B}\mathbf{X}^{(k)} + \mathbf{A}\mathbf{Y}^{(k)} = -\Omega_k \mathbf{Y}^{(k)} \end{cases}. \quad (\text{A2})$$

After sequential addition and subtraction of Eqs. (A2), we obtain, respectively, equations of the form

$$\begin{cases} (\mathbf{A} + \mathbf{B})(\mathbf{X}^{(k)} + \mathbf{Y}^{(k)}) = \Omega_k (\mathbf{X}^{(k)} - \mathbf{Y}^{(k)}) \\ (\mathbf{A} - \mathbf{B})(\mathbf{X}^{(k)} - \mathbf{Y}^{(k)}) = \Omega_k (\mathbf{X}^{(k)} + \mathbf{Y}^{(k)}) \end{cases}. \quad (\text{A3})$$

Expressing the difference $(\mathbf{X}^{(k)} - \mathbf{Y}^{(k)})$ on the right-hand side of the first equation in (A3) as

$$(\mathbf{X}^{(k)} - \mathbf{Y}^{(k)}) = \Omega_k (\mathbf{A} - \mathbf{B})^{-1} (\mathbf{X}^{(k)} + \mathbf{Y}^{(k)}), \quad (\text{A4})$$

we obtain the following equation for the vector $(\mathbf{X}^{(k)} + \mathbf{Y}^{(k)})$:

$$(\mathbf{A} + \mathbf{B})(\mathbf{X}^{(k)} + \mathbf{Y}^{(k)}) = \Omega_k^2 (\mathbf{A} - \mathbf{B})^{-1} (\mathbf{X}^{(k)} + \mathbf{Y}^{(k)}) \quad (\text{A5})$$

After premultiplying and postmultiplying Eq. (A5) by the matrix $(\mathbf{A} - \mathbf{B})^{-1/2}$ and using the obvious relation

$$(\mathbf{A} - \mathbf{B})^{1/2} (\mathbf{A} - \mathbf{B})^{-1/2} = 1, \quad (\text{A6})$$

Eq. (A5) can be reduced to a more symmetrical form:

$$\left((\mathbf{A} - \mathbf{B})^{1/2} (\mathbf{A} + \mathbf{B}) (\mathbf{A} - \mathbf{B})^{1/2} \right) (\mathbf{A} - \mathbf{B})^{-1/2} (\mathbf{X}^{(k)} + \mathbf{Y}^{(k)}) = \Omega_k^2 (\mathbf{A} - \mathbf{B})^{-1/2} (\mathbf{X}^{(k)} + \mathbf{Y}^{(k)}). \quad (\text{A7})$$

If we introduce new notations

$$\begin{aligned} \mathbf{F} &= (\mathbf{A} - \mathbf{B})^{1/2} (\mathbf{A} + \mathbf{B}) (\mathbf{A} - \mathbf{B})^{1/2} \\ \mathbf{Z}^{(k)} &= (\mathbf{A} - \mathbf{B})^{-1/2} (\mathbf{X}^{(k)} + \mathbf{Y}^{(k)}) \end{aligned} \quad (\text{A8})$$

then the matrix equation with respect to the eigenvectors $\mathbf{Z}^{(k)}$ takes the form

$$\mathbf{F} \mathbf{Z}^{(k)} = \Omega_k^2 \mathbf{Z}^{(k)}. \quad (\text{A9})$$

Now it remains to determine the normalization condition for $\mathbf{Z}^{(k)}$ in accordance with Eq. (17); it follows the identity

$$(\mathbf{X}^{(k)} + \mathbf{Y}^{(k)}) (\mathbf{X}^{(k)} - \mathbf{Y}^{(k)}) \equiv \sum_{im} (X_{im}^{(k)} + Y_{im}^{(k)}) (X_{im}^{(k)} - Y_{im}^{(k)}) = 1. \quad (\text{A10})$$

It follows from Eqs. (A7) and (A3), respectively, that

$$(\mathbf{X}^{(k)} + \mathbf{Y}^{(k)}) = (\mathbf{A} - \mathbf{B})^{1/2} \mathbf{Z}^{(k)}, \quad (\text{A11})$$

$$(\mathbf{X}^{(k)} - \mathbf{Y}^{(k)}) = \Omega_k (\mathbf{A} - \mathbf{B})^{-1} (\mathbf{X}^{(k)} + \mathbf{Y}^{(k)}) = \Omega_k (\mathbf{A} - \mathbf{B})^{-1/2} \mathbf{Z}^{(k)}. \quad (\text{A12})$$

Thus, according to equalities (A10)–(A12), normalization of the eigenvectors follows the expression

$$\sum_{im} (X_{im}^{(k)} + Y_{im}^{(k)}) (X_{im}^{(k)} - Y_{im}^{(k)}) = \Omega_k (\mathbf{A} - \mathbf{B})^{1/2} (\mathbf{A} - \mathbf{B})^{-1/2} \sum_{im} (Z_{im}^{(k)})^2 = \Omega_k \sum_{im} (Z_{im}^{(k)})^2 = 1. \quad (\text{A13})$$

We assume that the eigenvectors obtained by solving Eq. (A9) are initially normalized in accordance with the condition $\sum_{im} (Z_{im}^{(k)})^2 = 1$, so their elements should be subsequently renormalized to satisfy the requirement

$$\sum_{im} (Z_{im}^{(k)})^2 = \Omega_k^{-1}. \quad (\text{A14})$$

In turn, this transforms expression (16) for the oscillator strengths as follows:

$$D_k = \Omega_k^{-1/2} \sum_{im} d_{im} \left((\mathbf{A} - \mathbf{B})^{1/2} \mathbf{Z}^{(k)} \right)_{im}, \quad (\text{A15})$$

where the elements of the vector $\mathbf{Z}^{(k)}$ are normalized by unity, i.e., $|\mathbf{Z}^{(k)}| = 1$.

Now, after considering the general case, let us examine the special one, when the interparticle exchange interaction is described in the local density approximation, for example, using local exchange potentials (6) and (14). In this case, the elements of matrices (12) turn out to be equal, namely

$$\langle in | U | mj \rangle = \langle ij | U | mn \rangle,$$

and, consequently, the following equations hold true:

$$\begin{aligned} \mathbf{A} + \mathbf{B} &= \boldsymbol{\omega} + 2\mathbf{U}, \\ \mathbf{A} - \mathbf{B} &= \boldsymbol{\omega}, \end{aligned} \quad (\text{A16})$$

and, thus, expressions (A8) take the following form:

$$\begin{aligned} \mathbf{F} &= \boldsymbol{\omega}^{1/2} (\boldsymbol{\omega} + 2\mathbf{U}) \boldsymbol{\omega}^{1/2}, \\ \mathbf{Z}^{(k)} &= \boldsymbol{\omega}^{-1/2} (\mathbf{X}^{(k)} + \mathbf{Y}^{(k)}). \end{aligned} \quad (\text{A17})$$

In turn, the oscillator strengths (A15) are now expressed in terms of the elements of the eigenvectors $\mathbf{Z}^{(k)}$ as

$$D_k = \Omega_k^{-1/2} \sum_{im} \omega_{im}^{1/2} d_{im} Z_{im}^{(k)}. \quad (\text{A18})$$

Thus, applying the RPAX equation in the form (A9) taking into account expressions (A17) allows to reduce the dimension of the matrix by two times compared to the initial expression (10), but unfortunately, this makes it impossible to independently analyze the contribution of the forward-in-time and backward-in-time amplitudes to superposition (8) characterizing the many-particle excited state.

If the dominant contribution to superposition of single-particle excitations (8) is given by only two ground-state transitions, conventionally denoted by the subscripts 1 and 2, the matrix equation (A9) takes the form of a system of two linear equations:

$$\begin{cases} (\Omega^2 - \omega_1(\omega_1 + 2U_{11}))Z^{(1)} - 2(\omega_1\omega_2)^{1/2}U_{12}Z^{(2)} = 0, \\ -2(\omega_1\omega_2)^{1/2}U_{21}Z^{(1)} + (\Omega^2 - \omega_2(\omega_2 + 2U_{22}))Z^{(2)} = 0, \end{cases} \quad (\text{A19})$$

where ω_1, ω_2 are the frequencies of the corresponding transitions and the condition $U_{12} = U_{21}$ is satisfied for matrix elements.

The condition that the determinant of system (A19) be equal to zero implies a second-order algebraic equation with respect to the squared frequencies of collective excitations Ω^2 :

$$\Omega^4 + b\Omega^2 + c = 0, \quad (\text{A20})$$

where

$$\begin{aligned} b &= -(\omega_1^2 + \omega_2^2 + 2(\omega_1 U_{11} + \omega_2 U_{22})), \\ c &= \omega_1 \omega_2 ((\omega_1 + 2U_{11})(\omega_2 + U_{22}) - 4U_{12}^2). \end{aligned} \quad (\text{A21})$$

It is easy to verify that in the limiting case of non-interacting particles at

$$U_{ij} = 0, b = -(\omega_1^2 + \omega_2^2) \text{ and } c = \omega_1^2 \omega_2^2$$

we obtain the following trivial solution:

$$\Omega_{1,2} = \frac{1}{2} \left((\omega_1^2 + \omega_2^2) \pm \sqrt{(\omega_1^2 + \omega_2^2)^2 - 4\omega_1^2 \omega_2^2} \right) = \begin{cases} \omega_1 \\ \omega_2 \end{cases}.$$

REFERENCES

1. Klimov V. V., Nanoplasmonics, Jenny Stanford Publishing, New York, 2014.
2. Bozhevolnyi S. I., Martin-Moreno L., Garcia-Vidal F. (Eds.), Quantum plasmonics (Springer Series in Solid-State Sciences. Vol. 185), Springer International Publishing, Cham, Switzerland, 2017.
3. Enoch S., Bonod N., Plasmonics: From basics to advanced topics. (Springer Series in Optical Sciences. Vol. 167), Springer-Verlag, Heidelberg, Berlin, 2012.
4. Tame M. S., McEnery K. R., Özdemir Ş. K., et al., Quantum plasmonics, Nat. Phys. 9 (June) (2013) 329–340.
5. Fedorov A. V., Rukhlenko I. D., Baranov A. V., Kruchinin S. Yu., Optical properties of semiconductor quantum dots, Nauka, Saint-Petersburg, 2011 (in Russian).
6. Gusev A. I., Nanomaterials, nanostructures, and nanotechnologies, Fizmatlit, Moscow, 2005 (in Russian).
7. Gaponenko S. V., Optical properties of semiconductor nanocrystals, Cambridge University Press, Cambridge, 1998.
8. Routzahn A. L., White S. L., Fong L.-K., Jain P. K., Plasmonics with doped quantum dots, Isr. J. Chem. 52 (11–12) (2012) 983–991.
9. Klimov V. I., Thompson B. J., Nanocrystal quantum dots, Second edition, CRC Press, Boca Raton, Florida, USA, 2010.
10. Kriegel I., Scotognella F., Manna L., Plasmonic doped semiconductor nanocrystals: Properties, fabrication, applications and perspectives, Phys. Rep. 674 (28 Febr) (2017) 1–52.
11. Scotognella F., Della Valle G., Kandada A. R. S., et al., Plasmonics in heavily-doped semiconductor nanocrystals, Eur. Phys. J. B. 86 (4) (2013) 154.
12. Liu X., Swihart M. T., Heavily-doped colloidal semiconductor and metal oxide nanocrystals, an emerging new class of plasmonic nanomaterials, Chem. Soc. Rev. 43 (11) (2014) 3908–3920.
13. El-Sayed M. A., Small is different: Shape-, size-, and composition-dependent properties of some colloidal semiconductor nanocrystals, Acc. Chem. Res. 37 (5) (2004) 326–333.
14. Luther J. M., Jain P. K., Ewers T., Alivisatos A. P., Localized surface plasmon resonances arising from free carriers in doped quantum dots, Nat. Mater. 10 (May) (2011) 361–366.
15. Faucheaux J. A., Stanton A. L. D., Jain P. K., Plasmon resonances of semiconductor nanocrystals: Physical principles and new opportunities, J. Phys. Chem. Lett. 5 (6) (2014) 976–985.
16. Lounis S. D., Runnerstrom E. L., Bergerud A., et al., Influence of dopant distribution on the plasmonic properties of indium tin oxide nanocrystals, J. Am. Chem. Soc. 136 (19) (2014) 7110–7116.
17. Zhang H., Kulkarni V., Prodan E., et al., Theory of quantum plasmon resonances in doped semiconductor nanocrystals, J. Phys. Chem. C. 118 (29) (2014) 16035–16042.
18. Schimpf A. M., Thakkar N., Gunthardt C. E., et al., Charge-tunable quantum plasmons in colloidal semiconductor nanocrystals, ACS Nano. 8 (1) (2014) 1065–1072.
19. Schimpf A. M., Gunthardt C. E., Rinehart J. D., et al., Controlling carrier densities in photochemically reduced colloidal ZnO nanocrystals, J. Am. Chem. Soc. 135 (44) (2013) 16569–16577.
20. Ipatov A. N., Gerchikov L. G., Guet C., Plasmon resonance in photoabsorption of colloidal highly doped ZnO nanocrystals, Nanoscale Res. Lett. 13 (1) (2018) 297.
21. Gerchikov L. G., Ipatov A. N., Rotational dipole plasmon mode in nanoscale semiconductor particles, J. Exp. Theor. Phys., 132 (6) (2021) 922–940.
22. Ipatov A. N., Dipole plasmon mode in nanosize semiconductor core-shell quantum dots with a type II heterojunction, J. Exp. Theor. Phys., 136 (6) (2023) 765–777.

23. **Gerchikov L. G., Guet C., Ipatov A. N.**, Multiple plasmons and anharmonic effects in small metallic clusters, *Phys. Rev. A*. 66 (5) (2002) 053202.
24. **Ipatov A. N., Gerchikov L. G., Guet C.**, Resonant photoabsorption of metallic clusters in a strong laser field, *Comput. Mater. Sci.* 35 (3) (2006) 347–353.
25. **Ipatov A. N., Kupriianov G. A.**, The plasmon resonance in the cadmium selenide semiconductor nanocrystals with different doping types, *St. Petersburg State Polytechnical University J. Phys. and Math.* 16 (2) (2023) 27–51 (in Russian).
26. **Dreizler R. M., Gross E. K. U.**, Density functional theory: An approach to the quantum many-body problem, Springer, Berlin, 1990.
27. **Madjet M., Guet G., Johnson W. R.**, Comparative study of exchange-correlation effects on electron and optical properties of alkali-metal clusters, *Phys. Rev. A*. 51 (2) (1995) 1327–1339.
28. **Mukherjee D.**, Applied many-body methods in spectroscopy and electronic structure, Springer, New York, 1992.
29. **Landau L. D., Lifshitz E. M.**, Quantum mechanics. Non-relativistic theory (Course of theoretical physics. Vol. 3), Pergamon Press, Oxford, London, New York, Paris, 1965.
30. **Bertsch G. F., Broglia R. A.**, Oscillations in finite quantum systems, Cambridge University Press, Cambridge, 1994.

СПИСОК ЛИТЕРАТУРЫ

1. **Климов В. В.** Наноплазмоника. М.: Физматлит, 2009. 480 с.
2. **Bozhevolnyi S. I., Martin-Moreno L., Garcia-Vidal F.** (Eds.) Quantum plasmonics. (Springer Series in Solid-State Sciences. Vol. 185). Cham, Switzerland: Springer International Publishing, 2017. 327 p.
3. **Enoch S., Bonod N.** Plasmonics: From basics to advanced topics. (Springer Series in Optical Sciences. Vol. 167). Heidelberg, Berlin: Springer-Verlag, 2012. 321 p.
4. **Tame M. S., McEneaney K. R., Özdemir Ş. K., Lee J., Maier S. A., Kim M. S.** Quantum plasmonics // *Nature Physics*. 2013. Vol. 9. June. Pp. 329–340.
5. **Федоров А. В., Рухленко И. Д., Баранов А. В., Кручинин С. Ю.** Оптические свойства полупроводниковых квантовых точек. СПб.: Наука, 188. 2011 с.
6. **Гусев А. И.** Наноматериалы, наноструктуры, нанотехнологии. М.: Физматлит, 2005. 416 с.
7. **Gaponenko S. V.** Optical properties of semiconductor nanocrystals. Cambridge, UK: Cambridge University Press, 1998. 245 p.
8. **Routzahn A. L., White S. L., Fong L.-K., Jain P. K.** Plasmonics with doped quantum dots // *Israel Journal of Chemistry*. 2012. Vol. 52. No. 11–12. Pp. 983–991.
9. **Klimov V. I., Thompson B. J.** Nanocrystal quantum dots. Second edition. Boca Raton, Florida, USA: CRC Press, 2010. 485 p.
10. **Kriegel I., Scotognella F., Manna L.** Plasmonic doped semiconductor nanocrystals: Properties, fabrication, applications and perspectives // *Physics Reports*. 2017. Vol. 674. 28 February. Pp. 1–52.
11. **Scotognella F., Della Valle G., Kandada A. R. S., Zavelani-Rossi M., Longhi S., Lanzani G., Tassone F.** Plasmonics in heavily-doped semiconductor nanocrystals // *The European Physical Journal B*. 2013. Vol. 86. No. 4. P. 154.
12. **Liu X., Swihart M. T.** Heavily-doped colloidal semiconductor and metal oxide nanocrystals, an emerging new class of plasmonic nanomaterials // *Chemical Society Reviews*. 2014. Vol. 43. No. 11. Pp. 3908–3920.
13. **El-Sayed M. A.** Small is different: Shape-, size-, and composition-dependent properties of some colloidal semiconductor nanocrystals // *Accounts of Chemical Research*. 2004. Vol. 37. No. 5. Pp. 326–333.
14. **Luther J. M., Jain P. K., Ewers T., Alivisatos A. P.** Localized surface plasmon resonances arising from free carriers in doped quantum dots // *Nature Materials*. 2011. Vol. 10. May. Pp. 361–366.
15. **Faucheaux J. A., Stanton A. L. D., Jain P. K.** Plasmon resonances of semiconductor nanocrystals: Physical principles and new opportunities // *The Journal of Physical Chemistry Letters*. 2014. Vol. 5. No. 6. Pp. 976–985.
16. **Lounis S. D., Runnerstrom E. L., Bergerud A., Nordlund D., Milloron D. J.** Influence of dopant distribution on the plasmonic properties of indium tin oxide nanocrystals // *Journal of the American Chemical Society*. 2014. Vol. 136. No. 19. Pp. 7110–7116.

17. Zhang H., Kulkarni V., Prodan E., Nordlander P., Govorov A. O. Theory of quantum plasmon resonances in doped semiconductor nanocrystals // *The Journal of Physical Chemistry C*. 2014. Vol. 118. No. 29. Pp. 16035–16042.
18. Schimpf A. M., Thakkar N., Gunthardt C. E., Masiello D. J., Gamelin D. R. Charge-tunable quantum plasmons in colloidal semiconductor nanocrystals // *ACS Nano* (The American Chemical Society). 2014. Vol. 8. No. 1. Pp. 1065–1072.
19. Schimpf A. M., Gunthardt C. E., Rinehart J. D., Mayer J. M., Gamelin D. R. Controlling carrier densities in photochemically reduced colloidal ZnO nanocrystals // *Journal of the American Chemical Society*. 2013. Vol. 135. No. 44. Pp. 16569–16577.
20. Ipatov A. N., Gerchikov L. G., Guet C. Plasmon resonance in photoabsorption of colloidal highly doped ZnO nanocrystals // *Nanoscale Research Letters*. 2018. Vol. 13. No. 1. P. 297.
21. Герчиков Л. Г., Ипатов А. Н. Вращательная дипольная плазмонная мода в наноразмерных полупроводниковых частицах // *Журнал экспериментальной и теоретической физики*. 2021. Т. 159. № 6. С. 1047–1069.
22. Ипатов А. Н. Дипольная плазмонная мода в наноразмерных полупроводниковых квантовых точках типа «ядро-оболочка» с гетеропереходом второго рода // *Журнал экспериментальной и теоретической физики*. 2023. Т. 163. № 6. С. 858–872.
23. Gerchikov L. G., Guet C., Ipatov A. N. Multiple plasmons and anharmonic effects in small metallic clusters // *Physical Review A*. 2002. Vol. 66. No. 5. P. 053202.
24. Ipatov A. N., Gerchikov L. G., Guet C. Resonant photoabsorption of metallic clusters in a strong laser field // *Computational Materials Science*. 2006. Vol. 35. No. 3. Pp. 347–353.
25. Ипатов А. Н., Куприянов Г. А. Плазмонный резонанс в полупроводниковых нанокристаллах селенида кадмия с различным типом легирования // *Научно-технические ведомости СПбГПУ. Физико-математические науки*. 2023. Т. 16. № 2. С. 27–51.
26. Dreizler R. M., Gross E. K. U. Density functional theory: An approach to the quantum many-body problem. Berlin: Springer, 1990. 302 p.
27. Madjet M., Guet G., Johnson W. R. Comparative study of exchange-correlation effects on electron and optical properties of alkali-metal clusters // *Physical Review A*. 1995. Vol. 51. No. 2. Pp. 1327–1339.
28. Mukherjee D. Applied many-body methods in spectroscopy and electronic structure. New York, USA: Springer, 1992. 299 p.
29. Ландау Л. Д., Лифшиц Е. М. Теоретическая физика. В 10 тт. Т. 3. Квантовая механика (нерелятивистская теория). – 4е изд., испр. М.: Наука. Гл. ред. физ.-мат. лит.-ры, 1989. 768 с.
30. Bertsch G.F., Broglia R.A. Oscillations in finite quantum systems. Cambridge, UK: Cambridge University Press, 1994. 232 p.

THE AUTHORS

IPATOV Andrei N.

*Peter the Great St. Petersburg Polytechnic University,
Alferov University of RAS*
29 Politechnicheskaya St., St. Petersburg, 195251, Russia
andrei_ipatov@mail.ru
ORCID: 0000-0003-1457-8236

KUPRIANOV Genrikh A.

Peter the Great St. Petersburg Polytechnic University
29 Politechnicheskaya St., St. Petersburg, 195251, Russia
henryweis3@gmail.com
ORCID: 0009-0001-5775-2276



СВЕДЕНИЯ ОБ АВТОРАХ

ИПАТОВ Андрей Николаевич — доктор физико-математических наук, профессор кафедры физики Санкт-Петербургского политехнического университета Петра Великого и профессор кафедры физики и технологии наногетероструктур Санкт-Петербургского академического университета имени Ж. И. Алфёрова РАН.

195251, Россия, г. Санкт-Петербург, Политехническая ул., 29

andrei_ipatov@mail.ru

ORCID: 0000-0003-1457-8236

КУПРИЯНОВ Генрих Александрович — ассистент кафедры физики Санкт-Петербургского политехнического университета Петра Великого.

195251, Россия, г. Санкт-Петербург, Политехническая ул., 29

henryweis3@gmail.com

ORCID: 0009-0001-5775-2276

Received 06.05.2024. Approved after reviewing 02.12.2024. Accepted 02.12.2024.

Статья поступила в редакцию 06.05.2024. Одобрена после рецензирования 02.12.2024. Принята 02.12.2024.

Научное издание

**НАУЧНО-ТЕХНИЧЕСКИЕ ВЕДОМОСТИ САНКТ-ПЕТЕРБУРГСКОГО
ГОСУДАРСТВЕННОГО ПОЛИТЕХНИЧЕСКОГО УНИВЕРСИТЕТА.
ФИЗИКО-МАТЕМАТИЧЕСКИЕ НАУКИ**

**«ST. PETERSBURG STATE POLYTECHNICAL UNIVERSITY JOURNAL.
PHYSICS AND MATHEMATICS»**

ТОМ 18, № 2, 2025

Учредитель и издатель – Федеральное государственное автономное образовательное учреждение высшего образования «Санкт-Петербургский политехнический университет Петра Великого»

Журнал зарегистрирован Федеральной службой по надзору в сфере информационных технологий и массовых коммуникаций (Роскомнадзор).
Свидетельство о регистрации ПИИ № ФС77-51457 от 19.10.2012 г.

Редакция

д-р физ.-мат. наук, профессор *В. К. Иванов* – председатель ред. коллегии
д-р физ.-мат. наук, профессор *А. Э. Фотиади* – зам. председателя ред. коллегии
д-р физ.-мат. наук, профессор *В. В. Дубов*
д-р физ.-мат. наук, профессор *П. А. Карасёв*
канд. физ.-мат. наук, доцент *В. М. Капралова*
канд. физ.-мат. наук *О. А. Яцурижнская* – научный редактор, корректор
А. С. Колгатина – переводчик
Н. А. Бушманова – ответственный секретарь

Телефон редакции 8 (812) 552-62-16

Сайт <https://physmath.spbstu.ru/>

E-mail: physics@spbstu.ru

Компьютерная верстка *Н. А. Бушмановой*

Подписано в печать 30.06.2025. Формат 60х84/8. Печать цифровая.
Усл. печ. л. Тираж 1000. Заказ .

Отпечатано с готового оригинал-макета, предоставленного ИЦ "ИКИ",
в Издательско-полиграфическом центре
Санкт-Петербургского политехнического университета.
195251, Санкт-Петербург, Политехническая ул., 29.
Тел.: (812) 552-77-17; 550-40-14.

УСЛОВИЯ ПУБЛИКАЦИИ СТАТЕЙ

в журнале «Научно-технические ведомости
Санкт-Петербургского государственного политехнического университета.
Физико-математические науки»

1. ОБЩИЕ ПОЛОЖЕНИЯ

Журнал «Научно-технические ведомости Санкт-Петербургского государственного политехнического университета. Физико-математические науки» является периодическим печатным научным рецензируемым изданием. Зарегистрирован в Федеральной службе по надзору в сфере информационных технологий и массовых коммуникаций (Свидетельство ПИ №ФС77-52144 от 11 декабря 2012 г.) и распространяется по подписке агентства «Роспечать» (индекс издания 71823).

С 2008 года журнал издавался в составе сериального издания "Научно-технические ведомости СПбГПУ". **Сохраняя преемственность и продолжая научные и публикационные традиции сериального издания «Научно-технические ведомости СПбГПУ», журнал издавали под сдвоенными международными стандартными сериальными номерами ISSN 1994-2354 (сериальный) 2304-9782.** В 2012 году он зарегистрирован как самостоятельное периодическое издание **ISSN 2304-9782** (Свидетельство о регистрации ПИ № ФС77-52144 от 11 декабря 2012 г.). С 2012 г. начат выпуск журнала в двуязычном оформлении.

Издание входит в Перечень ведущих научных рецензируемых журналов и изданий (перечень ВАК) и принимает для печати материалы научных исследований, а также статьи для опубликования основных результатов диссертаций на соискание ученой степени доктора наук и кандидата наук по следующим основным научным направлениям: **Физика, Математика, Механика**, включая следующие шифры научных специальностей: 1.1.8., 1.1.9., 1.3.2., 1.3.3., 1.3.4., 1.3.5., 1.3.6., 1.3.7., 1.3.8., 1.3.11., 1.3.19.

Журнал представлен в Реферативном журнале ВИНТИ РАН и включен в фонд научно-технической литературы (НТЛ) ВИНТИ РАН, а также в международную систему по периодическим изданиям «Ulrich's Periodicals Directory». Индексирован в базах данных «Российский индекс научного цитирования» (РИНЦ), Web of Science (Emerging Sources Citation Index).

Периодичность выхода журнала – 4 номера в год.

Редакция журнала соблюдает права интеллектуальной собственности и со всеми авторами научных статей заключает издательский лицензионный договор.

2. ТРЕБОВАНИЯ К ПРЕДСТАВЛЯЕМЫМ МАТЕРИАЛАМ

2.1. Оформление материалов

1. Рекомендуемый объем статей – 12-20 страниц формата А-4 с учетом графических вложений. Количество графических вложений (диаграмм, графиков, рисунков, фотографий и т.п.) не должно превышать шести.

2. Число авторов статьи, как правило, не должно превышать пяти человек.

3. Авторы должны придерживаться следующей обобщенной структуры статьи: вводная часть (актуальность, существующие проблемы – объем 0,5 – 1 стр.); основная часть (постановка и описание задачи, методика исследования, изложение и обсуждение основных результатов); заключительная часть (предложения, выводы – объем 0,5 – 1 стр.); список литературы (оформление по ГОСТ 7.0.5-2008).

В списки литературы **рекомендуется** включать ссылки на научные статьи, монографии, сборники статей, сборники конференций, электронные ресурсы с указанием даты обращения, патенты.

Как правило, **нежелательны** ссылки на диссертации и авторефераты диссертаций (такие ссылки допускаются, если результаты исследований еще не опубликованы, или не представлены достаточно подробно).

В списки литературы **не рекомендуется** включать ссылки на учебники, учебно-методические пособия, конспекты лекций, ГОСТы и др. нормативные документы, на законы и постановления, а также на архивные документы (если все же необходимо указать такие источники, то они оформляются в виде сносок).

Рекомендуемый объем списка литературы для обзорных статей – не менее 50 источников, для остальных статей – не менее 10.

Доля источников давностью менее 5 лет должна составлять не менее половины. Допустимый процент самоцитирования – не выше 10 – 20. Объем ссылок на зарубежные источники должен быть не менее 20%.

4. УДК (UDC) оформляется и формируется в соответствии с ГОСТ 7.90-2007.

5. Набор **текста** осуществляется в редакторе **MS Word**.

6. **Формулы** набираются в редакторе MathType (не во встроенном редакторе Word) (мелкие формулы, символы и обозначения набираются без использования редактора формул). **Таблицы** набираются в том же формате, что и основной текст. В тексте буква «ё» заменяется на букву «е» и оставляется только в фамилиях.

7. **Рисунки** (в формате .tiff, .bmp, .jpeg) и **таблицы** оформляются в виде отдельных файлов. Шрифт – **Times New Roman**, размер шрифта основного текста – 14, интервал – 1,5. Таблицы большого размера могут быть набраны кеглем 12. Параметры страницы: поля слева – 3 см, сверху и снизу – 2 см, справа – 1,5 см. Текст размещается без знаков переноса. Абзацный отступ – 1 см.

2.2. Представление материалов

1. Представление всех материалов осуществляется в электронном виде через электронную редакцию (<http://journals.spbstu.ru>). После регистрации в системе электронной редакции автоматически формируется персональный профиль автора, позволяющий взаимодействовать как с редакцией, так и с рецензентом.

2. Вместе с материалами статьи должно быть представлено экспертное заключение о возможности опубликования материалов в открытой печати.

3. Файл статьи, подаваемый через электронную редакцию, должен содержать только сам текст без названия, списка литературы, аннотации и ключевых слов, фамилий и сведений об авторах. Все эти поля заполняются отдельно через электронную редакцию.

2.3. Рассмотрение материалов

Предоставленные материалы (п. 2.2) первоначально рассматриваются редакционной коллегией и передаются для рецензирования. После одобрения материалов, согласования различных вопросов с автором (при необходимости) редакционная коллегия сообщает автору решение об опубликовании статьи. В случае отказа в публикации статьи редакция направляет автору мотивированный отказ.

При отклонении материалов из-за нарушения сроков подачи, требований по оформлению или как не отвечающих тематике журнала материалы не публикуются и не возвращаются.

Редакционная коллегия не вступает в дискуссию с авторами отклоненных материалов.

При поступлении в редакцию значительного количества статей их прием в очередной номер может закончиться **ДОСРОЧНО**.

E-mail: physics@spbstu.ru,

Тел. редакции 8 (812) 552-62-16.

Сайт журнала: <https://phymath.spbstu.ru/>